Universidade do Porto

Faculdade de Engenharia

FEUP

Continuum Modelling and Numerical Simulation of Damage for Ductile Materials

Dissertation presented to the Faculty of Engineering, University of Porto, as a requirement to obtain the Ph.D. degree in Mechanical Engineering, carried out under the supervision of Professor Francisco Manuel Andrade Pires, Associate Professor, Faculty of Engineering, University of Porto and Professor José Manuel de Almeida César de Sá, Full Professor, Faculty of Engineering, University of Porto

Lucival Malcher

Faculdade de Engenharia Universidade do Porto

Porto

2012

à minha família

AGRADECIMENTOS

Em primeiro lugar, gostaria de agradecer o apoio dado pelo meus orientadores Dr. Francisco Manuel de Andrade Pires e Dr. José César de Sá, durante o desenvolvimento deste trabalho e principalmente pela oportunidade de ter feito este doutoramento na FEUP. Gostaria de agradecer também a Fundação para a Ciência e Tecnologia - FCT, pelo apoio financeiro dado.

Agradecimentos especiais vão também aos colegas de estudo e grandes amigos Dr. Filipe Xavier Costa Andrade, Dr. Thiago Doca e Dr. Fabio José Pinho Reis. Obrigado pelo apoio, conversas, discussões e pela grande troca de experiência e influência no tema deste trabalho. Agradeço o sempre apoio do Professor Dr. José Carlos Balthazar, da Universidade de Brasília, que foi meu orientador tanto durante minha graduação quanto no mestrado concluído na UnB.

Agradeço à minha mãe (Graça Malcher Ávila) e pai (Antonio Ávila) pelo grande incentivo em levar estes estudos com garra até o seu fim.

Por fim, meus maiores agradecimentos vão para minha esposa Cyntia de Souza Malcher, que acreditou no meu sonho e vontade de seguir estes estudos fora de nosso conforto e país.

RESUMO

A correta determinação da fratura em materiais dúcteis tem avançado enormemente nos últimos anos e assim, o aperfeiçoamento de novas formulações e técnicas que sejam capazes de melhorar o comportamento preditivo de modelos constitutivos tornou-se um grande objeto de estudo para pesquisadores em todo o mundo. O avanço da indústria e a procura de técnicas que possibilitem o aumento da competitividade, fez com que tais desenvolvimentos acadêmicos passassem a ser adotados por inúmeros setores como o automobilístico, o aeroespacial, o naval, entre outros. Desta forma, nesta tese, procura-se contribuir para o desenvolvimento e aperfeiçoamento de modelos constitutivos e numéricos que sejam capazes de determinar, da maneira mais realística possível, o comportamento mecânico de materiais metálicos. Para isto, como primeira etapa do trabalho, sugere-se um algoritmo de integração numérica implícita para um modelo elasto-plástico avançado, que inclui a influência da pressão hidrostática e do terceiro invariante do tensor desviador, na lei de fluxo plástico de um material metálico. Após esta proposição, busca-se avaliar o comportamento preditivo de três formulações constitutivas disponíveis na literatura para determinação do correto local e momento de início de uma fenda dúctil. São então avaliados, o modelo de Bai e Wierzbicki, o modelo de Lemaitre e o modelo de Gurson em uma versão modificada e conhecida por GTN. Como etapa seguinte desta tese, procurou-se avaliar o desempenho de dois mecanismos de corte, um proposto por Xue e outro por Nahshon et al., acoplados ao modelo GTN e aplicados à região de baixa triaxialidade. Nesta etapa, avaliou-se a influência da relação entre a condição de calibração dos parâmetros materiais e a condição de uso, na capacidade preditiva dos modelos com variáveis interna de dano acoplada. Com base nos resultados observados, na etapa seguinte, propõe-se um novo modelo constitutivo, baseado na formulação de Gurson e na dedução geométrica da lei de evolução do mecanismo de corte de Xue, de maneira a aumentar a capacidade preditiva no que se refere a: determinação do nível esperado de deformação plástica equivalente na fratura, o nível de deslocamento na fratura e o potencial local para início da fratura dúctil, bem como reduzir a influência do ponto de calibração na precisão dos resultados numéricos obtidos quando o modelo é aplicado a largas faixas de triaxialidade. Por fim, o modelo desenvolvido com base na teoria de Gurson, que agora passa a denominar de "extended GTN model", é testado em condições complexas de carregamento, com o intuito de se avaliar a influência da história do carregamento no comportamento mecânico de materiais e a capacidade preditiva do modelo. Para isto, introduz-se o efeito de Bauschinger no modelo, através do acoplamento da lei de fluxo plástico com uma lei de endurecimento cinemático, como proposto por Prager.

ABSTRACT

Accurate determination of fractures in ductile materials has improved significantly in recent years, and so the development of new formulations and techniques to improve the performance of predictive constitutive models has become a major topic of study for researchers worldwide. Industry progress and demand for techniques that allow for increased competitiveness caused such academic developments to spread into numerous industries, such as the automotive, aerospace and shipbuilding sectors, among others. Thus, this thesis seeks to contribute to the development and refinement of constitutive and numerical models to determine the mechanical behavior of metallic materials as realistically as possible. To this end, the first step is to propose an implicit numerical integration algorithm for an advanced elasto-plastic model, which includes the influence of hydrostatic pressure and third invariant of deviator tensor on the plastic flow rule for a metallic material. Once this proposition has been made, the predictive performance of three constitutive formulations available in the literature are analyzed for determining the exact place and time of development of a ductile crack. The Bai and Wierzbicki model, the Lemaitre model and the Gurson model are then evaluated in a modified version known as GTN. The next step in this thesis was to evaluate the performance of two shear mechanisms – a mechanism proposed by Xue and another mechanism proposed by Nahshon et al., coupled with the GTN model and applied to the range of low stress triaxiality. In this step, the influence of the relationship between the calibration condition material parameters and use condition was evaluated with regard to the predictive ability of the models with coupled internal damage variables. Based on the results, in the following step a new constitutive model is proposed that is based on Gurson's formulation and the geometric deduction of Xue's evolution law for the shear mechanism so as to increase predictive ability with respect to: determining the expected level of equivalent plastic strain at fracture, the level of displacement at fracture and the local potential for development of a ductile fracture, as well as reducing the influence of the calibration point on the accuracy of numerical results obtained when the model is applied to wide range of stress triaxiality. Finally, the model based on Gurson's theory – now called the "extended GTN model" – is tested under complex loading conditions in order to evaluate the influence of the loading history on the mechanical behavior of materials and predictive ability of the model. To this end, the Bauschinger effect is introduced in the model by coupling the plastic flow rule with a kinematic hardening law as proposed by Prager for the evolution of the back stress.

CONTENTS

CHAPTER 1

Introduction

1.1 GENERAL CONSIDERATIONS

The correct prediction of fracture in ductile materials has become, in recent years, a matter of great importance for several competitive sectors of industry such as automotive, aerospace, marine, military, among others. For example, weight reduction in vehicle structures such as chassis and bodies, without loss of performance and competitiveness, has used design criteria that neglect the determination of the correct time and place for the start of a crack. This approach has clearly significant limitations and the design of new products requires careful planning of each step for its development, and manufacturing optimization.

In the last two decades, there has been a substantial increase in the awareness, of the industrial environment, of the great potential that emerges from the application of scientific methods for the design of these new products. At each step, you must ensure that the products developed and the applied processes are optimized, especially in competitive sectors of the industry, such as metallurgical industry, and simultaneously meet the functionality requirements and low cost of production. To overcome the problems encountered during the design and development phases, and still maintain a competitive advantage, it is of the utmost importance to be constantly updated with the latest scientific and technological progress.

Since the end of the sixties, a number of mathematical models have been formulated to describe the macroscopic behavior of ductile metallic materials, like steel, aluminum alloys, among others. The model proposed by McClintock (1968), which assumes the void within a metal matrix in the form of a cylinder, the model proposed by Rice and Tracey (1969) that considers the void as a perfect sphere, the Gurson-Tvergaard-Needleman (GTN) model (1977 and 1984) which describes the elastic-plastic behavior of porous materials, the model proposed by Lemaitre

(1985) that assumes the principles of continuous damage mechanics, the models proposed by Oyane (1978), Cockcroft and Latham (1968) and Johnson and Cook (1985) based on experimental observations, are some of the best-known models in the literature to describe the elastic-plastic behavior of ductile materials. Figure 1.1 shows some examples of the use of mathematical models, within the finite element framework, to design and optimize structures and mechanical components. Such models can be used both in the simulation of failure of structures, stress analysis of mechanical components and optimization of production processes.

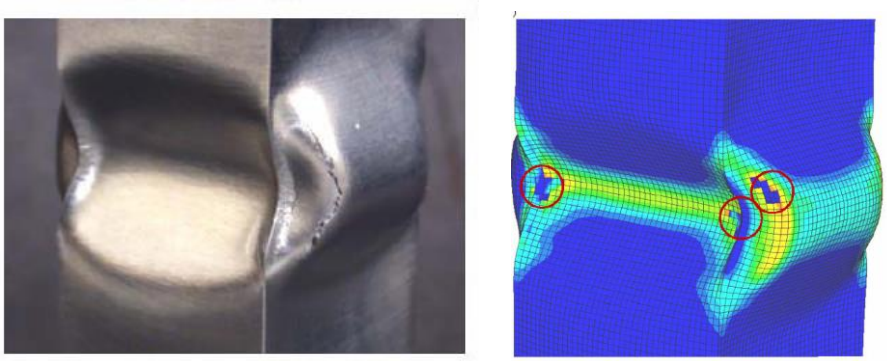

(a)

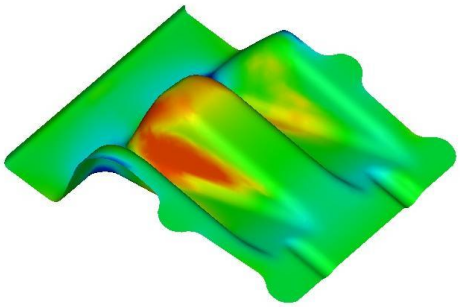

(b)

Figure 1.1. Examples of the use of constitutive models to describe the elastic-plastic behavior of structures and mechanical components, (Bai, 2008).

1.2 EVOLUTION AND IMPORTANCE OF DAMAGE MECHANICS

Since the pioneering work of Kachanov (1958), many developments in applied mechanics were made in order to formulate new constitutive models that are able to describe the internal degradation of solids, according to the principles of Continuum Mechanics. After five decades of research, significant progress has been observed and the so-called Continuum Damage Mechanics (CDM) theory has emerged as an alternative approach for the introduction of new state variables in constitutive models (Lemaitre, 1985).

The material behavior can be modeled by constitutive equations, taking into account its progressive deterioration. These models are based on the assumption that the internal damage can effectively be represented by one or more internal variables, which may be of scalar, vector or tensorial nature. These variables, called damage variables can represent a measure of defects within a representative volume (RV). Its development should comply with constitutive thermodynamic relations, usually represented by a system of differential equations in time. Based on CDM, many different constitutive models have already been proposed, such as Lemaitre (1985) model to characterize damage caused by plastic flow, Chaboche (1984) and Murakami & Ohmo (1981) models to describe fretting damage, Krajeinovic & Fonseka (1981) model for fragile damage, among others.

In recent years, the need to have robust and reliable models for use in engineering projects, coupled with the advent and the popularity of digital computers, led to the progressive development of numerical techniques. The constant improvement of numerical models and associated algorithms, together with the significant increase in processing capacity *versus* the cost of computers, made a significant impact on the acceptance of numerical techniques within the academic and industrial environments. The numerical methods, mainly based on the Finite Element Method, have been continuously developed and improved, for both linear and nonlinear applications. Particularly, in the solution of nonlinear problems of solid mechanics, there have been considerable advances in several topics of research. In many areas, the numerical methods have achieved a high

degree of predictive ability and, today, are of great help to the designer and an essential tool for solving real engineering problems.

During the development of numerical algorithms for the analysis of stress, the description of the constitutive response of the material was dominated by the theory of elasticity and elastic-(visco) plasticity. Over the years, the finite element techniques based on these constitutive models have been continuously modified and adapted to deal with more complex deformations, which may include: large deflections, finite deformations, viscous effects, among others. In particular, the advances made in the numerical simulation of large deformation problems in the presence of finite inelastic deformations (Peri'C & Owen, 2004), had a major impact on the simulation of metal forming.

Despite these advances, many questions remain open, such as the modeling problems related to failure (fracture) of materials resulting from the progressive deterioration associated with micro structural deformations. In such cases, the development of new and more sophisticated constitutive models deserves careful consideration and therefore, the subject remains an important area of research and development.

There are several technological processes, which should greatly benefit from a better understanding and quantification of the different physical phenomena that occur close to rupture of ductile materials. Metal cutting, for example, is a technological process used to manufacture a large number of products and is currently used by a large number of companies. The importance of this process is underlined by the fact that almost every object we use in our society, has one or more machined surfaces. Due to its massive use, the effectiveness of this process has a considerable impact on the quality and cost of the products obtained. Therefore, understanding the process of removing the chip is of vital importance in material selection and design tools, as well as in ensuring the dimensional accuracy and surface integrity of the final product.

1.3 LAYOUT

The thesis is divided into eight chapters. In the first one, the introduction and motivation of the work is undertaken. After that, Chapter 2 presents a brief review

over the physical aspects of the structure of metals and the theoretical aspects related to damage mechanics. In addition, the kinematics of deformation, the stress and equilibrium, the fundamental laws of thermodynamics, the constitutive theory, the weak equilibrium and the finite element modeling of finite strain plasticity are also addressed.

Chapter 3 describes in detail the derivation of an implicit solution for numerical integration of a new elastic-plastic model, which is dependent on both pressure and Lode angle. The constitutive model is presented as well as the numerical strategy employed. Several numerical tests are carried out in order to demonstrate the efficiency of the algorithm proposed.

In chapter 4, three well established ductile failure models employed to determine fracture onset are presented: the Gurson´s theory, highlighting the Gurson-Tvergaard-Needleman (GTN) model as well as the Lemaitre's model both with isotropic hardening and isotropic damage. Besides these, an advanced elastic-plastic model coupled with a fracture indicator is chosen, in order to perform an assessment of isotropic damage constitutive models under high and low stress triaxiality.

In chapter 5, a theoretical and numerical study is done, based on Gurson-Tvergaard-Needleman (GTN) model, in order to evaluate the prediction of fracture initiation under a low level of stress triaxiality. Some recently proposed shear mechanisms are presented and assessed as damage variables in the constitutive formulation. Besides that, the influence of the calibration point on the numerical results for coupled damage models is studied, presenting some numerical results for two different calibration points.

In chapter 6, an extension to the Gurson-Tvergaard-Needleman (GTN) model is proposed, in order to predict fracture onset. A new shear mechanism is presented and two independent nucleation mechanisms are created in order to trigger the growth contribution. The complete constitutive formulation and the numerical strategy are described in detail together with several numerical tests.

The loading history effect on ductile fracture is studied on chapter 7, based on the micromechanical formulation proposed in chapter 6. Three different loading

conditions are simulated and the numerical results are discussed, based on experimental data. Finally, in chapter 8, a short summary and the conclusions of this work are presented along with suggestions for future research.

CHAPTER 2

Continuum Mechanics, Laws of Thermodynamics and Constitutive Theory

In this chapter, a brief summary of the basic concepts of continuum mechanics is presented, as well as, the fundamental laws of thermodynamics of continuous media and the use of internal variables to formulate constitutive models of dissipative materials. The main subjects addressed are: the kinematics of deformation, stress and equilibrium, the laws of thermodynamics, constitutive theory and weak equilibrium through the principle of virtual.

2.1. KINEMATICS OF DEFORMATION

In this section, the theory related to the description of kinematics of deformation is presented where the concepts of motion and deformation are addressed.

2.1.1. Configurations and motions of continuum bodies

Within the three-dimensional Euclidean space, a continuum body, $\boldsymbol{\Omega}$, with each particle labeled by the coordinates, $\boldsymbol{p} \in \boldsymbol{\Omega}$, is analyzed at a given instant of time, t. Furthermore, the reference configuration is assumed to coincide with the initial configuration, and each material particle is expressed as a function of the coordinates of $\boldsymbol{p}$. In the deformed configuration, the continuum body, $\boldsymbol{\Omega}$, occupies the region $\boldsymbol{\varphi}(\boldsymbol{\Omega})$ with boundary $\boldsymbol{\varphi}(\boldsymbol{\partial\Omega})$ defined through the deformation map $\boldsymbol{\varphi}$. Thus, the current position of a particle $\boldsymbol{p}$ of $\boldsymbol{\Omega}$ in the deformed configuration can be defined as:

$$\boldsymbol{x} = \boldsymbol{\varphi}(\boldsymbol{p}) \ , \tag{2.1}$$

where $\boldsymbol{x}$ represents the current position, $\boldsymbol{\varphi}(\,.\,)$ is the deformation map and $\boldsymbol{p}$ represents a particle embedded in the continuum body.

Then, the displacement of particle $\boldsymbol{p}$ can be represented by the vector $\boldsymbol{u}(\boldsymbol{p})$, which can be expressed by the relation:

$$\boldsymbol{u}(\boldsymbol{p}) = \boldsymbol{\varphi}(\boldsymbol{p}) - \boldsymbol{p} \ , \tag{2.2}$$

where $\boldsymbol{u}(\,.\,)$ represents the displacement vector. However, substituting Equation (2.1) into (2.2), the current position of a particle, $\boldsymbol{x}$, can also be rewritten as function of initial configuration, $\boldsymbol{p}$, and the displacement of particle $\boldsymbol{u}(\boldsymbol{p})$:

$$\boldsymbol{x} = \boldsymbol{p} + \boldsymbol{u}(\boldsymbol{p}). \tag{2.3}$$

Figure 2.1 represents the initial and deformed configuration of the continuum body $\boldsymbol{\Omega}$ and the reference and current position of particle $\boldsymbol{p}$, regarding a displacement $\boldsymbol{u}(\boldsymbol{p})$.

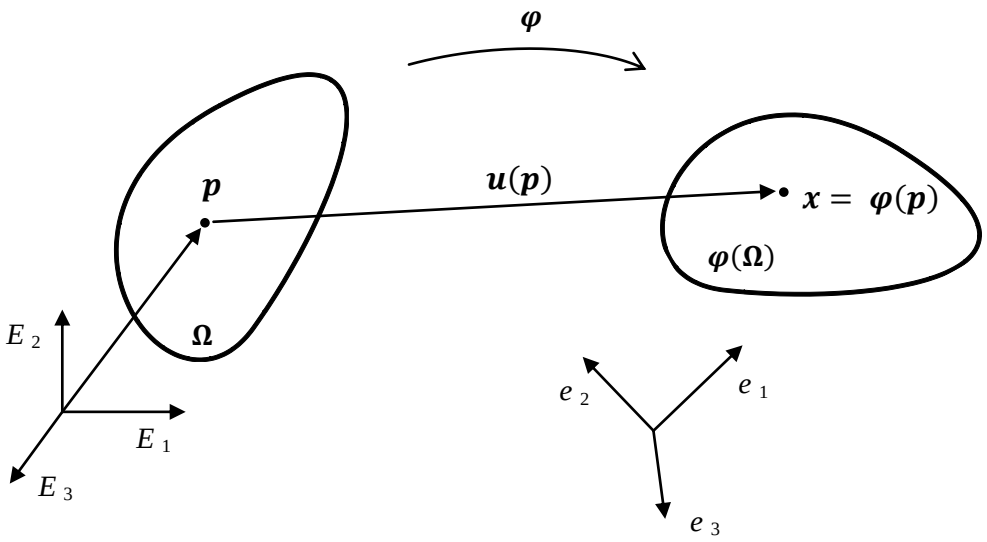

Figure 2.1. Configurations of a deformable body.

If we consider a rigid deformation, the deformation of the continuum body, $\boldsymbol{\Omega}$, preserves the distances between all material particles of the body, and can be: a translation, a rotation or a combination of a translation and a rotation. A rigid translation is a deformation with constant displacement vector, which is represented by:

$$\boldsymbol{\varphi}(\boldsymbol{p}) = \boldsymbol{p} + \boldsymbol{u} \, . \tag{2.4}$$

For a rigid rotation, the deformation is mathematically expressed as:

$$\boldsymbol{\varphi}(\boldsymbol{p}) = \boldsymbol{q} + \boldsymbol{R}(\boldsymbol{p} - \boldsymbol{q}) \, , \tag{2.5}$$

where $\boldsymbol{R}$ represents a proper orthogonal tensor (a rotation tensor) and $\boldsymbol{q}$ represents the point about which $\boldsymbol{\Omega}$ is rotated. A deformation is rigid, containing translations and rotations, if and only if it can be expressed as:

$$\boldsymbol{\varphi}(\boldsymbol{p}) = \boldsymbol{\varphi}(\boldsymbol{q}) + \boldsymbol{R}(\boldsymbol{p} - \boldsymbol{q}) , \tag{2.6}$$

where the above expression represents a deformation map for a rigid translation with displacement $\boldsymbol{\varphi}(\boldsymbol{q}) - \boldsymbol{q}$, superimposed on a rigid rotation $\boldsymbol{R}$ about point $\boldsymbol{q}$.

A time-dependent deformation of the continuum body $\boldsymbol{\Omega}$, is called like a motion of body $\boldsymbol{\Omega}$. Thus, the motion can be defined by a function $\boldsymbol{\varphi}$ so that for each time t, the map $\boldsymbol{\varphi}(\cdot, t)$ is a deformation of $\boldsymbol{\Omega}$. Now, regarding the motion $\boldsymbol{\varphi}$, the position $\boldsymbol{x}$ of a material particle $\boldsymbol{p}$ at time t is expressed by:

$$\boldsymbol{x} = \boldsymbol{\varphi}(\boldsymbol{p}, t) . \tag{2.7}$$

Furthermore, the deformed configuration of the continuum body, $\boldsymbol{\varphi}(\boldsymbol{\Omega}, t)$, denotes the region of three dimensional space occupied by the body $\boldsymbol{\Omega}$ at time t. Typically, the current position of these particles is located, by the coordinates $\boldsymbol{x}$ with respect to an alternative Cartesian basis $\boldsymbol{e}_i$ (see Figure 2.1). If we consider the displacement field, the motion can be expressed by:

$$\boldsymbol{\varphi}(\boldsymbol{p}, t) = \boldsymbol{p} + \boldsymbol{u}(\boldsymbol{p}, t) , \tag{2.8}$$

where $\boldsymbol{u}(\boldsymbol{p}, t)$ represents the displacement of particle $\boldsymbol{p}$ at time t. Since at each time t the map $\boldsymbol{\varphi}(\cdot, t)$ is one-to-one by assumption, the material points can be expressed as a function of the place that each one occupies at a time t by:

$$\boldsymbol{p} = \boldsymbol{\varphi}^{-1}(\boldsymbol{x}, t) = \boldsymbol{x} - \boldsymbol{u}(\boldsymbol{\varphi}^{-1}(\boldsymbol{x}, t), t) , \tag{2.9}$$

where $\boldsymbol{\varphi}^{-1}$ represents the reference map. In finite deformation analysis, no assumption is made for the magnitude of the displacement, $\boldsymbol{u}(\boldsymbol{p}, t)$, indeed it may even exceed the initial dimensions of the body as in the case, for instance, of metal forming. Nevertheless, in infinitesimal deformation analysis the displacement $\boldsymbol{u}(\boldsymbol{p}, t)$ is assumed to be small in comparison with the dimensions of the continuum body, and geometrical changes can be, a priori, ignored.

Time dependence

For non-linear problems, the dependency of deformation on the time, $\boldsymbol{\varphi}(\boldsymbol{p}, t)$, must be considered. Throughout a motion, $\boldsymbol{\varphi}$, the velocity and acceleration of a material particle, $\boldsymbol{p}$, can be determined by the first and second derivatives of the motion with respect to time. Equation (2.10) represents both quantities:

$$\dot{\boldsymbol{x}}(\boldsymbol{p}, t) = \frac{\partial \boldsymbol{\varphi}(\boldsymbol{p}, t)}{\partial t} \quad \text{and} \quad \ddot{\boldsymbol{x}}(\boldsymbol{p}, t) = \frac{\partial^2 \boldsymbol{\varphi}(\boldsymbol{p}, t)}{\partial^2 t} \,, \tag{2.10}$$

where $\dot{\boldsymbol{x}}(\boldsymbol{p}, t)$ and $\ddot{\boldsymbol{x}}(\boldsymbol{p}, t)$ represent, respectively, the first and second derivatives of the motion in respect to time. Using the reference map, $\boldsymbol{\varphi}^{-1}$, the following functions can be defined:

$$\boldsymbol{v}(\boldsymbol{x}, t) \equiv \dot{\boldsymbol{x}}(\boldsymbol{\varphi}^{-1}(\boldsymbol{x}, t), t) \quad \text{and} \quad \boldsymbol{a}(\boldsymbol{x}, t) \equiv \ddot{\boldsymbol{x}}(\boldsymbol{\varphi}^{-1}(\boldsymbol{x}, t), t) \,, \tag{2.11}$$

where $\boldsymbol{v}$ and $\boldsymbol{a}$ denote the spatial description of the velocity field and acceleration field, respectively.

2.1.2. Material and spatial descriptions

Under finite deformations, a judicious distinction has to be made between the coordinate systems that can be chosen to describe the behavior of the continuum body $\boldsymbol{\Omega}$. Considering, for the sake of simplicity, a scalar time dependent quantity, α, defined over the body $\boldsymbol{\Omega}$.

(a) *Material description*: if the value of α is expressed as a function of material particles, $\boldsymbol{p}$, and time, t, with respect to the domain $\boldsymbol{\Omega} \times \mathbb{R}^3$, then α can be called as a material field, defined as:

$$\alpha_m(\boldsymbol{p}, t). \tag{2.12}$$

(b) *Spatial description*: otherwise, if the value of α is expressed as a function of a spatial position, $\boldsymbol{x}$, and time, t, with respect to the domain $\boldsymbol{\varphi}_t(\Omega) \times \mathbb{R}^3$, then α can be called as a spatial field, defined as:

$$\alpha_s(\boldsymbol{x}, t). \tag{2.13}$$

The above descriptions are also employed for both vector and tensor fields. The material and spatial descriptions are alternatively referred to as Lagrangian and Eulerian descriptions, respectively.

Material and spatial gradients, divergences and time derivatives

If we consider a scalar field α, the material and spatial gradients can be defined by the following expressions:

$$\nabla_p \alpha = \frac{\partial}{\partial \boldsymbol{p}} \alpha_m(\boldsymbol{p}, t) \quad \text{and} \quad \nabla_x \alpha = \frac{\partial}{\partial \boldsymbol{x}} \alpha_s(\boldsymbol{x}, t) \ , \tag{2.14}$$

where $\nabla_p \alpha$ and $\nabla_x \alpha$ denote, respectively, the material and spatial gradients, which are the derivatives of α with respect to $\boldsymbol{p}$ and $\boldsymbol{x}$ holding t fixed. In addition, the material and spatial divergence of a vector field $\boldsymbol{r}$, are respectively, given by:

$$\mathrm{div}_p \boldsymbol{r} = \mathrm{tr}\left(\nabla_p \boldsymbol{r}\right) \quad \text{and} \quad \mathrm{div}_x \boldsymbol{r} = \mathrm{tr}(\nabla_x \boldsymbol{r}) \ . \tag{2.15}$$

Considering now, a tensor field $\boldsymbol{T}$, the spatial and material divergence are given, in Cartesian components, by:

$$\left(\mathrm{div}_p \boldsymbol{T}\right)_i = \frac{\partial T_{ij}}{\partial p_j} \quad \text{and} \quad (\mathrm{div}_x \boldsymbol{T})_i = \frac{\partial T_{ij}}{\partial x_j} \ . \tag{2.16}$$

Similarly, the material and spatial time derivatives of α, denoted respectively $\dot{\alpha}_m$ and $\dot{\alpha}_s$, are defined by:

$$\dot{\alpha}_m = \frac{\partial}{\partial t} \alpha_m(\boldsymbol{p}, t) \quad \text{and} \quad \dot{\alpha}_s = \frac{\partial}{\partial t} \alpha_s(\boldsymbol{x}, t) \ . \tag{2.17}$$

The material time derivative $\dot{\alpha}_m$ measures the rate of change of α at a fixed material particle $\boldsymbol{p}$. The spatial time derivative $\dot{\alpha}_s$, on the other hand, measures the rate of change of α observed at a fixed spatial position x.

2.1.3. The deformation gradient

Let us examine the deformation gradient of the motion $\boldsymbol{\varphi}$, which establishes the relation between quantities before deformation to corresponding quantities after (or during) deformation. Mathematically, the deformation gradient is defined by a second order tensor:

$$\boldsymbol{F}(\boldsymbol{p}, t) = \nabla_p \boldsymbol{\varphi}(\boldsymbol{p}, t) = \frac{\partial \boldsymbol{x}_t}{\partial \boldsymbol{p}} \ , \tag{2.18}$$

where $\boldsymbol{F}$ represents the deformation gradient. Having in mind Equation (2.5), the second order tensor $\boldsymbol{F}$ can be written as:

$$\boldsymbol{F} = \boldsymbol{I} + \nabla_p \boldsymbol{u} \ , \tag{2.19}$$

where $\boldsymbol{I}$ represents the second order identity tensor. The deformation gradient can also be expressed as function of Cartesian components:

$$F_{ij} = \frac{\partial x_i}{\partial p_j} = \delta_{ij} + \frac{\partial u_i}{\partial p_j} \ , \tag{2.20}$$

where the term x_i represents the components of $\boldsymbol{x}_t$. Furthermore, recalling the reference map, the tensor $\boldsymbol{F}$ may be expressed by the following expression:

$$\boldsymbol{F}(\boldsymbol{x}, t) = [\nabla_x \boldsymbol{\varphi}^{-1}(\boldsymbol{x}, t)]^{-1} = [\boldsymbol{I} - \nabla_x \boldsymbol{u}]^{-1} \ . \tag{2.21}$$

Considering an infinitesimal volume, dV, which can be written as a function of the infinitesimal vectors d$\boldsymbol{a}$, d$\boldsymbol{b}$ and d$\boldsymbol{c}$, that originates from the material particle $\boldsymbol{p}$ in the reference configuration (see Figure 2.2), the term dV is mathematically expressed by $dV = (\mathrm{d}\boldsymbol{a} \times \mathrm{d}\boldsymbol{b}).\,\mathrm{d}\boldsymbol{c}$.

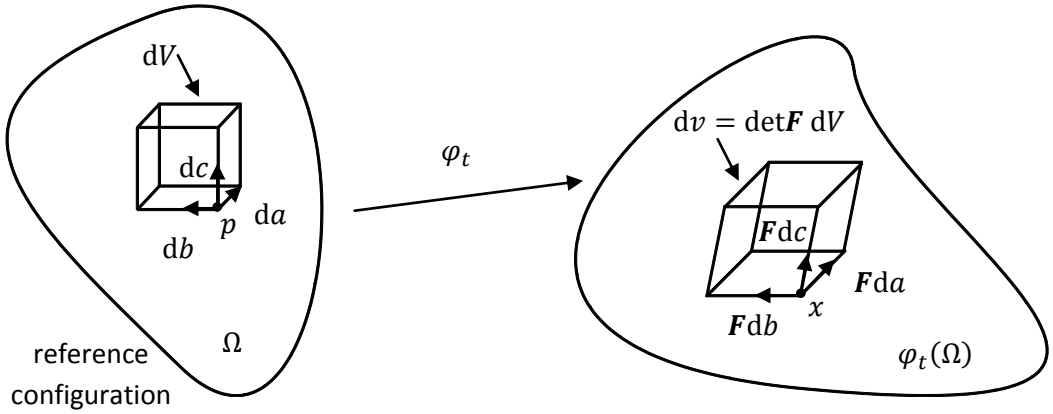

Figure 2.2. The determinant of the deformation gradient.

Consider now, a deformation map $\boldsymbol{\varphi}_t$ applied to the infinitesimal volume dV (see Figure 2.2). After mapping the infinitesimal vectors, the deformed infinitesimal volume is expressed as:

$$\mathrm{d}v = (\boldsymbol{F}\ \mathrm{d}\boldsymbol{a} \times \boldsymbol{F}\ \mathrm{d}\boldsymbol{b}).\,\boldsymbol{F}\ \mathrm{d}\boldsymbol{c} \ . \tag{2.22}$$

After some tensor manipulations, the determinant of the deformation gradient can also be denoted by Equation (2.23), which represents the volume after deformation per unit reference volume,

$$\det\boldsymbol{F} = \frac{(\boldsymbol{F}\ \mathrm{d}\boldsymbol{a} \times \boldsymbol{F}\ \mathrm{d}\boldsymbol{b}).\,\boldsymbol{F}\ \mathrm{d}\boldsymbol{c}}{(\mathrm{d}\boldsymbol{a} \times \mathrm{d}\boldsymbol{b}).\,\mathrm{d}\boldsymbol{c}} = \frac{\mathrm{d}v}{\mathrm{d}V} \ , \tag{2.23}$$

where the term $\det\boldsymbol{F}$ represents the determinant of the deformation gradient. In Continuum Mechanics, the term J is frequently employed to denote the determinant of $\boldsymbol{F}$.

$$J = \det\boldsymbol{F} \ . \tag{2.24}$$

From the analysis of Equation (2.23), it can be concluded that if $J = 0$ then the infinitesimal volume has collapsed into a material particle, which represents a physically unacceptable situation. In the reference configuration the deformation gradient is equal to the second order identity, $\boldsymbol{F} = \boldsymbol{I}$ and, consequently, the determinant of $\boldsymbol{F}$ is a unit, $J = 1$. Thus, a configuration with $J < 0$ cannot be reached from the reference configuration without having, at some stage, $J = 0$. Therefore, in any deformed configuration of a body, J satisfies:

$$J > 0 \, . \tag{2.25}$$

Isochoric/volumetric split of the deformation gradient

The deformation gradient, $\boldsymbol{F}$, can also, locally, be decomposed as a purely volumetric deformation followed by an isochoric deformation or as an isochoric deformation followed by a pure volumetric deformation. Mathematically, the multiplicative split of the deformation gradient is expressed by:

$$\boldsymbol{F} = \boldsymbol{F}_{\text{iso}} \, \boldsymbol{F}_{\text{v}} = \boldsymbol{F}_{\text{v}} \, \boldsymbol{F}_{\text{iso}} \, , \tag{2.26}$$

where the purely volumetric component $\boldsymbol{F}_{\text{v}}$ is defined as:

$$\boldsymbol{F}_{\text{v}} \equiv \ (\det\boldsymbol{F})^{\frac{1}{3}} \, \boldsymbol{I} \, , \tag{2.27}$$

and the isochoric component $\boldsymbol{F}_{\text{iso}}$, which is volume preserving or unimodular, is expressed by:

$$\boldsymbol{F}_{\text{iso}} \equiv \ (\det\boldsymbol{F})^{\frac{1}{3}} \, \boldsymbol{F} \, . \tag{2.28}$$

It is important highlight that, by construction, $\boldsymbol{F}_{\text{v}}$ corresponds indeed to a purely volumetric deformation and, since

$$\det\boldsymbol{F}_{\text{v}} = \ \left[(\det\boldsymbol{F})^{\frac{1}{3}}\right]^{3} \boldsymbol{I} = \det\boldsymbol{F} \, , \tag{2.29}$$

$\boldsymbol{F}_{\text{v}}$ produces the same volume change as $\boldsymbol{F}$. The isochoric component, in turn, represents a volume preserving deformation, that is,

$$\det \boldsymbol{F}_{\text{iso}} = \left[(\det \boldsymbol{F})^{\frac{1}{3}} \right]^3 \det \boldsymbol{F} = 1 \ . \tag{2.30}$$

2.1.4. Polar decomposition: Stretches and rotation

The deformation gradient $\boldsymbol{F}$ can be decomposed in terms of stretch and rotation components, by applying the polar decomposition, which is expressed as:

$$\boldsymbol{F} = \boldsymbol{R}\boldsymbol{U} = \boldsymbol{V}\boldsymbol{R} \, , \tag{2.31}$$

where $\boldsymbol{U}$ is the right stretch tensor, with a basis in the reference configuration, and $\boldsymbol{V}$ is the left stretch tensor, which is an object in the current configuration. The second order tensor $\boldsymbol{R}$ is a proper orthogonal tensor, which is a local rotation tensor, connecting both configurations. The right and left stretch tensors can be related by the rotation tensor, as:

$$\boldsymbol{V} = \boldsymbol{R}\boldsymbol{U}\boldsymbol{R}^{\mathrm{T}}, \tag{2.32}$$

where, the term $\boldsymbol{R}^{\mathrm{T}}$ represents the transposed of the rotation tensor. In fact, the following expressions can relate the tensors $\boldsymbol{F}$, $\boldsymbol{U}$ and $\boldsymbol{V}$:

$$\boldsymbol{U} = \sqrt{\boldsymbol{C}} \quad \text{and} \quad \boldsymbol{V} = \sqrt{\boldsymbol{b}} \, , \tag{2.33}$$

where $\boldsymbol{C}$ and $\boldsymbol{b}$ are called, respectively, as the right and left Cauchy-Green tensors. However, both Cauchy-Green tensors can also be defined as:

$$\boldsymbol{C} = \boldsymbol{U}^2 = \boldsymbol{F}^{\mathrm{T}}\boldsymbol{F} \quad \text{and} \quad \boldsymbol{b} = \boldsymbol{V}^2 = \boldsymbol{F}\boldsymbol{F}^{\mathrm{T}}, \tag{2.34}$$

where $\boldsymbol{F}^{\mathrm{T}}$ denotes the transposed of the deformation gradient.

Both right and left stretch tensors, which are represented by $\boldsymbol{U}$ and $\boldsymbol{V}$ respectively, are symmetric tensors. Therefore, according to the spectral theorem, they admit the spectral decomposition and can further be written as:

$$\boldsymbol{U} = \sum_{i=1}^{3} \lambda_i \boldsymbol{N}_i \otimes \boldsymbol{N}_i \quad \text{and} \quad \boldsymbol{V} = \textstyle\sum_{i=1}^{3} \lambda_i \boldsymbol{n}_i \otimes \boldsymbol{n}_i \ , \tag{2.35}$$

where the set of parameters $\{\lambda_1, \lambda_2, \lambda_3\}$ are the eigenvalues of $\boldsymbol{U}$ and $\boldsymbol{V}$ called the principal stretches. The vectors $\boldsymbol{N}_i$ and $\boldsymbol{n}_i$ are also unit eigenvectors of $\boldsymbol{U}$ and $\boldsymbol{V}$, respectively. The triads $\{\boldsymbol{N}_1, \boldsymbol{N}_2, \boldsymbol{N}_3\}$ and $\{\boldsymbol{n}_1, \boldsymbol{n}_2, \boldsymbol{n}_3\}$ form orthonormal bases for the space $\boldsymbol{U}$ of vectors in $\mathbb{R}^3$. They are called, respectively, the Lagrangian and Eulerian triads and define the Lagrangian and Eulerian principal directions.

Performing the substitution of Equation (2.32) into (2.35), the relationship between the eigenvectors of $\boldsymbol{V}$ and $\boldsymbol{U}$ can be established, which highlights that each vector $\boldsymbol{n}_i$ differs from the corresponding $\boldsymbol{N}_i$ by a rotation $\boldsymbol{R}$:

$$\boldsymbol{N}_i = \boldsymbol{R}\,\boldsymbol{n}_i\,. \tag{2.36}$$

The spectral decomposition of the right and left stretch tensors implies that in any deformation, the local stretching from a material particle can always be expressed as a superposition of stretches along three mutually orthogonal directions.

2.1.5. Strain Measures

Within an infinitesimal neighbourhood of a generic material particle $\boldsymbol{p}$, pure rotations can be distinguished from pure stretching by means of the polar decomposition of the deformation gradient $\boldsymbol{F}$. Furthermore, subjected to the action of pure rotations, the distances between particles within this neighbourhood remain fixed. In this case, the difference between the deformed neighbourhood of $\boldsymbol{p}$ and its reference configuration is a rigid deformation.

Otherwise, pure stretching is characterized by $\boldsymbol{U}$ or $\boldsymbol{V}$ and changes the distance between material particles. To quantify straining, which evaluates how much the tensor $\boldsymbol{U}$ or $\boldsymbol{V}$ departs from a rigid deformation $\boldsymbol{I}$, some type of strain measure has to be defined. In fact, the definition of a strain measure is somewhat arbitrary and a specific choice is usually dictated by mathematical and physical convenience. A well known family of Lagrangian strain tensors, which is based on the Lagrangian triad, is defined by:

$$\boldsymbol{E}^{(m)} = \begin{cases} \frac{1}{m}(\boldsymbol{U}^m - \boldsymbol{I}), & m \neq 0 \\ \ln[\boldsymbol{U}], & m = 0 \end{cases}, \tag{2.37}$$

where m is a real number and $\ln[\boldsymbol{U}]$ denotes the tensor logarithm of the right stretch tensor $\boldsymbol{U}$. Considering the spectral decomposition, the above expression can be rewritten as:

$$\boldsymbol{E}^{(m)} = \sum_{i=1}^{3} f(\lambda_i)\boldsymbol{N}_i \otimes \boldsymbol{N}_i\,, \tag{2.38}$$

where, the term $f(\lambda_i)$ is defined according to:

$$f(\lambda_i) = \begin{cases} \frac{1}{m}({\lambda_i}^m - 1), & m \neq 0 \\ \ln[\lambda_i], & m = 0 \end{cases}. \tag{2.39}$$

Examining particular members of the family of Lagrangian strain tensors, the Green-Lagrange strain tensor $\boldsymbol{E}^{(2)}$ arises for $m = 2$, the Biot strain tensor when $m = 1$, the Hencky ($m = 0$) and Almansi ($m = -2$) strain tensors. Note that for any m, the associated strain tensor vanishes if and only if the deformation gradient represents, locally, a rigid deformation:

$$\boldsymbol{E}^{(m)} = \boldsymbol{0} \Leftrightarrow \boldsymbol{U} = \boldsymbol{I} \Leftrightarrow \boldsymbol{F} = \boldsymbol{R}\,. \tag{2.40}$$

The same representation can also be employed to define tensors that measure strain along the principal Eulerian directions or Eulerian strain tensors. Based on the left stretch tensor, the Eulerian counterpart of the Lagrangian family of strain measures above is defined by:

$$\varepsilon^{(m)} = \begin{cases} \frac{1}{m}(\boldsymbol{V}^m - \boldsymbol{I}), & m \neq 0 \\ \ln[\boldsymbol{V}], & m = 0 \end{cases}, \tag{2.41}$$

or, employing the Eulerian triad,

$$\varepsilon^{(m)} = \sum_{i=1}^{3} f(\lambda_i)\boldsymbol{n}_i \otimes \boldsymbol{n}_i\ . \tag{2.42}$$

The relation between the Lagrangian and Eulerian strain tensors can be mathematically expressed by the equation below:

$$\varepsilon^{(m)} = \boldsymbol{R}\,\boldsymbol{E}^{(m)}\boldsymbol{R}^{\mathrm{T}}\,. \tag{2.43}$$

Both strain tensors differ by the local rotation $\boldsymbol{R}$.

2.1.6. The velocity gradient: Rate of deformation and spin

Equation (2.11) denotes the velocity, $\boldsymbol{v}(\boldsymbol{x}, t)$, as a function of the spatial coordinates. The derivative of this expression with respect to spatial coordinates defines the velocity gradient tensor as:

$$\boldsymbol{l} = \nabla_x \boldsymbol{v}\,, \tag{2.44}$$

where $\boldsymbol{l}$ represents the velocity gradient tensor. Applying the chain rule, the velocity gradient can be rephrased as:

$$\boldsymbol{l} = \frac{\partial}{\partial t}\left(\frac{\partial \boldsymbol{\varphi}}{\partial \boldsymbol{p}}\right)\frac{\partial \boldsymbol{p}}{\partial \boldsymbol{x}} = \dot{\boldsymbol{F}}\,\boldsymbol{F}^{-1}\ . \tag{2.45}$$

The tensor $\boldsymbol{l}$ can be split into its symmetric and skew parts. The symmetric component is named as the rate of deformation tensor, $\boldsymbol{d}$, and the skew component as spin tensor, $\boldsymbol{w}$, which are defined by:

$$\boldsymbol{d} = \mathrm{sym}(\boldsymbol{l}) \quad \text{and} \quad \boldsymbol{w} = \mathrm{skew}(\boldsymbol{l})\,. \tag{2.46}$$

The following notation has been used to represent both parts of the velocity gradient tensor:

$$\mathrm{sym}(\cdot) = \tfrac{1}{2}[(\cdot) + (\cdot)^T] \quad \text{and} \quad \mathrm{skew}(\cdot) = \tfrac{1}{2}[(\cdot) - (\cdot)^T]\,. \tag{2.47}$$

2.1.7. Superimposed rigid body motions and objectivity

The concept of objectivity can be understood by studying the effect of a rigid body motion superimposed on the deformed configuration. From the point of view of an observer attached to and rotating with a solid, many quantities describing the behavior of the solid remain unchanged. Such quantities, like the distance between two particles or the state of stress in the body, amongst others are said to be objective (see Holzapfel, 2000).

Although the intrinsic nature of these quantities remains unchanged, their spatial description may change. Let us consider an elemental vector d$\boldsymbol{p}$ in the initial configuration that deforms to d$\boldsymbol{x}$ and is subsequently rotated to d$\breve{\boldsymbol{x}}$ as represented in Figure 2.3.

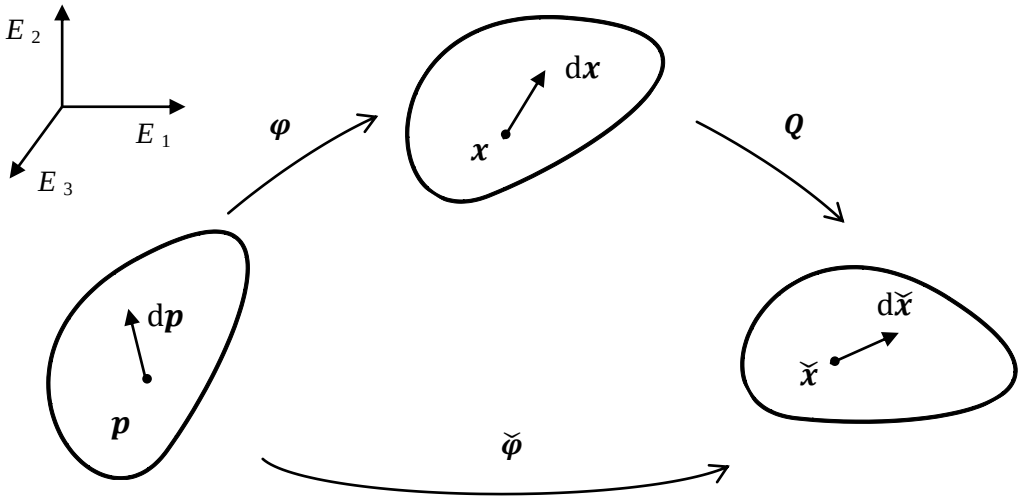

Figure 2.3. Superimposed rigid body motion.

The relationship between these elemental vectors can be established by:

$$\mathrm{d}\bar{\boldsymbol{x}} = Q\mathrm{d}\boldsymbol{x} = \boldsymbol{Q}\boldsymbol{F}\mathrm{d}\boldsymbol{p}\,, \tag{2.48}$$

where $\boldsymbol{Q}$ denotes an orthogonal tensor describing the superimposed rigid body rotation. Even though the vector $\mathrm{d}\bar{\boldsymbol{x}}$ is diferent from $\mathrm{d}\boldsymbol{x}$, their magnitudes are obviously equal. In this sense it can be said that $\mathrm{d}\boldsymbol{x}$ is objective under rigid body motions. This definition is extended to any vector $\boldsymbol{a}$ that transforms according to $\boldsymbol{a} \to \boldsymbol{Q}\boldsymbol{a}$. From Equation (2.48) it is possible to note that the deformation gradients with respect to the current and rotated configurations are related as,

$$\boldsymbol{F} \to \boldsymbol{Q}\boldsymbol{F}\ . \tag{2.49}$$

The next step consists in extending the definition of objectivity to second-order tensors. Objective second order tensors, $\boldsymbol{G}$, transform as

$$\boldsymbol{G} \to \boldsymbol{Q}\boldsymbol{G}\boldsymbol{Q}^{T}\ . \tag{2.50}$$

Obviously, material tensors (defined in the reference configuration), such as $\boldsymbol{C}$ and $\boldsymbol{E}$, are unchanged under superimposed rigid body motions.

2.2 STRESS AND EQUILIBRIUM

The stresses and equilibrium concepts need to be introduced for a deformable body subjected to a finite motion. It should be noted that, so far, no reference has been made to forces and how they are transferred within continuum bodies. Regarding the description of surface forces, the concept of stress as well as the different ways of quantifying it are presented in this section. The Cauchy's axiom is extremely important for the description of surface forces, and is stated in what follows. Consider a body $\boldsymbol{\Omega}$ in an arbitrarily deformed configuration. Let $\boldsymbol{S}$ be an oriented surface of $\boldsymbol{\Omega}$ with unit normal vector $\boldsymbol{n}$ at a point $\boldsymbol{x}$.

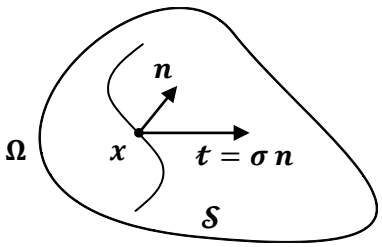

Figure 2.4. Surface forces. The Cauchy stress.

Cauchy's axiom states that: At $\boldsymbol{x}$, the surface force, or the force per unit area, exerted across $\boldsymbol{\mathcal{S}}$ by the material on the side of $\boldsymbol{\mathcal{S}}$ into which $\boldsymbol{n}$ is pointing upon the material on the other side of $\boldsymbol{\mathcal{S}}$ depends on $\boldsymbol{\mathcal{S}}$ only through its normal $\boldsymbol{n}$. This means that identical forces are transmitted across any surface with normal $\boldsymbol{n}$ at $\boldsymbol{x}$. This force (per unit area) is called the Cauchy stress vector and is represented by:

$$\boldsymbol{t}(\boldsymbol{n}) , \tag{2.51}$$

with dependence on $\boldsymbol{x}$ and time omitted for notational convenience. If $\boldsymbol{\mathcal{S}}$ belongs to the boundary of $\boldsymbol{\Omega}$ then the Cauchy stress vector represents the contact force exerted by the surrounding environment on $\boldsymbol{\Omega}$.

2.2.1 The Cauchy stress tensor

The dependency of the surface force $\boldsymbol{t}$ on the normal $\boldsymbol{n}$ is linear . This implies that there exists a tensor field $\boldsymbol{\sigma}(\boldsymbol{x})$ such that the Cauchy stress vector is given by:

$$\boldsymbol{t}(\boldsymbol{x}, \boldsymbol{n}) = \boldsymbol{\sigma}(\boldsymbol{x})\boldsymbol{n} . \tag{2.52}$$

The tensor $\boldsymbol{\sigma}$ is called the Cauchy stress tensor, which is symmetric:

$$\boldsymbol{\sigma} = \boldsymbol{\sigma}^T , \tag{2.53}$$

where $\boldsymbol{\sigma}^T$ represents the transposed stress tensor.

Deviatoric and hydrostatic stresses

Regarding constitutive modeling, it is often convenient to split the stress tensor $\boldsymbol{\sigma}$ into two parts: a spherical and a traceless component, which are represented by:

$$\boldsymbol{\sigma} = \boldsymbol{S} + p\boldsymbol{I} , \tag{2.54}$$

where the term p is a scalar that represents the hydrostatic pressure, which is defined as:

$$p \equiv \frac{1}{3}\mathrm{tr}\,\boldsymbol{\sigma} , \tag{2.55}$$

and the component $\boldsymbol{S}$ is a traceless tensor named the deviatoric stress or stress deviator:

$$\boldsymbol{S} \equiv \boldsymbol{\sigma} - p\boldsymbol{I} = \left[\mathbf{I} - \frac{1}{3}\boldsymbol{I} \otimes \boldsymbol{I}\right] : \boldsymbol{\sigma}\,, \tag{2.56}$$

where $\mathbf{I}$ is a forth order unit tensor. The spherical stress tensor can be determined by the following operation:

$$p\boldsymbol{I} = \frac{1}{3}(\boldsymbol{I} \otimes \boldsymbol{I}) : \boldsymbol{\sigma}\,, \tag{2.57}$$

and the hydrostatic pressure p is an invariant of the stress tensor.

Stress objectivity

Since the Cauchy stress tensor is of key importance to establish any equilibrium or constitutive equation, it is decisive to inquire whether $\boldsymbol{\sigma}$ is objective, as defined previously. Let us consider the transformations of the normal and traction vectors implied by the superimposed rigid body motion $\boldsymbol{Q}$ as:

$$\begin{aligned} \breve{\boldsymbol{t}}(\breve{\boldsymbol{n}}) &= \boldsymbol{Q}\boldsymbol{t}(\boldsymbol{n}) \\ \breve{\boldsymbol{n}} &= \boldsymbol{Q}\boldsymbol{n}\,, \end{aligned} \tag{2.58}$$

with dependence on $\boldsymbol{x}$ and time omitted for notational convenience. Using the relationship between the traction vector and stress tensor (Equation 2.52), in conjunction with the above quantities gives,

$$\boldsymbol{\sigma} \rightarrow \boldsymbol{Q}\boldsymbol{\sigma}\boldsymbol{Q}^{T}\,. \tag{2.59}$$

The rotation of $\boldsymbol{\sigma}$ given by the above equation conforms with the definition of objectivity for a second order tensor.

2.2.2 Alternative stress tensors

Numerous definitions of stress tensors have been proposed in the literature. Most of their components do not have a direct physical interpretation:

The Kirchhoff stress tensor: Often it is convenient to work with the so-called Kirchhoff stress tensor , $\boldsymbol{\tau}$, which differs from the Cauchy by the volume ratio J, and is defined by:

$$\boldsymbol{\tau} = J\boldsymbol{\sigma}\,. \tag{2.60}$$

Due to the symmetry of $\boldsymbol{\sigma}$**,** the Kirchhoff stress is also symmetric.

The first Piola-Kirchhoff stress tensor: The traction vector $\boldsymbol{t}$ measures the force exerted across a material surface per unit deformed area. Since in many situations the deformed configuration of $\boldsymbol{\Omega}$ is not known in advance, it is convenient to define the first Piola-Kirchhoff stress tensor,

$$\boldsymbol{P} = J\boldsymbol{\sigma}\boldsymbol{F}^{-T}. \tag{2.61}$$

This definition derives from the counterpart vector $\overline{\boldsymbol{t}}$ of $\boldsymbol{t}$ that measures, at the point of interest, the current force per unit reference area. The tensor $\boldsymbol{P}$ is often referred to as the nominal or engineering stress. Note that in contrast to the Cauchy stress, $\boldsymbol{P}$ is generally unsymmetric.

The second Piola-Kirchhoff stress tensor: It is possible to contrive a totally material symmetric stress tensor, known as the second Piola-Kirchhoff stress tensor $\boldsymbol{S}$, defined by:

$$\boldsymbol{S} = J\boldsymbol{F}^{-1}\boldsymbol{\sigma}\boldsymbol{F}^{-T}\,. \tag{2.62}$$

It often represents a very useful stress measure in computational mechanics and in the formulation of constitutive equations, in particular, for solids. In spite of the mathematical convenience, it does not admit a physical interpretation in terms of surface tractions.

2.3 FUNDAMENTAL LAWS OF THERMODYNAMICS

Firstly, it is necessary to introduce the scalar fields θ, e, s and r defined over $\boldsymbol{\Omega}$ which denote, respectively, the temperature, specific internal energy, specific entropy and the density of heat production. In addition, $\boldsymbol{f}$ and $\boldsymbol{q}$ will denote the vector fields corresponding, respectively, to the body force (force per unit volume in the deformed configuration) and heat flux.

2.3.1 Conservation of mass

The postulate of conservation of mass requires that:

$$\dot{\rho} + \rho\,\mathrm{div}_x\,\dot{\boldsymbol{u}} = 0\,, \tag{2.63}$$

where $\mathrm{div}_x\,\dot{\boldsymbol{u}}$ represents the spatial divergence of $\dot{\boldsymbol{u}}$.

2.3.2 Momentum balance

The momentum balance can be expressed by the following equations:

$$\begin{matrix} \mathrm{div}_x\, \boldsymbol{\sigma} + \boldsymbol{f} = \rho \ddot{\boldsymbol{u}} & \text{in } \varphi(\boldsymbol{\Omega}) \\ \boldsymbol{t} = \boldsymbol{\sigma}\, \boldsymbol{n} & \text{in } \varphi(\partial\boldsymbol{\Omega}) \end{matrix}, \tag{2.64}$$

where the momentum balance is expressed in local form. The term $\boldsymbol{n}$ is the outward unit vector normal to the deformed boundary $\varphi(\partial\boldsymbol{\Omega})$ of $\boldsymbol{\Omega}$, $\boldsymbol{t}$ is the boundary traction vector field on $\boldsymbol{\varphi}(\partial\boldsymbol{\Omega})$. The above momentum balance equations are formulated in the spatial (deformed) configuration. Equivalently, they may be expressed in the reference (or material) configuration of $\boldsymbol{\Omega}$ in terms of the first Piola-Kirchhoff stress tensor as:

$$\begin{matrix} \mathrm{div}_p\, \boldsymbol{P} + \bar{\boldsymbol{f}} = \bar{\rho} \ddot{\boldsymbol{u}} & \text{in } \boldsymbol{\Omega} \\ \bar{\boldsymbol{t}} = \boldsymbol{P}\, \boldsymbol{m} & \text{in } \partial\boldsymbol{\Omega} \end{matrix}, \tag{2.65}$$

where $\mathrm{div}_p\, \boldsymbol{P}$ represents the material divergence, $\bar{\boldsymbol{f}}$ is the body force measured per unit reference volume, $\bar{\rho}$ is the density in the reference configuration, which can be determined by:

$$\bar{\rho} = J\rho\,, \tag{2.66}$$

$\bar{\boldsymbol{t}}$ is the boundary traction force per unit reference area and m is the outward normal to the boundary of $\boldsymbol{\Omega}$ in its reference configuration.

2.3.3 The first principle

The first principle of thermodynamics postulates the conservation of energy. Before stating this principle, it is convenient to introduce the product:

$$\boldsymbol{\sigma}\colon \boldsymbol{d}\,, \tag{2.67}$$

which represents the stress power per unit volume in the deformed configuration of a body. The first principle of thermodynamics is mathematically expressed by the equation:

$$\rho \dot{e} = \boldsymbol{\sigma}\colon \boldsymbol{d} + \rho r - \mathrm{div}_x\, \boldsymbol{q}\,. \tag{2.68}$$

The previous equation states that the rate of internal energy per unit deformed volume must equal the sum of the stress power and heat production per unit deformed volume minus the spatial divergence of the heat flux.

2.3.4 The second principle

The second principle of thermodynamics postulates the irreversibility of entropy production. It is expressed by means of the inequality:

$$\rho\dot{s} + \mathrm{div}_x\left[\frac{\boldsymbol{q}}{\theta}\right] - \frac{\rho r}{\theta} \geq 0 \ . \tag{2.69}$$

2.3.5 The Clausius-Duhem inequality

With the first and second principles stated above, the Clausius-Duhem inequality is obtained by a combination of both principles. After some mathematical manipulation, it can be expressed by:

$$\rho\dot{s} + \mathrm{div}_x\left[\frac{\boldsymbol{q}}{\theta}\right] - \frac{1}{\theta}(\rho\dot{e} - \boldsymbol{\sigma}\colon\boldsymbol{d} + \mathrm{div}_x\,\boldsymbol{q}) \geq 0\,. \tag{2.70}$$

The introduction of the specific free energy ψ, which is also known as the Helmholtz free energy per unit mass, defined by:

$$\psi = e - \theta s\,, \tag{2.71}$$

together with the relation:

$$\mathrm{div}_x\left[\frac{\boldsymbol{q}}{\theta}\right] = \frac{1}{\theta}\mathrm{div}_x\,\boldsymbol{q} - \frac{1}{\theta^2}\boldsymbol{q}.\nabla_x\theta\,, \tag{2.72}$$

into in the Clausius-Duhem inequality, leads to:

$$\boldsymbol{\sigma}\colon\boldsymbol{d} - \rho\left(\dot{\psi} + s\dot{\theta}\right) - \frac{1}{\theta}\boldsymbol{q}.\boldsymbol{g} \geq 0\,, \tag{2.73}$$

where the term $\boldsymbol{g}$ is defined as: $\boldsymbol{g} = \nabla_x\theta$.

2.4 CONSTITUTIVE THEORY

The balance principles presented so far are valid for any continuum body, regardless of the material of which the body is made. In order to distinguish between different types of material, a constitutive model must be introduced. In this section, the use of internal variables to formulate constitutive models of dissipative materials is addressed.

2.4.1 Thermodynamics with internal variables

An effective alternative to describe the dissipative constitutive behavior is the adoption of the so-called thermodynamics with internal variables. The starting point of the thermodynamics with internal variables is the hypothesis that at any instant of a thermodynamical process the thermodynamic state (defined by $\boldsymbol{\sigma}$, ψ, s and $\boldsymbol{q}$) at a given point $\boldsymbol{p}$ can be completely determined by the knowledge of a finite number of state variables. The thermodynamic state depends only on the instantaneous value of the state variables and not on their past history. This hypothesis is intimately connected with the assumption of the existence of a (fictitious) state of thermodynamic equilibrium known as the local accompanying state (Kestin & Bataille, 1977) described by the current value of the state variables. In other words, every process is considered to be a succession of equilibrium states. Therefore, despite the success of the internal variable approach in numerous fields of continuum physics, phenomena induced by very fast external actions (at time scales comparable to atomic vibrations) which involve states far from thermodynamic equilibrium are excluded from representation by internal variable theories.

The state variables

Consider that at any time t, the thermodynamic state at a point is defined by the set of state variables, as follows:

$$\{\boldsymbol{F}, \theta, \boldsymbol{g}, \boldsymbol{\alpha}\}\,, \tag{2.74}$$

where the terms $\boldsymbol{F}, \theta$ and $\boldsymbol{g}$ are the instantaneous values of the deformation gradient, temperature and the temperature gradient. The term $\boldsymbol{\alpha}$ represents the set of internal variables containing, in general, entities of scalar, vector and tensor nature associated with dissipative mechanisms, $\boldsymbol{\alpha} = \alpha_k$.

Thermodynamic potential: Stress constitutive equation

Following the above hypothesis, the specific free energy is assumed to have the form:

$$\psi = \psi(\boldsymbol{F}, \theta, \alpha)\ , \tag{2.75}$$

so that its rate of change is given by:

$$\dot{\psi} = \frac{\partial \psi}{\partial \boldsymbol{F}} : \dot{\boldsymbol{F}} + \frac{\partial \psi}{\partial \theta}\dot{\theta} + \frac{\partial \psi}{\partial \alpha_k}\dot{\alpha}_k \ , \tag{2.76}$$

where summation over k is implied. In that case, using the connection:

$$\boldsymbol{\sigma} : \boldsymbol{d} = \boldsymbol{\sigma}\boldsymbol{F}^{-T} : \dot{\boldsymbol{F}} \ , \tag{2.77}$$

for the stress power, one obtains for the Clausius-Duhem inequality:

$$\left(\boldsymbol{\sigma}\boldsymbol{F}^{-T} - \rho\frac{\partial \psi}{\partial \boldsymbol{F}}\right) : \dot{\boldsymbol{F}} - \rho\left(s + \frac{\partial \psi}{\partial \theta}\right)\dot{\theta} - \rho\frac{\partial \psi}{\partial \alpha_k}\dot{\alpha}_k - \frac{1}{\theta}\boldsymbol{q}.\boldsymbol{g} \geq 0 \ . \tag{2.78}$$

Equivalently, in terms of power per unit reference volume, we have:

$$\left(\boldsymbol{P} - \bar{\rho}\frac{\partial \psi}{\partial \boldsymbol{F}}\right) : \dot{\boldsymbol{F}} - \bar{\rho}\left(s + \frac{\partial \psi}{\partial \theta}\right)\dot{\theta} - \bar{\rho}\frac{\partial \psi}{\partial \alpha_k}\dot{\alpha}_k - \frac{J}{\theta}\boldsymbol{q}.\boldsymbol{g} \geq 0 \ . \tag{2.79}$$

Equation (2.79) must remain valid for any pair of functions $\{\dot{\boldsymbol{F}}(t), \dot{\theta}(t)\}$. This implies the well known constitutive equations:

$$\boldsymbol{P} = \bar{\rho}\frac{\partial \psi}{\partial \boldsymbol{F}} \ , \qquad\qquad s = -\frac{\partial \psi}{\partial \theta} \ , \tag{2.80}$$

for the first Piola-Kirchhoff stress and entropy. Equation (2.80) is equivalent to the following constitutive relations for the Cauchy and Kirchoff stress tensors:

$$\boldsymbol{\sigma} = \frac{1}{J}\bar{\rho}\frac{\partial \psi}{\partial \boldsymbol{F}}\,\boldsymbol{F}^T \ , \qquad\qquad \boldsymbol{\tau} = \bar{\rho}\frac{\partial \psi}{\partial \boldsymbol{F}}\,\boldsymbol{F}^T \ . \tag{2.81}$$

Thermodynamical forces

For each internal variable α_k of the set $\boldsymbol{\alpha}$, we define the conjugate thermodynamical force:

$$A_k \equiv \bar{\rho}\frac{\partial \psi}{\partial \alpha_k} \ . \tag{2.82}$$

With this definition and the identities (see Equation 2.80), the Clausius-Duhem inequality can be rewritten as:

$$-A_k\dot{\alpha}_k - \frac{J}{\theta}\boldsymbol{q}.\boldsymbol{g} \geq 0 \ . \tag{2.83}$$

In what follows, we will adopt for convenience the notation:

$$\boldsymbol{A} \equiv \{A_k\} \ , \tag{2.84}$$

for the set of thermodynamical forces.

Dissipation. Evolution of the internal variables

In order to completely characterize a constitutive model, complementary laws associated with the dissipative mechanisms are required. Namely, constitutive equations for the flux variables $\frac{1}{\theta}\boldsymbol{q}$ and $\dot{\boldsymbol{\alpha}}$ must be postulated. In the general case, we assume that the flux variables are given functions of the state variables. The following constitutive equations are then postulated:

$$\begin{aligned} \dot{\boldsymbol{\alpha}} &= f(\boldsymbol{F}, \theta, \boldsymbol{g}, \boldsymbol{\alpha}) \ , \\ \frac{1}{\theta}\boldsymbol{q} &= h(\boldsymbol{F}, \theta, \boldsymbol{g}, \boldsymbol{\alpha}) \ . \end{aligned} \tag{2.85}$$

The Clausius-Duhem inequality, now expressed by Equation (2.83), must hold for any process. This requirement places restrictions on the possible forms of the general constitutive functions f and h in (Equation 2.85) (see Coleman & Gurtin, 1967; Truesdell, 1969). It is also important to mention that when internal variables of vectorial or tensorial nature are present, it is frequently convenient to re-formulate (Equation 2.85) in terms of so-called objective rates rather than the standard material time derivative of $\boldsymbol{\alpha}$. Objective rates are insensitive to rigid body motions and may be essential in the definition of frame invariant evolution laws for variables representing physical states associated with material directions.

Dissipation potential. Normal dissipativity

An effective way of ensuring that (Equation 2.83) is satisfied consists in postulating the existence of a scalar-valued dissipation potential of the form:

$$\Xi = \Xi(\boldsymbol{A}, \boldsymbol{g} : \boldsymbol{F}, \theta, \boldsymbol{\alpha}) \ , \tag{2.86}$$

where the state variables $\boldsymbol{F}$, θ and $\boldsymbol{\alpha}$ appear as parameters. The potential Ξ is assumed convex with respect to each A_k and $\boldsymbol{g}$, non-negative and zero valued at the origin, $\{\boldsymbol{A}, \boldsymbol{g}\} = \{\boldsymbol{0}, \boldsymbol{0}\}$. In addition, the hypothesis of normal dissipativity is introduced, which mean that flux variables are assumed to be determined by the laws:

$$\dot{\alpha}_k = -\frac{\partial \Xi}{\partial A_k} \,, \qquad\qquad \frac{1}{\theta}\boldsymbol{q} = -\frac{\partial \Xi}{\partial \boldsymbol{g}} \,. \tag{2.87}$$

A constitutive model defined by Equations (2.75), (2.80) and (2.87) satisfies "a priori" the dissipation inequality. It should be noted, however, that the constitutive description by means of convex potentials as described above is not a consequence of thermodynamics but, rather, a tool for formulating constitutive equations without violating thermodynamics. Examples of constitutive models supported by experimental evidence which do not admit representation by means of dissipation potentials are discussed by Onat & Leckie (1988).

2.4.2 Phenomenological and micromechanical approaches

The success of a constitutive model intended to describe the behavior of a particular material depends crucially on the choice of an appropriate set of internal variables. Since no plausible model will be general enough to describe the response of a material under all processes, we should have in mind that the choice of internal variables must be guided not only by the specific material in question but also by the material process. In general, due to the difficulty involved in the identification of the underlying dissipative mechanisms, the choice of the appropriate set of internal variables is somewhat subtle and tends to be biased by the preferences and background of the investigator.

In simple terms, we can say that constitutive modeling by means of internal variables relies either on a micromechanical or on a phenomenological approach. The micromechanical approach involves the determination of mechanisms and related variables at the atomic, molecular or crystalline levels. In general, these variables are discrete quantities and their continuum (macroscopic) counterparts can be defined by means of homogenization techniques. The phenomenological approach, on the other hand, is based on the study of the response of the representative volume element, which is the element of matter large enough to be regarded as a homogeneous continuum. The internal variables in this case will be directly associated with the dissipative behavior observed at the macroscopic level in terms of continuum quantities (such as strain, stress, temperature, etc.). Despite the macroscopic nature of theories derived on the basis of the phenomenological methodology, it should be expected that "good" phenomenological internal

variables will be somehow related to the underlying microscopic dissipation mechanisms (de Souza Neto *et al*., 2008).

2.4.3 The purely mechanical theory

Thermal effects are ignored in the constitutive theories addressed in this thesis. It is, therefore, convenient at this point to summarize the general internal variable-based constitutive equations in the purely mechanical case. By removing the thermally-related terms of the above theory, we end up with the following set of mechanical constitutive equations:

$$\begin{aligned} \psi &= \psi(\boldsymbol{F}, \boldsymbol{\alpha}) \ , \\ \boldsymbol{P} &= \bar{\rho} \frac{\partial \psi}{\partial \boldsymbol{F}} \ , \\ \dot{\boldsymbol{\alpha}} &= f(\boldsymbol{F}, \boldsymbol{\alpha}) \ . \end{aligned} \tag{2.88}$$

2.4.4 The constitutive initial value problem

Our basic constitutive problem is defined as follows: "Given the history of the deformation gradient (and the history of temperature and temperature gradient, if thermal effects are considered), find the free-energy and stress (plus entropy and heat flux, in the thermo mechanical case) according to the constitutive law". If the internal variable approach is adopted in the formulation of the constitutive equations, the generic constitutive problem reduces to the following fundamental mechanical initial value problem.

Problem 2.4.1 (The mechanical constitutive initial value problem)
Given the initial values of the internal variables $\boldsymbol{\alpha}(t_0)$ and the history of the deformation gradient

$$\boldsymbol{F}(t) \quad t \in [t_0, t] \ , \tag{2.89}$$

find the functions $\boldsymbol{P}(t)$ and $\boldsymbol{\alpha}(t)$, for the first Piola-Kirchhoff stress and the set of internal variables, such that the constitutive equations:

$$\begin{aligned} \boldsymbol{P}(t) &= \bar{\rho} \left. \frac{\partial \psi}{\partial \boldsymbol{F}} \right|_t \\ \dot{\boldsymbol{\alpha}}(t) &= f(\boldsymbol{F}(t), \boldsymbol{\alpha}(t)) \ , \end{aligned} \tag{2.90}$$

are satisfied for $t \in [t_0, t]$.

2.5 WEAK EQUILIBRIUM. THE PRINCIPLE OF VIRTUAL WORK

The strong (point-wise, local or differential) forms of the momentum balance have been stated in Section 2.3 by expressions (2.64) and (2.65). In this section, we state the momentum balance equations in their corresponding weak (global or integral) forms. The weak equilibrium statement – the Principle of Virtual Work – is fundamental to the definition of the basic initial boundary value problem and, is the starting point of finite element procedures.

Again, let us consider the body $\boldsymbol{\Omega}$ which occupies the region $\boldsymbol{\Omega} \subset R^3$ with boundary $\partial\boldsymbol{\Omega}$ in its reference configuration, subjected to body forces in its interior and surface tractions on its boundary. In its deformed configuration, $\boldsymbol{\Omega}$ occupies the region $\boldsymbol{\varphi}(\boldsymbol{\Omega})$ with boundary $\boldsymbol{\varphi}(\partial\boldsymbol{\Omega})$ defined through the deformation map $\boldsymbol{\varphi}$.

2.5.1 The spatial version

The spatial version of the principle of virtual work states that the body $\boldsymbol{\Omega}$ is in equilibrium if and only if its Cauchy stress field, $\boldsymbol{\sigma}$, satisfies the equation:

$$\int_{\boldsymbol{\varphi}(\boldsymbol{\Omega})} [\boldsymbol{\sigma} : \nabla_x \boldsymbol{\eta} - (\boldsymbol{f} - \rho \ddot{\boldsymbol{u}}) . \boldsymbol{\eta}] dv - \int_{\boldsymbol{\varphi}(\partial\boldsymbol{\Omega})} \boldsymbol{t} . \boldsymbol{\eta} \, da = 0 \quad \forall \ \boldsymbol{\eta} \in \mathcal{V} \ , \tag{2.91}$$

where $\boldsymbol{f}$ and $\boldsymbol{t}$ are the body force per unit deformed volume and boundary traction per unit deformed area and $\mathcal{V}$ is the space of virtual displacements of $\boldsymbol{\Omega}$, or in other words the space of sufficiently regular arbitrary displacements.

$$\boldsymbol{\eta} : \boldsymbol{\varphi}(\boldsymbol{\mathcal{B}}) \ \longrightarrow \boldsymbol{\mathcal{U}} \ . \tag{2.92}$$

2.5.2 The material version

The virtual work equation can be equivalently expressed in the reference configuration of $\boldsymbol{\Omega}$. The corresponding material (or reference) version of the Principle of Virtual Work states that $\boldsymbol{\Omega}$ is in equilibrium if and only if its first Piola-Kirchhoff stress field, $\boldsymbol{P}$, satisfies:

$$\int_{\boldsymbol{\Omega}} \left[\boldsymbol{P}: \nabla_p \boldsymbol{\eta} - \left(\bar{\boldsymbol{f}} - \bar{\rho}\ddot{\boldsymbol{u}}\right).\boldsymbol{\eta}\right] dv - \int_{\partial\boldsymbol{\Omega}} \bar{\boldsymbol{t}}.\boldsymbol{\eta}\, da = 0 \quad \forall\ \boldsymbol{\eta} \in \mathcal{V}\ , \tag{2.93}$$

where $\bar{\boldsymbol{f}} = J\,\boldsymbol{f}$ is the reference body force and $\bar{\boldsymbol{t}}$ is the boundary traction per unit reference area. The space of virtual displacements, $\mathcal{V}$, is accordingly defined as the space of sufficiently regular arbitrary displacement fields:

$$\boldsymbol{\eta}: \boldsymbol{\Omega} \longrightarrow \boldsymbol{\mathcal{U}}\ . \tag{2.94}$$

The material version of the virtual work equation is obtained by introducing, in its spatial counterpart, the identities:

$$\boldsymbol{\sigma} = \frac{1}{J}\boldsymbol{P}\boldsymbol{F}^T\ , \qquad\qquad \nabla_x \boldsymbol{a} = \nabla_p \boldsymbol{a}\boldsymbol{F}^{-1}\ , \tag{2.95}$$

where the second expression holds for a generic vector field a, and making use of the standard relation (Gurtin, 1981):

$$\int_{\varphi(\boldsymbol{\Omega})} a(\boldsymbol{x}) dv = \int_{\boldsymbol{\Omega}} J(\boldsymbol{p}) a\left(\boldsymbol{\varphi}(\boldsymbol{p})\right)\ dv\ , \tag{2.96}$$

valid for any scalar field a.

CHAPTER 3

An Implicit Numerical Integration Algorithm for an Elasto-plastic Model with Three Invariants

This chapter describes a simple and robust algorithm for numerical integration of a new model for metal plasticity and fracture. The constitutive model was proposed by Bai & Wierzbicki (2007) and critically includes both the pressure effect, through the stress triaxiality, and the effect of the third invariant of the deviatoric stress tensor, through the Lode angle, in the constitutive description of the material. These effects are directly introduced on the hardening rule of the material, which is typically only a function of the equivalent plastic strain. This approach is in contrast with the classical theory of metal plasticity, the so-called J_2 theory, which assumes that both hydrostatic pressure and third invariant of the deviatoric stress tensor have a negligible effect on the material strain hardening and the flow stress. The model proposed by Bai and Wierzbicki was selected from the models available in literature for a detailed study and an implicit solution for numerical integration of Bai & Wierzbicki's model is developed and implemented in an implicit quasi-static finite element environment. The algorithm is based on the operator split methodology, which to determine the stress update procedure, employs a fully implicit elastic predictor and plastic corrector (return mapping) step with general non-linear (piece-wise linear) isotropic hardening and the computation of the consistent tangent matrix (Simo *et al.*, 1985 and 1987). Then, to illustrate the accuracy and stability of the integration algorithm in practical situations (Ortiz & Popov, 1985), iso-error maps are built for specific cases. At the end, the robustness of the numerical integration algorithm is demonstrated by a large group of numerical simulations where the numerical results are compared with experimental results for classical specimens as: a cylindrical smooth bar and a cylindrical notched bar modelled as two dimensional problems together with a flat grooved plate specimen simulated in three-dimensions.

3.1 INTRODUCTION

The theory based on the second invariant of the deviatoric stress tensor, J_2, more widely known through von Mises's model is one of the most used formulations to describe the behavior of metals, during the elasto-plastic regime. The von Mises's model assumes that the effect of hydrostatic stress is negligible on the evolution of the plastic flow for ductile materials. The hydrostatic stress is a parameter responsible for controlling the size of the yield surface (Bardet, 1990; Bai, 2008). Furthermore, in the von Mises's formulation, the effect of the third invariant of the deviatoric stress tensor, normally denoted by J_3, is also ignored. The third invariant is a parameter used in the definition of the Lode angle or Azimuth angle, which is responsible for the shape of the yield surface (Bardet, 1990; Bai, 2008). Over the last five years, the importance of both hydrostatic stress and Lode angle, in the description of the behavior of ductile materials, has been clearly recognized and detail studies were conducted by several authors (Bai *et al.*, 2007; Bai, 2008; Driemeier *et al.*, 2010; Mirone *et al.*, 2010; Gao *et al.*, 2011). Many researchers have done extensive experimental studies as Richmond & Spitzing (1980 and 1984), who were the first researchers to study the effects of pressure on yielding of aluminum alloys. Latter, Bardet (1990), proposed a methodology to describe the Lode angle dependence for some constitutive models, and Wilson (2002), which conducted studies on notched 2024-T351 aluminum bars in tensile test and verified the importance of these effects. Brunig *et al.* (1999) proposed a constitutive model with three invariants that could be applied in metal plasticity and fracture. According to Mirone *et al.* (2010), the phenomenon of ductile failure is influenced by the relation with the variables from the stress–strain characterization and the failure prediction is better described by plastic strain, stress triaxiality and Lode angle parameters. An experimental program to study the influence of the stress tensor invariants in ductile failure was presented by Driemeier *et al.* (2010). This methodology can be seen as an efficient tool to investigate the effects of the stress intensity, stress triaxiality and Lode angle. Recently, Gao *et al.* (2011) have proposed an elasto-plastic model, which is a function of the hydrostatic stress as well as the second and third invariants of the stress deviator. These authors have carried out tests in specimens with a high level of stress triaxiality showing the dependence of the plastic flow rule on both stress

triaxiality and Lode angle. By examining these contributions, it is posible to conclude that ductile fracture is a local phenomenon and the stress and strain states over the expected fracture onset must be determined with accuracy. The fracture initiation is often preceded by large plastic deformation and there are considerable stress and strain gradients around the point of fracture. In this case, the J_2 theory is not accurate enough to capture the physical effects and more refined plasticity models have to be developed to be used in a large range of loading conditions.

3.2 PRELIMINARIES

Several factors have been systematically analyzed in the study of ductile fracture, nevertheless, there are three factors which have gained increased interest: the hydrostatic stress (p), stress triaxiality (η), and the Lode angle (θ) expressed by Equations (3.1-3.3) respectively (Brunig *et al.*, 2008; Bai & Wierzbicki, 2008; Zadpoor *et al.*, 2009; Tvergaard, 2008; Nahshon *et al.*, 2008).

$$p = -\sigma_m = -\frac{1}{3}\, tr\,(\boldsymbol{\sigma})\,, \tag{3.1}$$

$$\eta = -\frac{p}{q}\,, \tag{3.2}$$

$$\theta = \tan^{-1}\left\{\frac{1}{\sqrt{3}}\left[2\left(\frac{S_2 - S_3}{S_1 - S_3}\right) - 1\right]\right\}\,, \tag{3.3}$$

where $q = \sqrt{3/2\,\boldsymbol{S}:\boldsymbol{S}}$ is the von Mises equivalent stress, $\boldsymbol{S} = \boldsymbol{\sigma} - p\boldsymbol{I}$ is the deviatoric stress tensor and S_1, S_2 and S_3 are the components of the deviatoric stress tensor in the principal plane. The Lode angle can also be written as a function of the so-called normalized third invariant of the deviatoric stress tensor as:

$$\theta = \frac{1}{3} arccos(\xi)\,, \tag{3.4}$$

where ξ represents the normalized third invariant, that can be mathematically determined by a ratio between the third invariant and the von Mises equivalent stress:

$$\xi = \left(\frac{r}{q}\right)^3 . \tag{3.5}$$

The term r represents the third invariant, alternatively, defined by Bai *et al.* (2007) and can be determined as:

$$r = \left[\frac{27}{2} J_3\right]^{1/3} = \left[\frac{27}{2} det(\boldsymbol{S})\right]^{1/3} , \tag{3.6}$$

where J_3 is the third invariant of the deviatoric stress tensor, $\boldsymbol{S}$. The Lode angle can also be normalized ($\bar{\theta}$) and this parameter is known as the normalized Lode angle parameter (Bai & Wierzbicki, 2008).

$$\overline{\theta} = 1 - \frac{6\theta}{\pi} . \tag{3.7}$$

The range of $\bar{\theta}$ is $-1 \leq \bar{\theta} \leq 1$.

3.2.1 Lode Angle Parameter

The definition of the Lode angle, θ, can be better understood by analyzing the representation of the stress vector, $\overrightarrow{OB}$, on the space of principal stresses illustrated in Figure 3.1(a).

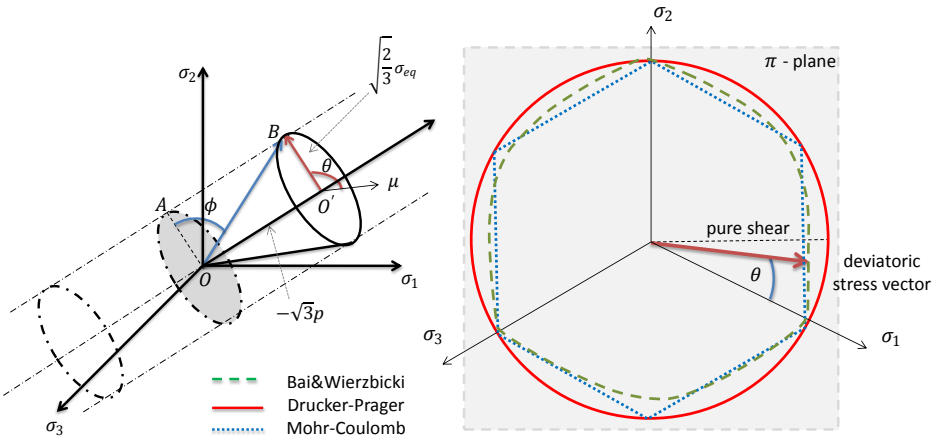

(a) (b)

Figure 3.1. (a) Schematic representation of the stress vector $\overrightarrow{OB}$ on the principal stresses space and (b) definition of the Lode angle on the π-plane. Adapted from Bai (2008).

The stress vector can be decomposed into a deviatoric $\overrightarrow{OA}$ and a hydrostatic $\overrightarrow{OO'}$ part. The ratio between the hydrostatic and deviatoric part is, by definition, the stress triaxiality which is associated with the angle ϕ, which is obtained between the stress vector $\overrightarrow{OB}$ and the π-plane. This angle, named elevator angle, is responsible for the size of the yield surface. The Lode angle is defined on the π-plane or deviatoric plane, see Figure 3.1b, and is the smallest angle between the line of pure shear and the projection of the stress tensor on the deviatoric plane. Bardet (1990) conducted several studies on the influence of the Lode angle on the shape of the yield surface and concluded, for exemple, that the Drucker-Prager model is Lode angle independent and Tresca and Mohr-Coulomb models are Lode angle dependent (Figure 3.1b).

In the context of ductile fracture, some researchers have suggested the introduction of the effect of the Lode angle either into the standard von Mises elasto-plastic constitutive model or into some damage evolution laws. In particular, Bao *et al.* (2004), Brünig *et al.* (2000) and Bai & Wierzbicki (2008) have proposed new elasto-plastic models that include the three invariants of the stress tensor on the definition of the material yield surface. On the other hand, in order to improve the evolution of the porosity obtained by Gurson's theory for low level of stress triaxiality, Nahshon & Hutchinson (2008), Barsoum & Faleskog (2007) and Xue (2008) have proposed the introduction of new shear mechanisms on the damage evolution law of Gurson's model, which are Lode angle dependent.

3.2.2 Fracture Surface

Experimental evidence of ductile fracture under high, low or even negative stress triaxiality has been presented by several authors (McClintock, 1971; Johnson and Cook, 1985). Nevertheless, recently Bao (2003) and Bao & Wierzbicki (2004) have conducted several tests in specimens with different geometries to determine the fracture location under a range of triaxiality. Figure 4.3 shows the behavior of two ductile materials on the three dimensional fracture locus for a range of stress triaxiality between [-1, 1]. The surfaces were originally proposed by Bai (2008) for an aluminum alloy and for steel.

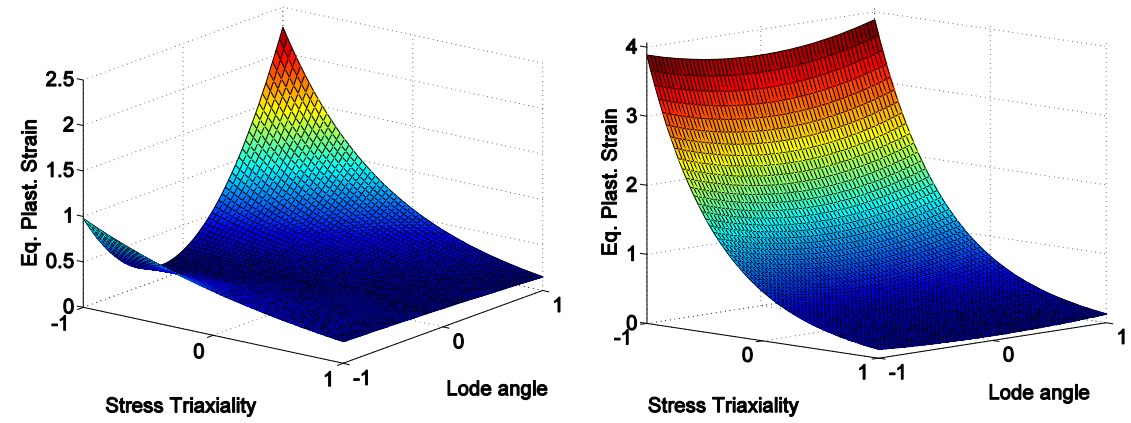

(a) (b)

Figure 3.2. Behavior of ductile materials in the three dimensional fracture *loci*: (a) material with a strong dependence of both hydrostatic pressure and Lode angle, the 2024-T351 aluminum alloy and (b) material with a weak dependence, the 1045 steel. Data adapted from Bai (2008).

The results have shown that the fracture strain does not have to be a monotonically decreasing function of the stress triaxiality (Bao *et al.*, 2004) for materials which are strongly dependent on both pressure and Lode angle (Figure 3.2a). In particular, Bai (2008) has studied the behavior of an aluminum alloy and proposed a three dimensional fracture locus where the fracture strain depends on both stress triaxiality and Lode angle. For a high level of stress triaxiality, where the spherical void growth mechanism plays a major role in the damage process, the equivalent plastic strain decreases with the increase of the stress triaxiality. However, within the range of zero and low level of stress triaxiality, where the elongation of voids is the predominant mechanism, the equivalent plastic strain increases with the increase of the stress triaxiality. This specific behavior is completely different for materials weakly dependent on pressure and Lode angle where the equivalent plastic strain decreases with the increase of the stress triaxiality (Figure 3.2b). The stress states which are promoted by specimens, employed in metal plasticity, can also be individually represented in the plane of stress triaxiality *versus* Lode angle. A representation of the initial stress state on the plane of stress triaxiality *versus* Lode angle is shown in Figure 3.3 where the influence of the Lode angle can be appreciated.

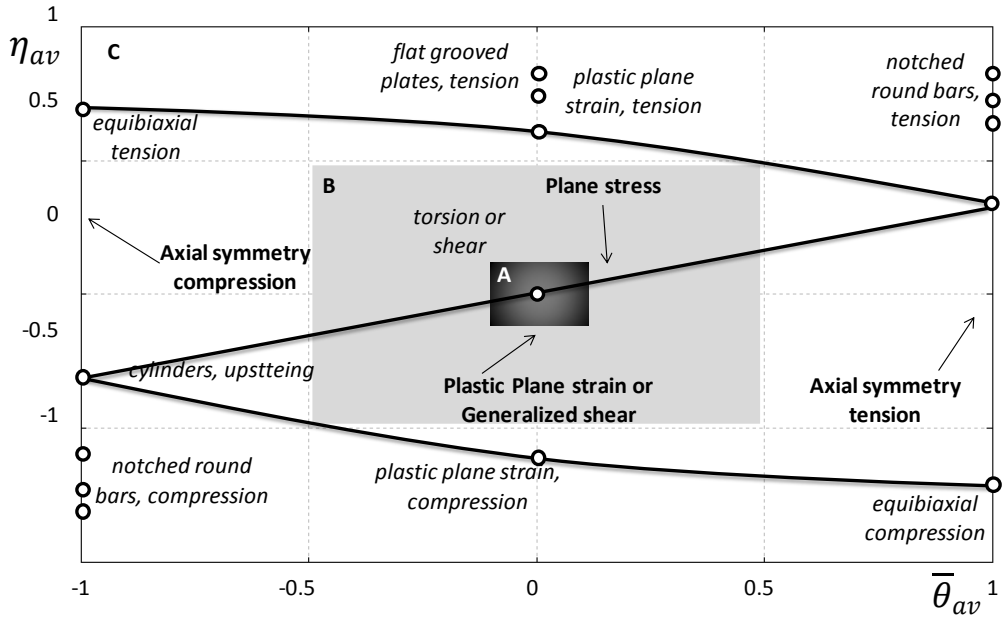

Figure 3.3. Representation on the space of stress triaxiality *versus* Lode angle. Adapted from Bai (2008).

Area "A" represents the region where we have the most significant contribution of shear effects on the material internal degradation, and in this case, both the stress triaxiality and the Lode angle are around zero. This behavior is observed under pure shear loading conditions, where the elongation of void drives the degradation of the material properties. In area "B" there is still a strong influence of shear effects, and this behavior is commonly observed in combined compression-shear and tensile-shear loading conditions, where both spherical and elongated void growths are present. Finally, in area "C" shear effects are neglectable and the predominant mechanism is the spherical void growth in the damage evolution.

3.3 CONSTITUTIVE MODEL

Bai & Wierzbicki (2007) have proposed an elasto-plastic model that includes the effect of pressure, through the stress triaxiality, and the effect of the third invariant, through the Lode angle. The effects are introduced on the well established von Mises model by redefining the hardening rule of the material. It is important to remark that in the classic von Mises model, the hardening rule is only

a function of the accumulated plastic strain $\sigma_y(\bar{\varepsilon}^p)$ and, in the Bai & Wierzbicki's model, the hardening rule becomes a function of the accumulated plastic strain, the stress triaxiality and the Lode angle through the parameter $\mu(\theta)$, $\sigma_y(\bar{\varepsilon}^p, \eta, \mu)$. Thus, the new definition of the hardening rule can be obtained as:

$$\sigma_y(\bar{\varepsilon}^p, \eta, \mu) = \sigma_y(\bar{\varepsilon}^p)\left[1 - C_\eta(\eta - \eta_0)\right]\left[C_\theta^s + (C_\theta^{ax} - C_\theta^s)\left(\mu - \frac{\mu^{m+1}}{m+1}\right)\right], \qquad (3.8)$$

where $\sigma_y(\bar{\varepsilon}^p)$ is the material strain hardening function, $C_\eta, C_\theta^s, C_\theta^{ax}$, and m are experimental parameters, η_0 is the reference value of the stress triaxiality, and $\mu(\theta)$ is a parameter defined as a function of the Lode angle:

$$\mu(\theta) = \frac{cos(\pi/6)}{1 - cos(\pi/6)}\left[\frac{1}{cos(\theta - \pi/6)} - 1\right] = 6.4641[sec(\theta - \pi/6) - 1]\ . \qquad (3.9)$$

The effect of the stress triaxiality and the Lode angle are included on the hardening rule through the functions $\left[1 - C_\eta(\eta - \eta_0)\right]$ and $\left[C_\theta^s + (C_\theta^{ax} - C_\theta^s)\left(\mu - \frac{\mu^{m+1}}{m+1}\right)\right]$, respectively. The new yield criterion replaces the standard hardening rule, $\sigma_y(\bar{\varepsilon}^p)$, by $\sigma_y(\bar{\varepsilon}^p, \eta, \mu)$ on the J_2 theory, such that the new yield surface can be expressed by:

$$\Phi = q - \sigma_y(\bar{\varepsilon}^p, \eta, \mu)\ . \qquad (3.10)$$

Substituting Equation (3.8) into Equation (3.10), we can obtain the yield function for Bai & Wierzbicki's model:

$$\Phi = q - \sigma_y(\bar{\varepsilon}^p)\left[1 - C_\eta(\eta - \eta_0)\right]\left[C_\theta^s + (C_\theta^{ax} - C_\theta^s)\left(\mu - \frac{\mu^{m+1}}{m+1}\right)\right]. \qquad (3.11)$$

From Equation (3.11), it is possible to express the pressure effect and Lode angle dependence by functions $A(\eta)$ and $B(\mu)$, respectively. The functions can be defined by Equations (3.12) and (3.13), as:

$$A(\eta) = \left[1 - C_\eta(\eta - \eta_0)\right], \qquad (3.12)$$

$$B(\mu) = \left[C_\theta^s + (C_\theta^{ax} - C_\theta^s)\left(\mu - \frac{\mu^{m+1}}{m+1}\right)\right]. \qquad (3.13)$$

Thus, Equation (3.11) can be re-written as:

$$\Phi = q - \sigma_y(\bar{\varepsilon}^p)A(\eta)B(\mu) \ . \tag{3.14}$$

The influence of the material parameters $\left(C_\eta, C_\theta^s, C_\theta^{ax}, \eta_0, m\right)$ on the behavior of the constitutive model can be analyzed as follows. The parameter C_η is a material constant and needs to be experimentally calibrated. This parameter describes the hydrostatic stress effect on material plasticity. If $C_\eta = 0$, the model loses the dependence of the stress triaxiality or the hydrostatic stress effect and recovers, as a limiting case, the behavior of the von Mises's model.

The triaxiality reference, η_0, depends on the type of test performed and the geometry of the specimen. For a cylindrical smooth bar, subjected to a tensile test, η_0 takes the value equal to $1/3$. Regarding the same specimen, now under a compressive test, η_0 takes the value equal to $-1/3$. Finally, for a torsion and a shear test $\eta_0 = 0$. It is important to remark that the hydrostatic stress effect, introduced by Bai & Wierzbicki, is a linear function. Nervertheless, some researchers (Karr *et al*., 1989), have claimed that this effect is non-linear for some materials, such as ice. Analyzing the third invariant effect, the experimental parameter C_θ^{ax} can assume one of two forms, according to the type of loading (tension/compression) applied or the value of the Lode angle:

$$C_\theta^{ax} = \begin{cases} C_\theta^t & for \quad \bar{\theta} \geq 0 \\ C_\theta^c & for \quad \bar{\theta} < 0 \end{cases} . \tag{3.15}$$

The parameters C_θ^s, C_θ^t and C_θ^c also depend on the type of test. For example, if a smooth bar is used in a tensile test $C_\theta^t = 0$, if a torsion test is performed $C_\theta^s = 1$, if a cylindrical specimen is used in a compressive test $C_\theta^c = 1$. The convexity of the yield surface is controlled by the ratio of these parameters. The range of the parameter μ is between $0 \leq \mu \leq 1$. When $\mu = 0$ it corresponds to plane strain or shear condition, when $\mu = 1$ it corresponds to an axisymmetric problem. The introduction of the term $\mu^{m+1}/m + 1$ is done to ensure the smoothness of the yield surface and its differentiability with respect to Lode angle around $\mu = 1$. More details about the calibration of the material parameters can be found in Bai (2008). In Box 3.1, a summary of the Bai & Wierzbicki´s model is presented. Details of how to determine the plastic flow rule and the evolution equation for the equivalent plastic strain can be found in appendix "A".

Box 3.1. Bai & Wierzbicki's model with isotropic hardening.

(i) Elasto-plastic split of the strain tensor

$$\boldsymbol{\varepsilon} = \boldsymbol{\varepsilon}^e + \boldsymbol{\varepsilon}^p$$

(ii) Elastic law

$$\boldsymbol{\sigma} = \mathbf{D}^e : \boldsymbol{\varepsilon}^e$$

(iii) Yield function

$$\Phi = q - \sigma_y(\bar{\varepsilon}^p)AB$$

with A and B given by:

$$A = \left[1 - C_\eta(\eta - \eta_0)\right] \quad ; \qquad B = \left[C_\theta^s + (C_\theta^{ax} - C_\theta^s)\left(\mu - \frac{\mu^{m+1}}{m+1}\right)\right]$$

and, $\quad \mu = \frac{cos(\pi/6)}{1-cos(\pi/6)}\left[\frac{1}{cos(\theta-\pi/6)} - 1\right]$

(iv) Plastic flow rule and evolution equation for $\dot{\bar{\varepsilon}}^p$

$$\dot{\boldsymbol{\varepsilon}}^p = \dot{\gamma}\frac{\partial \Phi}{\partial \boldsymbol{\sigma}} = \dot{\gamma}\boldsymbol{N} = \dot{\gamma}\left(\frac{3}{2q}\alpha\boldsymbol{S} + \frac{3}{2q}\lambda\boldsymbol{M} + \frac{1}{3}\beta\boldsymbol{I}\right)$$

$$\dot{\bar{\varepsilon}}^p = \dot{\gamma}\sqrt{\alpha^2 + \frac{2}{9}\beta^2 + \lambda^2\frac{\boldsymbol{M}:\boldsymbol{M}}{\boldsymbol{S}:\boldsymbol{S}} + 2\alpha\lambda\frac{\boldsymbol{S}:\boldsymbol{M}}{\boldsymbol{S}:\boldsymbol{S}}}$$

where:

$$\boldsymbol{M} = \boldsymbol{S^2} - \frac{1}{3}tr(\boldsymbol{S^2})\boldsymbol{I}$$

and α, β and λ:

$$\alpha = 1 - \frac{\sigma_y(\bar{\varepsilon}^p)}{q}\left[C_\eta B\eta + AD\xi\left(1 + 3I_1\frac{q^2}{r^3}\right)\right]$$

$$\beta = \frac{\sigma_y(\bar{\varepsilon}^p)C_\eta B}{q}$$

$$\lambda = \frac{3\sigma_y(\bar{\varepsilon}^p)AD}{q^2}$$

$$D = (C_\theta^{ax} - C_\theta^s)(1 - \mu^m)\frac{\cos(\pi/6)}{1 - \cos(\pi/6)}\frac{\tan(\theta - \pi/6)}{\cos(\theta - \pi/6)}\frac{1}{\sin 3\theta}$$

(v) Loading/unloading criterion

$$\dot{\gamma} \geq 0\,, \qquad \Phi \leq 0\,, \qquad \dot{\gamma}\Phi = 0.$$

3.4 NUMERICAL STRATEGY FOR THE INTEGRATION ALGORITHM

In this section, the constitutive equations of Bai and Wierzbicki's model, presented in section 3.3, will be treated and implemented within a finite element framework. The main contribution of this chapter is the development of an implicit numerical integration algorithm. The use of a path dependent constitutive model, as is the case of the model described in this chapter, invariably leads to the need for formulation of algorithms for numerical integration of the evolution equations. The problem consists in formulating numerical integration procedures for updating the known state variables, generically denoted by α_n, at a certain time t_n to obtain the state variables α_{n+1} at time t_{n+1}, where the incremental strain $\Delta\varepsilon$ is assumed given. Therefore, the discretization of the constitutive equations within a generic pseudo-time interval $[t_n, t_{n+1}]$ was performed for the Bai and Wierzbicki's model, which is summarized in Box 3.2, based on the backward Euler scheme (Simo & Hughes, 1998). Since the model was implemented in an implicit quasi-static finite element framework, it was also necessary to derive the tangent matrix which is consistent with the integration algorithm.

The stress update procedure is based on the so-called operator split concept (see Simo & Hughes, 1998; De Souza Neto, 2008), which is especially suitable for the numerical integration of the evolution problem and has been widely used in computational plasticity (see Simo & Hughes, 1998; De Souza Neto et al., 2008). This method, which was used in this development, consists in splitting the problem in two parts: an elastic predictor, where the problem is assumed to be elastic and, a plastic corrector, in which the system of residual equations comprising the elasticity law, plastic consistency and the rate equations is solved, taking the results of the elastic predictor stage as initial conditions. In the case of violation of the yield condition, the plastic corrector stage has to be initiated and the Newton-Raphson procedure is used to solve the discretised set of equations. The Newton-Raphson procedure was chosen motivated by the quadratic rates of convergence achieved, which results in return mapping procedures computationally efficient (see Simo & Hughes, 1998; De Souza Neto, 2008). The steps required to determine the state update procedure for the present model are described in the following.

3.4.1 State update procedure

Let us consider what happens in a typical Gauss point of a finite element mesh, within pseudo-time interval $[t_n, t_{n+1}]$. Given the incremental strain, the total strain at time t_{n+1} can be determined as:

$$\boldsymbol{\varepsilon}_{n+1} = \boldsymbol{\varepsilon}_n + \Delta\boldsymbol{\varepsilon} \ , \tag{3.16}$$

where $\boldsymbol{\varepsilon}_{n+1}$ represents the total strain at time t_{n+1}, $\boldsymbol{\varepsilon}_n$ is the total strain at time t_n and $\Delta\boldsymbol{\varepsilon}$ represents the incremental strain. Knowing also the values of the internal variables $\boldsymbol{\varepsilon}_n^p$ and $\bar{\varepsilon}_n^p$ at time t_n, the numerical integration algorithm should obtain the updated values at the end of the interval for $\boldsymbol{\sigma}_{n+1}$, $\boldsymbol{\varepsilon}_{n+1}^p$ and $\bar{\varepsilon}_{n+1}^p$, in a manner consistent with the constitutive equations of the model.

The elastic trial state

Assuming the incremental strain, $\Delta\boldsymbol{\varepsilon}$, as purely elastic, we have no evolution of the internal variables, which for this model is only the plastic strain tensor. In this case, the first step of the algorithm is evaluate the so-called elastic trial state. Hence, the elastic trial strain and the trial accumulated plastic strain at time t_{n+1} are given by:

$$\boldsymbol{\varepsilon}_{n+1}^{e\,trial} = \boldsymbol{\varepsilon}_n^e + \Delta\boldsymbol{\varepsilon} \quad \text{and} \quad \bar{\varepsilon}_{n+1}^{p\,trial} = \bar{\varepsilon}_n^p \ . \tag{3.17}$$

The corresponding trial stress tensor is computed through a double contraction between the elasticity matrix and the elastic trial strain tensor.

$$\boldsymbol{\sigma}_{n+1}^{trial} = \mathbf{D}^e : \boldsymbol{\varepsilon}_{n+1}^{e\,trial} \ , \tag{3.18}$$

where $\mathbf{D}^e$ is the standard isotropic elasticity tensor. Equivalently, in terms of deviatoric stress tensor and hydrostatic stress, Equation (3.18) can be split as:

$$\boldsymbol{S}_{n+1}^{trial} = 2G\boldsymbol{\varepsilon}_{d\,n+1}^{e\,trial} \quad \text{and} \quad p_{n+1}^{trial} = K\varepsilon_{v\,n+1}^{e\,trial} \ , \tag{3.19}$$

where $\boldsymbol{\varepsilon}_{d\,n+1}^{e\,trial}$ is the deviatoric elastic trial strain tensor, $\boldsymbol{\varepsilon}_{d\,n+1}^{e\,trial} = \text{dev}\,(\boldsymbol{\varepsilon}_{n+1}^{e\,trial})$, and $\varepsilon_{v\,n+1}^{e\,trial}$ is the volumetric elastic trial strain, $\varepsilon_{v\,n+1}^{e\,trial} = \text{trace}\,(\boldsymbol{\varepsilon}_{n+1}^{e\,trial})$. The parameters K and G represent, respectively, the bulk and shear modulu.

The trial yield stress is defined, in this case, as a function of the accumulated plastic strain at time t_n, which includes isotropic hardening.

$$\sigma_y^{trial} = \sigma_y\left(\bar{\varepsilon}_n^p\right) = \sigma_{y0} + H\bar{\varepsilon}_n^p \ , \tag{3.20}$$

where H represents the isotropic hardening modulu. The next step of the algorithm is to check whether $\boldsymbol{\sigma}_{n+1}^{trial}$ lies inside or outside of the trial yield surface. With the variable $\bar{\varepsilon}_n^p$ frozen at time t_n, we compute:

$$\Phi^{trial} = \sqrt{\frac{3}{2}}\left\|\boldsymbol{S}_{n+1}^{trial}\right\| - \sigma_y\left(\bar{\varepsilon}_n^p\right)\left[1 - C_\eta\left(\eta_{n+1}^{trial} - \eta_0\right)\right]\left[C_\theta^s + \left(C_\theta^{ax} - C_\theta^s\right)\left(\mu_{n+1}^{trial} - \frac{{\mu_{n+1}^{trial}}^{m+1}}{m+1}\right)\right]. \tag{3.21}$$

If Φ^{trial} is less than or equal to zero, the process is elastic within the interval and the trial state coincides with the updated state at time t_{n+1}. In this case, there is no plastic flow evolution within the interval and the trial state, $(*)_{n+1}^{trial}$, is equal to the real state, $(*)_{n+1}$.

$$(*)_{n+1} = (*)_{n+1}^{trial} \ . \tag{3.22}$$

Otherwise, if $\Phi^{\text{trial}} > 0$, it is necessary to apply the plastic corrector or return mapping algorithm whose step-by-step derivation is described in the following.

The plastic corrector step or return mapping algorithm

The plastic corretor step starts from the trial state. Firstly, the incremental strain is split in an elastic and plastic contributions. Hence, the increment of the plastic strain needs to be subtracted from the elastic trial strain at time t_{n+1} (Equation 3.17). Thus, the elastic strain can be computed as:

$$\begin{gathered}\boldsymbol{\varepsilon}_{n+1}^e = \boldsymbol{\varepsilon}_{n+1}^{e\,trial} - \Delta\boldsymbol{\varepsilon}^p = \boldsymbol{\varepsilon}_{n+1}^{e\,trial} - \Delta\gamma\boldsymbol{N}_{n+1} \ , \\ \boldsymbol{\varepsilon}_{n+1}^e = \boldsymbol{\varepsilon}_{n+1}^{e\,trial} - \Delta\gamma\left[\frac{3}{2q_{n+1}}\alpha_{n+1}\boldsymbol{S}_{n+1} + \frac{3}{2q_{n+1}}\lambda_{n+1}\boldsymbol{M}_{n+1} + \frac{1}{3}\beta_{n+1}\boldsymbol{I}\right] \ ,\end{gathered} \tag{3.23}$$

where $\boldsymbol{N}_{n+1}$represents the flow vector. The equivalent plastic strain at time t_{n+1} is also given by:

$$\bar{\varepsilon}_{n+1}^p = \bar{\varepsilon}_n^p + \Delta\bar{\varepsilon}^p = \bar{\varepsilon}_n^p + \Delta\gamma\sqrt{(*)} \ , \tag{3.24}$$

where the terms $\alpha_{n+1}, \beta_{n+1}, \lambda_{n+1}$ and $(*)$ are defined as:

$$\alpha_{n+1} = 1 - \frac{\sigma_y\left(\bar{\varepsilon}_{n+1}^p\right)}{q_{n+1}}\left[C_\eta B_{n+1}\eta_{n+1} + A_{n+1}D_{n+1}\xi_{n+1}\left(1 + 3I_1(\boldsymbol{\sigma}_{n+1})\frac{{q_{n+1}}^2}{{r_{n+1}}^3}\right)\right], \tag{3.25}$$

$$\beta_{n+1} = \frac{\sigma_y\left(\bar{\varepsilon}^p_{n+1}\right) C_\eta B_{n+1}}{q_{n+1}}, \tag{3.26}$$

$$\lambda_{n+1} = \frac{3\sigma_y\left(\bar{\varepsilon}^p_{n+1}\right) A_{n+1} D_{n+1}}{{q_{n+1}}^2}, \tag{3.27}$$

$$(*) = {\alpha_{n+1}}^2 + \frac{2}{9}{\beta_{n+1}}^2 + \lambda^2 \frac{\boldsymbol{M}_{n+1} : \boldsymbol{M}_{n+1}}{\boldsymbol{S}_{n+1} : \boldsymbol{S}_{n+1}} + 2\alpha_{n+1}\lambda_{n+1} \frac{\boldsymbol{S}_{n+1} : \boldsymbol{M}_{n+1}}{\boldsymbol{S}_{n+1} : \boldsymbol{S}_{n+1}} \ . \tag{3.28}$$

The parameter D_{n+1} is calculated through the following expression:

$$D_{n+1}(\theta_{n+1}) = (C_\theta^{ax} - C_\theta^s)(1 - {\mu_{n+1}}^m) \frac{\cos(\pi/6)}{1 - \cos(\pi/6)} \frac{\tan(\theta_{n+1} - \pi/6)}{\cos(\theta_{n+1} - \pi/6)} \frac{1}{\sin 3\theta_{n+1}} \ . \tag{3.29}$$

Equations (3.23) and (3.24) must be complemented by the so-called consistency condition that guarantees that the stress state at the end of the plastic step lies on the updated yield surface:

$$\Phi = q_{n+1} - \sigma_y\left(\bar{\varepsilon}^p_{n+1}\right) A_{n+1}(\eta_{n+1}) B_{n+1}(\mu_{n+1}) \ . \tag{3.30}$$

The previous set of discrete evolution equations needs to be solved for the unknowns variables $\boldsymbol{\varepsilon}^e_{n+1}$, $\bar{\varepsilon}^p_{n+1}$ and $\Delta\gamma$. Obtained the solution of the above system of non-linear equations, the plastic strain tensor can be updated according to following equation:

$$\boldsymbol{\varepsilon}^p_{n+1} = \boldsymbol{\varepsilon}^p_n + \Delta\gamma \left[\frac{3}{2q_{n+1}} \alpha_{n+1} \boldsymbol{S}_{n+1} + \frac{3}{2q_{n+1}} \lambda_{n+1} \boldsymbol{M}_{n+1} + \frac{1}{3}\beta_{n+1} \boldsymbol{I} \right] \ . \tag{3.31}$$

In the classical von Mises model, the system of equations to be solved for the plastic corrector state can be reduced by means of simple algebraic substitutions to a single non-linear equation having the incremental plastic multiplier, $\Delta\gamma$, as variable (De Souza Neto *et al*., 2008). Nevertheless, in Bai & Wierzbicki´s model, we cannot reduce the system of equations to a single non-linear equation for $\Delta\gamma$. Therefore, a system of couple equations needs to be solved at each integration (Gauss) point. In order to obtain this system of equations, let us start by re-writing Equation (3.23) as a function of the stress tensor, by multiplying the elastic

constants (Equation 3.18). After this manipulation, the following system of equation can be formulated for the unknowns $\boldsymbol{\sigma}_{n+1}$, $\bar{\varepsilon}^{p}_{n+1}$ and $\Delta\gamma$.

$$\begin{cases} \boldsymbol{\sigma}_{n+1} = \boldsymbol{\sigma}^{trial}_{n+1} - \Delta\gamma\, \mathbf{D}^{e} : \boldsymbol{N}_{n+1} \\ \bar{\varepsilon}^{p}_{n+1} = \bar{\varepsilon}^{p}_{n} + \Delta\gamma \sqrt{{\alpha_{n+1}}^{2} + \frac{2}{9}{\beta_{n+1}}^{2} + \lambda^{2}\frac{\boldsymbol{M}_{n+1} : \boldsymbol{M}_{n+1}}{\boldsymbol{S}_{n+1} : \boldsymbol{S}_{n+1}} + 2\alpha_{n+1}\lambda_{n+1}\frac{\boldsymbol{S}_{n+1} : \boldsymbol{M}_{n+1}}{\boldsymbol{S}_{n+1} : \boldsymbol{S}_{n+1}}} \\ \Phi = q_{n+1} - \sigma_{y}\left(\bar{\varepsilon}^{p}_{n+1}\right) A_{n+1}(\eta_{n+1}) B_{n+1}(\mu_{n+1}) \end{cases} . \quad (3.32)$$

More details about how to obtain the flow vector $\boldsymbol{N}_{n+1}$ *and* the plastic flow rule for the incremetal plastic strain $\Delta\boldsymbol{\varepsilon}^{p}_{n+1}$ and the accumulated plastic strain $\bar{\varepsilon}^{p}_{n+1}$, can be found in Appendix "A".

System of equations return mapping: The system of equations represented above is fully coupled and highly non-linear. Hence, we will describe in the following the procedure required to solve a non-linear system, which will lead to a computationally more efficient return mapping algorithm. The previous set of discrete evolution equations needs to be solved for the unknowns $\boldsymbol{\sigma}_{n+1}$, $\bar{\varepsilon}^{p}_{n+1}$ and $\Delta\gamma$. The Newton-Raphson method (N-R) is one of most efficient methods that can be used for the solution of the return mapping system of equations (Equation 3.32). Regarding the application of the N-R method, we firstly have to define the residual equations, based on the system above (Equation 3.32):

$$\begin{bmatrix} \boldsymbol{r}_{\sigma}\left(\boldsymbol{\sigma}_{n+1}, \bar{\varepsilon}^{p}_{n+1}, \Delta\gamma\right) \\ r_{\bar{\varepsilon}^{p}}\left(\boldsymbol{\sigma}_{n+1}, \bar{\varepsilon}^{p}_{n+1}, \Delta\gamma\right) \\ r_{\Delta\gamma}\left(\boldsymbol{\sigma}_{n+1}, \bar{\varepsilon}^{p}_{n+1}, \Delta\gamma\right) \end{bmatrix} = \begin{bmatrix} \boldsymbol{\sigma}_{n+1} - \boldsymbol{\sigma}^{trial}_{n+1} + \Delta\gamma \mathbf{D}^{e} : \boldsymbol{N}_{n+1} \\ \bar{\varepsilon}^{p}_{n+1} - \bar{\varepsilon}^{p}_{n} - \Delta\gamma\sqrt{(*)} \\ q_{n+1} - \sigma_{y}\left(\bar{\varepsilon}^{p}_{n+1}\right) A_{n+1}(\eta_{n+1}) B_{n+1}(\mu_{n+1}) \end{bmatrix}, \quad (3.33)$$

where $\boldsymbol{r}_{\sigma}$, $r_{\bar{\varepsilon}^{p}}$ and $r_{\Delta\gamma}$ represent the residual equations for $\boldsymbol{\sigma}_{n+1}$, $\bar{\varepsilon}^{p}_{n+1}$ and $\Delta\gamma$, respectively. The term $\boldsymbol{r}_{\sigma}$ represents a second order tensor, and both $r_{\bar{\varepsilon}^{p}}$ and $r_{\Delta\gamma}$ represent scalar equations.

According to the Newton-Raphson method, to obtain a new guess for each variable of the problem, we have to perform the linearization of the above residual equations. After some algebraic manipulations, we can obtain the system of equations in the linearized form, according to Equation (3.34):

$$\begin{bmatrix} \dfrac{\partial \boldsymbol{r_\sigma}}{\partial \boldsymbol{\sigma}_{n+1}} & \dfrac{\partial \boldsymbol{r_\sigma}}{\partial \bar{\varepsilon}^p_{n+1}} & \dfrac{\partial \boldsymbol{r_\sigma}}{\partial \Delta\gamma} \\ \dfrac{\partial r_{\bar{\varepsilon}^p}}{\partial \boldsymbol{\sigma}_{n+1}} & \dfrac{\partial r_{\bar{\varepsilon}^p}}{\partial \bar{\varepsilon}^p_{n+1}} & \dfrac{\partial r_{\bar{\varepsilon}^p}}{\partial \Delta\gamma} \\ \dfrac{\partial r_{\Delta\gamma}}{\partial \boldsymbol{\sigma}_{n+1}} & \dfrac{\partial r_{\Delta\gamma}}{\partial \bar{\varepsilon}^p_{n+1}} & \dfrac{\partial r_{\Delta\gamma}}{\partial \Delta\gamma} \end{bmatrix}^k \cdot \begin{bmatrix} \delta\boldsymbol{\sigma}_{n+1} \\ \delta\bar{\varepsilon}^p_{n+1} \\ \delta\Delta\gamma \end{bmatrix}^{k+1} = -\begin{bmatrix} \boldsymbol{r_\sigma}\left(\boldsymbol{\sigma}_{n+1}, \bar{\varepsilon}^p_{n+1}, \Delta\gamma\right) \\ r_{\bar{\varepsilon}^p}\left(\boldsymbol{\sigma}_{n+1}, \bar{\varepsilon}^p_{n+1}, \Delta\gamma\right) \\ r_{\Delta\gamma}\left(\boldsymbol{\sigma}_{n+1}, \bar{\varepsilon}^p_{n+1}, \Delta\gamma\right) \end{bmatrix}^k , \qquad (3.34)$$

where the terms $\partial(*)/\partial\boldsymbol{\sigma}_{n+1}$, $\partial(*)/\partial\bar{\varepsilon}^p_{n+1}$ and $\partial(*)/\partial\Delta\gamma$ represent the derivatives of each residual equation in relation to the stress tensor, equivalent plastic strain and plastic multiplier, respectively. By performing the derivatives and substituting them into Equation (3.34), we have:

$$\begin{bmatrix} \mathbb{I} + \Delta\gamma \mathbf{D}^e : \dfrac{\partial \boldsymbol{N}_{n+1}}{\partial \boldsymbol{\sigma}_{n+1}} & \Delta\gamma \dfrac{\partial \boldsymbol{N}_{n+1}}{\partial \bar{\varepsilon}^p_{n+1}} & \mathbf{D}^e : \boldsymbol{N}_{n+1} \\ -\Delta\gamma \dfrac{\partial \sqrt{(*)}}{\partial \boldsymbol{\sigma}_{n+1}} & 1 - \Delta\gamma \dfrac{\partial \sqrt{(*)}}{\partial \bar{\varepsilon}^p_{n+1}} & -\sqrt{(*)} \\ \boldsymbol{N}_{n+1} & -A_{n+1}B_{n+1}H & 0 \end{bmatrix}^k \cdot \begin{bmatrix} \delta\boldsymbol{\sigma}_{n+1} \\ \delta\bar{\varepsilon}^p_{n+1} \\ \delta\Delta\gamma \end{bmatrix}^{k+1} = -\begin{bmatrix} r_\sigma\left(\boldsymbol{\sigma}_{n+1}, \bar{\varepsilon}^p_{n+1}, \Delta\gamma\right) \\ r_{\bar{\varepsilon}^p}\left(\boldsymbol{\sigma}_{n+1}, \bar{\varepsilon}^p_{n+1}, \Delta\gamma\right) \\ r_{\Delta\gamma}\left(\boldsymbol{\sigma}_{n+1}, \bar{\varepsilon}^p_{n+1}, \Delta\gamma\right) \end{bmatrix}^k , \qquad (3.35)$$

where $\mathbb{I}$ represents the fourth order identity tensor.

In the above linearized system of equations, the first part on the left hand side of Equation (3.35) represents the derivative of each residual equation (Equation 3.33) with regard to each variable of the problem ($\boldsymbol{\sigma}_{n+1}$, $\bar{\varepsilon}^p_{n+1}$ and $\Delta\gamma$) at iteration k. Then, on the second term of the left hand side part, we have the incremental values of each variable of the problem at iteration, $k+1$, and the third part on the right hand side of Equation (3.35) represents the value of each residual equation at iteration k. Once the solution of the problema is obtained, we have the new guess for each variable ($\boldsymbol{\sigma}_{n+1}$, $\bar{\varepsilon}^p_{n+1}$ and $\Delta\gamma$), and the other state variables need to be updated, as $\boldsymbol{\varepsilon}^e_{n+1}$ and $\boldsymbol{\varepsilon}^p_{n+1}$. The overall algorithm for numerical integration is summarized in Box 3.2 and Box 3.3 in pseudo-code format. More details on how to obtain the derivative of each residual equation, can be found in Appendix "B".

Box 3.2. Fully implicit Elastic predictor/Return mapping algorithm.

i) Evaluate the elastic trial state: Given the incremental strain $\Delta\boldsymbol{\varepsilon}$ and the state variables at time t_n:

$$\boldsymbol{\varepsilon}^{e\,trial}_{n+1} = \boldsymbol{\varepsilon}^{e}_{n} + \Delta\boldsymbol{\varepsilon} \quad ; \quad \bar{\boldsymbol{\varepsilon}}^{p\,trial}_{n+1} = \bar{\boldsymbol{\varepsilon}}^{p}_{n}$$

$$\boldsymbol{S}^{trial}_{n+1} = 2G\boldsymbol{\varepsilon}^{e\,trial}_{d\,n+1} \quad ; \quad p^{trial}_{n+1} = K\varepsilon^{e\,trial}_{v\,n+1}$$

ii) Check plastic admissibility:

IF $\Phi = q^{trial}_{n+1} - \sigma_y\left(\bar{\varepsilon}^{p\,trial}_{n+1}\right)A^{trial}_{n+1}B^{trial}_{n+1} \leq 0$ THEN

set $(\cdot)_{n+1} = (\cdot)^{trial}_{n+1}$ (elastic step)

GO TO (*v*) – *"Exit"*

ELSE

GO TO (*iii*) – "*Continue*"

iii) Return mapping (plastic step):

Solve the system of equations below for $\boldsymbol{\sigma}_{n+1}$, $\bar{\varepsilon}^{p}_{n+1}$ and $\Delta\gamma$, *using the Newton-Raphson method:*

$$\begin{Bmatrix} \boldsymbol{\sigma}_{n+1} - \boldsymbol{\sigma}^{trial}_{n+1} + \Delta\gamma\mathbf{D}^{e}\!:\boldsymbol{N}_{n+1} \\ \bar{\varepsilon}^{p}_{n+1} - \bar{\varepsilon}^{p}_{n} - \Delta\gamma\sqrt{(*)} \\ q_{n+1} - \sigma_y\left(\bar{\varepsilon}^{p}_{n+1}\right)A_{n+1}(\eta_{n+1})B_{n+1}(\mu_{n+1}) \end{Bmatrix} = \begin{Bmatrix} \mathbf{0} \\ 0 \\ 0 \end{Bmatrix}$$

$$(*) = {\alpha_{n+1}}^2 + \frac{2}{9}{\beta_{n+1}}^2 + \lambda^2\frac{\boldsymbol{M}_{n+1}:\boldsymbol{M}_{n+1}}{\boldsymbol{S}_{n+1}:\boldsymbol{S}_{n+1}} + 2\alpha_{n+1}\lambda_{n+1}\frac{\boldsymbol{S}_{n+1}:\boldsymbol{M}_{n+1}}{\boldsymbol{S}_{n+1}:\boldsymbol{S}_{n+1}}$$

GOTO Box 3.3 (Newton Raphson procedure)

iv) Update the other state variables:

$$\boldsymbol{\varepsilon}^{e}_{d\ n+1} = \frac{1}{2G}\boldsymbol{S}_{n+1} \quad ; \quad \varepsilon^{e}_{v\ n+1} = \frac{1}{K}p_{n+1} \quad ; \quad \boldsymbol{\varepsilon}^{p}_{n+1} = \boldsymbol{\varepsilon}^{p}_{n} + \Delta\gamma\boldsymbol{N}_{n+1}$$

v) Exit

Box 3.3. The Newton-Raphson algorithm for solution of the return mapping system of equations.

1) Initialize iteration counter, $k := 0$, set initial guess for $\boldsymbol{\sigma}_{n+1}^{(0)} = \boldsymbol{\sigma}_n^{(0)}$, $\Delta\gamma^{(0)} = 0$, $\bar{\varepsilon}_{n+1}^{p\,(0)} = \bar{\varepsilon}_n^p$ and corresponding residual:

$$\begin{bmatrix} \boldsymbol{r}_{\boldsymbol{\sigma}}(\boldsymbol{\sigma}_{n+1}, \bar{\varepsilon}_{n+1}^p, \Delta\gamma) \\ r_{\bar{\varepsilon}^p}(\boldsymbol{\sigma}_{n+1}, \bar{\varepsilon}_{n+1}^p, \Delta\gamma) \\ r_{\Delta\gamma}(\boldsymbol{\sigma}_{n+1}, \bar{\varepsilon}_{n+1}^p, \Delta\gamma) \end{bmatrix} = \begin{bmatrix} \boldsymbol{\sigma}_{n+1} - \boldsymbol{\sigma}_{n+1}^{trial} + \Delta\gamma \mathbf{D}^e : \boldsymbol{N}_{n+1} \\ \bar{\varepsilon}_{n+1}^p - \bar{\varepsilon}_n^p - \Delta\gamma\sqrt{(*)} \\ q_{n+1} - \sigma_y(\bar{\varepsilon}_{n+1}^p) A_{n+1}(\eta_{n+1}) B_{n+1}(\mu_{n+1}) \end{bmatrix}$$

2) Perform Newton-Raphson iteration

$$\begin{bmatrix} \frac{\partial \boldsymbol{r}_{\boldsymbol{\sigma}}}{\partial \boldsymbol{\sigma}_{n+1}} & \frac{\partial \boldsymbol{r}_{\boldsymbol{\sigma}}}{\partial \bar{\varepsilon}_{n+1}^p} & \frac{\partial \boldsymbol{r}_{\boldsymbol{\sigma}}}{\partial \Delta\gamma} \\ \frac{\partial r_{\bar{\varepsilon}^p}}{\partial \boldsymbol{\sigma}_{n+1}} & \frac{\partial r_{\bar{\varepsilon}^p}}{\partial \bar{\varepsilon}_{n+1}^p} & \frac{\partial r_{\bar{\varepsilon}^p}}{\partial \Delta\gamma} \\ \frac{\partial r_{\Delta\gamma}}{\partial \boldsymbol{\sigma}_{n+1}} & \frac{\partial r_{\Delta\gamma}}{\partial \bar{\varepsilon}_{n+1}^p} & \frac{\partial r_{\Delta\gamma}}{\partial \Delta\gamma} \end{bmatrix}^k \cdot \begin{bmatrix} \delta\boldsymbol{\sigma}_{n+1} \\ \delta\bar{\varepsilon}_{n+1}^p \\ \delta\Delta\gamma \end{bmatrix}^{k+1} = -\begin{bmatrix} \boldsymbol{r}_{\boldsymbol{\sigma}}(\boldsymbol{\sigma}_{n+1}, \bar{\varepsilon}_{n+1}^p, \Delta\gamma) \\ r_{\bar{\varepsilon}^p}(\boldsymbol{\sigma}_{n+1}, \bar{\varepsilon}_{n+1}^p, \Delta\gamma) \\ r_{\Delta\gamma}(\boldsymbol{\sigma}_{n+1}, \bar{\varepsilon}_{n+1}^p, \Delta\gamma) \end{bmatrix}^k$$

New guess for $\boldsymbol{\sigma}_{n+1}$, $\bar{\varepsilon}_{n+1}^p$ *and* $\Delta\gamma$*:*

$$\boldsymbol{\sigma}_{n+1} = \boldsymbol{\sigma}_{n+1}{}^{(k)} + \delta\boldsymbol{\sigma}_{n+1}{}^{(k+1)}$$

$$\bar{\varepsilon}_{n+1}^p = \bar{\varepsilon}_{n+1}^{p\,(k)} + \delta\bar{\varepsilon}_{n+1}^{p\,(k+1)}$$

$$\Delta\gamma = \Delta\gamma^{(k)} + \delta\Delta\gamma^{(k+1)}$$

Update other state variables:

$$\boldsymbol{\varepsilon}_{n+1}^e = [\mathbf{D}^e]^{-1} : \boldsymbol{\sigma}_{n+1} \quad ; \quad p_{n+1} = \frac{1}{3} tr(\boldsymbol{\sigma}_{n+1}) \quad ; \quad \boldsymbol{S}_{n+1} = \boldsymbol{\sigma}_{n+1} - p_{n+1}\boldsymbol{I}$$

3) Check for convergence

$$\tilde{\Phi} = q_{n+1} - \sigma_y(\bar{\varepsilon}_{n+1}^p)\left[1 - C_\eta(\eta_{n+1} - \eta_0)\right]\left[C_\theta^s + (C_\theta^{ax} - C_\theta^s)\left(\mu_{n+1} - \frac{\mu_{n+1}{}^{m+1}}{m+1}\right)\right]$$

IF $\left|\tilde{\Phi}\right| \leq \epsilon_{tol}$ THEN

Return to Box 3.2.

4) GOTO step (*2*)

3.4.2 Accuracy and stability

In order to ascertain the accuracy and stability of the integration algorithm in practical situations, we can determine the so-called iso-error maps. This method of analysis was introduced by Krieg & Krieg (1977) and discussed by Ortiz & Popov (1985), Simo & Taylor (1985), De Souza Neto *et al.* (2008), among others. To generate a typical iso-error map, le tus consider an arbitrary stress state at a point on the yield surface of Bai and Wierzibicki elasto-plastic model (see Figure 3.4).

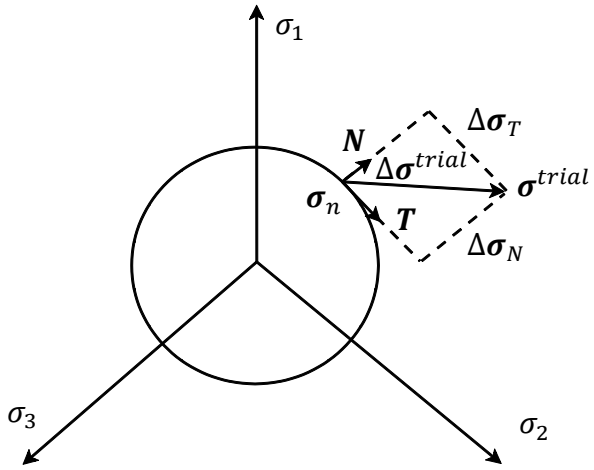

Figure 3.4. Iso-error map. Trial stress incremental directions.

From this point, a sequence of strain increments is applied corresponding to specified normalized elastic trial stress increments of the form:

$$\Delta\boldsymbol{\sigma}^{trial} = \frac{\Delta\boldsymbol{\sigma}_T}{q}\,\boldsymbol{T} + \frac{\Delta\boldsymbol{\sigma}_N}{q}\,\boldsymbol{N}\ , \tag{3.36}$$

where $\boldsymbol{T}$ and $\boldsymbol{N}$ are , respectively, the unit normal and tangent vectors to the yield surface and q is the von Mises equivalent stress. For each increment of the trial stress, we obtain a "*numerical solution"*, $\boldsymbol{\sigma}^{num}$, with the above described algorithm in one step. In addition, a solution assumed to be "*exact*", $\boldsymbol{\sigma}^{exact}$, is obtained with the same algorithm by dividing the corresponding strain (and time) increment into 1000 sub-increments of equal size. For each point, where a "*numerical"* and "*exact*" solution are obtained, the error associated with each increment is defined as:

$$ERROR = \frac{\sqrt{(\boldsymbol{\sigma}^{exact} - \boldsymbol{\sigma}^{num}) : (\boldsymbol{\sigma}^{exact} - \boldsymbol{\sigma}^{num})}}{\sqrt{(\boldsymbol{\sigma}^{exact} - \boldsymbol{\sigma}^{exact})}}\ X\ 100\ . \tag{3.37}$$

The material properties adopted for the present analysis, are listed in Table 3.1. These parameters were taken from Bai (2008) for an aluminium alloy.

Table 3.1. Basic material properties for aluminum 2024-T351. Taken from Bai (2008).

Parameter	Symbol	Value
Young's modulus	$E\ [MPa]$	71500
Poisson´s ratio	ν	0.33
Yield stress	$\sigma_{yo}\ [MPa]$	370
Stress strain curve	$\sigma_y(\bar{\varepsilon}^p)[MPa]$	$908.\ (0.0058 + \bar{\varepsilon}^p)^{0.1742}$
Hydrostatic stress influence	C_η	0.09
Triaxiality ratio reference	η_0	0.33
Lode dependence - shear	C_θ^s	0.855
Lode dependence - tensile	C_θ^t	1.0
Lode dependence - compression	C_θ^c	0.9
Lode dependence - exponent	m	6.0

By varying the prescribed increment sizes $\Delta\boldsymbol{\sigma}_T$ and $\Delta\boldsymbol{\sigma}_N$, respectively, associated with the tangential and normal directions to the yield surface, an error field is obtained. In Figure 3.5, we present the iso-error maps for Bai & Wierzbicki's model without pressure and Lode dependence, with only pressure effect dependence and with both effects. It is possible to conclude that the range of the integration error is almost the same for all cases and it attains a maximum value of 21%. Nevertheless, some differences can be noticed on the shape of the iso-error map when pressure (Figure 3.5b) or both pressure and Lode angle dependence (Figure 3.5c) are activated in the algorithm. When we change the experimental parameters for Bai & Wierzbicki model, the convergence of the return mapping algorithm is not significantly affected.

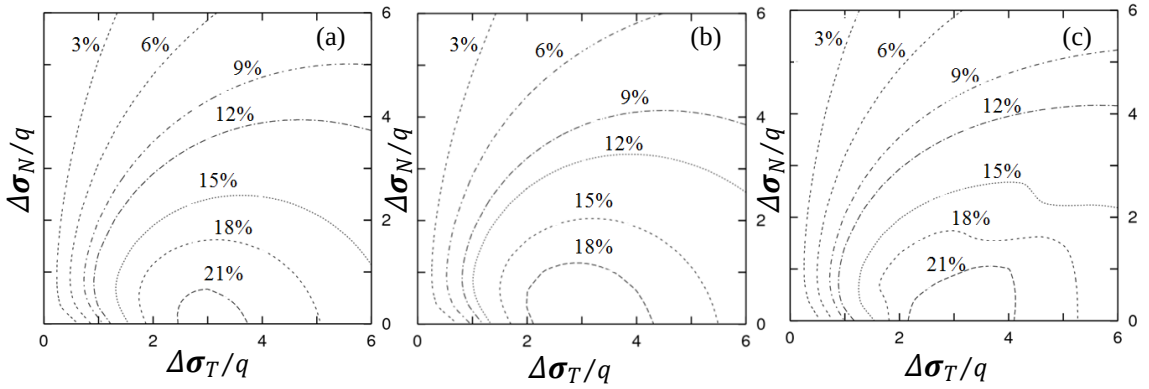

Figure 3.5. Iso-error maps for Bai & Wierzbicki state update algorithm. (a) without pressure effect and Lode dependence. (b) with only pressure dependence. (c) with dependence of both pressure and Lode angle.

Figure 3.6 presents iso-error maps for Bai & Wierzbicki's state update algorithm with only pressure effect introduced. In this case, the analysis of the behavior of the integration error for different triaxiality reference values, η_0, is undertaken. The integration maps for the triaxiality reference value equal to 0.0, 0.3, 0.9 and 1.3, were obtained. When this experimental parameter changes for Bai & Wierzbicki´s model, the convergence of the return mapping algorithm is not affected.

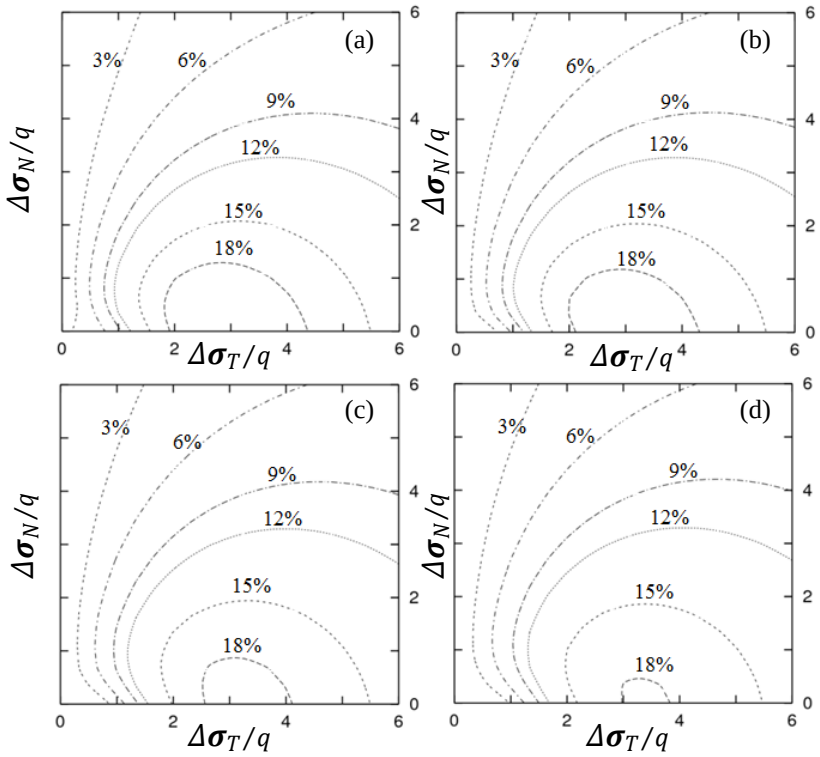

Figure 3.6. Iso-error maps for Bai & Wierzbicki model with triaxiality reference equal to (a) 0.0, (b) 0.3, (c) 0.9 and (d) 1.3, respectively.

3.4.3 Consistent tangent operator

In this section, we describe the procedure to obtain a symbolic expression for the elasto-plastic tangent operator, consistent with the implicit return mapping algorithm for Bai & Wierzbicki's model, which was presented in *Box 3.2*. The tangent operator consistent with the above integration scheme is required for the assembly of the tangent stiffness matrix of the elements into the global stiffness.

In the elasto-plastic case, i.e, when it is assumed that plastic flow accurs within the step, the tangent operator is called the elasto-plastic consistent tangent and is denoted by $\widehat{\mathbf{D}}^{ep}$. The consistent tangent operator is simply a derivative of the implicit function $\widehat{\boldsymbol{\sigma}}$ for the updated stress defined by the return mapping procedure as a function of the elastic trial strain tensor:

$$\widehat{\mathbf{D}}^{ep} \equiv \frac{\mathrm{d}\widehat{\boldsymbol{\sigma}}}{\mathrm{d}\boldsymbol{\varepsilon}_{n+1}^{e\ trial}} \ . \tag{3.38}$$

Its follows the standard procedure for differentiation of implicit functions. Since the return mapping algorithm cannot be reduced to one-equation, in the present case, it is not possible to obtain a closed form expression for $\widehat{\mathbf{D}}^{ep}$. To obtain the tangent operator, the first step (in its derivation) is to obtain the linearized form for the corresponding return mapping system of equations for the general implicit algorithm. The residual system of equations can be represented by:

$$\begin{Bmatrix} \boldsymbol{\sigma}_{n+1} - \boldsymbol{\sigma}_{n+1}^{trial} + \Delta\gamma \mathbf{D}^{e} \colon \boldsymbol{N}_{n+1} \\ \bar{\varepsilon}_{n+1}^{p} - \bar{\varepsilon}_{n}^{p} - \Delta\gamma\sqrt{(*)} \\ q_{n+1} - \sigma_y\left(\bar{\varepsilon}_{n+1}^{p}\right) A_{n+1}(\eta_{n+1}) B_{n+1}(\mu_{n+1}) \end{Bmatrix} = \begin{Bmatrix} \mathbf{0} \\ 0 \\ 0 \end{Bmatrix}, \tag{3.39}$$

After some algebraic manipulations, the linearized return mapping system of equations can be expressed in the following form:

$$\begin{bmatrix} \dfrac{\partial \boldsymbol{r}_{\boldsymbol{\sigma}}}{\partial \boldsymbol{\sigma}_{n+1}} & \dfrac{\partial \boldsymbol{r}_{\boldsymbol{\sigma}}}{\partial \bar{\varepsilon}_{n+1}^{p}} & \dfrac{\partial \boldsymbol{r}_{\boldsymbol{\sigma}}}{\partial \Delta\gamma} \\ \dfrac{\partial r_{\bar{\varepsilon}^p}}{\partial \boldsymbol{\sigma}_{n+1}} & \dfrac{\partial r_{\bar{\varepsilon}^p}}{\partial \bar{\varepsilon}_{n+1}^{p}} & \dfrac{\partial r_{\bar{\varepsilon}^p}}{\partial \Delta\gamma} \\ \dfrac{\partial r_{\Delta\gamma}}{\partial \boldsymbol{\sigma}_{n+1}} & \dfrac{\partial r_{\Delta\gamma}}{\partial \bar{\varepsilon}_{n+1}^{p}} & \dfrac{\partial r_{\Delta\gamma}}{\partial \Delta\gamma} \end{bmatrix} \cdot \begin{bmatrix} \mathrm{d}\boldsymbol{\sigma}_{n+1} \\ \mathrm{d}\bar{\varepsilon}_{n+1}^{p} \\ \mathrm{d}\Delta\gamma \end{bmatrix} = \begin{bmatrix} \mathrm{d}\boldsymbol{\varepsilon}_{n+1}^{e\ trial} \\ 0 \\ 0 \end{bmatrix} . \tag{3.40}$$

Finally, by inverting the above linear relation, we can obtain:

$$\begin{bmatrix} \mathrm{d}\boldsymbol{\sigma}_{n+1} \\ \mathrm{d}\bar{\varepsilon}^{p}_{n+1} \\ \mathrm{d}\Delta\gamma \end{bmatrix} = \begin{bmatrix} \mathbb{I} + \Delta\gamma \mathbf{D}^{e} : \dfrac{\partial \boldsymbol{N}_{n+1}}{\partial \boldsymbol{\sigma}_{n+1}} & \Delta\gamma \dfrac{\partial \boldsymbol{N}_{n+1}}{\partial \bar{\varepsilon}^{p}_{n+1}} & \mathbf{D}^{e} : \boldsymbol{N}_{n+1} \\ -\Delta\gamma \dfrac{\partial \sqrt{(*)}}{\partial \boldsymbol{\sigma}_{n+1}} & 1 - \Delta\gamma \dfrac{\partial \sqrt{(*)}}{\partial \bar{\varepsilon}^{p}_{n+1}} & -\sqrt{(*)} \\ \boldsymbol{N}_{n+1} & -A_{n+1} B_{n+1} H & 0 \end{bmatrix}^{-1} : \begin{bmatrix} \mathrm{d}\boldsymbol{\varepsilon}^{e\,trial}_{n+1} \\ 0 \\ 0 \end{bmatrix} . \tag{3.41}$$

The above linear relation can be rewritten in a compressed form, as:

$$\begin{bmatrix} \mathrm{d}\boldsymbol{\sigma}_{n+1} \\ \mathrm{d}\bar{\varepsilon}^{p}_{n+1} \\ \mathrm{d}\Delta\gamma \end{bmatrix} = \begin{bmatrix} \mathbb{M}_{\mathbf{11}} & \boldsymbol{M}_{\mathbf{12}} & \boldsymbol{M}_{\mathbf{13}} \\ \boldsymbol{M}_{\mathbf{21}} & M_{\mathbf{22}} & M_{\mathbf{23}} \\ \boldsymbol{M}_{\mathbf{31}} & M_{\mathbf{32}} & M_{\mathbf{33}} \end{bmatrix} : \begin{bmatrix} \mathrm{d}\boldsymbol{\varepsilon}^{e\,trial}_{n+1} \\ 0 \\ 0 \end{bmatrix} , \tag{3.42}$$

where $\mathbb{M}_{11}$ represents a fourth order tensor; $\boldsymbol{M}_{12}$, $\boldsymbol{M}_{21}$, $\boldsymbol{M}_{13}$ and $\boldsymbol{M}_{31}$ represent second order tensors and M_{22} , M_{23} , M_{32} and M_{33} are scalars.

From the above representation, it is possible to obtain the tangent operator that is consistent with the implicit return mapping algorithm, proposed in *Box 3.2*. The elasto-plastic consistent tangent operator can be expressed by:

$$d\boldsymbol{\sigma}_{n+1} = \mathbb{M}_{\mathbf{11}} : \mathrm{d}\boldsymbol{\varepsilon}^{e\,trial}_{n+1} \tag{3.43}$$

or,

$$\mathbf{D}^{\boldsymbol{ep}} = \frac{d\boldsymbol{\sigma}_{n+1}}{d\boldsymbol{\varepsilon}^{e\,trial}_{n+1}} = \mathbb{M}_{\mathbf{11}} . \tag{3.44}$$

3.4.4 Convergence of the equilibrium problem

In order to show that the quadratic convergence is also attained for large excursions outside the elastic domain, in this section we tested the convergence of the global Newton-Raphson algorithm, represented by the solution of the equilibrium problem. We present here, the so-called relative residual of the solution for some typical load increments, which has both effects disabled, the pressure effect active and both pressure effect and Lode angle dependence active.

The global Newton-Raphson iterations are repeated until, in some iteration (m), the following convergence criterion is satisfied (see Equation 3.45):

$$\frac{\left|r^{(m)}\right|}{\left|\bar{\mathrm{f}}_{n+1}^{\mathrm{ext}}\right|} \leq tolerance \ , \tag{3.45}$$

where $r^{(m)}$ is the residual or out-of-balance force vector and $\bar{\mathrm{f}}_{n+1}^{\mathrm{ext}}$ represents the external force vector, which can be calculated as:

$$r = \mathrm{f}^{\mathrm{int}} - \lambda_{n+1}\bar{\mathrm{f}}^{\mathrm{ext}} \quad \text{and} \quad \mathrm{f}_{(e)}^{\mathrm{int}} := \sum_{i=1}^{ngausp} w_i \, j_i \mathbf{B}_i^{\mathrm{T}} \boldsymbol{\sigma}_{n+1}^{(k)}\Big|_i \ , \tag{3.46}$$

where λ_{n+1} is the load factor, $\mathbf{B}_{\mathrm{i}}^{\mathrm{T}}$ represents the strain matrix that is generally composed by the derivatives of the shape functions and $\boldsymbol{\sigma}_{\mathrm{n+1}}^{(\mathrm{k})}$ represents the incremental constitutive function for the stress tensor.

The problem was solved using 25 pseudo-load steps and a tolerance of $1.0\mathrm{x}10^{-6}$ was imposed. The convergence rates obtained, for all cases, were quadratic, see Table 3.2 that represets the global convengence for a smooth bar specimen under tensile loading.

Table 3.2. Relative residual for the global problem.

Increment	without effects introduced		with only pressure effect		with both pressure effect and lode angle dependence	
	Iter.	relative residual	Iter.	relative residual	Iter.	relative residual
5/25	1	1.14708	1	1.20068	1	1.30510
	2	0.216182E-02	2	0.296808E-02	2	0.124367E-01
	3	0.233401E-07	3	0.600232E-07	3	0.690970E-05
	4	----	4	----	4	0.684965E-08
15/25	1	1.19274	1	1.20787	1	1.21652
	2	0.102427E-02	2	0.371704E-02	2	0.154117E-01
	3	0.724211E-08	3	0.779755E-07	3	0.569143E-04
	4	----	4	----	4	0.567116E-07
25/25	1	3.24953	1	3.32520	1	0.201128
	2	0.670759	2	0.743644	2	0.659221E-02
	3	0.567872E-01	3	0.564556E-01	3	0.121698E-06
	4	0.105264E-02	4	0.734190E-06	4	----
	5	0.684967E-08	5	----	5	----

3.5 NUMERICAL SIMULATION

In this section, several numerical examples are presented to illustrate the robustness of the proposed implicit algorithm with two types of materials: aluminum alloy 2024-T351 and 1045 steel. Tensile tests on cylindrical smooth bars with necking and on notched bars specimens are initially used and for complementary analysis, flat grooved specimens are also employed. The materials properties for the aluminum alloy are listed in Table 3.1, and for the 1045 steel can be observed in Table 3.3.

Table 3.3. Material properties for 1045 steel. Taken from Bai (2008)

Parameter	Symbol	Value
Young's modulus	$E\ [MPa]$	220.000
Poisson´s ratio	ν	0.33
Yield stress	$\sigma_{yo}\ [MPa]$	830
Stress strain curve	$\sigma_y(\bar{\varepsilon}^p)[MPa]$	$830 - 500(1 - \exp(-0.4\bar{\varepsilon}^p))$
Hydrostatic stress influence	C_η	0.00
Triaxiality ratio reference	η_0	-0.76
Lode dependence - shear	C_θ^s	1.0
Lode dependence - tensile	C_θ^t	1.0
Lode dependence - compression	C_θ^c	1.0
Lode dependence - exponent	m	6.0

3.5.1 Geometry and mesh definition

In the following, the geometries of each specimen, which will be used in the numerical simulations, are presented as well as the mesh definition. Regarding the aluminum alloy, both cylindrical bars have a gauge equal to 25.4 mm, and for the 1045 steel, the gauge used was equal to 20.6 mm. The notched bars have a notch radius of $R = 4.0\,mm$ and $R = 10.5\,mm$ for the aluminum alloy and steel, respectively. For the flat grooved, grooves of $R = 1.59\ mm$ and $R = 3.97\ mm$ were used for the aluminum alloy and steel, respectively. In both cases, the gauge used

was equal to 25.0 *mm*. Figure 3.7 shows the dimensions for both cylindrical smooth and notched bars and for the flat grooved plate specimens.

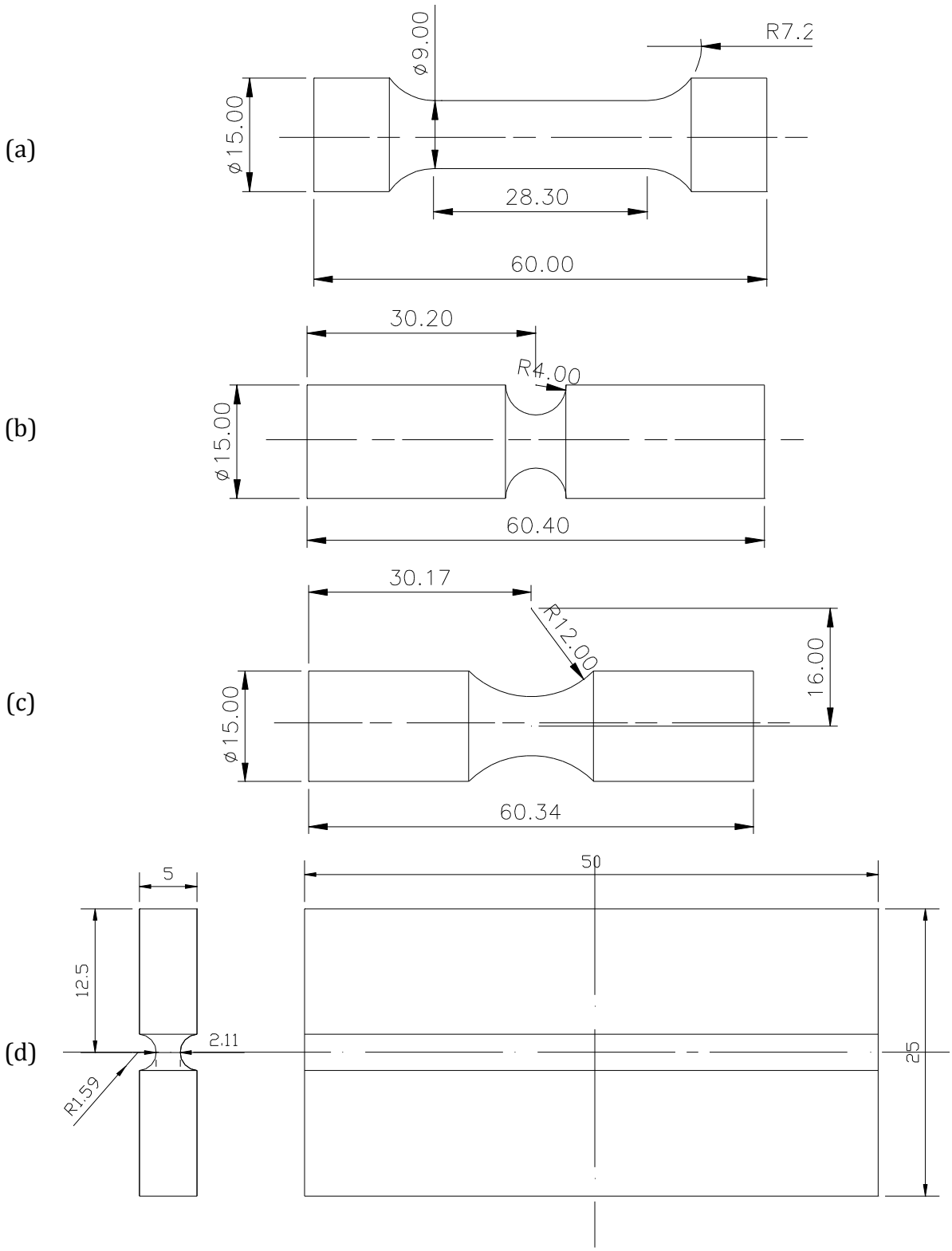

Figure 3.7. Geometry of the cylindrical smooth and notched bars, and for the flat grooved plate specimens (dimensions in mm), see Bai (2008).

In order to capture the necking pattern and the evolution of internal variables, a relatively fine discretisation is used in the region surrounding the smaller cross-section of the specimens (see Figure 3.8). The standard eight-noded axisymmetric quadrilateral element, with four Gauss integration points, is adopted for both cylindrical bars. The initial mesh discretization of the specimens for the two types of materials is illustrated in Figure 3.8, where only one symmetric quarter of the problem, with the appropriate symmetric boundary conditions imposed to the relevant edges, is modeled.

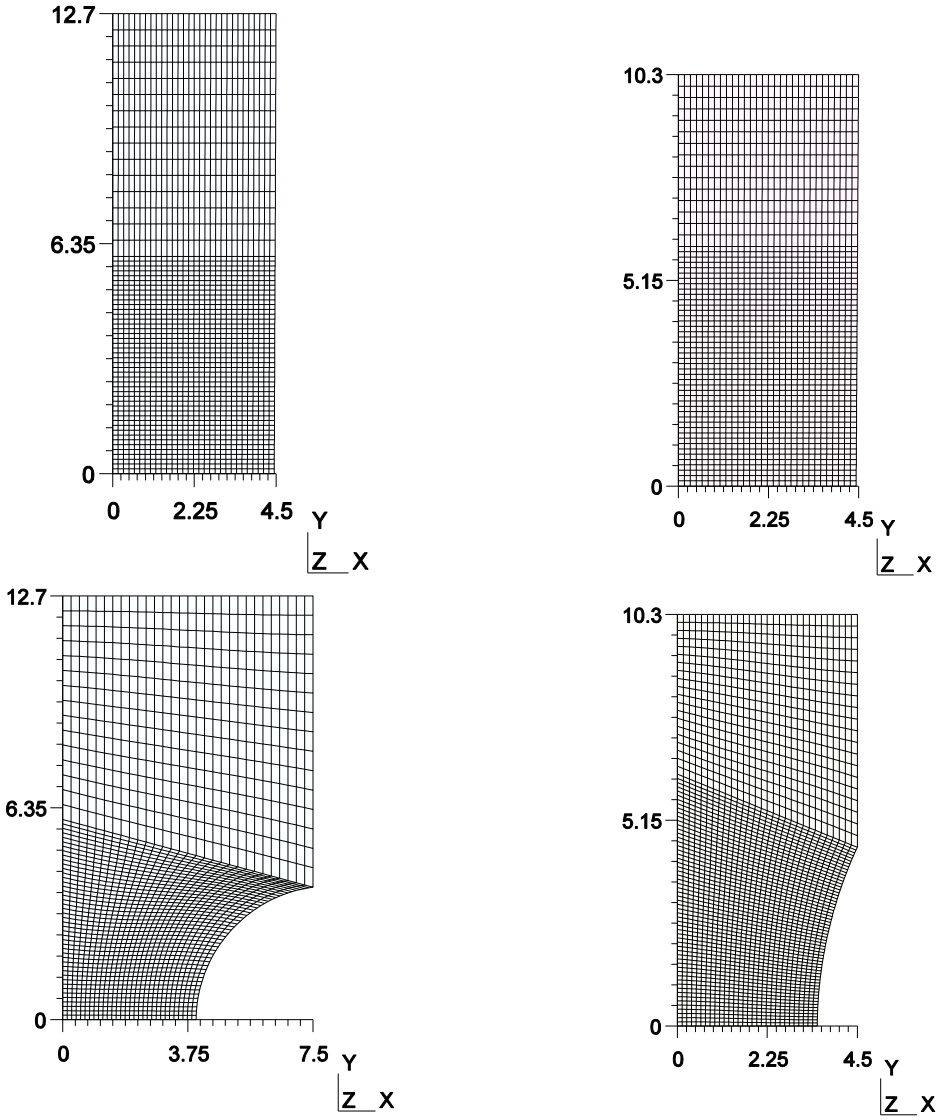

Figure 3.8. Finite element meshes for the cylindrical smooth and notched bar specimens. (a) aluminum alloy and (b) 1045 steel.

A total number of 1800 elements have been used in the discretization of both smooth and notched bars, amounting to a total of 5581 nodes.

The stretching of flat grooved plates is also undertaken. The initial geometry of the specimen is shown in Figure 3.7(d). Due to symmetry, only half of the geometry is modeled, with appropriate boundary conditions imposed to the symmetry planes. A three dimensional hexahedra mesh of eight noded elements (F-Bar), with four Gauss integration points, is used to discretise half of the specimen. A total number of 4500 elements have been used amounting to a total of 5712 nodes for the specimen with a groove equal to $R = 1.59\ mm$ (see Figure 3.9a), and 2700 elements amounting to a 3472 nodes for the specimen with Groove equal to $R = 3.97\ mm$ (see Figure 3.9b).

(a)

(b)

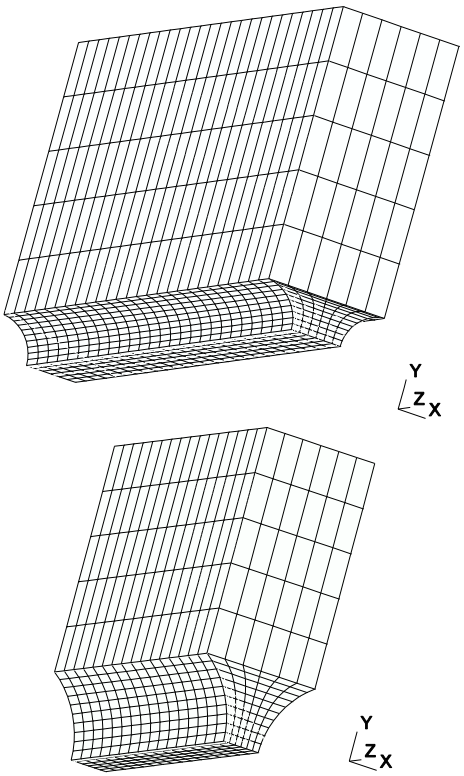

Figure 3.9. Three dimensional finite element meshes for the flat grooved plate specimen. (a) $R = 1.59\ mm$ for aluminum alloy and (b) $R = 3.97\ mm$ for steel.

3.5.2 Numerical results

Numerical simulations were carried out for three types of specimens with two different materials. The results obtained with the Bai & Wierzbicki's model have been grouped into three different cases: "*case 1 (c1)"*, which represents the Bai & Wierzbicki model without the pressure effect and Lode angle dependence, "*case 2 (c2)"*, which represents the model with only pressure effect and "*case 3 (c3)"*, which represents the model with both pressure effect and Lode angle dependence (see Figures 3.10 and 3.11).

Figure 3.10 presents the numerical results obtained from the numerical simulations for the force (reaction) *versus* displacement curve, together with the experimental ones, for the specimens selected. In Figure 3.10(a), we have the numerical results for an aluminum alloy and Figure 3.10(b), for a 1045 steel.

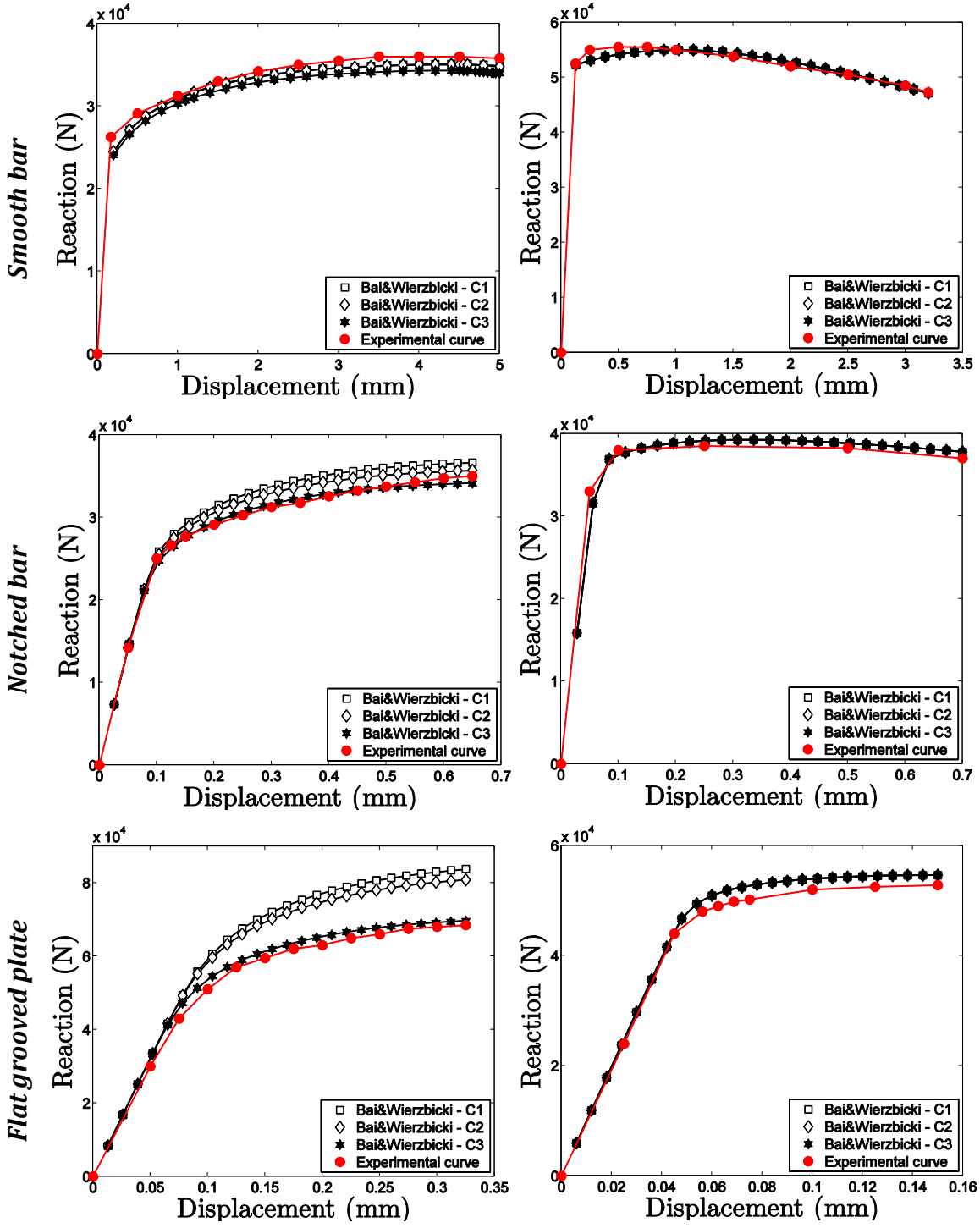

Figure 3.10. Reaction *versus* displacement curves for (a) aluminum alloy and (b) 1045 steel, regarding three different specimens.

From the analysis of Figure 3.10, it is possible to conclude that the agreement between numerical results with experimental ones improves when the effect of pressure and Lode angle are included in the model. The enhancement is particularly noticeable for the aluminum alloy. Table 3.4 represents the difference between numerical and experimental results for reaction *versus* displacement curves, in all the cases that have been studied. For the aluminum alloy and the notched bar specimen, the numerical results with both pressure and Lode angle dependence are more realistic than without both effects. In this case, the difference between the reaction *versus* displacement curve, without both effects, and the experimental curve is around 6%. When both effects are active for the same specimen, the difference reduces to less than 1%, which highlighs the importance of pressure and Lode angle in the behavior of some ductile materials. For the flat grooved plate specimen, the correction on the reaction *versus* displacement curve, when both effects are active, is more visible and, in this case, the difference between the model without effects and the experimental curve is around 20%. This value is reduced to less than 2%, when both pressure effect and Lode angle dependence are active. Nevertheless, for the 1045 steel, the numerical results agree well with experimental data with or without the inclusion of the dependence of pressure and Lode angle. Hence, we can conclude that the aluminum alloy is a material strongly dependent on both pressure and Lode angle and the 1045 steel is weakly dependent on both effects.

Table 3.4. Difference between numerical and experimental results for the reaction *versus* displacement curve, regarding two types of materials.

	Specimen	*Case 1*	*Case 2*	*Case 3*
Aluminum alloy	Smooth bar	1%	1%	1%
	Notched bar $R = 4.0\ mm$	6%	4%	1%
	Flat grooved $R = 1.59\ mm$	20%	16%	1%
1045 steel	Smooth bar	1%	1%	1%
	Notched bar $R = 10.5\ mm$	1%	1%	1%
	Flat grooved $R = 3.97\ mm$	2%	2%	2%

The contribution of both effects to the plastic flow rule can also be observed through the evolution of the equivalent plastic strain on the central node of the

specimens (see Figure 3.11). From the analysis of the results for the aluminum alloy (Figure 3.11a), it is possible to conclude that only on the smooth bar and the flat grooved plate the differences on the evolution of the equivalent plastic strain can be noticed. In particular, for the flat grooved plate specimen, the evolution of this internal variable has presented different evolutions (see Figure 3.11a).

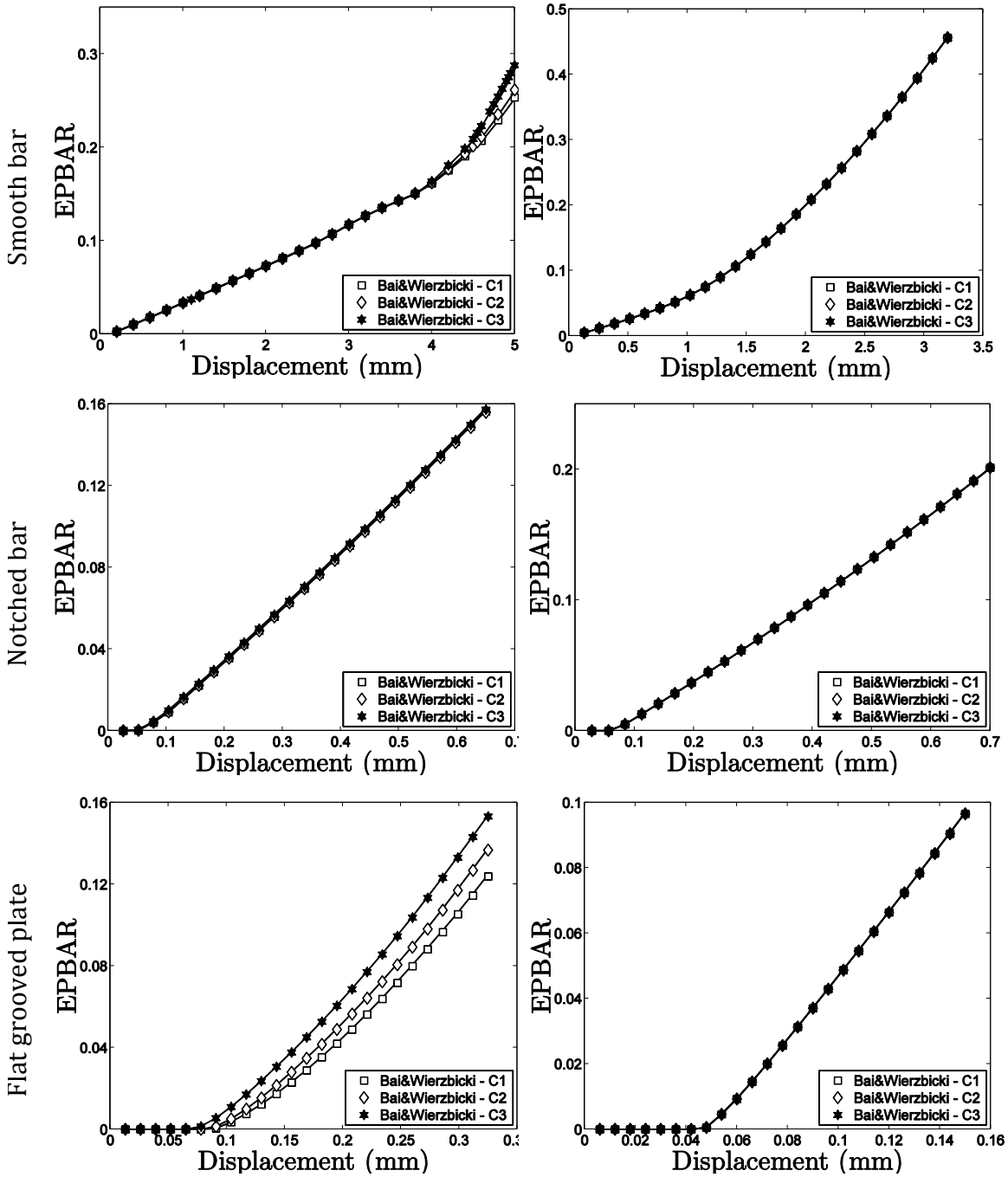

Figure 3.11. Evolution of the equivalent plastic strain for (a) aluminum alloy and (b) 1045 steel, regarding three different specimens.

Nevertheless, regarding the behavior of 1045 steel, the evolution of the equivalent plastic strain was the same, for all specimens, whether pressure effect and Lode angle dependence are active or not. For this type of material, the contribution of both effects to the plastic flow rule is negligible, and the von Mises' model can adequately represent the material behavior, which is not true, for the behavior of an aluminum alloy.

The contour of the equivalent plastic strain can also be analyzed, in order to study the influence of both effects on the ability to predict the location to crack initiation. Some authors, such as Freudenthal (1950), Gillemont (1976) and Datsko (1966) have suggested the use of the plastic strain as a fracture indicator, throught the total plastic work or the equivalent plastic strain criterions. Nevertheless, several researchers (Wilson, 2002; Gouveia, 1995) have also shown that this parameter alone is not enough to characterize fracture initiation, and in some cases, can indicate potential sites to fracture initiation in disagreement with experimental evidence. According to Wilson (2002), for both smooth and notched bars specimens, the crack begins on the center and grows to the surface of the specimens. Analyzing Figure 3.12 and 3.13 and considering the equivalent plastic strain as a fracture indicator, both numerical results for the smooth bars specimens agree with experimental evidence (see Figure 3.12a and 3.13a). For the notched bars specimens, this internal variable has a maximum on the surface, for the aluminum alloy (see Figure 3.12b), and by this reason cannot be employed as a criterion for the prediction of fracture onset. Nevertheless, regarding the 1045 steel, the numerical predition agrees with the experimental observation (see Figure 3.13b). In addition, we can also observe, that for both cylindrical specimens, the activation of pressure effect and Lode angle dependence does not influence the location of the maximum value of the equivalent plastic strain. However, according to experimental tests conducted by Bai (2008) for the flat grooved plate specimen, the crack starts on center of the specimen and propagates towards the surface. This behavior is only captured when both effects are active, for the aluminum alloy (see Figure 3.12c), and is captured by all cases for the 1045 steel (see Figure 3.13c).

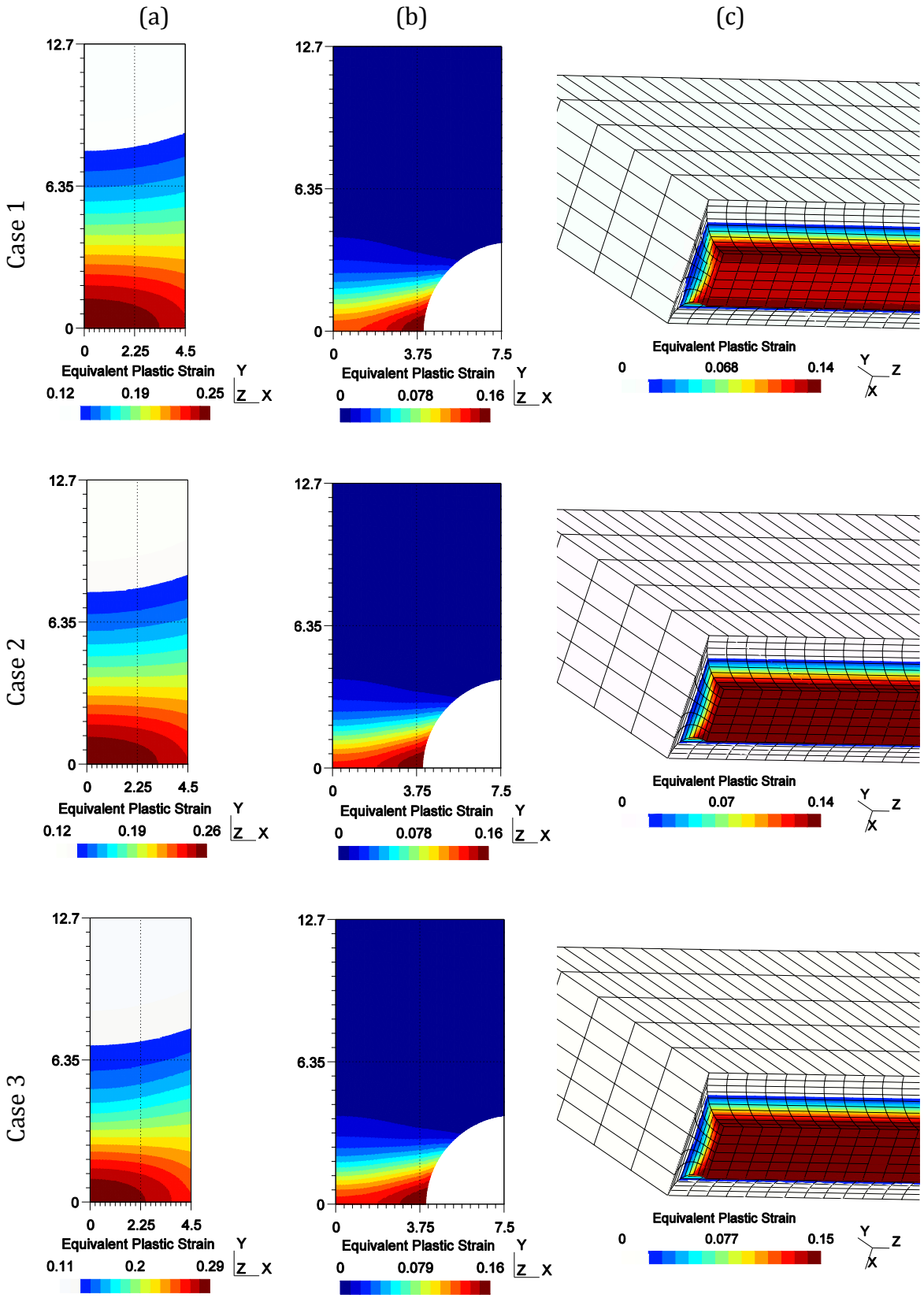

Figure 3.12. Contour of the equivalent plastic strain: (a) a smooth bar specimen, (b) a notched bar specimen with $R = 4.0\ mm$, and (c) a flat grooved plate specimen with $R = 1.59\ mm$, for the aluminum alloy.

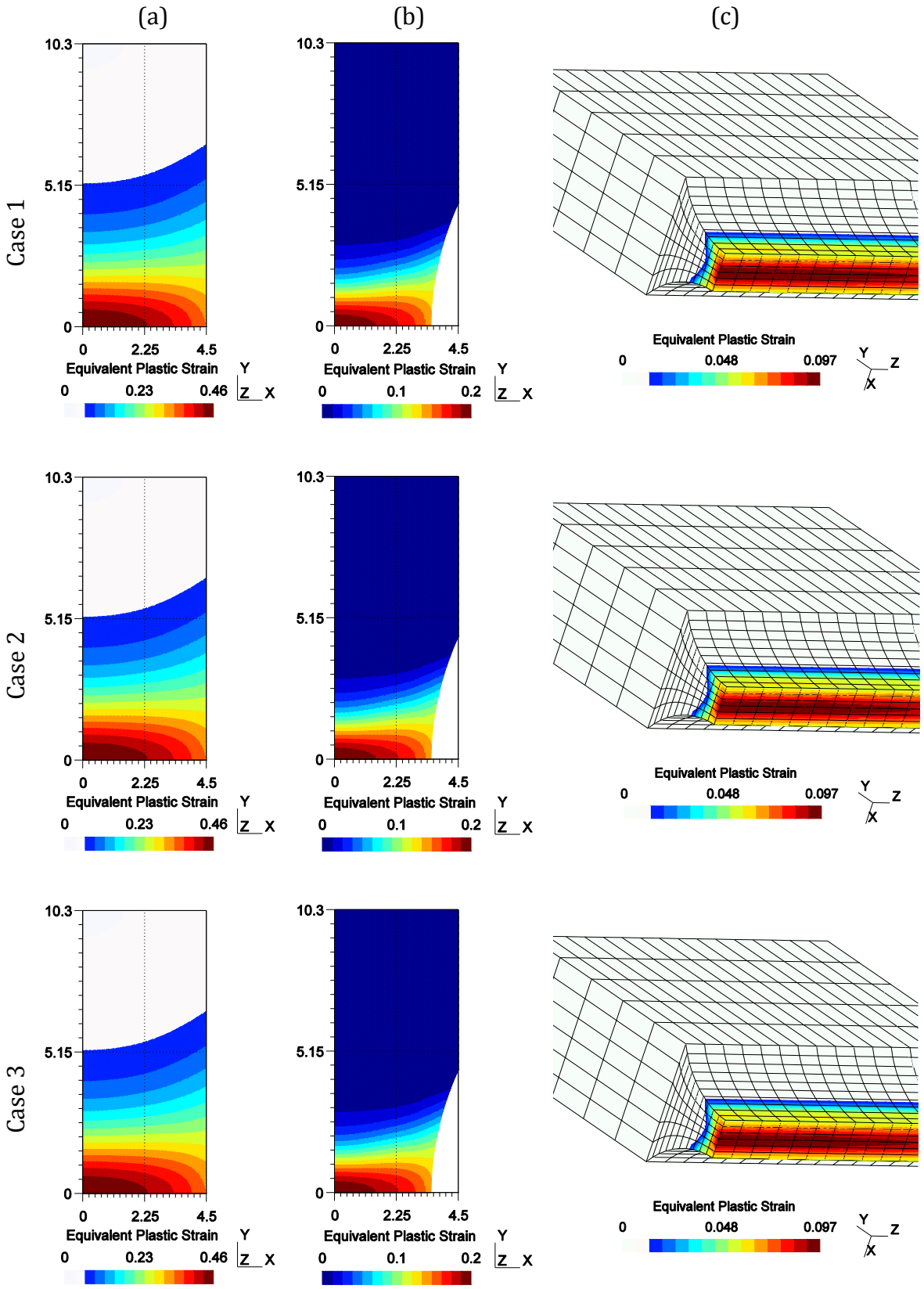

Figure 3.13. Contour of the equivalent plastic strain: (a) a smooth bar specimen, (b) a notched bar specimen with $R = 10.5\ mm$, and (c) a flat grooved plate specimen with $R = 3.97\ mm$, for the steel 1045.

3.6 CONCLUSIONS

In this chapter, an implicit numerical integration algorithm for Bai & Wierzbicki´s model was developed based on the operator split method. As expected, a quadratic rate of convergence is achieved by using the Newton Raphson method at both local and global problems and from the analysis of the iso-error maps, it is possible to conclude that the integration error is lower than 21% for all cases studied (see Figure 3.5 and 3.6). In addition, cylindrical smooth and notched ($R = 4\,mm$ and $R = 10.5\,mm$) bars specimens and flat grooved ($R = 1.56\,mm$ and $R = 3.97\,mm$) plate specimens were used to illustrate the robustness of the proposed algorithm, for two types of materials (aluminum alloy and steel). According to numerical and experimental results, we can conclude that both pressure effect and Lode angle dependence cannot be neglected and have to be taken into account in the plastic flow rule of the aluminum alloy. From the analysis of the reaction *versus* displacement curves of the aluminum alloy (Figure 3.10a) and steel (Figure 3.10b), we can suggest the following classification of materials: strongly dependent on both pressure and Lode angle, such as the aluminum alloy that achieved the best agreement for case 3 (see Table 3.4), and weakly dependent on both effects, such as the 1045 steel that without the introduction of any effect had a good agreement with experimental results.

Regarding the evolution of the equivalent plastic strain, Figure 3.11a has shown different rates of evolution for this internal variable, depending on the activation of both effects, which can also be used to demonstate the importance of both parameters in the behavior of ductile materials. At the end, analyzing the contour of the equivalent plastic strain, we can observe that the introduction of additional effects does not change the maximum location of the contour plot for the tests conducted. Nevertheless, for the flat grooved plate of aluminum alloy (see Figure 3.12c), the introduction of both effects brought a correction in the fracture onset location.

CHAPTER 4

An Assessment of Isotropic Constitutive Models for Ductile Fracture under High and Low Stress Triaxiality

In this chapter, a numerical assessment of three isotropic constitutive models is performed in order to identify their applicability and reliability in the prediction of ductile failure under a wide range of stress triaxiality. The well established isotropic coupled damage models proposed by Gurson-Tvergaard-Needleman (GTN), which is based on micromechanical grounds and here extended with a shear mechanism, and by Lemaitre, which is based on continuum damage mechanics, are selected and investigated. Besides these, an uncoupled damage elasto-plastic model proposed by Bai and Wierzibicki and presented in Chapter 3, which includes the effect of three invariants of the stress tensor, is also selected and examined. All constitutive formulations are implemented in a quasi-static finite element scheme and applied to simulate the behavior of the 2024-T351 aluminum alloy, which is strongly dependent on both pressure and Lode angle. To assess the predictive ability of the constitutive models under different levels of stress triaxiality, specimens with different geometries and dimensions are used, such as: smooth and notched cylindrical bars, a plate hole specimen and a butterfly specimen. The evaluation of the models is initially carried out under pure tensile loading conditions and then under shear dominated deformation modes. In addition, a combination of both tensile and shear loading is also studied. Finally, the results obtained from the numerical simulations are analyzed and critically compared with experimental results available in the literature. The performance of each constitutive approach under each range of stress triaxiality is highlighted and the main observations are discussed.

4.1 INTRODUCTION AND MOTIVATION

The prediction of ductile failure in metals still represents an important challenge for the simulation of rupture in structural components and for the design of both sheet and bulk metal forming processes. According to Kachanov (1986), large deformations in metals, which can induce the phenomenon of initiation and growth of cavities and micro cracks, has been studied in detail leading to the concept of ductile fracture. Pioneering work undertaken on the subject was carried out by McClintock (1968) and Rice and Tracey (1969), where the effect of the geometry of defects in a continuous matrix was taken into account in the study of ductile damage. Experimental evidence has shown that the nucleation and growth of voids and micro cracks, which accompany large plastic flow, causes a reduction of the elastic modulus, induces a softening effect in the material and can be strongly influenced by the level of stress triaxiality (McClintock, 1968; Rice & Tracey, 1969; Hancock & Mackenzie, 1976). The equivalent plastic strain at fracture and the level of stress triaxiality were initially employed to characterize material ductility in engineering applications (Bridgman, 1952; McClintock, 1968; Rice & Tracey, 1969; Johnson & Cook, 1985). A simple exponential expression for the evolution of the equivalent strain with stress triaxiality was established by McClintock (1968) and Rice and Tracey (1969) based on the analysis of void growth under hydrostatic loads, which is usually referred to as the two dimensional fracture *loci*. The work performed by Mirza *et al.* (1996) on pure iron, mild steel and aluminum alloy BS1474 over a wide range of strain rates confirmed the strong dependence of the equivalent strain to crack formation with the level of stress triaxiality.

The ductile fracture phenomenon can be described, based on micromechanical analysis by the growth of micro cavities, especially for the fracture computation within local approaches to fracture (Pineau, 1981; Mudry, 1985; Rousselier, 1987; Besson *et al*., 2001). Alternatively, it can be rooted in the Continuum Damage Mechanics theory within a thermodynamic framework, either phenomenological or micromechanically based, such as the model proposed by Lemaitre (1985) for damage caused by plastic flow, Chaboche (1984) and Murakami and Ohno (1981) for creep damage, Krajčinović & Fonseka (1981) for

brittle damage, among many others. The current two principal methodologies for ductile damage modeling can be summarized by Lemaitre and Gurson theories (Chaboche *et al*., 2006). These well established theories have been extended and modified by many researchers in order to circumvent some limitations and also to improve the ability of predicting both the loss of stiffness of the material and the correct fracture location. This has mainly been accomplished through the introduction of additional effects either on the constitutive formulation or the damage evolution law, such as: the pressure effect, temperature, viscoplastic effects, crack closure effects, among others (e.g. Rousselier, 1980 and 2001; Tvergaard & Needleman, 1984; Lemaitre and Chaboche, 1990; Voyiadjis and Kattan, 1999; Chaboche, 2003; Andrade Pires *et al*., 2004; Chaboche *et al*., 2006). For a recent review on constitutive models, which were developed to simulate ductile failure, see Besson (2010) and references therein.

A different strategy has also been pursued by some researchers which combines elasto-plastic constitutive formulations with the so-called fracture indicators to predict the ductile behavior of materials. The use of fracture indicators to predict the collapse in problems subjected to plastic deformation emerged when a criterion based on the total plastic work was proposed by Freudenthal (1950). Since then, many others indicators were proposed such as Datsko´s criterion (1966) based on the equivalent plastic strain, the criterion of Rice and Tracey (1969) based on the geometry of defects, the criterion proposed by Cockcroft and Lathan (1968) based on the mechanism of void growth driven by the principal stress, among others. The development of experimental techniques and plasticity models helped the study of these strategies in plastic forming operations, as presented by Clift *et al*. (1990), Cescotto and Zhu (1995) and Gouveia *et al*. (1996). These uncoupled approaches have been adopted due to its simple formulation and ease of calibration. The development of fracture criteria was pursued later within the continuum damage mechanics framework (Lemaitre, 1985; Tai and Yang, 1986, 1987; Vaz Jr., 1998).

Recently, several researchers (Kim *et al*., 2003; Kim *et al*., 2004; Bao and Wierzbicki, 2004; Gao *et al*., 2005; Gao *et al*., 2006, Kim *et al*., 2007; Barsoum and Faleskog, 2007a; Barsoum and Faleskog, 2007b; Bai and Wierzbicki, 2008; Brünig

et al., 2008; Gao *et al*., 2009) have shown that the Lode angle, which is associated to the third invariant of the deviatoric stress tensor, is an essential parameter in the characterization of the effect of the stress state on material yielding and on ductile fracture. In particular, Bai and Wierzbicki (2008) have suggested a three dimensional fracture *loci* on the space of equivalent strain, stress triaxiality and Lode angle. This fracture surface is clearly different for materials weakly or strongly dependent on both pressure and Lode angle and can be calibrated by means of conventional and butterfly specimens. Mirone *et al*. (2010) have proposed a local viewpoint for evaluating the influence of the stress triaxiality and Lode angle on ductile failure, analyzing three theories, namely the Tresca criteria and two models proposed by Wierzbicki. According to Mirone *et al*. (2010), the phenomenon of ductile failure is influenced by the relation with the variables from the stress–strain characterization and failure predictions are better described by plastic strain, stress triaxiality and Lode angle parameters. An experimental program to study the influence of the stress tensor invariants in ductile failure was presented by Driemeier *et al*. (2010). This methodology can be seen as an efficient tool to investigate the effects of the stress intensity, stress triaxiality and Lode angle. Gao *et al*. (2011) have proposed a new elasto-plastic model, which is a function of the hydrostatic stress as well as the second and third invariants of the stress deviator, and carried out tests in specimens with a high level of stress triaxiality showing the dependence of the plastic flow rule of both stress triaxiality and Lode angle.

The study of the previous references allows us to conclude that the appropriate modeling of the physical mechanisms that precede ductile fracture is by no means trivial. This is particularly true when volumetric and shear effects are combined through complex strain paths. Figure 4.1 schematically illustrates the micromechanical behavior of a ductile material under shear and tensile loading conditions.

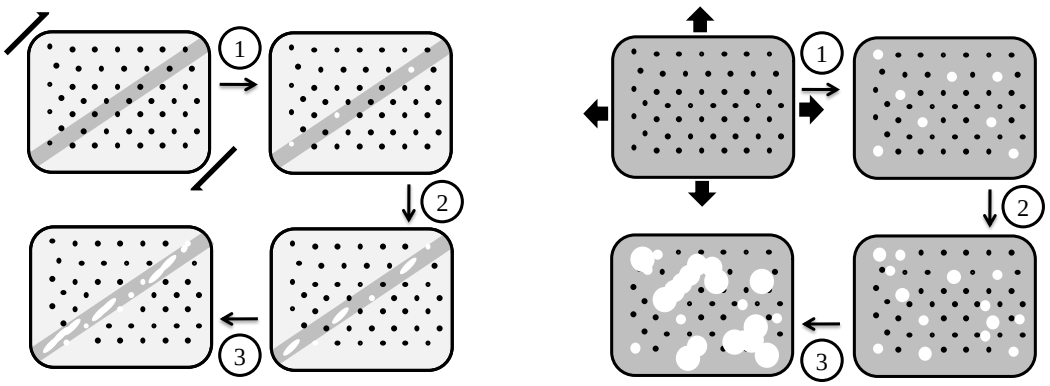

(a) (b)

Figure 4.1. Schematic representation of: (a) elongated and (b) spherical void growth. Adapted from Pineau & Pardoen (2003) and Engelen (2005).

Under shear dominated loads, see Figure 4.1a, the material nucleates micro voids (stage 1 in Figure 4.1a) that elongate when the load increases (stage 2 in Figure 4.1a). Then, coalescence of elongated voids occurs (stage 3 in Figure 4.1a) due to instabilities in the shear bands. Under tensile dominant loads, see Figure 4.1b, the micro voids nucleate and expand (stages 1 and 2 in Figure 4.1b) due to high tensile hydrostatic stresses and, at the end, coalescence occurs due to the impingement of neighboring voids (stage 3 in Figure 4.1b).

Although significant research efforts have been devoted to the understanding of the phenomenon of ductile fracture and to the formulation of constitutive models, the improper application of the models to various deformations processes may result in misleading ductile fracture predictions. This is critical in many practical applications where the prediction of the material ductile failure behavior is vital for the design and optimization of structures and components. In addition, there are not many systematic evaluations of the predictive ability of constitutive models, under the same circumstances, and it is still difficult to know which model to use. These facts have restricted their widespread application to practical problems (Zadpoor *et al*., 2009). A recent contribution to this discussion was presented by Li *et al*. (2011) that conducted a thorough assessment of the performance of a posteriori fracture indicators and two coupled damage models: the Gurson-Tvergaard-Needleman (GTN) model and Lemaitre´s model. The authors concluded that there is no approach that works well on the entire range of stress triaxiality. Nevertheless, new models have been formulated that have the

potential to address some of the identified shortcomings. Therefore, the main objective of this contribution is to perform a comparison between recently improved coupled isotropic ductile damage models, based on Lemaitre and Gurson´s frameworks (Gurson, 1977; Lemaitre, 1985), and a newly developed uncoupled damage elasto-plastic model, formulated by Bai and Wierzbicki (2008) that includes both the effect of pressure and the Lode angle dependence on the material behavior. A critical analysis of the results of the models is made in order to verify their ability to predict the location of fracture, under both high and low levels of stress triaxiality, for the 2024-T351 aluminum alloy that strongly depends on both pressure and Lode angle.

The layout of this chapter is as follows. The set of equations that govern the behavior of the Gurson-Tvergaard-Needleman (GTN) model, Lemaitre´s model and Bai and Wierzbicki´s model will be firstly reviewed and summarized. In addition, an improved version of the GTN model, proposed by Xue (2007), and a fracture indicator, introduced by Bao and Wierzbicki (2004), which can be employed in conjunction with the Bai and Wierzbicki´s model, will also be described. The numerical strategy adopted in this work to solve the evolution problem, for each constitutive model, will be then presented. It is based on the well established operator split methodology (Simo & Hughes, 1998). A comprehensive set of numerical examples is later presented for specimens subjected to high and low levels of stress triaxiality. The evolution of representative variables close to fracture is critically analyzed. In particular, the evolution of the equivalent plastic strain, damage and reaction force together with the contour plots of the internal variables at the critical zones. Finally, some conclusions will be drawn based on comparisons of numerical and experimental results.

4.2 CONSTITUTIVE MODELS FOR DUCTILE FRACTURE

The governing equations of the constitutive models under analysis are briefly reviewed in this section together with the basic concepts and hypothesis underlying each of them. Firstly, the Gurson-Tvergaard-Needleman (GTN) model, which includes nucleation, growth and coalescence of microvoids (Gurson, 1977; Tvergaard & Needleman, 1984) is presented, then Lemaitre's model with both

isotropic hardening and isotropic damage (Lemaitre, 1985) and, finally Bai & Wierzbicki model (Bai *et al*., 2008) that includes both the pressure effect and the Lode angle dependence. In addition, a shear mechanism proposed by Xue (2008) is described and incorporated in the GTN model to enhance the behavior under shear dominated loads, as well as Bao's fracture indicator (Bao, 2003), which is used in conjunction with Bai & Wierzbicki model to allow the prediction of damage with this model.

4.2.1 The Gurson-Tvergaard-Needleman Model

Inspired by the work of Gurson (1977), Tvergaard and Needleman (1984) have proposed a model for the description of damage and fracture in ductile materials. The original Gurson model introduces a strong coupling between plastic strain and damage (Chaboche *et al*., 2006) and the presence of micro voids in the formulation leads to a yield surface that depends on both the hydrostatic pressure and porosity. The material degradation is measured through a parameter called the void volume fraction, which is represented by the variable f. This parameter is defined by the ratio between the volume of micro voids, V_{voids}, and the representative volume element, V_{RVE} .

$$f = \frac{V_{voids}}{V_{RVE}} \ . \tag{4.1}$$

The Gurson-Tvergaard-Needleman (GTN) model, which is one of the most well known extensions of Gurson's model, assumes both isotropic hardening and damage. Nevertheless, the damage variable in this model is represented by an effective porosity f^*. The flow potential is generalized into the form:

$$\Phi(\boldsymbol{\sigma}, r, f^*) = J_2(\boldsymbol{S}) - \frac{1}{3}\left\{1 + q_3 f^{*2} - 2q_1 f^* \cosh\left(\frac{q_2 3p}{2\sigma_y}\right)\right\}{\sigma_y}^2 \ , \tag{4.2}$$

where, J_2 represents the second invariant of the deviatoric stress tensor, σ_y is the isotropic hardening law and r represents the isotropic hardening internal variable. The parameters q_1, q_2 and q_3 are introduced into the yield surface definition in order to bring the model predictions into closer agreement with full numerical analyses of a periodic array of voids and p represents the hydrostatic pressure.

The evolution of spherical voids can be reproduced by three simultaneous or successive steps: nucleation, growth and coalescence of voids (Tvergaard & Needleman, 1984). The effective porosity is determined by the following bilinear function:

$$f^* = \begin{cases} f, & f < f_c \\ f_c + \left(\frac{1}{q_1} - f_c\right)\frac{(f - f_c)}{(f_f - f_c)}, & f \geq f_c \end{cases} \tag{4.3}$$

where the parameter f represents the porosity, the constant f_c is the porosity to trigger coalescence and the parameter f_f represents the porosity at fracture. The evolution of the porosity is given by the sum of both the nucleation and growth mechanisms, as:

$$\dot{f} = \dot{f}^N + \dot{f}^G \ . \tag{4.4}$$

The nucleation mechanism is driven by the plastic strain and can be represented as:

$$\dot{f}^N = \frac{f_{\mathrm{N}}}{s_{\mathrm{N}}\sqrt{2\pi}} \exp\left[-\frac{1}{2}\left(\frac{\overline{\varepsilon}^p - \varepsilon_{\mathrm{N}}}{s_{\mathrm{N}}}\right)^2\right]\dot{\overline{\varepsilon}}^p \ , \tag{4.5}$$

where f_{N} represents the volume fraction of all second-phase particles (see Figure 4.1b) with potential for micro void nucleation, ε_{N} and s_{N} are the mean strain for void nucleation and its standard deviation. The variable $\overline{\varepsilon}^p$ represents the equivalent plastic strain and $\dot{\overline{\varepsilon}}^p$ is the rate of the equivalent plastic strain.

The most significant contribution to the evolution of spherical voids is the growth mechanism, which is obtained from the condition of plastic incompressibility of the matrix material, and can be expressed by:

$$\dot{f}^G = (1 - f)\, tr(\dot{\boldsymbol{\varepsilon}}^p) = (1 - f)\dot{\varepsilon}_v^p \ , \tag{4.6}$$

where $\dot{\boldsymbol{\varepsilon}}^p$ represents the rate of the plastic strain tensor and $\dot{\varepsilon}_v^p$ is the rate of the volumetric plastic strain. In this work, the GTN's model implementation includes both nucleation and growth of micro voids. The coalescence effect was not addressed since our main objective is the prediction of fracture onset.

4.2.1.1 Shear Mechanism

One important limitation associated with Gurson based models is that shear effects are not considered in the formulation, which excludes the possibility of predicting shear localization and fracture under conditions of low stress triaxiality. Under shear dominated loading conditions, the distortion of voids and inter-void linking play a critical role in the evolution of the material internal degradation. Therefore, in order to improve the GTN´s model predictive ability, under both zero and low levels of stress triaxialities, Xue (2008) has proposed the introduction of a shear mechanism. The mechanism is based on geometrical considerations of a unit cell structure, containing a circular void at the center, which is subjected to a simple shear strain (Xue, 2008). The evolution of shear damage, according to Xue (2008), depends on the porosity, the equivalent strain and the Lode angle. After some straightforward algebraic manipulations, the rate of this mechanism can be mathematically expressed by (Xue, 2008):

$$\dot{f}^{Shear} = q_4 f^{q_5} g_o \varepsilon_{eq} \dot{\varepsilon}_{eq} \ , \tag{4.7}$$

where q_4 and q_5 are parameters related to two or three dimensional problems. For two dimensional problems $q_4 = 1.69$ and $q_5 = 1/2$ and for three dimensional problems $q_4 = 1.86$ and $q_5 = 1/3$. The variable f represents the porosity, ε_{eq} is the equivalent strain and g_o is a parameter that introduces the Lode angle dependence in the shear mechanism. If the Lode angle function g_o is different from zero, the mechanism is triggered and shear effects are taken into account. However, if g_o is null, there is no effect of the shear mechanism, on the damage evolution, and only the nucleation and growth mechanisms are active. The Lode angle function, g_o, can be defined by:

$$g_o = 1 - \frac{6|\theta|}{\pi} \ , \tag{4.8}$$

where θ is the Lode angle that is determined according to Equation (3.4). The shear mechanism proposed by Xue (2008) can be included in the GTN's model, which already features the mechanisms of nucleation and growth of micro voids. Thus, the evolution of the porosity originally expressed by Equation (4.4), for this model, is re-defined as:

$$\dot{f} = \dot{f}^{N} + \dot{f}^{G} + \dot{f}^{Shear} \ . \tag{4.9}$$

The evolution of damage in the material inevitably reduces the overall elastic properties. However, this effect is small when compared to the influence of damage on the plastic behavior. Therefore, the evolution of damage due to shear effects, employed in this work, will neglect the influence of damage on elasticity as is usually done in this type of model. The shear damage evolution law is redefined as a function of both the accumulated plastic strain and the rate of the accumulated plastic strain instead of the total strain and total strain rate (see Equation 4.7):

$$\dot{f}^{Shear} = q_4 f^{q_5} g_o \overline{\varepsilon}^{p} \dot{\overline{\varepsilon}}^{p} \ . \tag{4.10}$$

The Lode angle function can also be rewritten as a function of the normalized third invariant, such as:

$$g_o = 1 - \left|\overline{\theta}\right| \ , \tag{4.11}$$

where $\overline{\theta}$ represents the normalized Lode angle that is a function of the normalized third invariant, such as:

$$\overline{\theta} = 1 - \frac{6\theta}{\pi} = 1 - \frac{2}{\pi}\arccos\xi \ , \tag{4.12}$$

where ξ represents the normalized third invariant that is calculated by:

$$\xi = \frac{27}{2}\frac{\det \boldsymbol{\varepsilon}_d^e}{\left(\frac{3}{2}\boldsymbol{\varepsilon}_d^e : \boldsymbol{\varepsilon}_d^e\right)^{3/2}} \ , \tag{4.13}$$

where, $\boldsymbol{\varepsilon}_d^e$ represents the deviatoric elastic strain tensor. Box 4.1 summarizes the GTN constitutive model that includes the shear mechanism on the damage evolution law. It is important to remark that the set of constitutive equations listed in Box 4.1, has got as a particular case, the previously described GTN model (when $q_4 = 0$). The original Gurson´s model can also be recovered as a limiting case, by appropriately setting the constants q_1, q_2 and q_3.

Box 4.1. GTN's model including nucleation, growth of micro voids and a shear mechanism.

(i) Elasto-plastic split of the strain tensor

$$\boldsymbol{\varepsilon} = \boldsymbol{\varepsilon}^e + \boldsymbol{\varepsilon}^p$$

(ii) Elastic law

$$\boldsymbol{\sigma} = \mathbf{D}^e : \boldsymbol{\varepsilon}^e$$

(iii) Yield function

$$\Phi(\boldsymbol{\sigma}, r, f) = J_2(\boldsymbol{S}) - \frac{1}{3}\left\{1 + q_3 f^2 - 2q_1 f \cosh\left(\frac{q_2 3p}{2\sigma_y}\right)\right\}{\sigma_y}^2$$

(iv) Plastic flow and evolution equations for r and f

$$\dot{\boldsymbol{\varepsilon}}^p = \dot{\gamma}\left[\boldsymbol{S} + \frac{1}{3}q_1 q_2 f \sigma_y \sinh\left(\frac{q_2 3p}{2\sigma_y}\right)\boldsymbol{I}\right]$$

$$\dot{R} = \dot{\gamma}\frac{\left\{q_1 q_2 f p \sinh\left(\frac{q_2 3p}{2\sigma_y}\right) + \frac{2}{3}\left[1 + q_3 f^2 - 2q_1 f \cosh\left(\frac{q_2 3p}{2\sigma_y}\right)\right]\sigma_y\right\}}{(1-f)}$$

$$\dot{f} = \dot{f}^N + \dot{f}^G + \dot{f}^{Shear}$$

$$= \frac{f_{\mathrm{N}}}{s_{\mathrm{N}}.\sqrt{2\pi}}\exp\left[-\frac{1}{2}\left(\frac{\overline{\varepsilon}^p - \varepsilon_{\mathrm{N}}}{s_{\mathrm{N}}}\right)^2\right]\dot{\overline{\varepsilon}}^p + (1-f)\dot{\varepsilon}_v^p$$

$$+ q_4 f^{q_5} g_o \overline{\varepsilon}^p \dot{\overline{\varepsilon}}^p$$

and,

$$\dot{\overline{\varepsilon}}^p = \dot{\gamma}\sqrt{\frac{2}{3}\left\{\boldsymbol{S}:\boldsymbol{S} + \frac{1}{3}\left[q_1 q_2 f \sigma_y \sinh\left(\frac{q_2 3p}{2\sigma_y}\right)\right]^2\right\}}$$

$$\dot{\varepsilon}_v^p = \dot{\gamma} q_1 q_2 f \sigma_y \sinh\left(\frac{q_2 3p}{2\sigma_y}\right) \qquad g_o = 1 - \left|\overline{\theta}\right|$$

(v) Loading/unloading criterion

$$\dot{\gamma} \geq 0\,, \qquad \Phi \leq 0\,, \qquad \dot{\gamma}\Phi = 0.$$

4.2.2 Lemaitre's Damage Model

The constitutive equations for ductile damage, described in this section, have been proposed by Lemaitre (1985). Based on the concept of effective stress and the hypothesis of strain equivalence, Lemaitre's model includes the evolution of internal damage, as well as non-linear isotropic and kinematic hardening in the description of the behavior of ductile materials. The constitutive formulation starts from the definition of the Helmholtz specific free energy that can be taken as the state potential of the material and is a function of all state variables. The free energy can be expressed as a function of the set $\{\boldsymbol{\varepsilon}^e, r, D\}$ of state variables:

$$\psi = \psi(\boldsymbol{\varepsilon}^e, r, D) \ , \tag{4.14}$$

where, ψ represents the specific free energy, $\boldsymbol{\varepsilon}^e$ is the elastic strain tensor, r is the isotropic hardening internal variable and D represents the isotropic damage internal variable.

Under the hypothesis of decoupling between elasticity-damage and plastic hardening, the specific free energy is assumed to be given by the sum:

$$\psi = \psi^{ed}(\boldsymbol{\varepsilon}^e, D) + \psi^p(r) \ , \tag{4.15}$$

where ψ^{ed} represents the elastic-damage contribution and ψ^p is the plastic contribution to the free energy. The elastic-damage contribution for the free energy can be postulated by the following expression (Lemaitre, 1985):

$$\bar{\rho}\psi^{ed}(\boldsymbol{\varepsilon}^e, D) = \frac{1}{2}\boldsymbol{\varepsilon}^e : (1-D)\mathbf{D}^e : \boldsymbol{\varepsilon}^e \ , \tag{4.16}$$

where $\mathbf{D}^e$ represents the isotropic elasticity tensor. The plastic potential can be represented by the isotropic hardening contribution as (if we disregard kinematic hardening):

$$\bar{\rho}\psi^p(r) = \bar{\rho}\psi^I(r) \ . \tag{4.17}$$

The elasticity law is obtained by performing the derivative of the elastic-damage potential (Equation 4.16) in order to the elastic strain tensor, as:

$$\boldsymbol{\sigma} = \bar{\rho}\frac{\partial \psi^{ed}}{\partial \boldsymbol{\varepsilon}^e} = (1-D)\mathbf{D}^e : \boldsymbol{\varepsilon}^e \ . \tag{4.18}$$

The thermodynamical forces conjugated with damage and isotropic hardening internal variable are obtained, respectively, by performing the derivative of the elastic-damage contribution, $\bar{\rho}\psi^{ed}(\boldsymbol{\varepsilon}^e, D)$ (Equation 4.16) with regard to the damage variable, D, and by taking the derivative of the plastic potential, $\bar{\rho}\psi^{p}(r)$ (Equation 4.17) with regard to the isotropic hardening variable, r, respectively (Lemaitre *et al.*, 2005):

$$-Y \equiv -\bar{\rho}\frac{\partial \psi^{ed}}{\partial D} = \frac{q^2}{6G(1-D)^2} + \frac{p^2}{2K(1-D)^2} \ , \tag{4.19}$$

$$R \equiv -\bar{\rho}\frac{\partial \psi^{I}}{\partial r} = R(r) \ , \tag{4.20}$$

where Y represents the thermodynamic force associated with damage, q is the von Mises equivalent stress, p is the hydrostatic pressure, G is the shear elasticity modulus, K is the elastic compressibility modulus and R represents the thermodynamic force associated with the isotropic hardening variable.

The evolution of the internal variable can be obtained by assuming the existence of the flow potential, Ψ, given by:

$$\Psi = \Phi + \frac{S}{(1-D)(s+1)}\left(\frac{-Y}{S}\right)^{s+1} \ , \tag{4.21}$$

where the parameters S and s are damage evolution constants and Φ represents the yield function, which is, defined as:

$$\Phi = \frac{q}{(1-D)} - \sigma_{y_0} - R(r) \ , \tag{4.22}$$

where σ_{y_0} is the initial uniaxial yield stress. According to the hypothesis of generalized normality, the plastic flow is given by:

$$\dot{\boldsymbol{\varepsilon}}^p = \dot{\gamma}\frac{\partial \Phi}{\partial \boldsymbol{\sigma}} = \dot{\gamma}\boldsymbol{N} \ , \tag{4.23}$$

$$\boldsymbol{N} = \sqrt{\frac{3}{2}}\frac{\boldsymbol{S}}{\|\boldsymbol{S}\|}.\frac{1}{(1-D)} \ , \tag{4.24}$$

where $\dot{\gamma}$ is the plastic multiplier, $\boldsymbol{N}$ represents the flow vector and $\boldsymbol{S}$ is the deviatoric stress tensor. The evolution law for damage and for the isotropic

hardening internal variable can be established by performing, firstly, the derivative of the flow potential (Equation 4.21) with regard to the thermodynamic force associated with damage, Y, and, secondly, with regard to the isotropic hardening variable, r, respectively:

$$\dot{D} \equiv \dot{\gamma} \frac{\partial \Psi}{\partial Y} = \dot{\gamma} \frac{1}{(1-D)} \left(\frac{-Y}{S} \right)^{s} , \tag{4.25}$$

$$\dot{r} \equiv \dot{\gamma} \frac{\partial \Psi}{\partial R} = \dot{\gamma} . \tag{4.26}$$

The complementary law of rate-independent plasticity also needs to be fulfilled:

$$\dot{\gamma} \geq 0 , \qquad \Phi \leq 0 , \qquad \dot{\gamma}\Phi = 0 . \tag{4.27}$$

The constitutive equations of Lemaitre's model with isotropic hardening and isotropic damage, employed in this work, are conveniently summarized in Box 4.2.

Box 4.2. Lemaitre's model with isotropic hardening and isotropic damage.

(i) Elasto-plastic split of the strain tensor

$$\boldsymbol{\varepsilon} = \boldsymbol{\varepsilon}^{e} + \boldsymbol{\varepsilon}^{p}$$

(ii) Coupled elastic-damage law

$$\boldsymbol{\sigma} = (1-D)\mathbf{D}^{e} : \boldsymbol{\varepsilon}^{e}$$

(iii) Yield function

$$\Phi = \frac{q}{(1-D)} - \sigma_{y_0} - R(r)$$

(iv) Plastic flow and evolution equations for r and D

$$\dot{\boldsymbol{\varepsilon}}^{p} = \dot{\gamma}\boldsymbol{N} = \dot{\gamma}\sqrt{\frac{3}{2}}\frac{\boldsymbol{S}}{\|\boldsymbol{S}\|}\frac{1}{(1-D)}$$

$$\dot{r} = \dot{\gamma}$$

$$\dot{D} = \dot{\gamma}\frac{1}{(1-D)}\left(\frac{-Y}{S}\right)^{s}$$

with Y given by:

$$-Y = \frac{q^2}{6G(1-D)^2} + \frac{p^2}{2K(1-D)^2}$$

(v) Loading/unloading criterion

$$\dot{\gamma} \geq 0 , \qquad \Phi \leq 0 , \qquad \dot{\gamma}\Phi = 0.$$

4.2.3 Bai & Wierzbicki Model

The elasto-plastic model proposed by Bai & Wierzbicki (2008), which was presented in detail in Chapter 3, will de employed in the numerical assessment described in this chapter. More detail about Bai & Wierzbicki (2008) model, see Box 3.1 in the previous chapter.

Due to the fact that Bai & Wierzbicki's model (Bai *et al.*, 2008) does not include a damage variable in the constitutive formulation, we will use in our comparisons with the previously described damage models a fracture indicator that was proposed by Bao (2003). This fracture indicator is a post-processed variable, which was developed after conducting a thorough experimental investigation on the behavior of ductile crack formation, expressed by:

$$D = \int_0^{\varepsilon_f} \frac{p}{q} d\bar{\varepsilon} = \eta_{av}.\bar{\varepsilon}_f \ , \tag{4.28}$$

where $\bar{\varepsilon}$ represents the equivalent strain, $\bar{\varepsilon}_f$ is the equivalent strain to fracture and η_{av} is the so-called stress triaxiality average. The Lode angle average, θ_{av}, is also a parameter widely used to represent the three dimensional fracture locus and both parameters can be expressed by:

$$\eta_{av} = \frac{1}{\bar{\varepsilon}_f}\int_0^{\bar{\varepsilon}_f} \frac{p}{q} d\bar{\varepsilon} \ , \qquad \theta_{av} = \frac{1}{\bar{\varepsilon}_f}\int_0^{\bar{\varepsilon}_f} \theta \, d\bar{\varepsilon} \ . \tag{4.29}$$

More details about this fracture indicator can be obtained in References (Bai, 2008; Bai & Wierzbicki, 2008).

4.3 NUMERICAL SOLUTION STRATEGY

In this section, the numerical solution strategy adopted in this work to perform the numerical simulations is summarized. The use of path dependent constitutive models, as is the case of the models described in this chapter, invariably leads to the need for formulation of algorithms for numerical integration of the evolution equations. The problem consists in formulating

numerical integration procedures for updating the known state variables, generically denoted by α_n, at a certain time t_n to obtain the state variables α_{n+1} at time t_{n+1}, where the incremental strain $\Delta\boldsymbol{\varepsilon}$ is assumed given. Therefore, the discretization of the constitutive equations within a generic pseudo-time interval $[t_n, t_{n+1}]$ was performed for all models, which are summarized in Boxes 4.1, 4.2 and 3.1 (see Chapter 3), based on the backward Euler scheme (Simo & Hughes, 1998). Since the models were implemented in a quasi-static finite element framework, it was also necessary to derive the tangent matrix which is consistent with the integration algorithm.

Stress update procedures, which are based on the so-called operator split concept (see Simo & Hughes, 1998; De Souza Neto *et al.*, 2008), are specially suitable for the numerical integration of the evolution problem and have been widely used in computational plasticity (see Simo & Hughes, 1998; De Souza Neto *et al.*, 2008). This method, which was used in our developments, consists in splitting the problem in two parts: an *elastic predictor*, where the problem is assumed to be elastic and, a *plastic corrector*, in which the system of residual equations comprising the elasticity law, plastic consistency and the rate equations is solved, taking the results of the elastic predictor stage as initial conditions. In the case of violation of the yield condition, the plastic corrector stage has to be initiated and the Newton- Raphson procedure is used to solve the discretised set of equations. The Newton-Raphson procedure was chosen motivated by the quadratic rates of convergence achieved, which results in return mapping procedures computationally efficient (see Simo & Hughes, 1998; De Souza Neto *et al.*, 2008). In Figure 4.2, a schematic representation of the procedure, which departs from the initial value problem to the elastic predictor/plastic corrector integration algorithm, is illustrated.

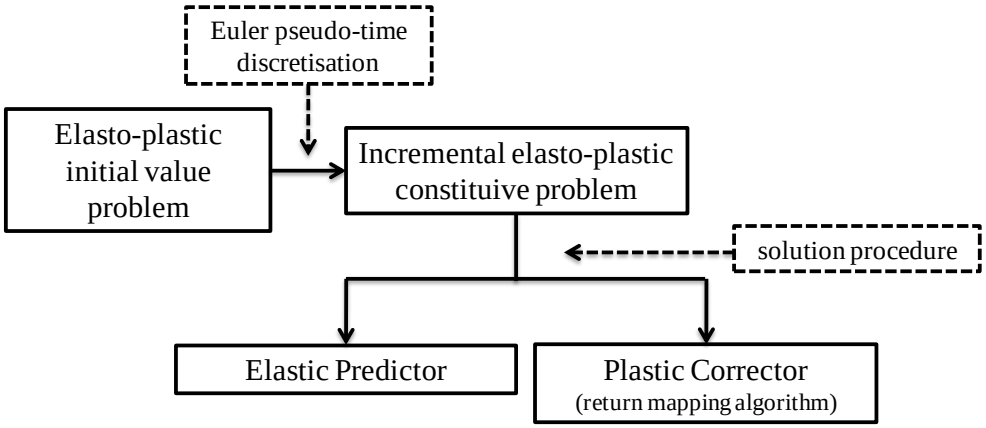

Figure 4.2. Schematic diagram of the procedure from the initial value problem to the elastic predictor/plastic corrector integration algorithm (adapted from De Souza Neto *et al*., 2008).

In a typical return mapping algorithm, the following steps are required: given the values of the elastic strain, ε_n^e , and internal variables set, α_n, at the beginning of the pseudo-time interval $[t_n, t_{n+1}]$, and given the prescribed incremental strain, $\Delta\varepsilon$ for this interval, the *elastic trial state* needs to be computed:

$$\varepsilon_{n+1}^{e\,trial} = \varepsilon_n^e + \Delta\varepsilon$$

$$\alpha_{n+1}^{trial} = \alpha_n$$

$$\sigma_{n+1}^{trial} = \overline{\rho}\,\frac{\partial\psi}{\partial\varepsilon^e}\bigg|_{n+1}^{trial} \qquad A_{n+1}^{trial} = \overline{\rho}\,\frac{\partial\psi}{\partial\alpha}\bigg|_{n+1}^{trial} \tag{4.30}$$

where, σ_{n+1}^{trial} and A_{n+1}^{trial} are respectively the elastic trial stress and elastic trial internal force. The constant $\overline{\rho}$ is the reference mass density and ψ represents the free energy function of the constitutive model under consideration.

The next step is to check whether the trial state lies inside or outside the yield surface:

$$\text{IF } \Phi\left(\sigma_{n+1}^{trial}, A_{n+1}^{trial}\right) \leq 0 \text{ THEN,}$$

$$(*)_{n+1} = (*)_{n+1}^{trial} \text{ and EXIT} \tag{4.31}$$

If the above condition is satisfied, the final state is equal to the trial state. Nevertheless, if the elastic trial state is out of the elastic domain or on the yield surface, the plastic corrector procedure is required to update the state variables at

time t_{n+1}. In the following, the non linear system of equations that was employed for each model, on the return mapping stage, is briefly described. The Newton Raphson procedure is used in all models to solve a linearized system of equations.

(a) Return mapping of Gurson-Tvergaard-Needleman damage model

For the Gurson-Tvergaard-Needleman constitutive model summarized in the Box 4.1, the implicit numerical integration algorithm was derived by the authors. The non linear system of equations can be reduced to a system of only four non linear scalar equations. The Newton-Raphson procedure has to be solved for the set of unknowns $\{\Delta\gamma,\ p_{n+1},\ f_{n+1},\ R_{n+1}\}$. The fully implicit elastic predictor/return mapping algorithm for GTN's model with shear mechanism is summarized in Box 4.3. More details about the linearization of the non linear system of equation for GTN model can be found in Appendix "C" and "D".

Box 4.3. Fully implicit Elastic predictor/Return mapping algorithm for GTN model with shear mechanism.

(i) Evaluate elastic trial state: Given the incremental strain $\Delta\varepsilon$ and the state variables at t_n:

$$\boldsymbol{\varepsilon}_{n+1}^{e\,trial} = \boldsymbol{\varepsilon}_n^e + \Delta\boldsymbol{\varepsilon} \quad ; \quad \bar{\varepsilon}_{n+1}^{p\,trial} = \bar{\varepsilon}_n^p \quad ; \quad R_{n+1}^{trial} = R_n$$

$$f_{n+1}^{trial} = f_n \quad ; \quad \boldsymbol{S}_{n+1}^{trial} = 2G\boldsymbol{\varepsilon}_{n+1}^{e\,trial} \quad ; \quad p_{n+1}^{trial} = K\varepsilon_{v\,n+1}^{e\,trial}$$

(ii) Check plastic admissibility:

IF $\Phi^{trial} = J_2^{trial} - \frac{1}{3}\left[1 + q_3 {f_{n+1}^{trial}}^2 - 2q_1 f_{n+1}^{trial} \cosh\left(\frac{3q_2 p_{n+1}^{trial}}{2\sigma_y^{trial}}\right)\right]\left(\sigma_y^{trial}\right)^2 \leq 0$ THEN set $(\cdot)_{n+1} = (\cdot)_{n+1}^{trial}$ ***(elastic step)*** and go to *(v)*

ELSE go to (iii)

(iii) Return mapping ***(plastic step)***: *Solve the system of equations below for* $\Delta\gamma$,p_{n+1},f_{n+1} and R_{n+1}, *using Newton-Raphson method.*

$$\begin{Bmatrix} \dfrac{J_{2\,n+1}^{trial}}{[1+2G.\Delta\gamma]^2} - \dfrac{1}{3}\left[1 + q_3 {f_{n+1}}^2 - 2q_1 f_{n+1}\cosh\left(\dfrac{3q_2 p_{n+1}}{2.\sigma_y}\right)\right]\sigma_y^2 \\ p_{n+1} - p_{n+1}^{trial} + \Delta\gamma K\sigma_y q_1 q_2 f_{n+1}\sinh\left(\dfrac{3q_2 p_{n+1}}{2\sigma_y}\right) \\ f_{n+1} - f_{n+1}^{trial} - \dfrac{f_N}{S_N\sqrt{2\pi}}\exp\left[-\dfrac{1}{2}\left(\dfrac{\bar{\varepsilon}_{n+1}^p - \varepsilon_N}{S_N}\right)^2\right]\Delta\bar{\varepsilon}^p - \Delta f^g - \Delta f^{shear} \\ R_{n+1} - R_{n+1}^{trial} - \Delta R \end{Bmatrix} = \begin{Bmatrix} 0 \\ 0 \\ 0 \\ 0 \\ 0 \end{Bmatrix}$$

continue Box 4.3.

where,

$$\Delta f^{g} = (1 - f_{n+1})\Delta\gamma\sigma_y q_1 q_2 f_{n+1} \sinh\left(\frac{3q_2 p_{n+1}}{2\sigma_y}\right)$$

$$\Delta f^{shear} = g_0 q_4 {f_{n+1}}^{q_5}\, \bar{\varepsilon}^{p}_{n+1} \Delta\bar{\varepsilon}^{p}$$

$$\Delta R = \frac{\Delta\gamma}{(1 - f_{n+1})}\left\{ q_1 q_2 f_{n+1} p_{n+1} \sinh\left(\frac{3q_2 p_{n+1}}{2\sigma_y}\right) + \frac{2}{3}\sigma_y \left[1 + {q_3 f_{n+1}}^{2} - 2q_1 f_{n+1} \cosh\left(\frac{3q_2 p_{n+1}}{2\sigma_y}\right)\right]\right\}$$

(iv) Update the other state variables:

$$\boldsymbol{\varepsilon}^{e}_{n+1} = \boldsymbol{\varepsilon}^{e\,trial}_{n+1} - \Delta\gamma\left[\frac{\boldsymbol{S}^{trial}_{n+1}}{1 + 2G\Delta\gamma} + \frac{1}{3}\sigma_y q_1 q_2 f_{n+1} \sinh\left(\frac{3q_2 p_{n+1}}{2\sigma_y}\right)\boldsymbol{I}\right]$$

$$\boldsymbol{S}_{n+1} = \frac{\boldsymbol{S}^{trial}_{n+1}}{1 + 2G\Delta\gamma}$$

$$\bar{\varepsilon}^{p}_{n+1} = \bar{\varepsilon}^{p\,trial}_{n+1} + \Delta\gamma\sqrt{\frac{2}{3}\left\{\frac{\boldsymbol{S}^{trial}_{n+1} : \boldsymbol{S}^{trial}_{n+1}}{[1 + 2G\Delta\gamma]^2} + \frac{1}{3}\left[\sigma_y q_1 q_2 f_{n+1} \sinh\left(\frac{3q_2 p_{n+1}}{2\sigma_y}\right)\right]^2\right\}}$$

(v) Exit

(b) Return mapping of Lemaitre´s damage model

The implicit numerical integration algorithm for Lemaitre´s constitutive model (see Box 4.2) was proposed by De Souza Neto (2002). The non linear system of equations, in this case, was reduced, through algebraic manipulations, to a single scalar non linear equation, which is solved by the Newton-Raphson (N-R) method, for the unknown $\Delta\gamma$. Box 4.4 describes, in pseudo-code format, the fully implicit elastic predictor/return mapping algorithm for Lemaitre's model.

Box 4.4. Fully implicit Elastic predictor/Return mapping algorithm for Lemaitre´s model.

(i) Evaluate elastic trial state: Given the incremental strain $\Delta\varepsilon$ and the state variables at t_n:

$$\boldsymbol{\varepsilon}_{n+1}^{e\,trial} = \boldsymbol{\varepsilon}_{n}^{e} + \Delta\boldsymbol{\varepsilon} \quad ; \quad R_{n+1}^{trial} = R_n \quad ; \quad D_{n+1}^{trial} = D_n$$

$$\tilde{\boldsymbol{S}}_{n+1}^{trial} = 2G\boldsymbol{\varepsilon}_{n+1}^{e\,trial} \quad ; \quad \tilde{p}_{n+1} = K\varepsilon_{v\,n+1}^{e\,trial} \quad ; \quad \tilde{q}_{n+1}^{trial} = \sqrt{\frac{3}{2}}\left\|\tilde{\boldsymbol{S}}_{n+1}^{trial}\right\|/(1-D_n)$$

(ii) Check plastic admissibility:

IF $\Phi^{trial} = \tilde{q}_{n+1}^{trial} - \sigma_y^{trial}\left(R_{n+1}^{trial}\right) \leq 0$ THEN

set $(\cdot)_{n+1} = (\cdot)_{n+1}^{trial}$ ***(elastic step)*** and go to *(v)*

ELSE go to (iii)

(iii) Return mapping ***(plastic step)***: *Solve the equation below for* $\Delta\gamma$, *using N-R method.*

$$F(\Delta\gamma) \equiv \omega(\Delta\gamma) - \omega_n + \frac{\Delta\gamma}{\omega(\Delta\gamma)}\left(\frac{-Y(\Delta\gamma)}{S}\right)^{s} = 0$$

where,

$$\omega(\Delta\gamma) = 1 - D_{n+1} = \frac{3G.\Delta\gamma}{\tilde{q}_{n+1}^{trial} - \sigma_y(R_n + \Delta\gamma)}$$

$$-Y(\Delta\gamma) \equiv \frac{\left[\sigma_y(R_n + \Delta\gamma)\right]^2}{6G} + \frac{\tilde{p}_{n+1}{}^2}{2K}$$

(iv) Update the other state variables:

$$p_{n+1} = \omega(\Delta\gamma)\,\tilde{p}_{n+1} \quad ; \quad q_{n+1} = \omega(\Delta\gamma)\,\sigma_y(R_{n+1})$$

$$\boldsymbol{S}_{n+1} = \frac{q_{n+1}}{\tilde{q}_{n+1}^{trial}}\tilde{\boldsymbol{S}}_{n+1}^{trial} \quad ; \quad \boldsymbol{\sigma}_{n+1} = \boldsymbol{S}_{n+1} + p_{n+1}\boldsymbol{I}$$

$$\boldsymbol{\varepsilon}_{n+1}^{e} = \frac{1}{2G}\boldsymbol{S}_{n+1} + \frac{1}{3}\boldsymbol{\varepsilon}_{v\,n+1}^{e\,trial}\boldsymbol{I} \quad ; \quad R_{n+1} = R_n + \Delta\gamma$$

(v) Exit

(c) Return mapping of Bai & Wierzbicki´s constitutive model

A fully implicit solution was derived by the authors (Malcher *et al.*, 2009) for Bai & Wierzbicki´s constitutive model (Bai & Wierzbicki, 2008), which is summarized in Box 3.1 (see Chapter 3). The return mapping consists on the solution of a non linear system of eight equations, for three dimensional problems, and six equations, for two dimensional problems. The set of unknowns is

composed by tensor and scalar variables $\{\boldsymbol{\sigma}_{n+1}, \bar{\varepsilon}^{p}_{n+1}, \Delta\gamma\}$. Box 3.2 of chapter 3 describes the fully implicit elastic predictor/return mapping algorithm. More details about the linearization of the non linear system of equation for the Bai & Wierzbicki model can be found in Appendix "A" and "B".

Finally, it is remarked that the extension of the models to the finite strain range was done by adopting the well established multiplicative hyperelasto-plastic framework (see Peric´ *et al.*, 1992; Eterovic & Bathe, 1990).

4.4 NUMERICAL EXAMPLES

In this section, the results obtained by performing numerical simulations of several specimens with the previously described constitutive formulations, will be presented and discussed. Firstly, the description of specimens with different geometries, which promote a wide range of stress triaxiality, is undertaken. Then, the calibration of the material parameters for the 2024-T351 aluminum alloy is performed in order to determine both the true stress-strain curve of the material, up to the point of fracture, and the critical value for the damage variable. Finally, the predictive ability of the constitutive models is assessed and compared for specimens who promote different levels of stress triaxiality.

4.4.1 General Information

In order to compare, both qualitatively and quantitatively, the constitutive models, based on different levels of stress triaxiality, several specimens were chosen such that they promote representative points on the graph of the equivalent plastic strain *versus* stress triaxiality and Lode angle (see Figure 3.2). The specimens can be grouped as follows: specimens that promote a high level of stress triaxiality ($1/3 \leq \eta < 1$), and specimens that promote a low level of stress triaxiality ($0 \leq \eta < 1/3$). For a high level of stress triaxiality, four different specimens were selected. Two notched bars, one with a notch radius equal to $R = 4\,mm$ and other with $R = 12\,mm$, a smooth bar specimen and a plate hole specimen. In all four cases, a tensile stress state was monotonically applied. For a low level of stress triaxiality, a butterfly specimen, which was initially proposed by Bai & Wierzbicki (see Bai, 2008; Bai *et al.*, 2008), was selected and both pure shear

and combined tensile-shear loading conditions were applied. Figure 4.3 schematically represents the specimen's geometry as a function of the initial level of stress triaxiality.

In order to perform the numerical simulations, it is indispensable to obtain the material properties, the stress-strain curve and the damage parameters employed by the constitutive models. The elastic properties, the density and the initial yield stress adopted in the present analysis were taken from Bao and Wierzbicki (2004). The damage parameters of Lemaitre´s model, namely the exponent, *s*, and denominator, *S*, of the evolution law, were obtained from Teng (2008) that conducted a study on the numerical prediction of slant fracture with continuum damage mechanics. The set of parameters required by the GTN model with the inclusion of shear effects were taken from Xue (2007) and references therein. Finally, the set of parameters of Bai & Wierzbicki´s model were acquired from Reference (Bai & Wierzbicki, 2008). All the aforementioned parameters are conveniently listed in Table 4.1.

Specimen					
Butterfly (pure shear)	*Butterfly (tension/ shear, 10º)*	*Smooth bar*	*Plate with hole*	*Notched bar (R=12mm)*	*Notched bar (R=4 mm)*
$\eta_0 = 0$ $\overline{\theta}_0 = 0$	$\eta_0 = 0.11$ $\overline{\theta}_0 = 0.22$	$\eta_0 = 0.33$ $\overline{\theta}_0 = 1$	$\eta_0 = 0.37$ $\overline{\theta}_0 = 1$	$\eta_0 = 0.47$ $\overline{\theta}_0 = 1$	$\eta_0 = 0.75$ $\overline{\theta}_0 = 1$
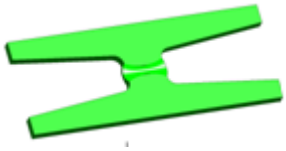	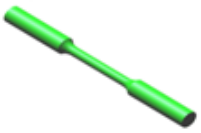				

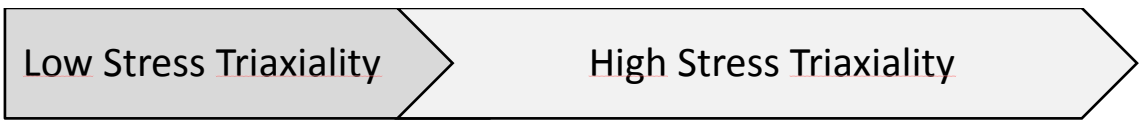

Figure 4.3. The specimens' geometry is represented as a function of the initial level of stress triaxiality and normalized Lode angle.

The stress-strain curve and the critical damage values, necessary for the different material models, were not taken from the literature but instead numerically determined. This procedure is described in detail in Section 4.4.3.

Table 4.1. Material properties for the 2024-T351 aluminum alloy.

Description	*Symbol*	*Value*	*Reference*
Density	ρ	2.7 x 10^3 [Kg/m^3]	Bao (2004)
Elastic Modulus	E	72.400 [MPa]	Bao (2004)
Poisson's ratio	ν	0.33	Bao (2004)
Initial yield stress	σ_{y_0}	352 [MPa]	Bao (2004)
Damage data (exponent)	s	1	Teng (2008)
Damage data (denominator)	S	6 [MPa]	Teng (2008)
GTN material parameter	q_1	1.5	Xue (2007)
GTN material parameter	q_2	1.0	Xue (2007)
GTN material parameter	q_3	2.25	Xue (2007)
Xue shear mechanism parameter	q_4	1.69 ($2D$) / 1.86 ($3D$)	Xue (2007)
Xue shear mechanism parameter	q_5	0.50 ($2D$) / 0.33 ($3D$)	Xue (2007)
Volume fraction of void nucleation	f_N	0.04	Xue (2007)
Stand. dev. plas. strain of void nucl.	s_N	0.1	Xue (2007)
Mean plas. strain dist. of void nucl.	ε_N	0.2	Xue (2007)
Bai pressure parameter	C_η	0.09	Bai (2008)
Triaxiality reference	η_0	0.33	Bai (2008)
Bai tensile parameter	C_θ^t	1.0	Bai (2008)
Bai compression parameter	C_θ^c	0.9	Bai (2008)
Bai shear parameter	C_θ^s	0.855	Bai (2008)
Bai exponent parameter	m	6	Bai (2008)

4.4.2 Geometry and Mesh Definition

In the following, the geometry of each specimen, which will be used in the numerical simulations under high level of stress triaxiality, is presented as well as the mesh definition. Figure 4.4 shows the dimensions for both cylindrical notched bars, one with a notch radius equal to $R = 4\,mm$ and other with $R = 12\,mm$, together with a smooth bar specimen.

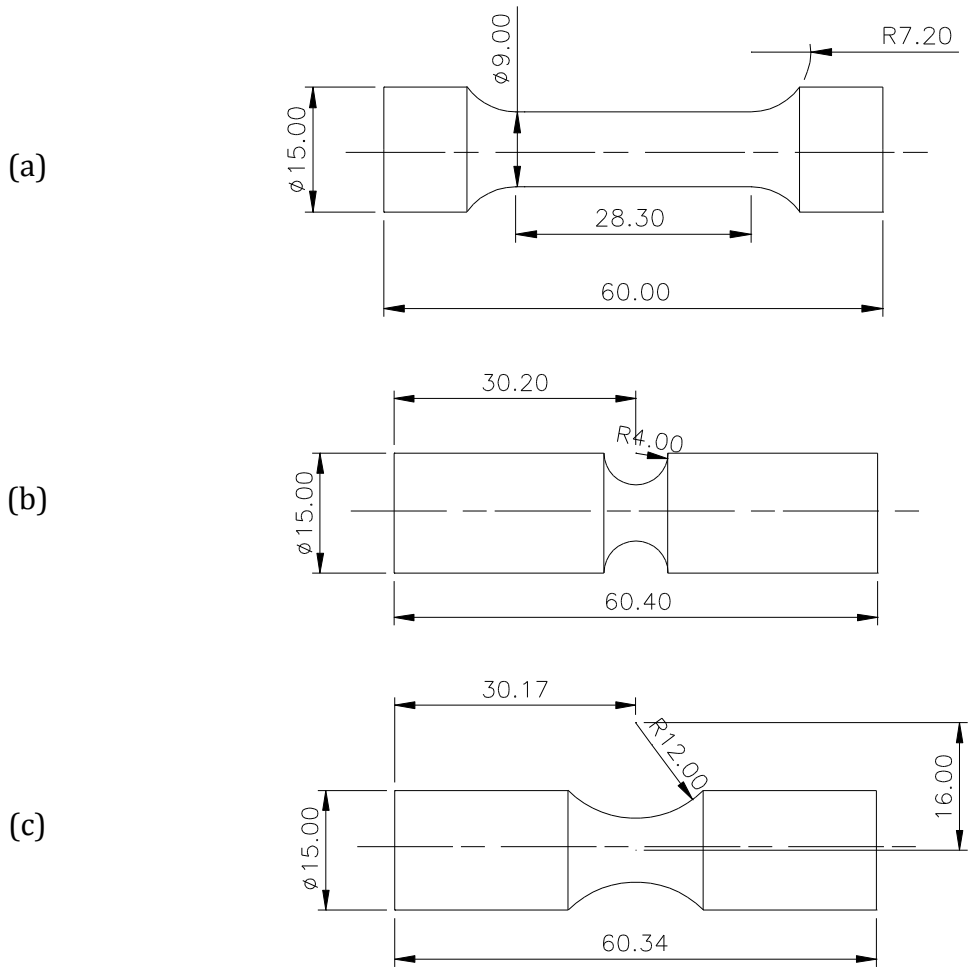

Figure 4.4. Geometry of the cylindrical notched bars and the smooth bar specimen (dimensions in mm). The specimens were reproduced from Teng (2008).

In order to capture the necking pattern and the evolution of internal variables, a relatively fine discretization is used in the region surrounding the smaller cross-section of the specimens (see Figure 4.5). The standard eight-noded axisymmetric quadrilateral element, with four Gauss integration points, is adopted. The initial mesh discretization for the three cases is illustrated in Figure 4.5, where only one symmetric quarter of the problem, with the appropriate symmetric boundary conditions imposed to the relevant edges, is modeled.

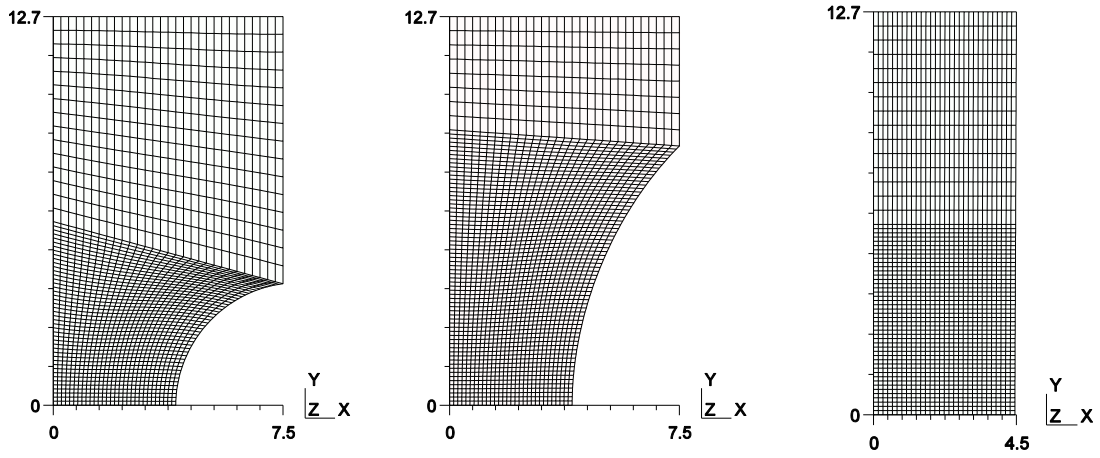

(a) (b) (c)

Figure 4.5. Finite element meshes for the cylindrical notched bar specimens (a) $R = 4\ mm$, (b) $R = 12\ mm$ and for the (c) smooth bar specimen.

A total number of 1800 elements has been used in the discretization of both the smooth bar (see Figure 4.5c) and the notched bar with radii of $R = 4\ mm$ (see Figure 4.5a), amounting to a total of 5581 nodes. The mesh of the notched bar with radii of $R = 12\ mm$ (see Figure 4.5b) has got 2250 elements and 681 nodes. In all cases, the gauge used is equal to 25.4 mm.

The stretching of a plate with a circular hole is also used. The initial geometry of the specimen is shown in Figure 4.6. Due to symmetry, only one quarter of the geometry is simulated, with appropriate boundary conditions imposed to the symmetry planes (see Figure 4.7). A three dimensional mesh of twenty noded elements, with eight Gauss integration points, is used to discretize one quarter of the specimen. A total number of 2280 elements have been used amounting to a total of 2768 nodes (see Figure 4.7).

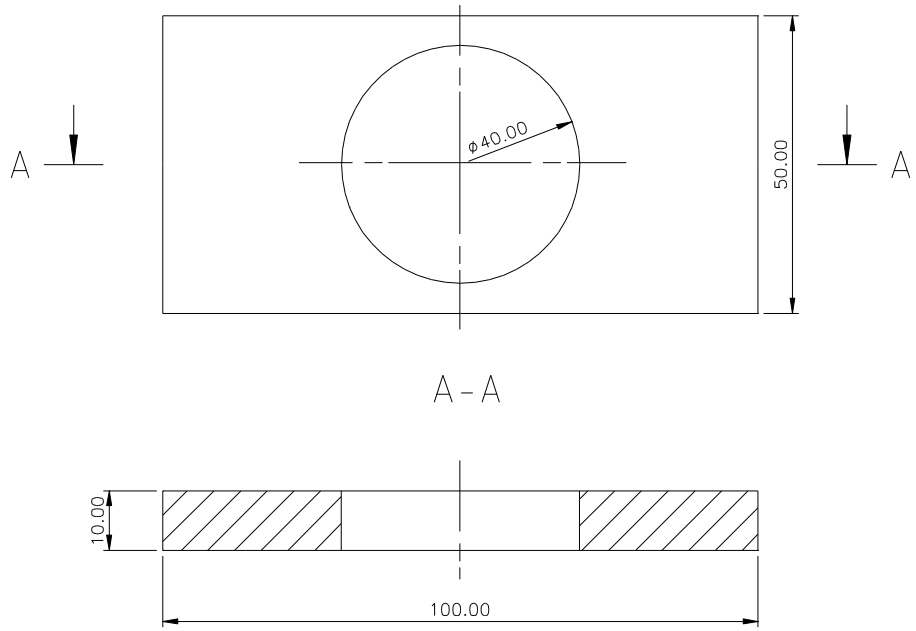

Figure 4.6. Geometry of the plate hole specimen (dimensions in mm). The specimen was taken from Bao (2003).

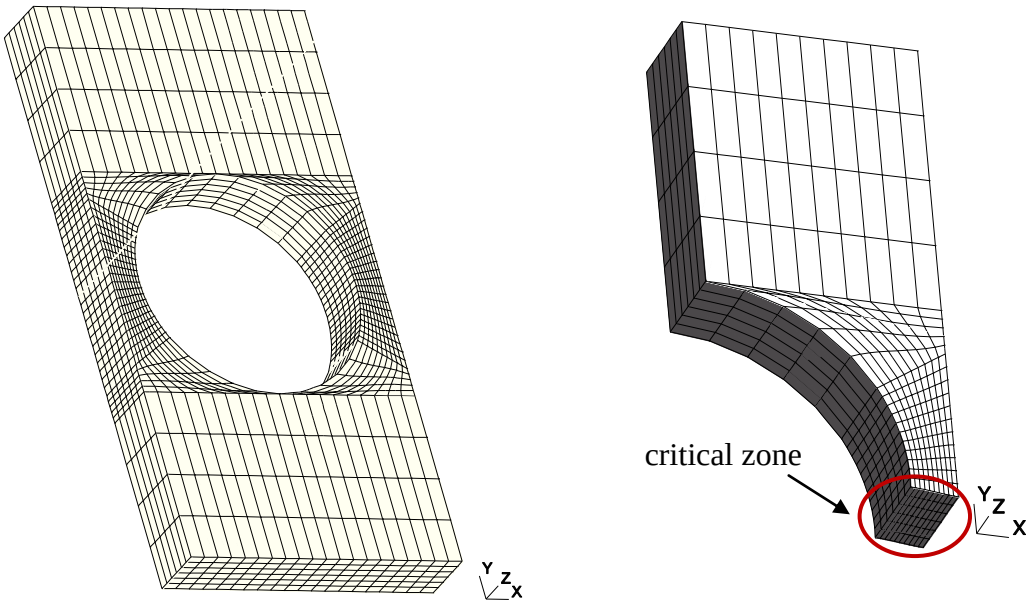

Figure 4.7. Finite element mesh for the plate hole specimen and critical zone to fracture.

The characterization of the material behavior under the range of low stress triaxiality, $(0 \leq \eta < 1/3)$, has been an extremely challenging task according to several authors (Bai, 2008). This is due to the fact that the magnitude of both local stresses and strains depend, to a large extent, on the shape of the free boundary. Nevertheless, a new type of flat compound curvature specimens was proposed recently (Bai, 2008) to characterize fracture behavior of metals under a wide range

of stress triaxiality. This specimen will be used here for low stress triaxiality tests. The geometry of the specimen, called "*butterfly specimen*", is illustrated in Figure 4.8. A three dimensional finite element mesh of 3392 twenty noded elements, with eight Gauss integration points, is used amounting to 17465 nodes (see Figure 4.9).

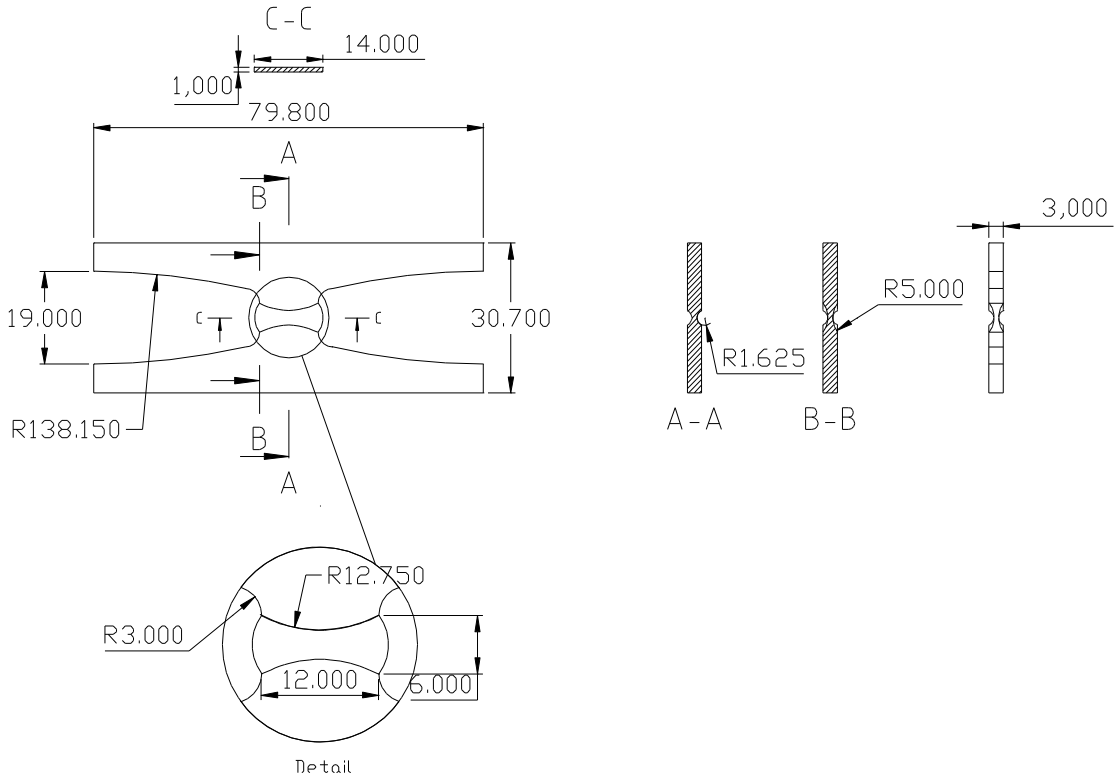

Figure 4.8. Geometry of the butterfly specimen (dimensions in mm). The specimen was reproduced from Bai (2008).

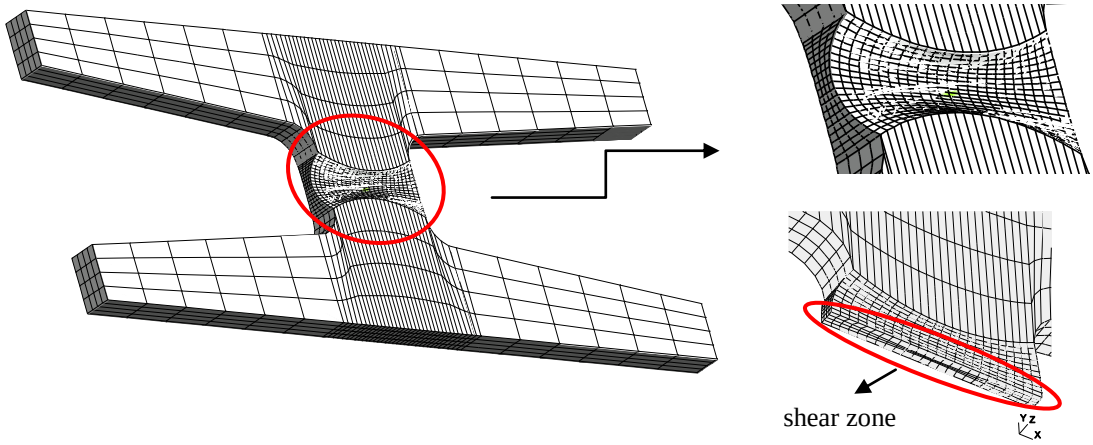

Figure 4.9. Finite elements mesh of the butterfly specimen and shear zone to fracture.

4.4.3 Calibration of Material Parameters for 2024-T351 Al

The strategy employed to determine the undamaged stress-strain curves and the critical damage values for the constitutive models was the following. Having at hand the displacement to fracture ($u_f = 6.65\,mm$) together with the force-displacement curve for a smooth bar tensile specimen, which were experimentally obtained by Bao and Wierzbicki (2004), an inverse and iterative methodology was conducted. The objective is to identify the stress-strain curve for each constitutive model such that the force-displacement curve is as close as possible to the experimental one. Figure 4.10a shows the reaction curves obtained for all the constitutive models after the application of the inverse identification method. It was possible to obtain a close agreement for all constitutive models.

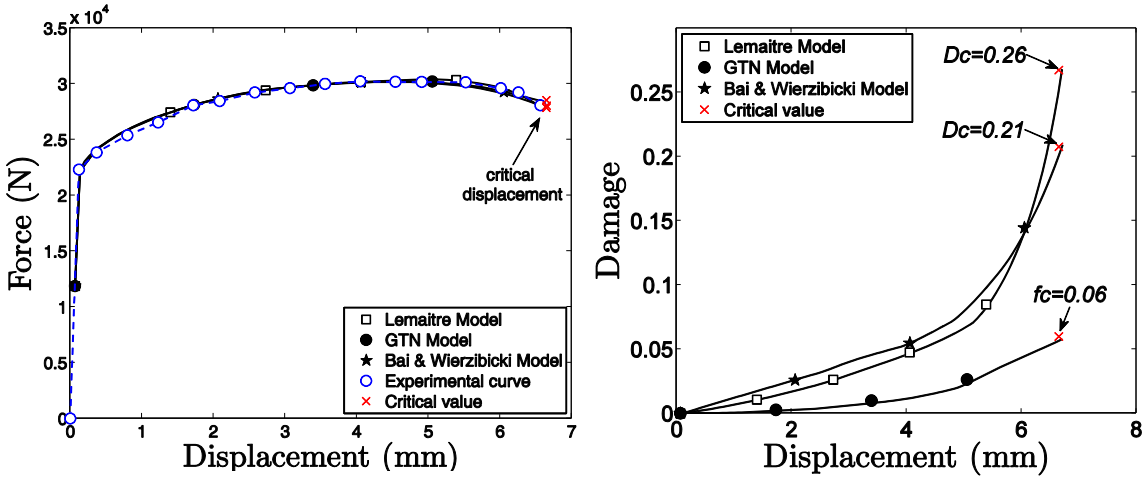

(a) (b)

Figure 4.10. (a) Force *versus* displacement curve for all models and experimental results. (b) Critical damage parameter calibrated for the experimental displacement to fracture ($u_f = 6.65\,mm$).

The critical value for the damage variable, of each constitutive model, was also obtained from the simulation of the stretching of the smooth bar. The value of the critical damage variable, of each constitutive model, is set to the value of the internal variable, which is used on the numerical simulation, when the numerical displacement is equal to the experimental displacement to fracture. The critical damage values obtained are listed in Table 4.2.

Table 4.2. Critical values for damage.

Model	*Critical Value*
Lemaitre	D_c = 0.26
GTN	f_c = 0.06
Bao	D_c = 0.21

The results of the calibration procedure for the stress-strain curves of all models can be observed in Figure 4.11. The undamaged stress-strain curve obtained for Lemaitre's model has got a more pronounced hardening than the GTN´s model and both are notably different. It is worth mentioning that the stress-strain curve used in Bai & Wierzbicki´s model (Bai & Wierzbicki, 2008), which is depicted in Figure 4.11 and labeled as "uncoupled damage model", is the curve that includes the effect of damage in the hardening.

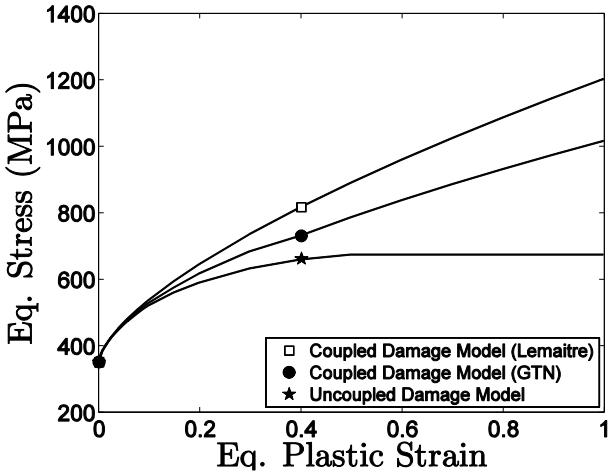

Figure 4.11. Stress-strain curves for all constitutive models.

It is important to mention that the material properties, the stress-strain curve and the damage parameters employed by Lemaitre's and GTN´s constitutive models can be obtained from one single experimental test, which is the stretching of a smooth round specimen. On the other hand, the parameters needed by the uncoupled model proposed by Bai & Wierzbicki, which are listed in Table 4.1, require four types of experimental tests (Bai & Wierzbicki, 2008): a smooth round bar tensile test, a notched round bar tensile test, a tensile test of flat grooved plate and an upsetting test.

Remark 4.1: In order to study the influence of the spatial discretization on the numerical results, several numerical simulations were performed using different

mesh refinements. It was possible to conclude that, although the numerical results can be affected by the discretization, there is no strong dependence of the numerical results with the level of mesh refinement. The location of fracture onset was also not affected by the level of mesh refinement. This is mainly due to the fact that the level of damage attained by the specimens is still relatively low, for the applied displacement to fracture, and the overall softening effect is very small (see Figure 4.10a). Therefore, the meshes selected and used in this paper have given numerical results that do not change noticeably with the spatial discretization and the conclusions of the assessment are not perceptibly affected.

4.5 NUMERICAL RESULTS

The predictive ability of the constitutive models is assessed here for the specimens illustrated in Figure 4.3 using the properties listed in Table 4.1 together with the calibrated parameters. Before proceeding, it is important to summarize the experimental results that will serve as reference for comparison. In Table 4.3, the initial stress triaxiality, the initial Lode angle, the equivalent strain at fracture and displacement at fracture are listed for each specimen. The displacements to fracture of the butterfly specimen, in both pure shear and combined tensile/shear loading conditions, were not available in the literature. The expected location for crack formation, experimentally observed is also included. The information presented in Table 4.3 was obtained from Bao (2003) and Bai (2008).

The displacement at fracture, listed in Table 4.3, was determined by measurements made during the experiments and the force-displacement behavior of the material (Bao, 2003). The determination of the equivalent strain at fracture, listed in Table 4.3, was accomplished using a combined experimental numerical method. The strain calculated by the finite element simulation at the critical location for the measured displacement at fracture, is considered the equivalent strain at fracture (Bao, 2003).

All the numerical simulations, which are presented in Sections 4.5.1 and 4.5.2, were conducted following the same strategy. The simulation was performed until the damage variable of the particular constitutive model, at any point in the specimen, reached the critical value that is listed in Table 4.2. Therefore, the value

of the displacement and effective plastic strain variables calculated from the finite element simulation, when the damage variable reaches its critical value, are understood as the displacement at fracture and effective strain at fracture from the numerical simulations.

Remark 4.2: On the forthcoming examples, for each particular specimen, the distributions of the effective plastic strain obtained by the models described in Section 4.2 will be presented for the sake of completeness. The objective is not to judge the models by comparing them directly to reference values, which were obtained with a particular constitutive model, since how each model determines the direction of plastic flow is different and the strain path is highly nonlinear. The intention is solely to highlight the fact that the effective plastic strain value and contour plot might not be an adequate criterion to analyze material fracture has advocated by several authors (McClintock, 1968; Rice & Tracey, 1969; Johnson & Cook, 1985; Mirza *et al*., 1996; Bao, 2003).

Table 4.3. Reference values for different specimens of the 2024-T351 (Bao, 2003; Bai, 2008).

Specimen	η_0	$\overline{\theta}_0$	$\bar{\varepsilon}_f$	u_f *(mm)*	*Fracture Location*
Notched bar *R*=4 mm	0.75	1	0.17	0.70	Center of specimen
Notched bar *R*=12 mm	0.47	1	0.28	1.40	Center of specimen
Smooth bar	0.33	1	0.47	6.65	Center of specimen
Plate hole	0.37	1	0.31	2.50	Middle of thickness on critical zone
Butterfly (pure shear)	0	0	0.21	---	Surface of shear zone
Butterfly (tension/shear, 10º)	0.11	0.22	0.26	---	Middle of thickness on shear zone

4.5.1 High Stress Triaxiality $(1/3 \leq \eta < 1)$

The numerical results obtained for the cylindrical notched bars, the cylindrical smooth bar and the plate hole specimens are presented in Table 4.4. The critical displacement to fracture, the stress triaxiality average, the Lode angle average and the equivalent plastic strain to fracture predicted by the numerical simulations are listed for the point, of each specimen, that reached the critical

value of damage. For ease of comparison, the values of the displacement to fracture and equivalent strain at fracture, which were obtained from references (Bao, 2003; Bai, 2008), are also included.

Analyzing Table 4.4, it is possible to conclude that for both notched bar specimens, the critical displacements obtained by Bai & Wierzbicki's model are in closer agreement with experimental values than the damage models. The prescribed displacements required to reach the critical damage values, for both Lemaitre and GTN model, were clearly higher than the experimental values. The difference between the numerical and experimental displacement to fracture, predicted by all models, is larger for the notched bar with a radius, R = 4 mm, than with a radius, R = 12 mm. This might be due to the fact that the notched bar with a radius, R = 4 mm, has got an initial triaxiality, η_0 = 0.75, that is higher than the notched bar with a radius, R = 12 mm, which is equal to, η_0 = 0.47 (see Table 4.3). This means that the notched bar with a radius, R = 12 mm, has got a stress triaxiality that is closer to the smooth bar (η_0 = 0.33), which was employed to calibrate the material properties. The equivalent plastic strain at fracture predicted numerically by all models is generally higher than the equivalent strain at fracture (see Table 4.4). Lemaitre´s model consistently predicts higher values than the other models. For the cylindrical notched bars, where there is a dominant tensile stress state, there was no perceptible difference between the original and modified GTN models and only the results of the original GTN model are included in Table 4.4.

In the case of the plate hole specimen, which has got an initial stress triaxiality and Lode angle that are close to the cylindrical smooth bar (see Table 4.3), all models predicted a displacement to fracture higher than the reference value. It is interesting to note that, due to the presence of shear effects, Lemaitre´s model and the enhanced GTN model were able to predict lower values for the displacement to fracture. The displacements obtained by these two models are closer to the experimentally determined value. The original GTN model, that does not include shear mechanisms in the formulation, gave the worst prediction. For this specimen, the equivalent plastic strain at fracture predicted numerically by all

models is again higher than the reference value, particularly for Lemaitre´s model (see Table 4.4).

Table 4.4. Numerical results obtained with the constitutive models for the 2024-T351 aluminum alloy. Specimens subjected to a high level of stress triaxiality.

Specimen	*Model*	u_f *(mm)*	u_f *(mm)**	η_{av}	$\overline{\theta}_{av}$	$\bar{\varepsilon}^p{}_f$	$\bar{\varepsilon}_f$
Notched bar $R = 4\ mm$	Bai & Wierzbicki	0.94	0.70	0.95	1.00	0.25	0.17
	Lemaitre	1.19		1.03	1.00	0.39	
	GTN	1.10		0.99	1.00	0.31	
Notched bar $R = 12\ mm$	Bai & Wierzbicki	1.55	1.40	0.64	1.00	0.32	0.28
	Lemaitre	1.82		0.71	1.00	0.50	
	GTN	1.70		0.66	1.00	0.38	
Smooth bar	Bai & Wierzbicki	6.65	6.65	0.42	1.00	0.50	0.47
	Lemaitre	6.65		0.45	1.00	0.57	
	GTN	6.65		0.40	1.00	0.48	
Plate hole	Bai & Wierzbicki	3.87	2.50	0.42	0.80	0.59	0.31
	Lemaitre	3.71		0.43	0.67	0.60	
	GTN original	4.00		0.41	0.83	0.54	
	GTN modified	3.73		0.40	0.84	0.49	

In general, for high levels of stress triaxiality, it is possible to see that the difference between predicted and observed values for the coupled damage models, such as Lemaitre and GTN, is not constant in terms of the displacement at fracture and fracture location over the entire range of high stress triaxiality ($1/3 \leq \eta < 1$). In addition, the coupled damage models lose their predictive capability when the conditions, of stress triaxiality and Lode angle of the specimen, are further way from the calibration point. This fact limits their applicability and reliability. The uncoupled constitutive model proposed Bai and Wierzbicki (Bai & Wierzbicki, 2008) has a more uniform behavior for different levels of stress triaxiality and Lode angle parameter. Nevertheless, it is important to mention that some of the parameters of the model, which are listed in Table 4.1, were obtained with a set of experimental tests that include the smooth and round bars analyzed in this contribution.

The force *versus* displacement curves, obtained from the numerical simulation of the constitutive models, for the cylindrical notched bars are plotted in Figure 4.12. The curve for each model is plotted till the moment that the critical damage is reached and it is possible to observe a close agreement between all models and the experimental results.

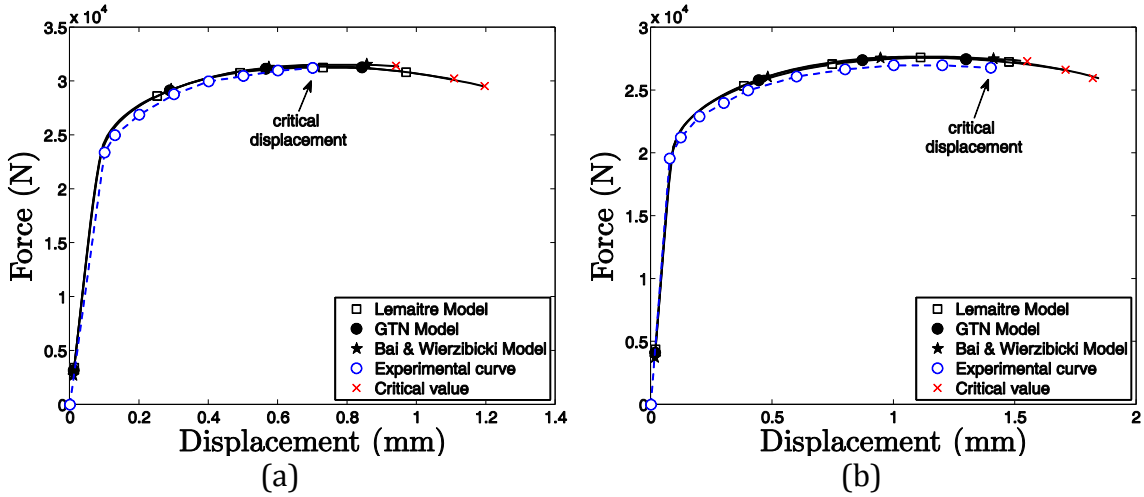

Figure 4.12. Force-displacement curves for a notched bar with: (a) $R = 4\ mm$ and (b) $R = 12\ mm$.

The critical displacement to fracture is highlighted in Figure 4.12, for both notched bars, and it is possible to observe a very small softening on the material behavior at the end of the analysis. Nevertheless, since the displacement observed at the beginning of the softening is almost the same as the displacement to fracture, there is almost no dependence of the results with the spatial discretization.

The evolution of the equivalent plastic strain is presented in Figure 4.13 for all specimens and, in general, it can be observed that the growth rate of this variable is higher for Lemaitre's model. The level of equivalent plastic strain reached by Lemaitre is, in fact, very high and in disagreement with the level of the equivalent strain at fracture cited in literature (see Table 4.4).

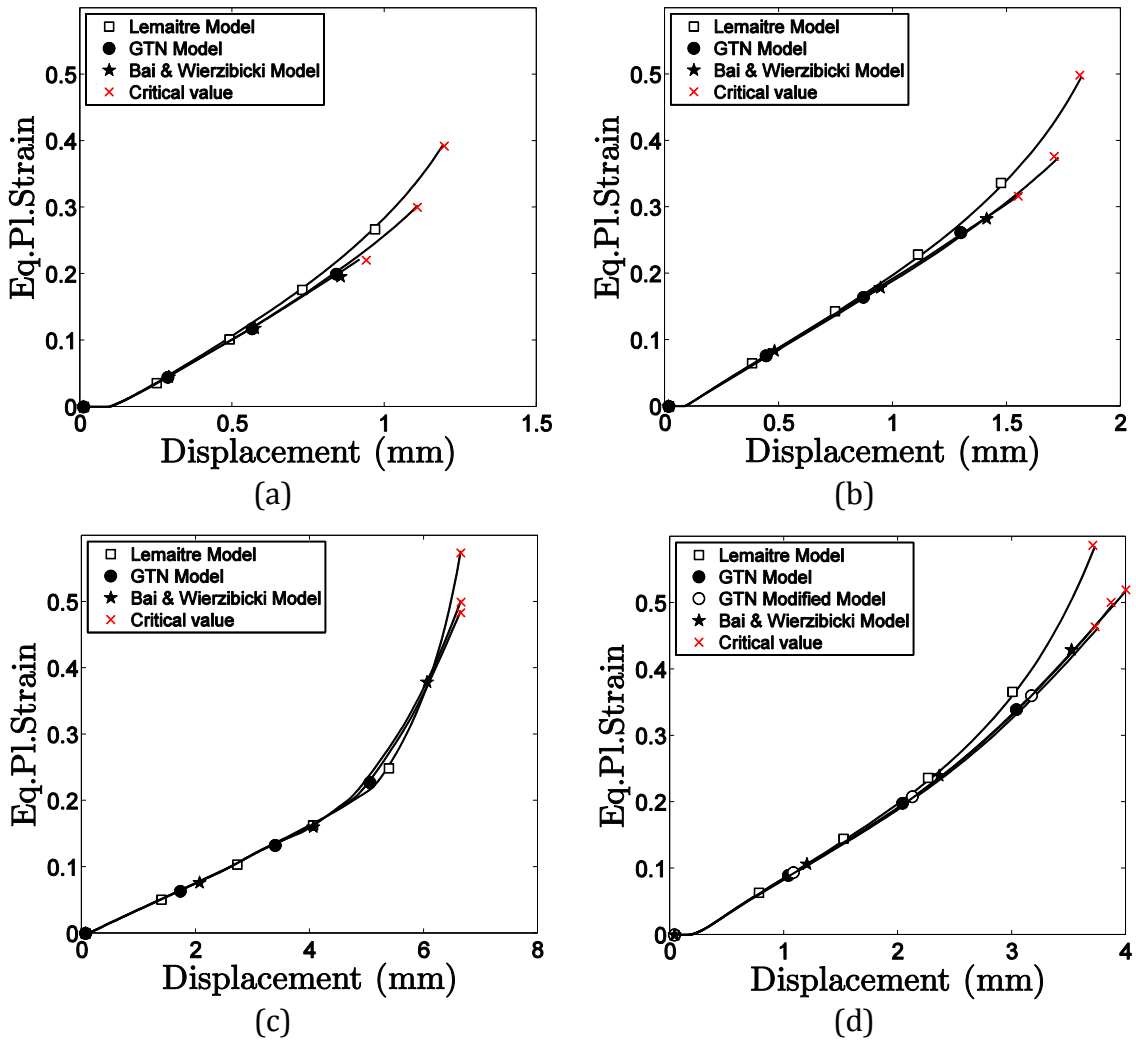

Figure 4.13. Equivalent plastic strain as a function of the prescribed displacement: notched bar specimens with (a) $R = 4\ mm$, (b) $R = 12\ mm$, and for (c) smooth bar specimen and (d) plate hole specimen.

The equivalent plastic strain contours are shown in Figure 4.14 for the two notched bars and the smooth bar specimen, where the distribution of this variable for all constitutive models can be analyzed. The displacement to fracture, which is reached when the damage variable attains the critical value, is included in the same Figure for all models and specimens. It can be seen, for the notched bar specimen with a radius, $R = 4\ mm$, that the equivalent plastic strain contour has a tendency to predict higher values on the outer surface for the three models (see Figure 4.14a, 4.14b and 4.14c). Nevertheless, the maximum values of equivalent plastic strain predicted by Lemaitre (Figure 4.14b) and GTN (Figure 4.14c) models also extend towards the center of the specimen.

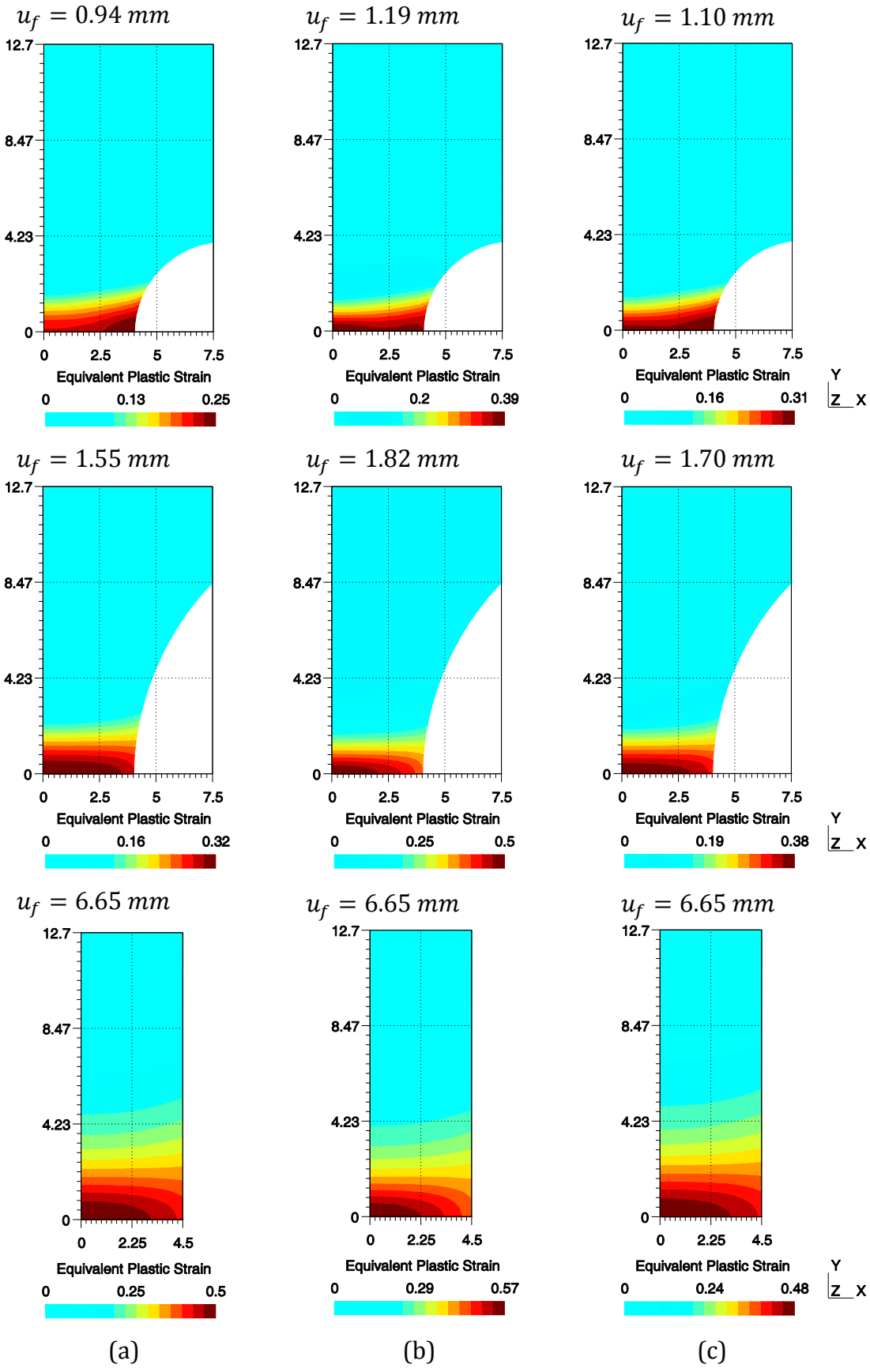

Figure 4.14. Equivalent plastic strain contours for notched bars and smooth bar specimens. (a) Bai & Wierzbicki model, (b) Lemaitre's model and (c) GTN model.

Experimental evidence has shown that fracture onset occurs at the centre of the specimen. Therefore, special care should be taken if the effective plastic strain is used as a fracture indicator, as suggested by Bao (2003), since none of the models clearly predicts a concentrated distribution of effective plastic strain at the centre of the specimen. For the two other specimens, namely the notched bar (*R=12 mm*) and the smooth bar, all constitutive models were able to predict the maximum location of the effective plastic strain at the central region of the specimen, which is in agreement with the location for fracture onset observed in the experimental tests.

The equivalent plastic strain contours, for the plate with a hole, are presented in Figure 4.15 together with the displacement to fracture predicted by each model. The maximum value for the internal variable is observed at the cross section of the specimen and close to the interior surface of the hole.

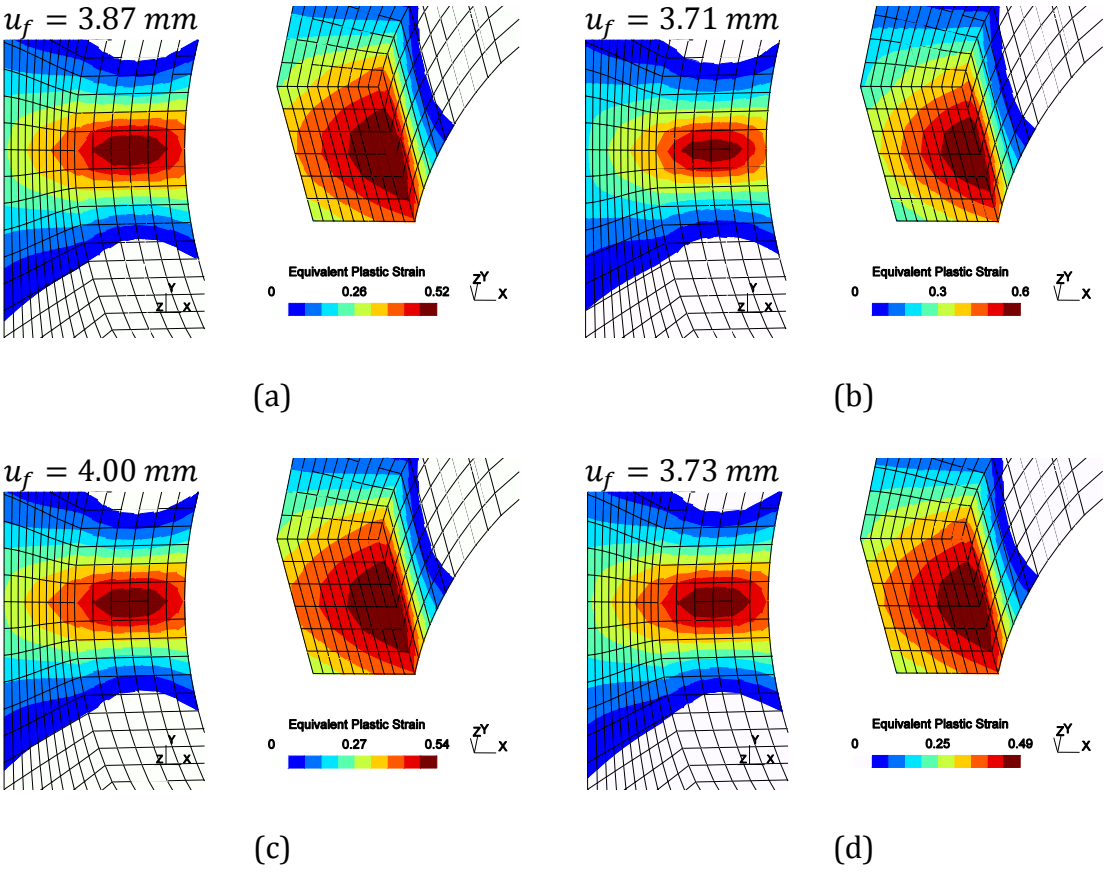

Figure 4.15. Equivalent plastic strain contours for the plate hole specimen. (a) Bai & Wierzbicki model, (b) Lemaitre's model, (c) GTN model and (d) GTN modified model.

Although the behavior is similar for all models, in Figure 4.16 is possible to appreciate in more detail the evolution of the normalized plastic strain at the nodes of the critical zone. Each model has got a slightly different evolution. As mentioned before, the level of equivalent plastic strain attained by Lemaitre's model is relatively high. In addition, it can be noticed that the introduction of the shear mechanism on the original GTN model, improved the prediction of the model.

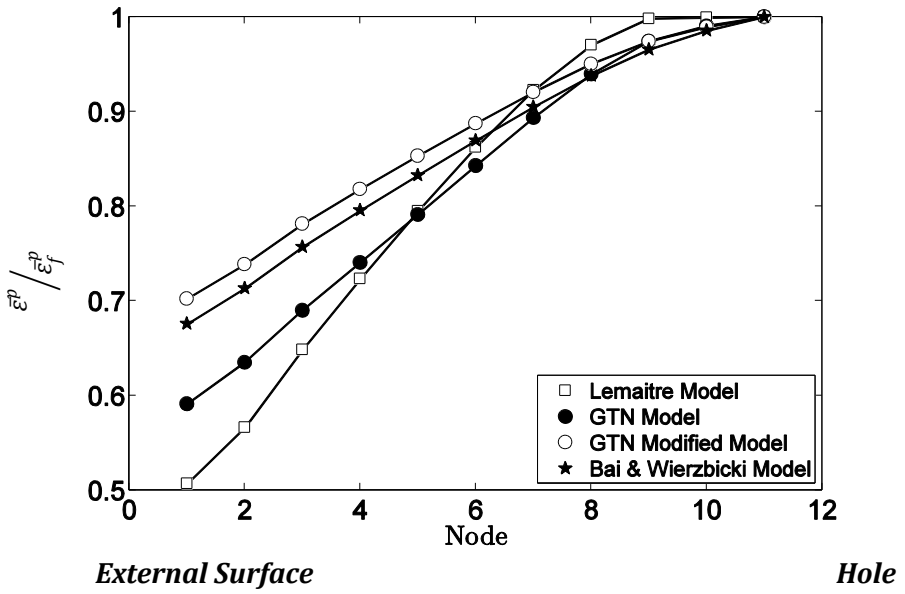

Figure 4.16. Equivalent plastic strain distribution at the critical zone for the plate with a hole specimen.

The damage variable field obtained in the finite element analysis is illustrated in Figure 4.17 for the cylindrical smooth bar and the two notched bars specimens.

The contour plots show the distribution of damage when one point of the problem reaches the critical damage for a specific constitutive model (see Table 4.2). The displacement to fracture, which is reached when the damage variable attains the critical value, is included in the same figure for all models and specimens. The location of the maximum damage occurs at the center of the specimen's and is correctly predicted by all models. This is in agreement with experimental evidence.

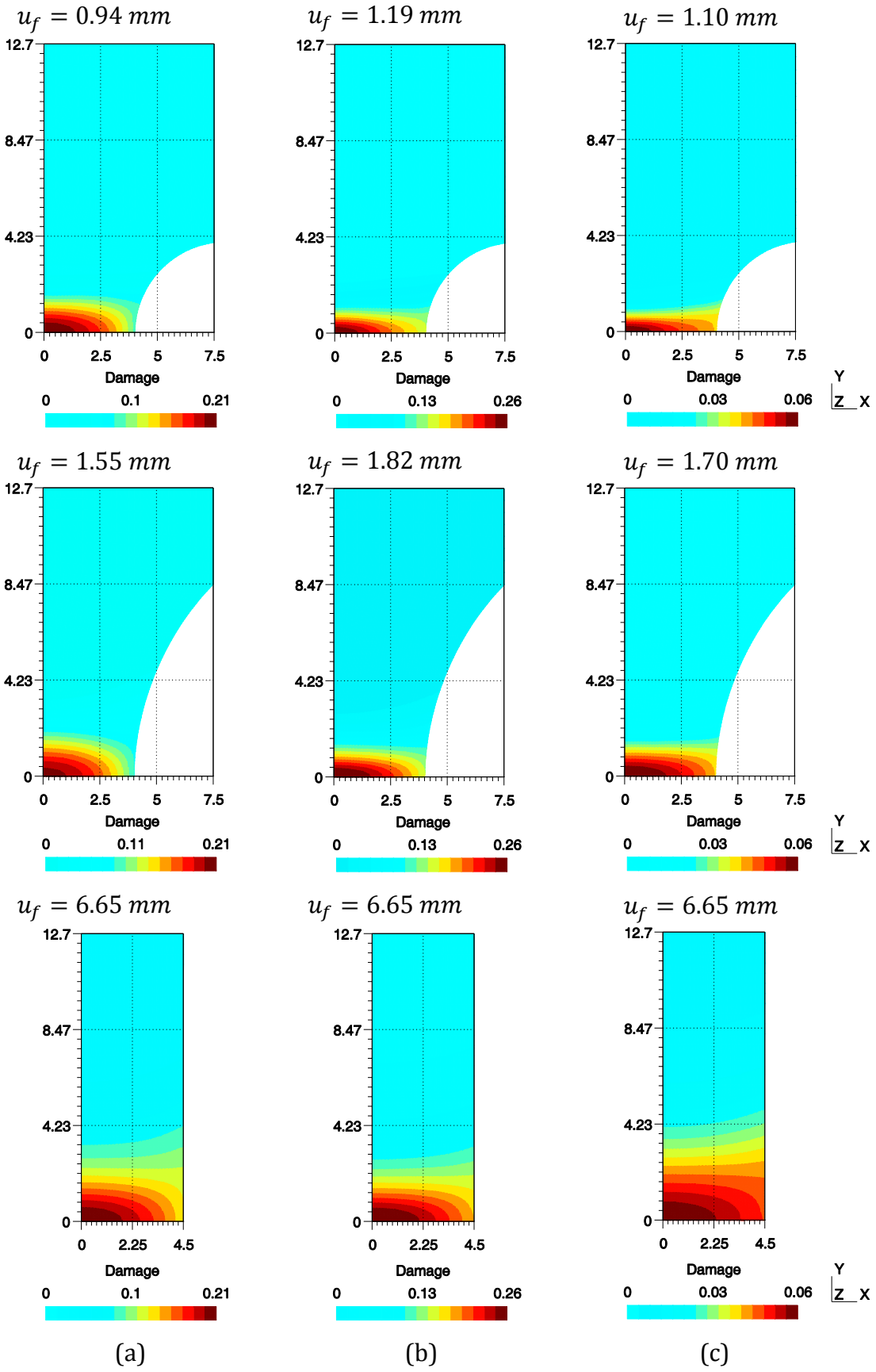

Figure 4.17. Damage contours for the notched bars and smooth bar specimens: (a) Bai & Wierzbicki's model, (b) Lemaitre's model, (c) GTN's model.

The damage variable field obtained in the numerical simulation for the plate hole specimen is illustrated by the contour plots shown in Figure 4.18. The maximum value of damage is predicted at the critical cross section of the specimen for all constitutive models, nevertheless, within the cross-section there are different evolutions for the damage variable.

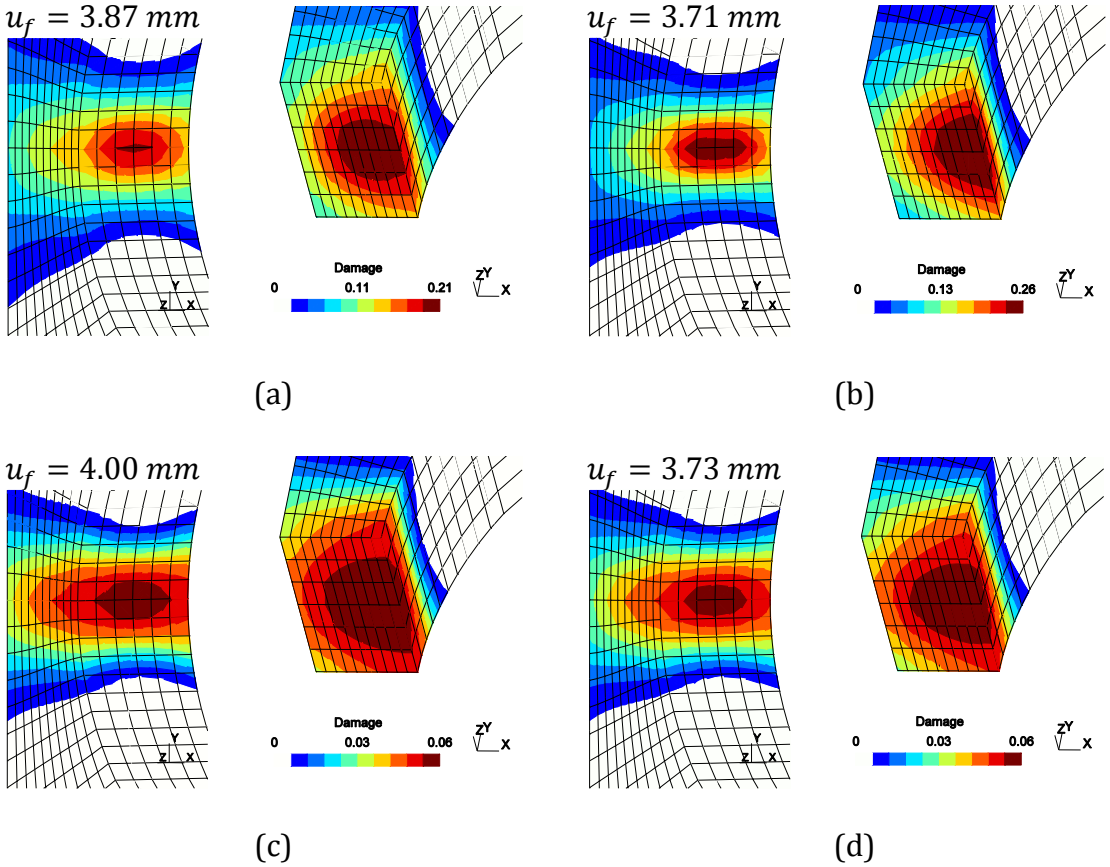

Figure 4.18. Damage contours for the plate hole specimen: (a) Bai & Wierzbicki's model, (b) Lemaitre's model, (c) GTN's model and (d) GTN modified model.

In Figure 4.19, it is possible to observe the evolution of the normalized damage at the critical cross section of the specimen. Lemaitre´s model predicts higher values of damage in the region close to the central hole attaining the maximum value at the edge on the surface of the hole. On the other hand, all the other models predict the maximum value inside the cross section, which is in agreement with experimental results (Bao *et al.*, 2004). Bai & Wierzbicki´s model together with the modified GTN models have a sharp prediction of damage around node 8 in Figure 4.19.

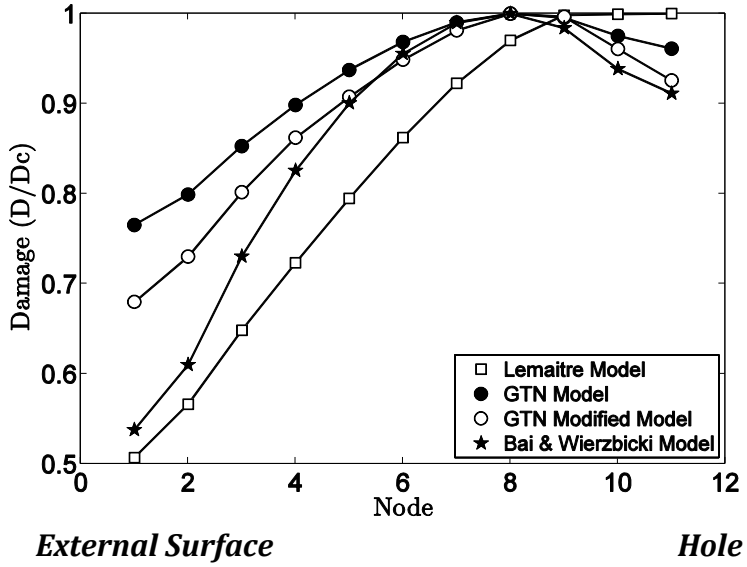

Figure 4.19. Damage evolution at the critical zone for the plate with a hole specimen.

4.5.2 Low Stress Triaxiality $(0 \leq \eta < 1/3)$

In this section, numerical results for the butterfly specimen, which is depicted in Figure 4.9, are presented. The focus here is to study the behavior of the constitutive models, previously described, under a low level of stress triaxiality and verify their ability to predict the correct fracture location. The butterfly specimen was simulated in both pure shear and combined tension/shear (10º with the x-axis) conditions. In Table 4.5, the numerical results, obtained by the finite element simulation, for the displacement at fracture, stress triaxiality average, Lode angle average and the equivalent plastic strain at fracture can be examined. In both loading scenarios, the prescribed displacement was imposed until the damage variable of the particular constitutive model, at any point in the specimen, reached its critical value, previously calibrated (see Table 4.2). The value of the displacement and effective plastic strain variables calculated from the finite element simulation, when the damage variable reaches its critical value, are understood as the displacement at fracture and effective strain at fracture from the numerical simulations.

The results obtained with the original GTN model, under shear dominated loading conditions, clearly emphasize the limitation of the model for predicting fracture under conditions of low stress triaxiality. In Table 4.5, it is possible to see that, according to this model, the critical damage value would never be reached for

pure shear stress states. Under combined tension/shear (10º with the x-axis) the predicted displacement to fracture is very high, when compared with the other models, since damage evolution is only due to the volumetric growth of voids. The displacements to fracture predicted by Lemaitre´s model, $u_f = 0.464$ mm, and the GTN modified model, $u_f = 0.348$ mm, are more or less close for pure shear. There is a slightly better agreement between the predicted displacements to fracture for these two models for combined tension/shear stress states: Lemaitre´s model predicts, $u_f = 0.408$ mm, and the GTN modified model predicts, $u_f = 0.34$ mm. Nevertheless, there is a marked difference between the levels of predicted equivalent plastic strain obtained with Lemaitre´s model and the GTN modified model for both loading conditions, which are clearly different from the reference value of the effective plastic strain listed in Table 4.3. Through the analysis of the results obtained by Bai & Wierzbicki´s model coupled with Bao´s fracture indicator (see Table 4.5), it is possible to conclude that the overall prediction is not satisfactory. In particular, for pure shear loading conditions the model predicts for both parameters, displacement and equivalent plastic strain to fracture, very high values ($u_f = 0.7$mm; $\bar{\varepsilon}^p{}_f = 1.4$) that are different from the reference values in Table 4.3. These results clearly suggest that Bao's damage fracture indicator coupled with Bai & Wierzbicki´s model might not be a good parameter to predict fracture under low level of stress triaxiality.

Table 4.5. A summary of the numerical results obtained by the damage constitutive models studied on aluminum alloy 2024-T351. Specimens subjected to a low level of stress triaxiality.

Specimen	*Model*	u_f *(mm)*	η_{av}	$\overline{\theta}_{av}$	$\bar{\varepsilon}^p{}_f$	$\bar{\varepsilon}_f$
Butterfly (pure shear)	Bai & Wierzbicki	0.700	0.00	0.00	1.40	0.21
	Lemaitre	0.464	0.08	0.04	0.64	
	GTN original	--	0.02	0.06	--	
	GTN modified	0.348	0.02	0.04	0.31	
Butterfly (tensile/shear 10º)	Bai & Wierzbicki	0.540	0.22	0.43	0.67	0.25
	Lemaitre	0.408	0.34	0.19	0.60	
	GTN original	0.642	0.30	0.47	0.64	
	GTN modified	0.340	0.27	0.43	0.35	

Figure 4.20 shows the evolution of the equivalent plastic strain for pure shear and combined shear/tensile (10º with the x-axis) loading conditions. It can be observed that the growth rate of this parameter for both Lemaitre and Bai & Wierzbicki models accelerates significantly after a particular value of the applied displacement. The GTN based models do not show this considerable increase. While the original GTN model predicts a very slow evolution for this variable, which is not realistic, the modified GTN model, under both loading conditions, predicts a faster evolution for the accumulated plastic strain.

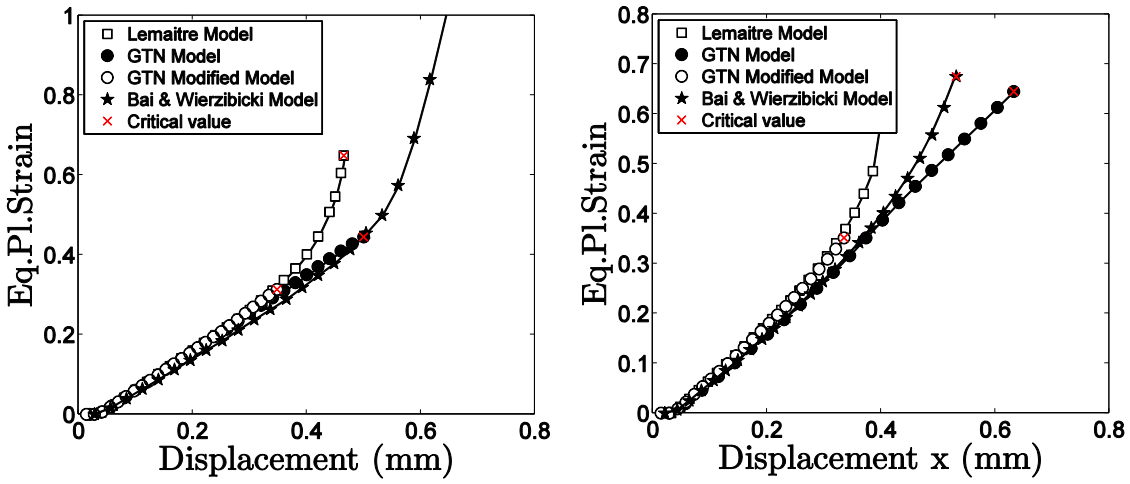

(a) (b)

Figure 4.20. Numerical results for the butterfly specimen in, (a) pure shear and (b) combined shear/tensile loading conditions.

The equivalent plastic strain contour for pure shear and combined shear/tensile (10º with the x-axis) loading conditions, for the constitutive models under analysis, can be observed in Figures 4.21 and 4.22, respectively. For the sake of completeness, the value of the displacement to fracture for each model is also included. Under pure shear loading (see Figure 4.21), the predicted location for the maximum value of the equivalent plastic strain, for all constitutive models, is on the surface of the shear zone. Since it is at this location that fracture onset is experimentally observed (Bai, 2008), the equivalent plastic strain could be used, in this case, as fracture indicator. From the analysis of Figure 4.21, it is possible to notice that the distribution of the maximum value of the equivalent plastic strain is more concentrated, on the surface of the shear zone, for Lemaitre´s model (Figure 4.21b) and less concentrated for both GTN´s original and modified models (Figure 4.21c and 4.21d). Although the maximum value of the equivalent plastic strain for

Bai and Wierzbicki´s model is on the surface of the shear zone, the distribution also spreads towards the centre of the specimen (see Figure 4.21a).

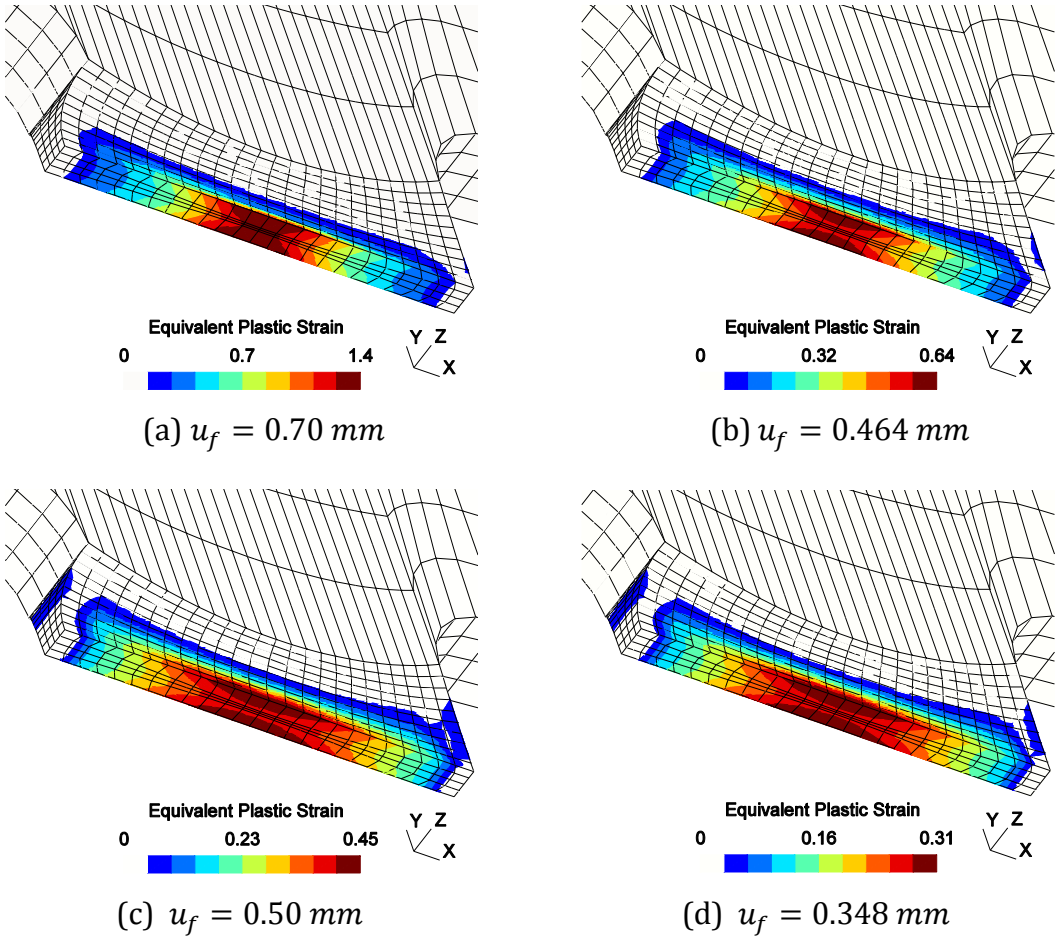

(a) $u_f = 0.70\ mm$ (b) $u_f = 0.464\ mm$

(c) $u_f = 0.50\ mm$ (d) $u_f = 0.348\ mm$

Figure 4.21. Equivalent plastic strain contours, for a butterfly specimen, under pure shear conditions. (a) Bai & Wierzbicki´s model, (b) Lemaitre's model, (c) GTN´s model and (d) GTN´s modified model.

However, under combined shear/tensile (10º with the x-axis) loading (see Figure 4.22), the predicted location for the maximum value of the equivalent plastic strain, for all constitutive models, is again on the surface of the shear zone. Since for this loading condition fracture onset is experimentally observed at the middle of the thickness on the shear zone (Bai, 2008), the equivalent plastic strain field would give a wrong prediction of the fracture location. From the analysis of Figure 4.22, it is possible to conclude that the distribution of the maximum value of the equivalent plastic strain is more concentrated, on the surface of the shear zone, for Bai and Wierzbicki´s model (Figure 4.22a). This maximum for Lemaitre´s model, GTN´s model and GTN´s modified model is on the surface of the shear zone but the distribution also spreads towards the centre of the specimen.

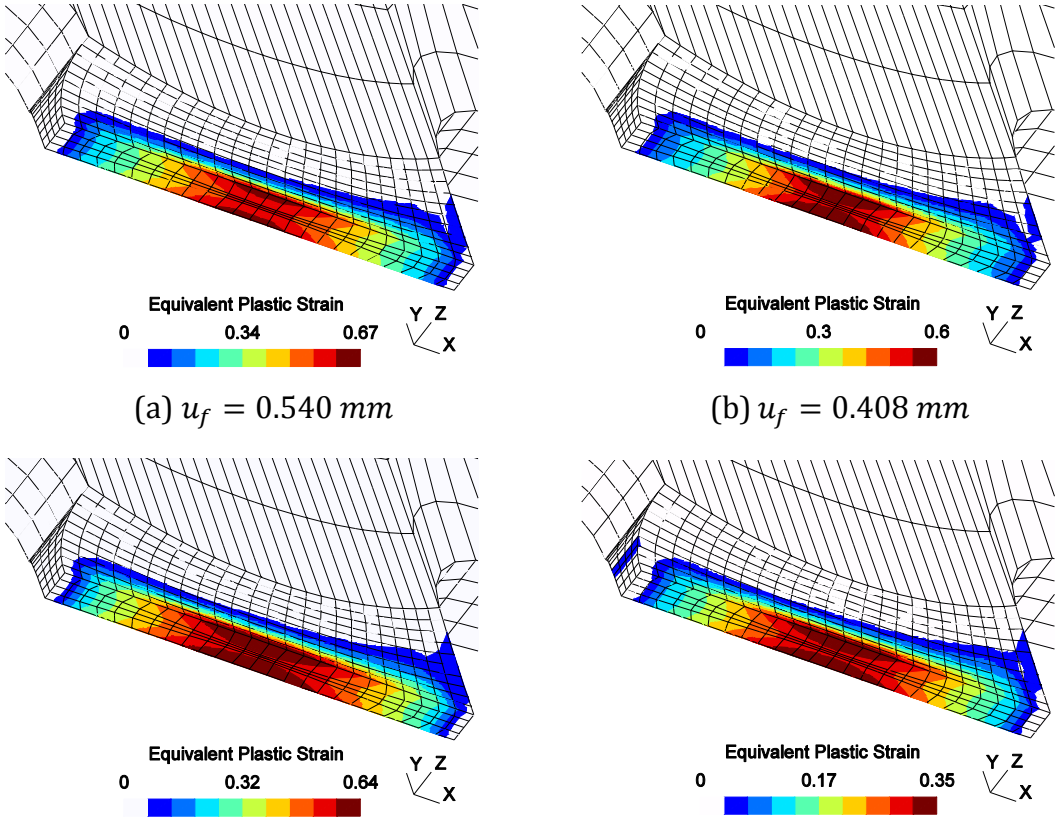

(a) $u_f = 0.540\ mm$ (b) $u_f = 0.408\ mm$

(c) $u_f = 0.642\ mm$ (d) $u_f = 0.340\ mm$

Figure 4.22. Equivalent plastic strain contours for the butterfly specimen under combined shear/tensile loading condition. (a) Bai & Wierzbicki , (b) Lemaitre (c) GTN original and (d) GTN modified models.

The evolution of the damage parameter, at the point where the damage variable reaches the maximum value, can be examined in Figure 4.23. The critical damage value for each model, which is listed in Table 4.2, is reached at different levels of displacement.

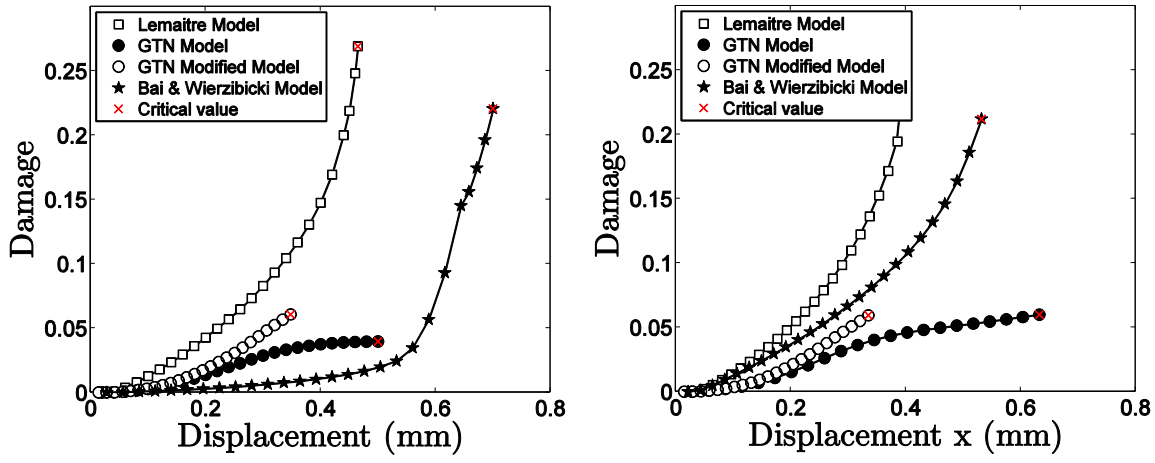

(a) (b)

Figure 4.23. Evolution of damage in (a) pure shear and, (b) combined shear/tensile loading conditions.

The evolution of the damage variable for the GTN original model under shear loading illustrates its limitation to predict shear localization and fracture under conditions of low triaxiality. After an initial increase of the damage variable, which is due to void nucleation, there is no further evolution of damage (see Figure 4.23a). Under a combined shear/tensile loading, this model predicts damage evolution. Nevertheless, since this growth is only due to volume void growth, the overall damage evolution is slow and the model predicts a high value for the displacement to fracture, which is not in agreement with experimental evidence. The inclusion of shear effects on the formulation of the model, here labeled modified GTN model, clearly improves the ability of the model to predict damage growth under shear and combined shear/tensile (10º with the x-axis) loading conditions since the distortion of voids and inter-void linking are taken into account in the model (see Figure 4.23a and 4.23b). It is important to observe that Lemaitre´s model can predict the evolution of damage under conditions of low stress triaxiality. In addition, Bao's damage fracture indicator coupled with Bai & Wierzbicki´s model is also able to predict the evolution of damage.

The damage distribution for each constitutive model, when the critical damage is attained, can be seen on Figure 4.24 for pure shear loading. Experimental evidence has shown that the potential zone for crack formation occurs on the surface of the shear zone. Both Lemaitre´s and GTN´s modified models, depicted in Figures 24b and 24d, have been able to predict the correct location of fracture onset. On the other hand, Bao's damage fracture indicator coupled with Bai & Wierzbicki´s model, depicted in Figures 24a, has predicted fracture at the middle of the thickness on the critical zone, which is wrong. The original GTN model predicts damage over the central region of the critical zone, never reaching the critical value (see Figures 24c).

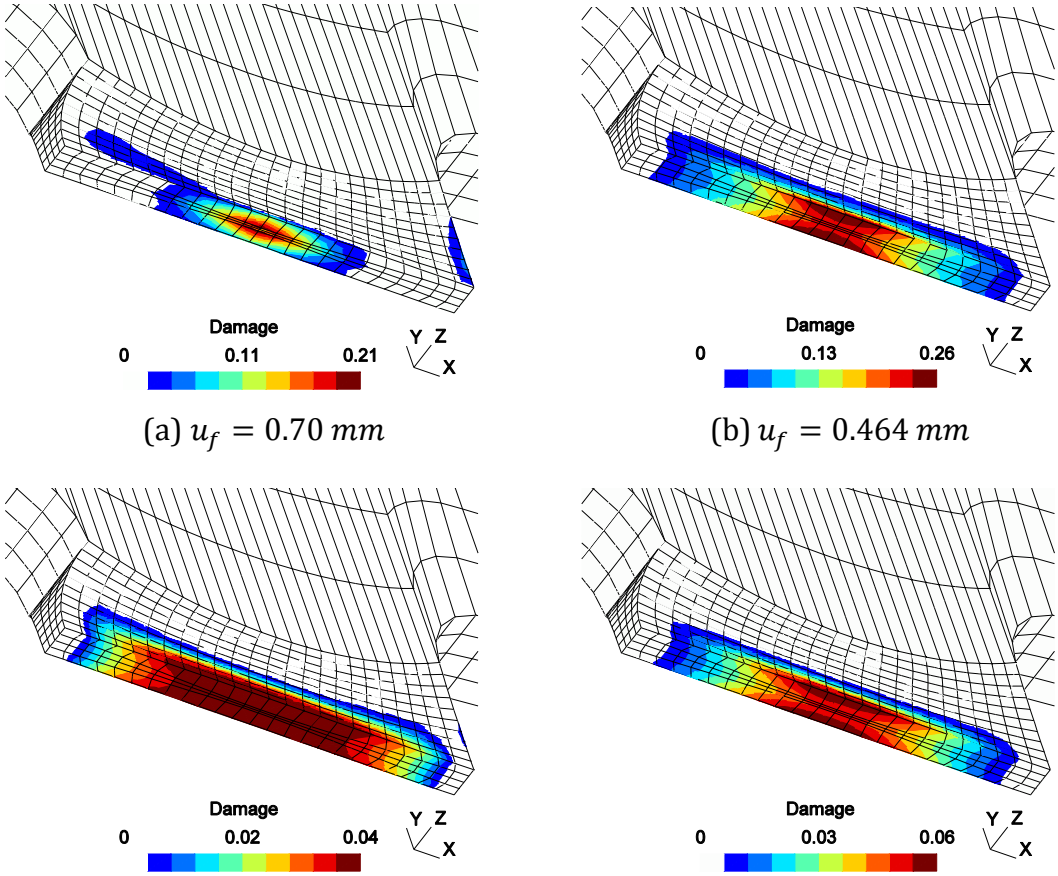

(a) $u_f = 0.70\ mm$ (b) $u_f = 0.464\ mm$

(c) $u_f = 0.50\ mm$ (d) $u_f = 0.348\ mm$

Figure 4.24. Damage contours for the butterfly specimen under pure shear conditions. (a) Bai & Wierzbicki´s model, (b) Lemaitre's model, (c) GTN´s model and (d) GTN´s modified model.

The damage variable field obtained in the numerical simulation, for a combined tensile/shear loading condition, is illustrated by the contour plots shown in Figure 4.25. For this loading condition, fracture onset is experimentally observed at the center of the shear zone. Therefore, from the analysis of Figure 4.25 it is possible to conclude that Bao's damage fracture indicator coupled with Bai & Wierzbicki´s model is able to predict the correct fracture location. The same happens with the GTN original model that also predicts fracture onset at the centre of the specimen. However, the damage evolution for these two models is relatively slow and consequently they predict a large displacement to fracture. In contrast, Lemaitre´s model and the GTN´s modified model have predicted fracture onset at the surface of the critical zone, which is in disagreement with experimental evidence. Therefore, these two models have not been able to predict the correct location of fracture under combined tensile/shear loading conditions.

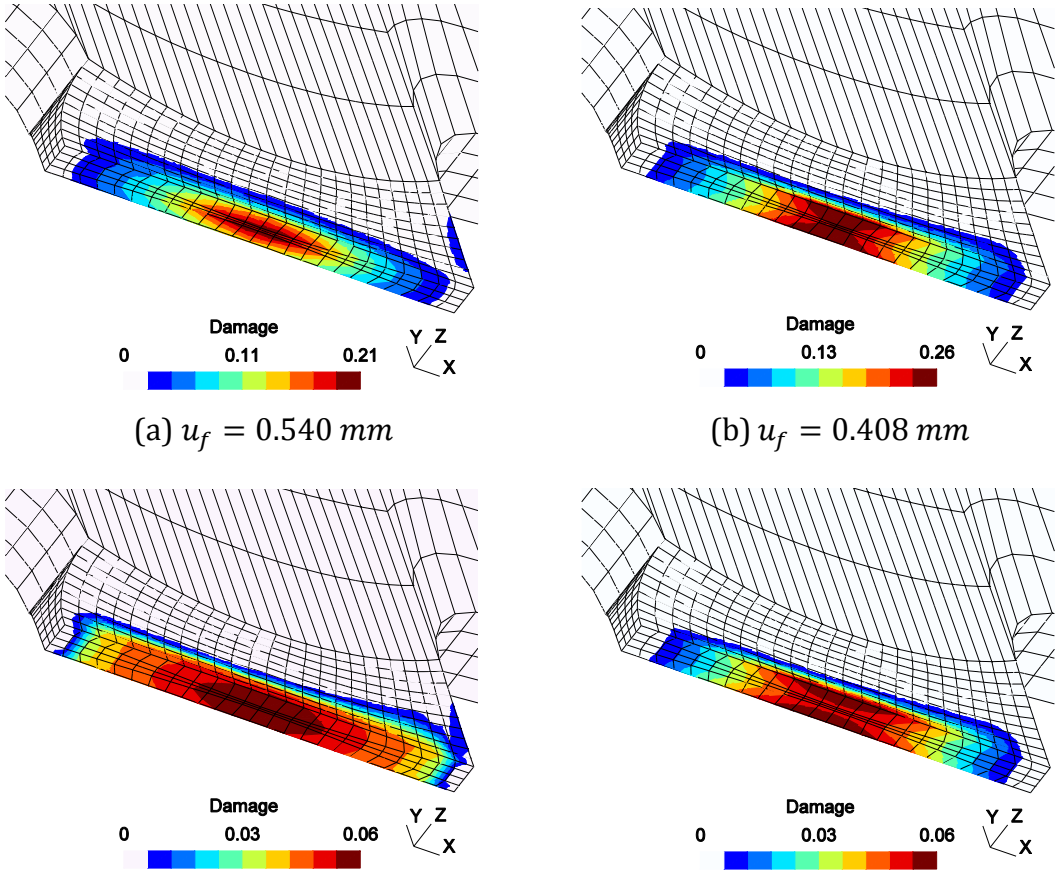

(a) $u_f = 0.540\ mm$ (b) $u_f = 0.408\ mm$

(c) $u_f = 0.624\ mm$ (d) $u_f = 0.340\ mm$

Figure 4.25. Damage contours for a butterfly specimen under combined shear/tensile load. (a) Bai & Wierzbicki, (b) Lemaitre (c) GTN original and (d) GTN modified models.

The inclusion of shear effects on the GTN model has got a significant impact on the evolution of the equivalent plastic strain. Due to the strong coupling between plastic flow and damage, which exists on the modified GTN model (see Box 4.1), an increase of overall damage due to the combination of void growth with the distortion of voids leads to an increase of the equivalent plastic strain. This enhances the model that predicts a level of equivalent plastic strain to fracture close to the expected value. In order to discuss the predictive ability of Lemaitre´s model, different values for the critical damage D_c were critically selected and the damage variable field obtained from the numerical simulation is illustrated by the contour plots shown in Figure 4.26. It is important to remark, that this is merely an exercise and the authors have not performed any additional calibration procedure.

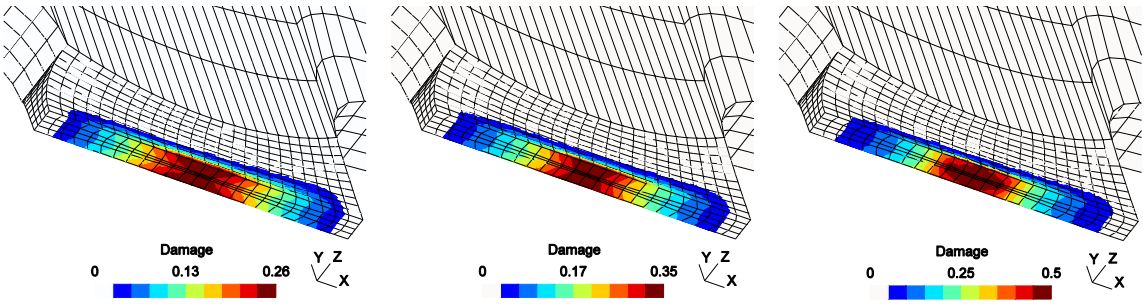

(a) (b) (c)

Figure 4.26. Lemaitre´s damage contour for the butterfly specimen under combined shear/tensile loading condition. (a) $D_c = 0.26$, (b) $D_c = 0.35$ and (c) $D_c = 0.50$.

From the analysis of the results depicted in Figure 4.26, it is possible to conclude that if the critical value of damage is increased, the location of fracture onset moves from the surface of the shear zone to the center of the shear zone. Therefore, for a high value of critical damage, $D_c = 0.50$, the prediction of fracture onset of Lemaitre´s model would be in agreement with experimental observations.

4.5.3 Discussion

A comprehensive set of numerical simulations, regarding specimens with different geometries, has been carried out to generate diverse stress and strain states covering a wide range of triaxiality and Lode angle. In Table 4.6, a qualitative summary of the predictive ability of the constitutive models for the specimens studied is presented. The classification takes primarily into account the correct prediction of the fracture location, the displacement to fracture predicted by the model and also the level of the accumulated plastic strain. The highest predictive ability is denoted by "+ + +" and the worst by "-".

Under a high level of stress triaxiality ($1/3 \leq \eta < 1$), the model proposed by Bai & Wierzbicki coupled with Bao's damage fracture indicator had the best performance. This conclusion is achieved through the combined analysis of the prediction of the fracture location, the displacement to fracture and the equivalent plastic strain to fracture. The model predictions, for all specimens, are in close agreement with experimental evidence. The coupled damage constitutive models (Lemaitre, GTN original and GTN modified) were also able to predict the correct

location for fracture regarding the cylindrical and smooth bars. Nevertheless, the predicted displacements to fracture and equivalent plastic strains to fracture lose their accuracy whenever the stress and strain states are far from the calibration point. The model proposed by Lemaitre consistently predicts high levels of equivalent plastic strain to fracture. For the plate with a hole specimen, Lemaitre´s model predicts the edge node of the critical zone as the potential location for crack initiation, which is in disagreement with experimental data. The other constitutive models are able to predict the correct location for fracture initiation.

Table 4.6. Qualitative summary of the predictive ability of the constitutive models for ductile fracture.

Model	*Specimen*					
	Notched bar (4 mm)	*Notched bar (12mm)*	*Plate hole*	*Smooth bar*	*Butterfly (tension/ shear 10º)*	*Butterfly (pure shear)*
	η_0= 0.75 $\overline{\theta}_0$ = 1	η_0= 0.47 $\overline{\theta}_0$ = 1	η_0= 0.37 $\overline{\theta}_0$= 1	η_0= 0.33 $\overline{\theta}_0$= 1	η_0= 0.11 $\overline{\theta}_0$= 0.22	η_0= 0 $\overline{\theta}_0$= 0
Bai & Wierzbicki	+ +	+ + +	+ +	+ + +	+	-
Lemaitre	+	+	-	+ + +	-	+
GTN original	+ +	+ +	+	+ + +	+	-
GTN modified	+ +	+ +	+ + +	+ + +	-	+ +

For a low level of stress triaxiality ($0 \leq \eta < 1/3$), it is possible to conclude that the GTN modified model is the model in closer agreement with experimental results with regard to the equivalent plastic strain. However, under combined loading condition, the model predicted the surface of critical zone as potential zone to crack initiation, which is not in accordance with experimental observations. Under this loading condition, only Bai & Wierzbicki´s model and the GTN original model predicted the correct fracture location. Nevertheless, they also incorrectly predict a large equivalent plastic strain to fracture. Lemaitre's model, for combined loading, is not able to predict both the correct fracture location and the equivalent plastic strain to fracture. Under a pure shear loading condition, the GTN modified model has the best agreement with regard to the equivalent plastic strain together

with the prediction of the fracture location. The model proposed by Lemaitre has been able to predict the correct zone to crack formation; nevertheless, the level of equivalent plastic strain to fracture is in complete disagreement with experimental results. The fracture indicator proposed by Bao is not appropriate for the prediction of fracture under a low level of stress triaxiality.

The predictive ability of the constitutive models is intimately related to their formulation. The fact that the effect of the stress state is taken into account on the behavior of the yield surface of Bai & Wierzbicki´s model, through the dependence of both pressure and triaxiality, can justify the more uniform performance of the model under a wide range of stress triaxiality. The loss of accuracy of the model under low level of stress triaxiality is due to the selection of a fracture indicator, which is not able to capture well shear effects on the damage evolution. The effect of the stress state on the yielding behavior is also considered in the GTN model, through the inclusion of the hydrostatic pressure. Nevertheless, the effect of the Lode angle is not included on the yield behavior. This fact combined with a damage evolution law based on volumetric void growth leads to a good behavior for high levels of stress triaxiality. The GTN modified model already includes this effect on the damage evolution law, which clearly improves the predictive ability of the model under low stress triaxiality. On the other hand, Lemaitre´s model does not include the effect of the stress state on the behavior of the yield surface but includes the effect of stress triaxiality on the damage evolution law.

With regard to the number of material properties and parameters, the constitutive models have different requirements. All of them necessitate the determination of the material´s elastic properties and hardening curve. Nevertheless, it is important to highlight that each of them involve the determination of several extra parameters. Bai & Wierzbicki´s model requires the determination of seven parameters obtained through four different specimens, the GTN´s model requires the determination of nine parameters obtained from one specimen and Lemaitre´s model requires the determination of three parameters obtained from one specimen (see Table 4.1 and 4.2).

4.5.4 Fracture Locus Representation

One of the pioneering methods to analyze material ductility in engineering applications was based on the level of effective plastic strain at fracture for specific stress triaxiality (McClintock, 1968; Rice and Tracey, 1969). More recently, other researchers (Johnson & Cook, 1985; Mirza *et al*., 1996; Bai and Wierzbicki, 2008, among others) have developed fracture criteria, which also define limit values for the strain for different stress states. In particular, Bai and Wierzbicki (2008) have proposed a three dimensional fracture surface, which defines the boundary between the fracture and no-fracture zone, on the space of equivalent plastic strain *versus* stress triaxiality average and Lode angle. This surface, which is based on boundary limit curves, requires the determination of six parameters that need to be calibrated for each specific material.

The three dimensional fracture locus for the 2024-T351 aluminium alloy has been obtained by Bai and Wierzbicki (2008) that employed the material fracture data points obtained by Bao (2003) to interpolate the surface. This surface can be mathematically represented by the following expression (Bai and Wierzbicki, 2008):

$$\hat{\varepsilon}_f\left(\eta,\overline{\theta}\right) = \left[\frac{1}{2}\left(0.5862\,\mathrm{e}^{-1.3576\,\eta} + 0.4859\,\mathrm{e}^{-0.7\,\eta}\right) - 0.217\,\mathrm{e}^{-0.04\,\eta}\right]\overline{\theta}^{3} + \frac{1}{2}\left(0.5862\,\mathrm{e}^{-1.3576\,\eta} - 0.4859\,\mathrm{e}^{-0.7\,\eta}\right)\overline{\theta} + 0.217\,\mathrm{e}^{-0.04\,\eta}. \tag{4.32}$$

The numerical results obtained in sections 4.5.1 and 4.5.2 for different constitutive models can be represented in this three dimensional space of equivalent plastic strain *versus* stress triaxiality average and Lode angle. Nevertheless, for the sake of clarity, we will represent the surface by its projections, for different values of the normalized Lode angle, on the space of equivalent plastic strain *versus* stress triaxiality. In Figure 4.27, three projections of the surface that correspond to normalized Lode angle values of 0.0, 0.5 and 1.0 are depicted together with the results obtained in Section 6 for the different constitutive models. It is important to recall that the smooth bar and notched bars have a normalized Lode angle equal to unity but the plate with a hole has an average normalized Lode angle less than unity (see Table 4.4). Furthermore, the

butterfly specimen under pure shear has a normalized Lode angle equal to zero, but under tensile/shear the normalized Lode angle is higher than zero (see Table 4.5).

The representation has revealed that GTN´s modified model, for low level of stress triaxiality, is able to reasonably follow the fracture surface trend. For high level of stress triaxiality, Bai and Wierzbicki´s model has the closest behavior with the reference values. It is also possible to conclude that Lemaitre's model predicts a high level of equivalent plastic strain to fracture for both high and low levels of stress triaxiality. Finally, the GTN original model has only been able to predict the behavior under conditions of high stress triaxiality exhibiting obvious limitations under low levels of stress triaxiality.

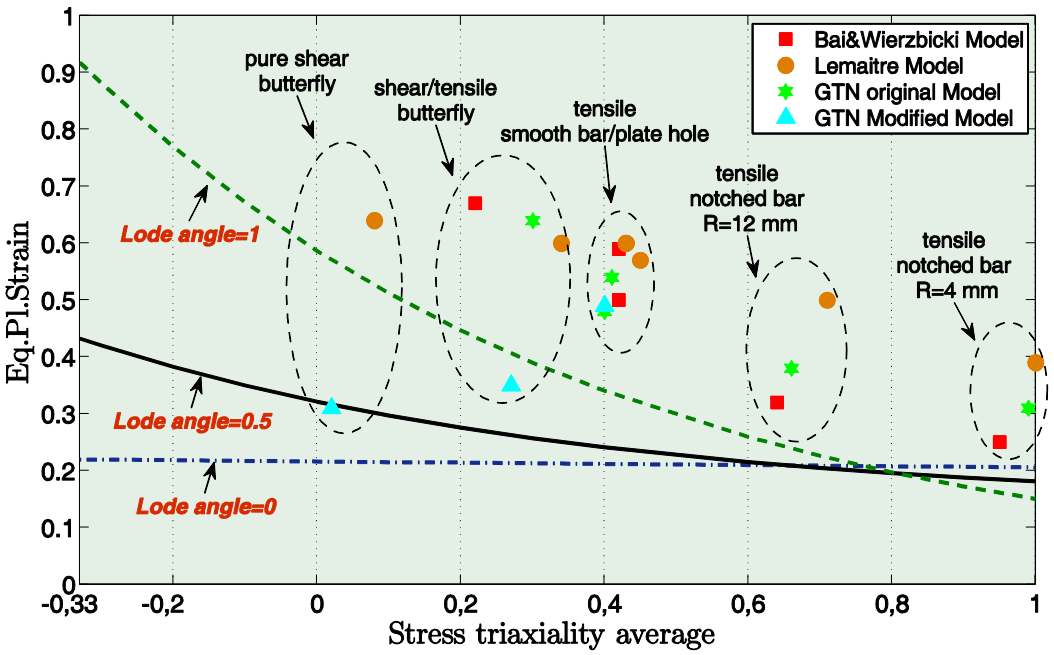

Figure 4.27. Fracture locus for an aluminum alloy 2024-T351 on the space of equivalent plastic strain *versus* stress triaxiality average.

4.6 CONCLUSIONS

In this contribution, the well established coupled damage constitutive models, proposed by Lemaitre and GTN, together with a recent constitutive formulation, proposed by Bai and Wierzbicki, were assessed in order to verify their ability to predict ductile failure under a wide range of stress triaxiality. To achieve

this objective, the constitutive formulations were implemented in a quasi-static finite element scheme and several numerical simulations, regarding specimens with different geometries, have been performed to generate diverse stress states. The behavior of some variables was critically analyzed such as, the displacement at fracture, the equivalent plastic strain at fracture, the evolution of the damage variable, force *versus* displacement curves as well as the contour plots of damage and equivalent plastic strain.

The results from the simulation have shown that for high levels of stress triaxiality, the constitutive model proposed by Bai and Wierzbicki combined with Bao´s fracture indicator is in closer agreement with experimental results and presents a uniform behavior for stress states close and far from the calibration point. The GTN model is also able to predict ductile failure with reasonable accuracy and Lemaitre´s model is the less accurate model. One possibility to enhance the predictive ability of the coupled damage models, which does not require changes in the constitutive formulation of the model, would be to calibrate them for stress states close to the loading condition. Under a low level of stress triaxiality, all constitutive models have limitations. These can be on the value of the displacement to fracture, the equivalent plastic strain to fracture or in terms of the prediction of fracture location. Therefore, it is possible to conclude that under combined loading, all models need to be improved. Under a pure shear loading condition, the GTN modified model has shown the ability of predicting ductile failure with reasonable accuracy.

Based on the results, it is possible to suggest further studies and developments. In particular, the assessment of the performance of the Bai and Wierzbicki constitutive model combined with other fracture indicators, which are able to capture shear effects, is recommended. The introduction of a shear mechanism, which depends on the Lode angle, on the GTN damage evolution law clearly improved the behavior of the model under low stress triaxiality. Therefore, new damage evolution laws should be developed to increase the ability of the model to capture ductile failure under more complex loading conditions. The same suggestion can be made for Lemaitre's model.

CHAPTER 5

Evaluation of Shear Mechanisms and Influence of the Calibration Point on the Numerical Results of the GTN Model

In this chapter, a numerical comparative study is undertaken based on Gurson-Tvergaard-Needleman (GTN) original model and two recent enhancements that include shear mechanisms, employing two different strategies to calibrate the material parameters. The assessment is motivated by the fact that the accuracy of the numerical results obtained with coupled damage models is strongly dependent on the calibration point. Hence, the numerical results obtained with these models are more realistic and in agreement with experimental evidence when the external loading conditions are close to the calibration point. Two distinct shear mechanisms, proposed by Xue and Nahshon & Hutchison, were selected and added into damage variable of GTN model, in order to allow the prediction of crack formation when predominant shear loading conditions are present. This chapter is structured as follows: In the first part of this study, the mathematical formulations that describe both mechanisms are presented as well as the GTN original model. In addition, the numerical strategy followed in this work is described, based on an implicit quasi-static finite element framework. In the following section, a specimen under high and other under low stress triaxiality are used as calibration points and by using an inverse method, the material parameters are identified. Regarding the performance of the numerical results and its dependence with the calibration point, numerical tests are carried out for a set of loading conditions, such as: pure shear, combinations of shear/tensile and pure tensile conditions. These simulations were conducted assuming first, the material parameters obtained by the first calibration point and then, using the properties which resulted from the second calibration point. Both numerical results are compared with experimental data, regarding the ability to predict the correct fracture location and the determination of the correct displacement at fracture.

5.1 INTRODUCTION

The formulations proposed by Gurson (1977) and Lemaitre (1985) are the most well established ductile damage theories to describe the material internal degradation (see Chaboche *et al*., 2006). These classical coupled damage models have the ability to predict the correct fracture location under a specific range of stress triaxialities (see Xue, 2007; Nahshon *et al*.; 2008; Teng, 2008) and are extremely accurate for loading conditions close to the calibration point (see Reis *et al*., 2010; Malcher *et al*., 2012). For example, within the range of high levels of stress triaxiality, where the spherical void growth is the predominant mechanism, the models based on Gurson's theory, like the Gurson-Tvergaard-Needleman model (GTN), have a good performance in the prediction of both the location of fracture onset and the displacement at fracture. However, under shear dominated loads, where failure is mainly driven by the shear localization of plastic strain of the inter-voids ligaments due to void rotation and distortion, the model has an irregular performance, (see Engelen, 2005; Chaboche, 2006). Figure 5.1 illustrates the ductile failure mechanism, which can occur by internal necking (Figure 5.1a), where the large primary voids are formed due to high stress triaxiliaty and the inter ligaments are created mainly by a sharp volumetric growth, or by void sheeting (Figure 5.1b), where primary voids remain small due to low stress triaxiality and the inter ligament occurs mainly by elongation of voids and formation of secondary voids in strain localization bands.

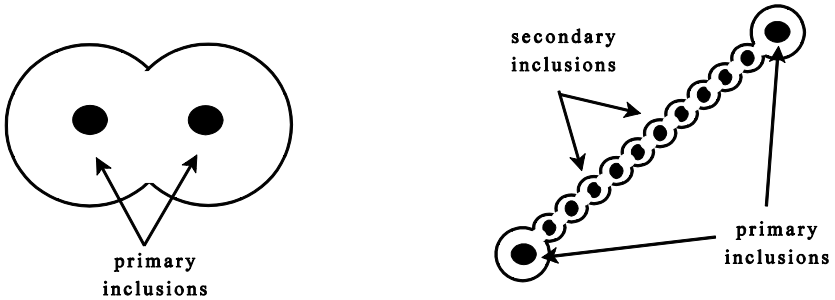

Figure 5.1. Schematic representation of ductile failure mechanism (a) internal necking and (b) void sheeting. Adapted from Besson, (2010).

The GTN original model is able to predict fracture in ductile materials, especially when the damage mechanism is caused by a significant growth of the volume void fraction (Figure 5.1a) and has got limitations when the material damage is induced predominantly by the elongation of voids (see Xue, 2007; Nahshon *et al*.; 2008).

In the following sections, mathematical aspects related to GTN model and shear mechanisms are discussed and an assessment between both mechanisms is performed, based on two calibration strategies.

5.2 CONSTITUTIVE MODEL

The model proposed by Gurson (1977) is one of the first micromechanical based models for the description of ductile damage and fracture, which introduces a strong coupling between plastic strain and damage, in the presence of finite strains. It mainly includes the description of the void growth stage and was based on the Rice and Tracey analysis of an isolated void (Rice and Tracey 1969). Gurson (1977) suggested the appearance of micro voids associated with a large plastic deformation as the internal degradation mechanism. The governing equations of the model were established by assuming a spherical cavity embedded in a cubic rigid-plastic matrix without hardening (see Figure 5.2) and use of the upper bound plasticity theorem. The degradation of the material is measured through the relation between the volume of the void and the volume of the representative volume element.

$$f = \frac{V_{void}}{V_{RVE}}, \tag{5.1}$$

where f represents the void volume fraction, V_{void} is the volume of the void and V_{RVE} denotes the volume of the representative volume element.

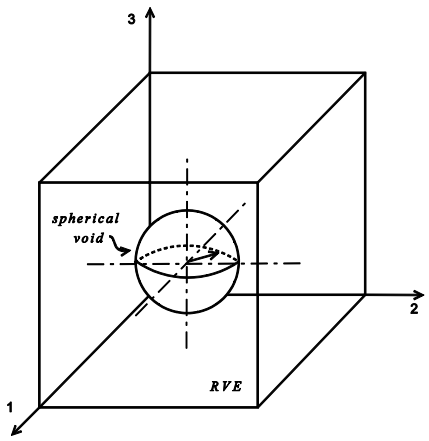

Figure 5.2: Schematic representation of the representative volume element with a spherical void (adapted from Gurson, 1977).

The relationship between the degradation of the material micro structure, which is due to the presence of micro voids or the formation of new ones in the material matrix, and the macroscopic loading evolution can be illustrated by Figure 5.3 for tensile dominant loads. In the elastic domain, the material is represented by stage (a), there is no appreciable change in the micro structure. Nevertheless, with the increase of the macroscopic load the nucleation of micro voids is trigged due to existence of localized plastic strain (stage b). In stage (c), the growth of micro voids is promoted by the high tensile hydrostatic stresses followed by coalescence of voids in stage (d).

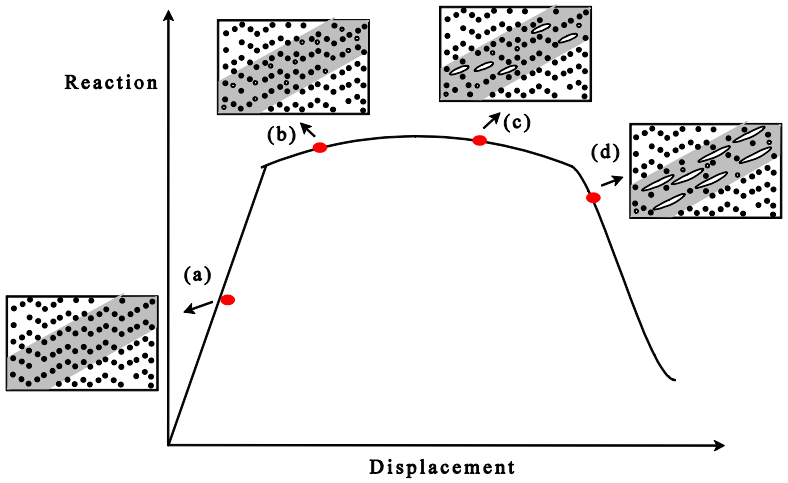

Figure 5.3: Schematic representation of the process of nucleation, growth, and coalescence of micro voids and the relationship with the macroscopic load (Adapted from Pineau & Pardoen, 2003).

The evolution of the volume void fraction predicted by Gurson´s model follows as a direct consequence of the requirement for mass conservation of a rigid-plastic material assuming plastic incompressibility. Hence, the density of a representative volume element of a material with voids (Figure 5.2) can be determined by:

$$\rho = \rho_m \frac{V_m}{V_{RVE}}, \tag{5.2}$$

where, ρ represents the density of the RVE, ρ_m represents the density of the matrix of the material and V_m is the volume of the matrix of the material. Thus, the relationship between the volume of the matrix of the material, V_m, and the void volume fraction, f, can be established by:

$$\frac{V_m}{V_{RVE}} = (1 - f). \tag{5.3}$$

Substituting Equation (5.3) into Equation (5.2), we have:

$$\rho = \rho_m(1 - f). \tag{5.4}$$

The density rate of the representative volume element, $\dot{\rho}$, can be expressed as a relation between the density rate of the material matrix, $\dot{\rho}_m$, and the volume void fraction rate, $\dot{f}$, by time differentiation of Equation (5.4):

$$\dot{\rho} = \dot{\rho}_m(1 - f) - \rho_m\dot{f}. \tag{5.5}$$

The matrix material is assumed to be plastically incompressible. In addition, the elastic volumetric strains are neglected by assumption. Therefore, the principle of mass conservation requires that $\dot{\rho}_m = 0$. Thus, substituting Equation (5.4) into Equation (5.5) and after some algebraic manipulations, the following expression can be obtained:

$$\dot{f} = -\frac{\dot{\rho}}{\rho_m} = -\frac{\dot{\rho}}{\rho}(1 - f). \tag{5.6}$$

The principle of mass conservation establishes that the volumetric strain rate is determined by:

$$-\frac{\dot{\rho}}{\rho} = \dot{\varepsilon}_v = \dot{\varepsilon}_v^e + \dot{\varepsilon}_v^p, \tag{5.7}$$

where, the elastic and plastic strain rate contributions are represented by $\dot{\varepsilon}_v^e$ and $\dot{\varepsilon}_v^p$, respectively. In Gurson´s model the matrix material is assumed to be rigid-plastic, therefore, by disregarding the elastic contribution Equation (5.6) can be re-written as:

$$\dot{f} = -\frac{\dot{\rho}}{\rho_m} = \dot{\varepsilon}_v^p(1-f). \tag{5.8}$$

The previous equation is the most significant contribution to the degradation of a porous material and expresses the evolution law for the void volume fraction. The original yield function derived by Gurson (1977) for a void-matrix aggregate is expressed by:

$$\Phi(\boldsymbol{\sigma}, k, f) = \left(\frac{q}{\sigma_y}\right)^2 + 2f\cosh\left(\frac{\mathrm{tr}\boldsymbol{\sigma}}{2\sigma_y}\right) - 1 - f^2, \tag{5.9}$$

where, q is the von Mises equivalent stress, σ_y is the isotropic hardening rule, which can be defined as $\sigma_y = k - \sigma_0$, where k represents the thermodynamical force associated to the isotropic hardening state variable and σ_0 is initial yield stress. The pressure-sensitive yield function proposed by Gurson (1977) can alternatively be expressed by:

$$\Phi(\boldsymbol{\sigma}, k, f) = J_2(\boldsymbol{S}) - \frac{1}{3}\left\{1 + f^2 - 2f\cosh\left(\frac{3p}{2\sigma_y}\right)\right\}{\sigma_y}^2, \tag{5.10}$$

where, J_2 represents the second invariant of the deviatoric stress tensor and p is the hydrostatic pressure.

According to the hypothesis of generalized normality, the plastic flow rule is given by

$$\dot{\varepsilon}^p = \dot{\gamma}\frac{\partial\Phi}{\partial\boldsymbol{\sigma}} = \dot{\varepsilon}_d^p + \dot{\varepsilon}_v^p = \dot{\gamma}\boldsymbol{S} + \frac{1}{3}\dot{\gamma}f\sigma_y\sinh\left(\frac{3p}{2\sigma_y}\right)\boldsymbol{I}, \tag{5.11}$$

where the plastic strain rate tensor, $\dot{\varepsilon}^p$, involves two terms: the deviatoric, $\dot{\varepsilon}_d^p$, and volumetric plastic strains, $\dot{\varepsilon}_v^p$, and $\dot{\gamma}$ represents the plastic multiplier. With the volumetric flow, $\dot{\varepsilon}_v^p$, constitutive equation (Equation 5.11), it is possible to obtain

the evolution law for the void volume fraction, $\dot{f}$, after the substitution of $\dot{\varepsilon}_v^p$ in Equation (5.8):

$$\dot{f} = (1-f)\dot{\varepsilon}_v^p = (f-f^2)\dot{\gamma}\sigma_y \sinh\left(\frac{3p}{2\sigma_y}\right). \tag{5.12}$$

5.2.1 Gurson–Tvergaard–Needleman (GTN)´s Model

One of the shortcomings of the Gurson model is the fact that, whatever strain history the material might be subjected; no void volume fraction evolution will be predicted if the initial void ratio is zero. Therefore, in order to enhance the model, several mechanisms for damage nucleation have been proposed such that voids can nucleate depending on the strain history. One of the most well known nucleation laws was proposed by Chu & Needleman (1980) and latter used by Tvergaard–Needleman (1984) in the GTN model. The damage evolution is represented by three simultaneous or successive mechanisms: nucleation, growth and coalescence of voids. The effective porosity, f^*, is determined by the following bilinear function:

$$f^* = \begin{cases} f & , \quad f < f_c \\ f_c + \left(\frac{1}{q_1} - f_c\right)\frac{(f-f_c)}{(f_f-f_c)}, & f \geq f_c \end{cases}, \tag{5.13}$$

where f_c represents the critical void volume fraction and f_f is the void volume fraction at fracture. The effective porosity, f^*, is obtained from both nucleation and growth mechanisms if the void volume fraction is less than the critical value, f_c. The coalescence mechanism becomes active when the void volume fraction is higher than the critical value, f_c. The void volume fraction rate, $\dot{f}$, is given by the sum of the nucleation and growth mechanism as:

$$\dot{f} = \dot{f}^n + \dot{f}^g. \tag{5.14}$$

The nucleation mechanism can be driven either by plastic strain or hydrostatic pressure. The definition of the nucleation mechanism based on the equivalent plastic strain is given by:

$$\dot{f}^n = \frac{f_N}{s_N\sqrt{2\pi}} \exp\left[-\frac{1}{2}\left(\frac{\bar{\varepsilon}^p - \varepsilon_N}{s_N}\right)^2\right]\dot{\bar{\varepsilon}}^p, \tag{5.15}$$

where, f_N represents the volume fraction of all particles with potential for microvoid nucleation, ε_N and s_N are the mean strain/pressure for void nucleation and its standard deviation. The variable $\overline{\varepsilon}^p$ represents the equivalent plastic strain and $\dot{\overline{\varepsilon}}^p$ is the rate of the accumulated plastic strain. The nucleation mechanism only occurs if the hydrostatic pressure is greater than zero, $p > 0$. If the hydrostatic pressure is less or equal to zero, $p \leq 0$, the nucleation rate is equal to zero. The evolution of the growth mechanism in the GTN model is given by the same expression as the original Gurson model (see Equation 5.8).

The yield function of the GTN's model, which assumes isotropic hardening and isotropic damage, is expressed by:

$$\Phi(\boldsymbol{\sigma}, k, f) = J_2(\boldsymbol{S}) - \frac{1}{3}\left\{1 + q_3 f^{*2} - 2q_1 f^* \cosh\left(\frac{q_2 3p}{2\sigma_y}\right)\right\}{\sigma_y}^2, \qquad (5.16)$$

where the parameters q_1, q_2 and q_3 are introduced to bring the model predictions into closer agreement with full numerical analyses of a periodic array of voids.

5.2.2 Shear Mechanisms

The original formulation of Gurson based models did not include shear effects, which excludes the possibility of predicting shear localization and fracture under conditions of low triaxiality. Under shear dominated loading conditions, the distortion of voids and inter-void linking promotes an effective increase in the material internal degradation and contributes to the material softening. Therefore, in order to improve Gurson based models predictive ability, under both zero and low levels of stress triaxialities, several researchers (Barsoum & Faleskog, 2007; McVeigh *et al.*, 2007; Xue, 2008; Nahshon & Hutchinson, 2008; Butcher *et al.*, 2009) have suggested the introduction of shear effects. The formulation of shear mechanisms, which can be based on geometrical or phenomenological considerations, resulted in evolutions laws that include the influence of the third invariant of the deviatoric stress tensor, the plastic strain tensor and its rate.

The shear damage mechanism proposed by Xue (2007) is based upon the solution of McClintock *et al.* (1968) for the coalescence of holes in a shear band. Due to its geometrical and physical appeal, we will revise here the shear damage

mechanism proposed by Xue (2008) and also describe an extended version proposed by Butcher & Zhen (2009). The mechanism is based on geometrical considerations of a representative square cell, containing a circular void at the center, which is subjected to a simple shear strain (see Figure 5.4). The length of the cell is equal to L and the radius of the central void is given by R. When the cell structure is loaded, the void rotates and elongates in the preferred direction. Due to the requirement of volume conservation of the cell structure, Xue (2008) assumes that the relative position of the void does not change with respect to the cell (see Figure 5.4). As the shear strain increases, the distance between the free surface of the void and the boundary of the representative volume element decreases. Figure 5.4 shows the cell structure in the initial configuration (a) and in the deformed configuration (b).

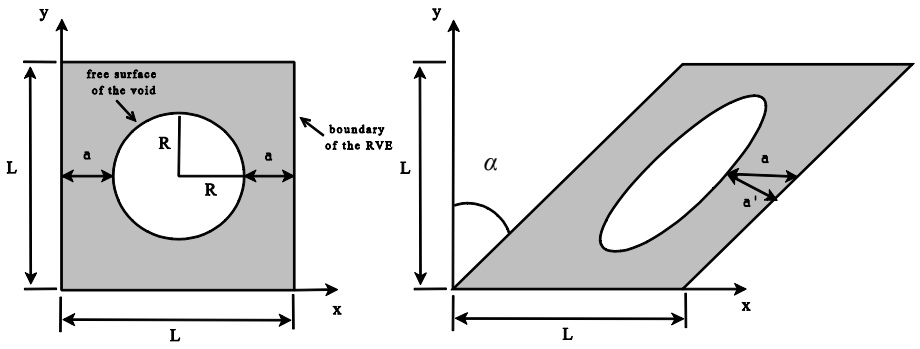

(a) (b)

Figure 5.4. Void shear mechanism: (a) initial configuration; (b) deformed configuration (adapted from Xue, 2007).

The minimum distance between the free surface of the void and the boundary of the RVE, which is represented by the parameter a, can be expressed by the relation between the length of the cell and the radius of the void (see Figure 5.4a):

$$a = \frac{L}{2} - R. \tag{5.17}$$

The application of a simple shear strain, γ, leads to the appearance of a deformation angle, α, on the deformed configuration given by:

$$\tan\alpha = \gamma. \tag{5.18}$$

The minimum distance at the deformed configuration can be related with the initial distance, a, and the deformation angle, α. In addition, it can also be related with the simple shear strain as:

$$a' = a\cos\alpha = a\sqrt{\frac{1}{1+\gamma^2}}. \tag{5.19}$$

An artificial strain can be defined (Xue, 2008), using the logarithmic definition of strain, which can be associated with the reduction of this minimum distance as:

$$\varepsilon_{art} = \ln\frac{a}{a'} = \ln\sqrt{1+\gamma^2}. \tag{5.20}$$

The fracture initiation in a shear band, according to McClintock *et al.* (1968), can be defined by the boundary contact condition of the sheared void with the longitudinal direction of the shear band. For small void volume fraction, Xue (2008) expressed the failure macroscopic shear strain in the shear band as:

$$\varepsilon_{shearband} = \frac{L}{2R}. \tag{5.21}$$

Consequently, the damage associated with the shearing of the void, D_{shear}, is defined by the ratio of the artificial and the macroscopic shear strain in a shear band (Xue, 2008):

$$D_{shear} = \frac{\varepsilon_{art}}{\varepsilon_{shearband}} = \frac{\ln\sqrt{1+\gamma^2}}{\frac{L}{2R}}. \tag{5.22}$$

Xue (2008) performed a Taylor series expansion and simplified the expression of the artificial strain term to:

$$\varepsilon_{art} \approx \frac{1}{2}\gamma^2. \tag{5.23}$$

The shear strain can be expressed as a function of the von Mises equivalent strain, $\gamma = \sqrt{3}\varepsilon_{eq}$. Therefore, for simple shear and for small void volume fractions, Equation (5.22) can be approximated by:

$$D_{shear} \approx \frac{\frac{1}{2}\gamma^2}{\frac{1}{2}\sqrt{\pi/f}} = \frac{3}{\sqrt{\pi}} f^{(1/2)} {\varepsilon_{eq}}^2, \tag{5.24}$$

where $f = \pi R^2/L^2$ is the void volume fraction of the cell in a two dimensional problem. For the three dimensional case, with a spherical void of radius R at the center of the representative cell of length L, the void volume fraction is expressed by $f = 4\pi R^3/3L^3$ for the cell. A similar three dimensional relation can also be obtained:

$$D_{shear} = \frac{3}{2}\left(\frac{6}{\pi}\right)^{(1/3)} f^{(1/3)} {\varepsilon_{eq}}^2. \tag{5.25}$$

The evolution of shear damage can be represented in the rate form as:

$$\dot{D}_{shear} = q_4 f^{q_5} \varepsilon_{eq} \dot{\varepsilon}_{eq}, \tag{5.26}$$

where q_4 and q_5 are geometrical parameters that can be defined for two or three dimensional problems. For a two dimensional problem, $q_4 = \frac{3}{\sqrt{\pi}}$ and $q_5 = (1/2)$ and for a three dimensional problem, $q_4 = \frac{3}{2}\left(\frac{6}{\pi}\right)^{(1/3)}$ and $q_5 = (1/3)$.

A modified shear damage expression was later derived by Butcher & Zhen (2009) that, contrary to Xue (2008), did not perform a Taylor series expansion of the artificial strain (Equation 5.20) and expressed the failure strain with the logarithmic definition as:

$$D_{shear} = \frac{\varepsilon_{art}}{\varepsilon_{shearband}} = \frac{\ln\sqrt{1+\gamma^2}}{\ln\sqrt{1/\chi}}, \tag{5.27}$$

where the parameter χ is the ligament size ratio defined for two or three dimensional problems, respectively, as:

$$\chi = R_x/L_x = \left(\frac{4}{\pi} f \frac{\lambda_2}{\lambda_1}\right)^{\frac{1}{2}}, \qquad \chi = R_x/L_x = \left(\frac{6}{\pi} f \frac{\lambda_2}{\lambda_1}\right)^{\frac{1}{3}}. \tag{5.28}$$

The parameters λ_1 and λ_2 are the void aspect ratios defined by:

$$\lambda_1 = \frac{R_y}{R_x}, \qquad \lambda_2 = \frac{L_y}{L_x}, \tag{5.29}$$

where R_y and R_x represent the radii of the void in the direction y and x. The dimensions L_y and L_x are the length of the cell in the direction y and x. The ratios λ_1 and λ_2 are equal to one in Xue´s model (Xue, 2008), which implies that the rotation of the cell structure is proportional to elongation of the void. According to Butcher & Zhen (2009), these parameters can more generically be expressed as a function of the stress state and, as a result, the evolution of the ligament size ratio is related to the normal strains.

Under the assumption of simple shear and small void volume fractions, the shear strain is related to the equivalent von Mises strain as $\gamma = \sqrt{3}\varepsilon_{eq}$ and the evolution of shear damage is given by:

$$\dot{D}_{shear} = \frac{1}{\ln \sqrt{1/\chi}} \left(\frac{3\varepsilon_{eq}}{1 + 3{\varepsilon_{eq}}^2} \right) \dot{\varepsilon}_{eq} \, . \tag{5.30}$$

Butcher & Zhen (2009) have shown that the shear damage expression (Equation 5.27) complies with McClintock criterion while Xue´s expression (Equation 5.24) does not. In addition, it was emphasized that the simplifications proposed by Xue (2008) have a critical role on the shear damage criterion and evolution rule.

In order to understand the role of the different shear damage evolutions, expressed by Equations 5.26 and 5.30, on a square cell subjected to a pure shear loading condition, we have coupled both evolutions with the GTN constitutive model. The results obtained from the numerical simulations for both models, which have exactly the same geometry and material properties, can be analyzed in Figure 5.5. It is possible to conclude that for the same applied displacement, the level of both equivalent plastic strain and shear damage predicted by Butcher and Zhen (2009) are significantly higher than Xue's model. Therefore, Butcher' model will predict failure before Xue's model, being extremely conservative on the moment of crack initiation whenever shear effects are present.

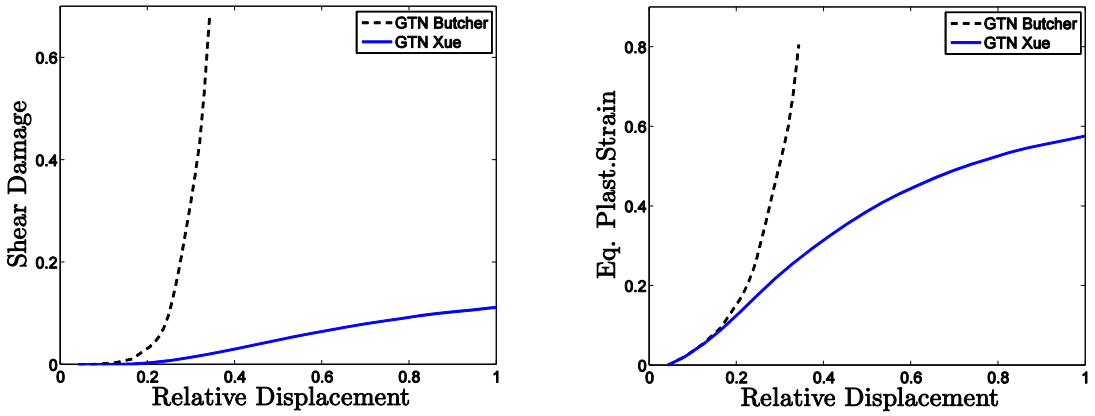

(a) (b)

Figure 5.5. Evolution of (a) the shear damage parameter and (b) the equivalent plastic strain by Xue and Butcher, coupled with the GTN's model.

Nahshon & Hutchinson (N&H) have also suggested a shear mechanism, based on phenomenological aspects that can be expressed by (see Nahshon *et al*, 2008):

$$\dot{D}_{shear} = k\, f\, \frac{\boldsymbol{S}:\boldsymbol{\varepsilon}^{p}}{q}, \tag{5.31}$$

where, k is a material parameter and needs to be calibrated, $\boldsymbol{\varepsilon}^{p}$ denotes the plastic strain tensor, $\boldsymbol{S}$ represents the deviatoric stress tensor, q is the von Mises equivalent stress and f represents the volume void fraction. According to Nahshon (2008) the term $\boldsymbol{S}:\boldsymbol{\varepsilon}^{p}$ can be replaced by $\boldsymbol{\sigma}:\boldsymbol{\varepsilon}^{p}$, which represents the plastic work. Hence, Equation 5.21 can be re-written as:

$$\dot{D}_{shear} = k\, f\, \frac{\boldsymbol{\sigma}:\boldsymbol{\varepsilon}^{p}}{q} = k\, f\, \dot{\bar{\varepsilon}}^{p}\ , \tag{5.32}$$

where, the term $\dot{\bar{\varepsilon}}^{p}$ represents the equivalent plastic strain rate.

Thus, the rate of the damage variable (Equation 5.14) can be re-written according to Equation 5.33.

$$\dot{f} = \dot{f}^{n} + \dot{f}^{g} + \dot{D}_{shear}\,. \tag{5.33}$$

When either of shear mechanisms is introduced in the GTN original model in order to improve the ability to predict failure in dominant shear loading conditions, a so-called Lode angle function, which can assumes values $0 \leq g_0 \leq 1$

according to loading condition, needs to be introduced to generalize the shear damage evolution for arbitrary stress state. In predominant tensile load conditions, the function showed assumes a value equal to 0 and the shear mechanism is not active. However, when predominant shear load is presented, the function showed assumes a value equal to 1 or an intermediate value, allowing the activation of the mechanism. Thus, in Equations 5.26, 5.30 and 5.32 a Lode angle dependent function, which is represented by g_0 is also included.

5.2.3 Lode Angle Function

The shear damage evolutions, which were described for a pure shear loading condition in Section 5.2.2, need to be generalized for arbitrary stress states. This can be accomplished with the introduction of a Lode angle dependence function. The Lode angle, which is associated to the third invariant of the deviatoric stress tensor, is an essential parameter in the characterization of the effect of the stress state on ductile fracture (Kim *et al.*, 2003 and 2004; Bao and Wierzbicki, 2004; Gao *et al.*, 2005; Barsoum and Faleskog, 2007a and 2007b; Bai and Wierzbicki, 2008; Gao *et al.*, 2009). The Lode angle dependence function ranges between 0, for dominant tensile stress states, and 1, for shear dominant stress states. For intermediate values there is a combined stress state and the function should define the relative magnitude of each stress condition. The Lode angle dependence function proposed by Xue (2008) is defined by a linear expression of the normalized Lode angle, as:

$$g_0 = 1 - \left|\bar{\theta}\right|, \tag{5.34}$$

where g_0 represents the so-called Lode angle function and $\bar{\theta}$ is the normalized Lode angle (see Equation 3.7).

An alternative Lode angle dependence function as been proposed by Nahshon & Hutchinson (2008), which discriminates between uniaxial and biaxial tension and expresses a quadratic relation with the normalized third invariant:

$$g_0 = 1 - \xi^2. \tag{5.35}$$

where ξ represents the normalized third invariant (see Equation 3.5).

Expressions (5.34) and (5.35) can be used to activate the shear mechanisms,

described in Section 5.2.2, whenever shear effects are present. Figure 5.6 represents the shape of both functions with regard to the third invariant of the deviatoric stress tensor.

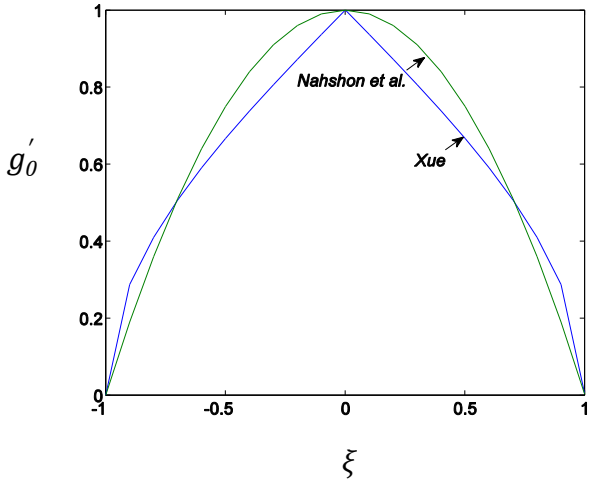

Figure 5.6. Evolution of the Lode angle functions, g_0, with regard to the normalized third invariant, ξ, proposed by Xue (2008) and by Nahshon & Hutchinson (2008).

The shear damage evolutions, expressed by Equations 5.26, 5.30 and 5.32, can be rephrased for arbitrary loading conditions as:

$$\dot{D}_{shear} = g_0\left(q_4 f^{q_5}\varepsilon_{eq}\dot{\varepsilon}_{eq}\right), \tag{5.36}$$

$$\dot{D}_{shear} = g_0\left[\frac{1}{\ln\sqrt{1/\chi}}\left(\frac{3\varepsilon_{eq}}{1+3{\varepsilon_{eq}}^2}\right)\dot{\varepsilon}_{eq}\right]. \tag{5.37}$$

$$\dot{D}_{shear} = g_0 k\, f\, \dot{\bar{\varepsilon}}^{p} \tag{5.38}$$

In Box 5.1, a summary of the GTN model extended with the shear mechanisms is presented. Details about how to determine the plastic flow rule and evolution equation for the internal variables can be found in Appendix "C".

Remark: In this study, the Xue shear damage evolution law (Equations 5.36) is redefined as a function of both equivalent plastic strain and its rate instead of the total strain and total strain rate.

Box 5.1. GTN model extended with shear mechanisms.

(i) Elasto-plastic split of the strain tensor : $\boldsymbol{\varepsilon} = \boldsymbol{\varepsilon}^e + \boldsymbol{\varepsilon}^p$

(ii) Elastic law : $\boldsymbol{\sigma} = \mathbf{D}^e : \boldsymbol{\varepsilon}^e$

(iii) Yield function : $\Phi(\boldsymbol{\sigma}, r, f) = J_2(\boldsymbol{S}) - \frac{1}{3}\left\{1 + q_3 f^2 - 2q_1 f \cosh\left(\frac{3q_2 p}{2\sigma_y}\right)\right\}{\sigma_y}^2$

(iv) Plastic flow and evolution equations for r and f

$$\dot{\boldsymbol{\varepsilon}}^p = \dot{\gamma}\left[\boldsymbol{S} + \frac{1}{3}q_1 q_2 f \sigma_y \sinh\left(\frac{3q_2 p}{2\sigma_y}\right)\boldsymbol{I}\right]$$

$$\dot{R} = \dot{\gamma}\frac{\left\{q_1 q_2 f p \sinh\left(\frac{3q_2 p}{2\sigma_y}\right) + \frac{2}{3}\left[1 + q_3 f^2 - 2q_1 f \cosh\left(\frac{3q_2 p}{2\sigma_y}\right)\right]\sigma_y\right\}}{(1-f)}$$

$$\dot{f} = \dot{f}^N + \dot{f}^G + \dot{D}_{shear}$$

$$= \frac{f_{\mathrm{N}}}{s_{\mathrm{N}}\sqrt{2\pi}}\exp\left[-\frac{1}{2}\left(\frac{\bar{\varepsilon}^p - \varepsilon_{\mathrm{N}}}{s_{\mathrm{N}}}\right)^2\right]\dot{\bar{\varepsilon}}^p + (1-f)\dot{\varepsilon}_v^p + \dot{D}_{shear}$$

where,

$$\dot{\bar{\varepsilon}}^p = \dot{\gamma}\sqrt{\frac{2}{3}\left\{\boldsymbol{S}:\boldsymbol{S} + \frac{1}{3}\left[q_1 q_2 f \sigma_y \sinh\left(\frac{3q_2 p}{2\sigma_y}\right)\right]^2\right\}}$$

$$\dot{\varepsilon}_v^p = \dot{\gamma} q_1 q_2 f \sigma_y \sinh\left(\frac{3q_2 p}{2\sigma_y}\right)$$

$$\dot{D}_{shear} = \begin{cases} q_4 f^{q_5} g_0 \bar{\varepsilon}^p \dot{\bar{\varepsilon}}^p, & for\ Xue's\ model \\ k f g_0 \dot{\bar{\varepsilon}}^p, & for\ Nahshon's\ model \end{cases}$$

$$g_0 = \begin{cases} 1 - |\bar{\theta}|, & for\ Xue's\ model \\ 1 - \xi^2, & for\ Nahshon's\ model \end{cases}$$

(v) Loading/unloading criterion

$$\dot{\gamma} \geq 0\,, \qquad \Phi \leq 0\,, \qquad \dot{\gamma}\Phi = 0.$$

5.3 NUMERICAL INTEGRATION ALGORITHM

The constitutive equations of the GTN original model extended with the shear mechanisms, described in section 5.2 were integrated using an implicit solution based on the operator split methodology (see Simo & Hughes, 1998; De Souza Neto *et al*., 2008). This method consists of splitting the problem in two parts: an elastic

predictor, where the problem is assumed to be elastic and, a plastic corrector, in which the system of residual equations comprising the elasticity law, plastic consistency and the rate equations is solved, taking the results of the elastic predictor stage as initial conditions. Straightforward (pseudo)-time discretization of the constitutive equations for the plastic regime, which are listed in Box 5.1, leads to the following system of non-linear residual equations:

$$\begin{cases} Res_{\Delta\gamma} = \dfrac{J_{2_{n+1}}^{trial}}{[1+2G\Delta\gamma]^2} - \dfrac{1}{3}\left[1 + {q_3 f_{n+1}}^2 - 2q_1 f_{n+1}\cosh\left(\dfrac{3q_2 p_{n+1}}{2\sigma_y}\right)\right]\sigma_y^2 = 0 \\ Res_p = p_{n+1} - p_{n+1}^{trial} + \Delta\gamma K\sigma_y q_1 q_2 f_{n+1}\sinh\left(\dfrac{3q_2 p_{n+1}}{2\sigma_y}\right) = 0 \\ Res_f = f_{n+1} - f_{n+1}^{trial} - \dfrac{f_N}{S_N\sqrt{2\pi}}\exp\left[-\dfrac{1}{2}\left(\dfrac{\bar{\varepsilon}_{n+1}^p - \varepsilon_N}{S_N}\right)^2\right]\Delta\bar{\varepsilon}^p - \Delta f^g - \Delta D_{shear} = 0 \\ Res_R = R_{n+1} - R_{n+1}^{trial} - \Delta R = 0 \end{cases} \tag{5.39}$$

which needs to be solved for $\Delta\gamma$, p_{n+1}, f_{n+1} and R_{n+1}. In the previous system of residual equations, the terms K and G represent, respectively, the bulk and shear modulus. The terms Δf^g, ΔD_{shear} and ΔR are defined according to:

$$\Delta f^g = (1 - f_{n+1})\Delta\gamma\sigma_y q_1 q_2 f_{n+1}\sinh\left(\frac{3q_2 p_{n+1}}{2\sigma_y}\right) \ , \tag{5.40}$$

$$\Delta D_{shear} = \begin{cases} q_4\, {f_{n+1}}^{q_5}\left(1 - \left|\bar{\theta}_{n+1}\right|\right)\ \bar{\varepsilon}_{n+1}^p\ \Delta\bar{\varepsilon}^p, & for\ Xue's\ model \\ k\, f_{n+1}\left(1 - {\xi_{n+1}}^2\right)\Delta\bar{\varepsilon}^p, & for\ Nahshon's\ model \end{cases} \tag{5.41}$$

$$\Delta R = \frac{\Delta\gamma}{(1 - f_{n+1})}\left\{q_1 q_2 f_{n+1} p_{n+1}\sinh\left(\frac{3q_2 p_{n+1}}{2\sigma_y}\right) + \frac{2}{3}\sigma_y\left[1 + {q_3 f_{n+1}}^2 - 2q_1 f_{n+1}\cosh\left(\frac{3q_2 p_{n+1}}{2\sigma_y}\right)\right]\right\} . \tag{5.42}$$

Here, when the yield condition has been violated, the plastic corrector stage is initiated and the Newton- Raphson procedure is used to solve the non-linear residual system of equations. The Newton-Raphson procedure was chosen motivated by the quadratic rates of convergence achieved, which results in return mapping procedures computationally efficient (see Simo & Hughes, 1998; De Souza Neto *et al*., 2008). The residual system of equations in the linearized form

can be expressed by:

$$\begin{bmatrix} \frac{\partial Res_{\Delta\gamma}}{\partial \Delta\gamma} & \frac{\partial Res_{\Delta\gamma}}{\partial p_{n+1}} & \frac{\partial Res_{\Delta\gamma}}{\partial f_{n+1}} & \frac{\partial Res_{\Delta\gamma}}{\partial R_{n+1}} \\ \frac{\partial Res_{p}}{\partial \Delta\gamma} & \frac{\partial Res_{p}}{\partial p_{n+1}} & \frac{\partial Res_{p}}{\partial f_{n+1}} & \frac{\partial Res_{p}}{\partial R_{n+1}} \\ \frac{\partial Res_{f}}{\partial \Delta\gamma} & \frac{\partial Res_{f}}{\partial p_{n+1}} & \frac{\partial Res_{f}}{\partial f_{n+1}} & \frac{\partial Res_{f}}{\partial R_{n+1}} \\ \frac{\partial Res_{R}}{\partial \Delta\gamma} & \frac{\partial Res_{R}}{\partial p_{n+1}} & \frac{\partial Res_{R}}{\partial f_{n+1}} & \frac{\partial v_{R}}{\partial R_{n+1}} \end{bmatrix}^{k} \begin{bmatrix} \delta\Delta\gamma \\ \delta p_{n+1} \\ \delta f_{n+1} \\ \delta R_{n+1} \end{bmatrix}^{k+1} = -\begin{bmatrix} Res_{\Delta\gamma}(\Delta\gamma, p, f, R) \\ Res_{p}(\Delta\gamma, p, f, R) \\ Res_{f}(\Delta\gamma, p, f, R) \\ Res_{R}(\Delta\gamma, p, f, R) \end{bmatrix}^{k} \quad (5.43)$$

where, the terms $\partial Res_*/(*)$ represent the derivative of each residual equation with regard to the variables of the problem. Details about the determination of these derivatives can be found in Appendix "D". The overall algorithm for numerical integration is summarized in Box 5. 2.

Box 5.2. Fully implicit Elastic predictor/Return mapping algorithm for the GTN model extended with shear mechanisms.

(i) Evaluate the elastic trial state: Given the incremental strain $\Delta\varepsilon$ and the state variables at t_n:

$$\boldsymbol{\varepsilon}_{n+1}^{e\,trial} = \boldsymbol{\varepsilon}_n^e + \Delta\boldsymbol{\varepsilon} \quad ; \quad \bar{\varepsilon}_{n+1}^{p\,trial} = \bar{\varepsilon}_n^p \quad ; \quad R_{n+1}^{trial} = R_n$$

$$f_{n+1}^{trial} = f_n \quad ; \quad \boldsymbol{S}_{n+1}^{trial} = 2G\boldsymbol{\varepsilon}_{n+1}^{e\,trial} \quad ; \quad p_{n+1}^{trial} = K\varepsilon_{v\,n+1}^{e\,trial}$$

(ii) Check plastic admissibility:

IF $\Phi^{trial} = J_2^{trial} - \frac{1}{3}\left[1 + q_3 {f_{n+1}^{trial}}^2 - 2q_1 f_{n+1}^{trial} \cosh\left(\frac{3q_2 p_{n+1}^{trial}}{2\sigma_y^{trial}}\right)\right]\left(\sigma_y^{trial}\right)^2 \leq 0$ THEN

set $(\cdot)_{n+1} = (\cdot)_{n+1}^{trial}$ ***(elastic step)*** and go to *(v)*

ELSE go to (iii)

(iii) Return mapping ***(plastic step)***: *Solve the system of equations below for* $\Delta\gamma$,p_{n+1},f_{n+1} and R_{n+1}, *using Newton-Raphson method.*

$$\begin{Bmatrix} \frac{J_{2\,n+1}^{trial}}{[1+2G\Delta\gamma]^2} - \frac{1}{3}\left[1 + q_3 {f_{n+1}}^2 - 2q_1 f_{n+1}\cosh\left(\frac{3q_2 p_{n+1}}{2\sigma_y}\right)\right]\sigma_y^2 \\ p_{n+1} - p_{n+1}^{trial} + \Delta\gamma K\sigma_y q_1 q_2 f_{n+1}\sinh\left(\frac{3q_2 p_{n+1}}{2\sigma_y}\right) \\ f_{n+1} - f_{n+1}^{trial} - \frac{f_N}{S_N\sqrt{2\pi}}\exp\left[-\frac{1}{2}\left(\frac{\bar{\varepsilon}_{n+1}^p - \varepsilon_N}{S_N}\right)^2\right]\Delta\bar{\varepsilon}^p - \Delta f^g - \Delta D_{shear} \\ R_{n+1} - R_{n+1}^{trial} - \Delta R \end{Bmatrix} = \begin{Bmatrix} 0 \\ 0 \\ 0 \\ 0 \\ 0 \end{Bmatrix}$$

Continue Box 5.2.

where,

$$\Delta f^{g} = (1 - f_{n+1})\Delta\gamma\sigma_y q_1 q_2 f_{n+1} \sinh\left(\frac{3q_2 p_{n+1}}{2\sigma_y}\right)$$

$$\Delta D_{shear} = \begin{cases} q_4\, {f_{n+1}}^{q_5} \left(1 - \left|\bar{\theta}_{n+1}\right|\right)\, \bar{\varepsilon}^{p}_{n+1}\, \Delta\bar{\varepsilon}^{p}, & for\ Xue \\ k\, f_{n+1} \left(1 - {\xi_{n+1}}^{2}\right) \Delta\bar{\varepsilon}^{p}, & for\ Nahshon \end{cases}$$

$$\Delta R = \frac{\Delta\gamma}{(1 - f_{n+1})} \left\{ q_1 q_2 f_{n+1} p_{n+1} \sinh\left(\frac{3q_2 p_{n+1}}{2\sigma_y}\right) + \frac{2}{3}\sigma_y \left[1 + {q_3 f_{n+1}}^{2} - 2q_1 f_{n+1} \cosh\left(\frac{3q_2 p_{n+1}}{2\sigma_y}\right)\right]\right\}$$

(iv) Update the others state variables:

$$\boldsymbol{\varepsilon}^{e}_{n+1} = \boldsymbol{\varepsilon}^{e\,trial}_{n+1} - \Delta\gamma \left[\frac{\boldsymbol{S}^{trial}_{n+1}}{1 + 2G\Delta\gamma} + \frac{1}{3}\sigma_y q_1 q_2 f_{n+1} \sinh\left(\frac{3q_2 p_{n+1}}{2\sigma_y}\right)\boldsymbol{I}\right]$$

$$\boldsymbol{S}_{n+1} = \frac{\boldsymbol{S}^{trial}_{n+1}}{1 + 2G\Delta\gamma}$$

$$\bar{\varepsilon}^{p}_{n+1} = \bar{\varepsilon}^{p\,trial}_{n+1} + \Delta\gamma \sqrt{\frac{2}{3}\left\{\frac{\boldsymbol{S}^{trial}_{n+1} : \boldsymbol{S}^{trial}_{n+1}}{[1 + 2G\Delta\gamma]^2} + \frac{1}{3}\left[\sigma_y q_1 q_2 f_{n+1} \sinh\left(\frac{3q_2 p_{n+1}}{2\sigma_y}\right)\right]^2\right\}}$$

(v) Exit

5.3.1 The consistent tangent operator

Under the elastic loading condition, the tangent operator for this constitutive formulation is the standard linear elasticity tensor. Nevertheless, for the plastic step, the elasto-plastic tangent operator is obtained by the linearization procedure of the above system of residual equations. Hence, the first step for determining the operator is to differentiate the stress tensor updated expression:

$$\boldsymbol{\sigma}_{n+1} = \frac{\boldsymbol{S}_{n+1}^{trial}}{[1 + 2G\Delta\gamma]} + p_{n+1}\,\boldsymbol{I}\ . \tag{5.44}$$

After some algebraic manipulation, the above equation can be re-written in its differentiate form as:

$$\mathrm{d}\boldsymbol{\sigma}_{n+1} = \frac{2G}{[1 + 2G\Delta\gamma]}\mathrm{d}\boldsymbol{\varepsilon}_{d\,n+1}^{e\,trial} - \left\{\frac{2G}{[1 + 2G\Delta\gamma]}\right\}^{2} \boldsymbol{\varepsilon}_{d\,n+1}^{e\,trial}\mathrm{d}\Delta\gamma + \mathrm{d}p_{n+1}\boldsymbol{I}\ . \tag{5.45}$$

The terms $\mathrm{d}\Delta\gamma$ and $\mathrm{d}p_{n+1}$ can be obtained by the linearization procedure of the residual system of equations. After some algebraic manipulation, the term $\mathrm{d}\Delta\gamma$ and $\mathrm{d}p_{n+1}$ can be expressed by:

$$\begin{aligned}
\mathrm{d}\Delta\gamma &= -C_{1,1}\,\frac{\partial r_{\Delta\gamma}}{\partial \boldsymbol{\varepsilon}_{d\,n+1}^{e\,trial}} - C_{1,2}\,\frac{\partial r_p}{\partial \boldsymbol{\varepsilon}_{v\,n+1}^{e\,trial}} - C_{1,3}\,\frac{\partial r_f}{\partial \boldsymbol{\varepsilon}_{d\,n+1}^{e\,trial}}, \\
\mathrm{d}p_{n+1} &= -C_{2,1}\,\frac{\partial r_{\Delta\gamma}}{\partial \boldsymbol{\varepsilon}_{d\,n+1}^{e\,trial}} - C_{2,2}\,\frac{\partial r_p}{\partial \boldsymbol{\varepsilon}_{v\,n+1}^{e\,trial}} - C_{2,3}\,\frac{\partial r_f}{\partial \boldsymbol{\varepsilon}_{d\,n+1}^{e\,trial}},
\end{aligned} \tag{5.46}$$

where, the terms $C_{i,j}$ belong to the **C** matrix, which is the matrix obtained by inverting the linearized system of residual equations in order to each variable of the problem. Finally, the elasto-plastic operator is determined by:

$$\mathbb{D}^{ep} = \frac{\mathrm{d}\boldsymbol{\sigma}_{n+1}}{\mathrm{d}\boldsymbol{\varepsilon}_{n+1}^{e\,trial}}\ . \tag{5.47}$$

5.4 CALIBRATION PROCEDURE

Regarding the determination of the material parameters for the GTN original model and the GTN model improved with shear mechanisms, two different calibration points are investigated. The material parameters obtained with the first calibration point are used to perform a comparative study between Xue's (2008) and Nahshon's (2008) shear mechanisms. In particular, the ability to predict the correct displacement and equivalent plastic strain at fracture as well as the correct potential location to crack formation. In addition, a second calibration point is used in order to assess the influence of the calibration point in the predictive ability of the coupled damage models.

The conventional cylindrical smooth bar specimen subjected to a tensile loading condition is used for the first calibration point and a butterfly specimen under a pure shear loading condition, is employed for the second calibration point. In both cases, the hardening law, $\sigma_y(R)$, for the undamaged material is determined as well as the set of parameters required for the nucleation of micro voids $[f_N, S_N, \varepsilon_N]$ and the critical value for the damage variable, f_c. Experimental data for a steel 1045 is used in both tensile and pure shear calibration conditions. Based on an inverse method and optimisation procedure, the material parameters are identified and used in the following simulations.

5.4.1 Inverse method for parameter identification

In this section, the procedure used for parameter identification is described based on a simple optimisation algorithm. The method starts from the definition of an objective function that can be expressed by:

$$S(b_j) = \sqrt{\frac{1}{N}\sum_{i=1}^{N}\left(\frac{F_{0,i}^{MEF}(b_j) - F_i^{exp}}{F_i^{exp}}\right)^2}\ , \tag{5.48}$$

where b_j is the vector of variables of the problem, N represents the number of experimental points, F_i^{exp} is the value of the experimental point, F_i^{MEF} is the value of the numerical point, F_0^{MEF} is the value of the numerical point determined by linear interpolation for a specific displacement. The optimisation procedure forces the numerical solution to be, as close as possible to the experimental results. In other words, the difference between numerical and experimental curves, which is measured by the objective function, is given by the sum of the differences between numerical and experimental forces to the square. During the parameter identification procedure, it is expected that the objective function, $S(b_j)$, is equal to zero, which means that the numerical curve is equal to the experimental curve. However, in practical situations, this ideal condition is never reached and a value very small for $S(b_j)$ is expected. Figure 5.7 represents the difference between experimental and numerical data for an optimisation procedure.

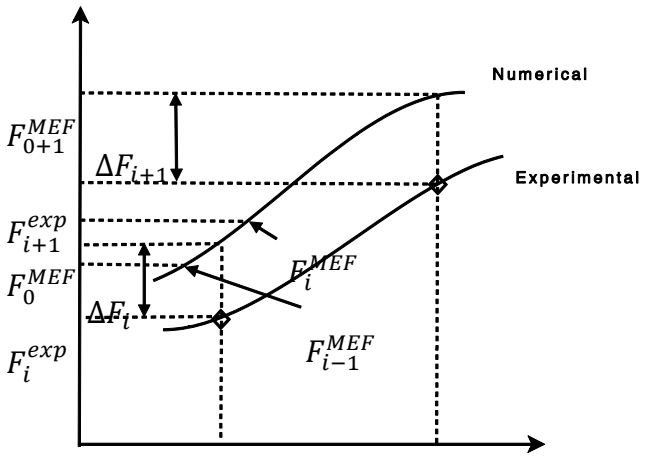

Figure 5.7. Optimisation procedure and difference between numerical and experimental data. Adapted from Trentin (2009).

In a general approach, it is necessary to assign upper and lower values for the variables of the problem, where the optimisation procedure could be presented as:

$$\begin{cases} S(b_j) = \min\left[\sqrt{\frac{1}{N}\sum_{i=1}^{N}\left(\frac{F_{0,i}^{MEF}(b_j) - F_i^{exp}}{F_i^{exp}}\right)^2}\right] \\ where, b_{low} \leq b \leq b_{up} \end{cases}. \quad (5.49)$$

In order to minimize the objective function, which is established for the two specimens under scrutiny, an optimization algorithm based on sequential quadratic programming is used (see Schittkowski, 2001). The method requires the determination of the derivative of objective function, with regard to the variable of the problem, to be used in the sensitivity analysis. Equation (5.50) was used for calculating the sensitivity matrix.

$$\frac{dS}{db_j} = \frac{1}{2}\left[\frac{1}{N}\sum_{i=1}^{N}\left(\frac{F_i^{MEF}(b_j) - F_i^{exp}}{F_i^{exp}}\right)^2\right]^{-1/2} \frac{1}{N}\sum_{i=1}^{N} 2\left(\frac{F_i^{MEF}(b_j) - F_i^{exp}}{F_i^{exp}}\right)\frac{1}{F_i^{exp}}\frac{dF_i^{MEF}}{db_j}, \quad (5.50)$$

where, the term $\frac{dF_i^{MEF}}{db_j}$ is determined with the finite difference method. In this approach, the vector b_j, which represents the set of unknowns variables of the problem, is composed by the set of parameters $\{f_N, S_N, \varepsilon_N, \sigma_y\}$, where σ_y represents the hardening law which is defined by $\sigma_y(R) = \sigma_{y0} + \alpha_1 \exp(-\alpha_2 R)$.

5.4.2 Geometry and mesh definition

In order to identify the material properties for the first calibration point, a *classical smooth bar specimen* is used and Figure 5.8a presents the dimensions employed. In order to trigger necking, a dimensional reduction of 5% in the central diameter of the specimen is used. Besides that, based on the experimental data, a gauge section of 20.6 mm is also used. The standard eight-noded axsymmetric quadrilateral element, with four Gauss integration points, is adopted. The initial mesh discretization is illustrated in Figure 5.8b, where only one symmetric quarter of the problem, with the appropriate symmetric boundary conditions imposed to the relevant edges, is modelled. A total number of 1800 elements have been used in the discretization of the smooth specimen, amounting to a total of 5581 nodes.

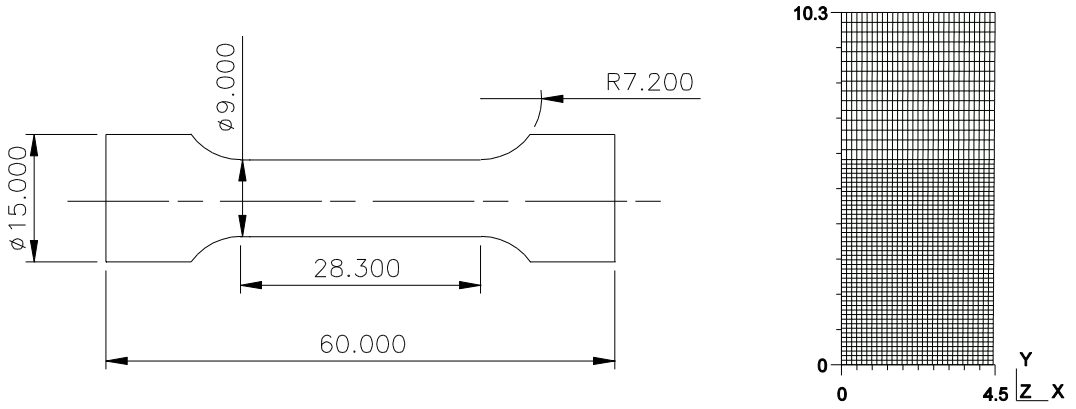

(a) (b)

Figure 5.8. (a) The geometry for the smooth bar specimen (dimension in mm). Reproduced from Teng (2008). (b) Finite element mesh, regarding the gauge section.

For the second calibration point and for all numerical tests that will be presented to assess the influence of the calibration point, on the predictive ability of the constitutive models, a *butterfly specimen* is used. The specimen was initially designed by Bai (2008) and the geometry and general dimensions can be verified in Figure 5.9. In this case, a three dimensional finite element mesh of 3.392 twenty noded elements, with eight Gauss integration points, is used amounting to 17.465 nodes is employed.

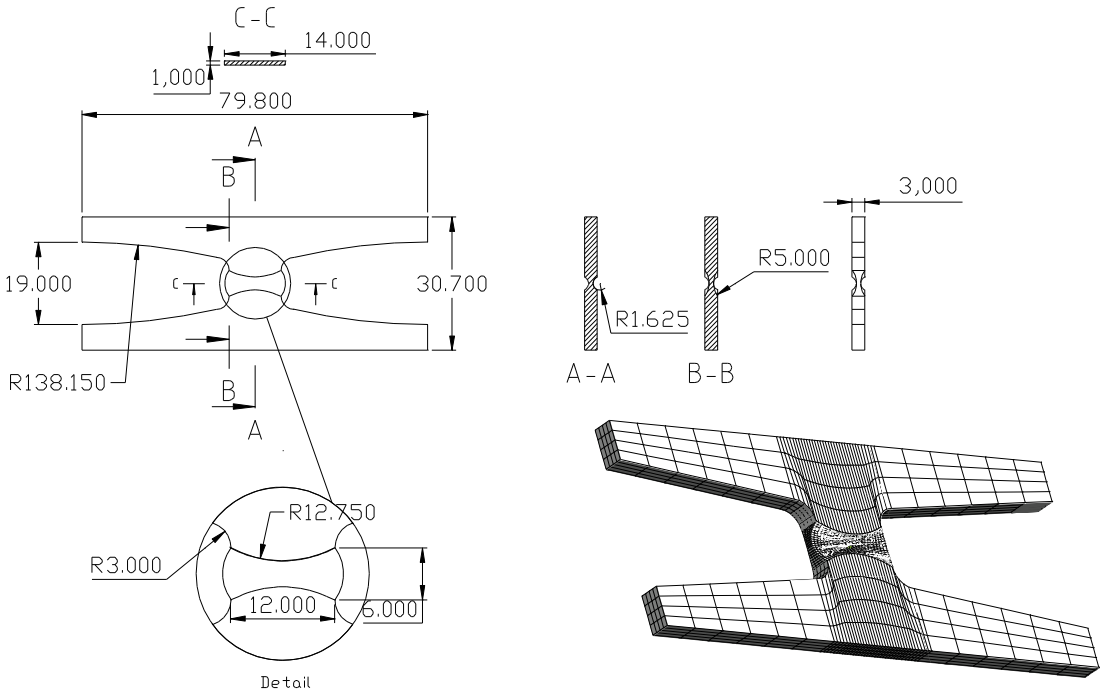

(a) (b)

Figure 5.9. (a) The geometry for butterfly specimen (Dimensions in mm). Reproduced from Bai (2008). (b) Finite elements mesh for the butterfly specimen.

5.4.3 First Calibration Point: smooth bar specimen (tensile loading test)

In the present section, the hardening law, $\sigma_y(R)$, for the undamaged material is determined as well as the set of parameters for the nucleation of micro voids $\{f_N, S_N, \varepsilon_N\}$ and the critical value for the damage variable, f_c. By performing the numerical simulation of experimental tests conducted by Bai 2008, the reaction *versus* displacement curve is determined as well as the stress-strain curve for an elasto-plastic model of von Mises type. The inverse method, described in the previous sections, is adopted in order to identify the material parameters for the coupled damage model by forcing the numerical solution to be, as close as possible to the experimental results. Figure 5.10a shows the reaction curve obtained for the model after the application of the inverse method. A good agreement between the experimental and numerical results can be observed. Furthermore, the critical volume void fraction is also determined from the numerical simulation at the point where the model attains the displacement to fracture, experimentally observed (see Figure 5.10b). The critical value obtained is $f_c = 0.076$.

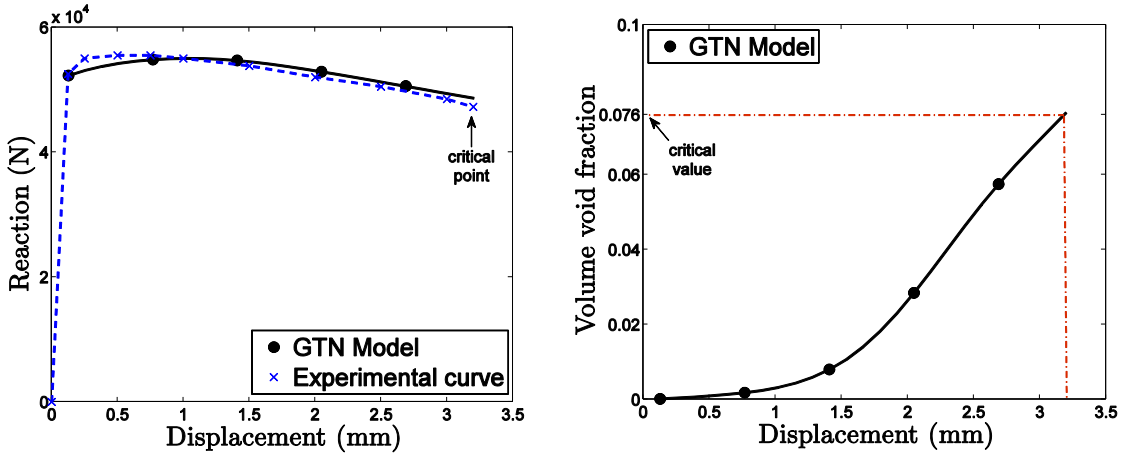

Figure 5.10. (a) Reaction curve. (b) Critical volume void fraction parameter.

The results of the calibration procedure, in terms of stress-strain curve, can also be observed in Figure 5.11, where the curves, for uncoupled and coupled damage models, were presented.

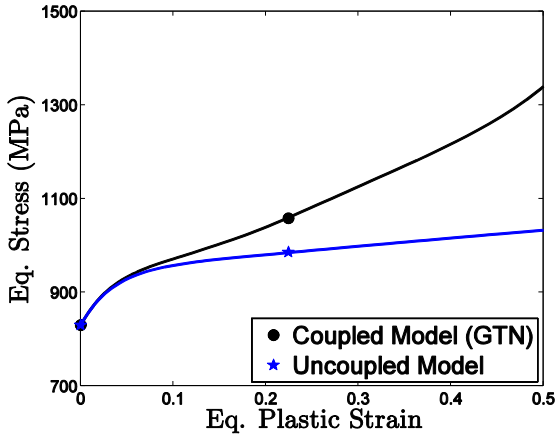

Figure 5.11. Stress-strain curves determined for an uncoupled and coupled models.

The material properties and other parameters related to the micro void nucleation mechanism obtained by employing an inverse method are listed in Table 5. 1:

Table 5.1. Materials properties and parameters related to the nucleation of micro-void mechanism, for steel 1045. Based on the first calibration point.

Material	f_N	S_N	ε_N	q_1	q_2	q_3	f_c	E (MPa)	υ
GTN	*0.05*	*0.2*	*0.1*	*1.5*	*1.0*	*2.25*	*0.076*	*220.000*	*0.33*

5.4.4 Second Calibration Point: butterfly specimen (shear loading test)

In this calibration point, also the hardening law, $\sigma_y(R)$, for the undamaged model is determined as well as the set of parameters for nucleation of micro void mechanism $\{f_N, S_N, \varepsilon_N\}$ and the critical value for the damage variable, f_c. The butterfly specimen is used here under a pure shear loading condition and the displacement to fracture was experimental determined by Bai (2008). The inverse method described in section 5.4.1 is also adopted, for the identification of the parameters by forcing the numerical results to be as close as possible to the experimental data. A critical damage value is obtained from the simulation, when the numerical displacement matches the experimental one for each shear mechanism and the results obtained for the second calibration can be observed in Figure 5.12.

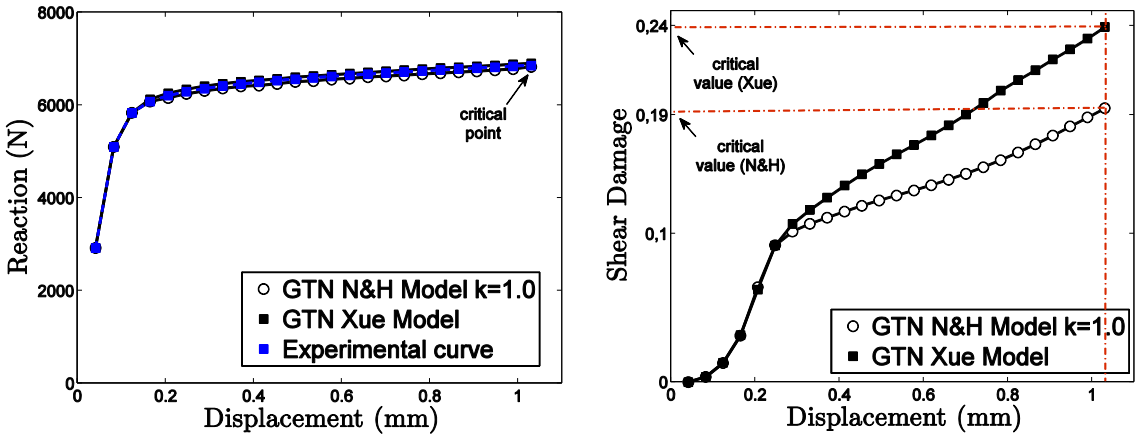

Figure 5.12. (a) Reaction *versus* displacement curve. (b) Shear damage parameter.

The results of the calibration procedure for the stress-strain curve can also be observed in Figure 5.13, for the uncoupled and coupled damage models. The material parameters related to the micro void nucleation mechanism can be found in Table 5.2.

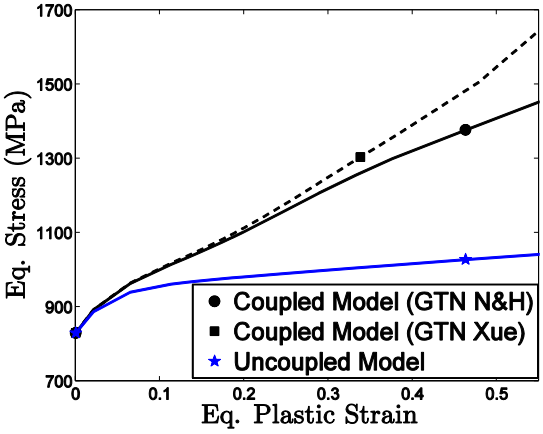

Figure 5.13. Stress-strain curves determined for the uncoupled and coupled models.

Table 5.2. Material parameters related to the nucleation of micro-voids mechanism, for the steel 1045. Based on the second calibration point.

Material	f_N	S_N	ε_N	q_1	q_2	q_3	f_c	E (MPa)	υ
N&H	*0.10*	*0.15*	*0.1*	*1.5*	*1.0*	*2.25*	*0.19*	*220.000*	*0.33*
Xue	*0.10*	*0.15*	*0.1*	*1.5*	*1.0*	*2.25*	*0.24*	*220.000*	*0.33*

5.5 NUMERICAL RESULTS

In this section, numerical simulations are carried out in order to assess the predictive ability of the GTN improved models, with regard to the determination of fracture onset, the correct displacement and the level of equivalent plastic strain at fracture. Therefore, both improved models are tested with the material parameters determined by the first and second calibration points (see Table 5.1 and 5.2).

The numerical results were conducted following the same strategy. The simulation was performed until the damage variable of the improved GTN models, at any point in the specimen reaches the critical value listed in Table 5.1 and 5.2. Several numerical simulations with different loading conditions are conducted: pure shear, pure tensile and a combination of shear/tensile loading with an angle of prescribed displacement equal to 10°, 22° and 30°. The value of some parameters, such as, the equivalent plastic strain and displacement at fracture as well as the ability to predict the correct site to crack initiation are evaluated for

each calibration point. Tables 5.3 and 5.4 list the numerical results obtained after the numerical simulations for both calibration points.

Table 5.3. Numerical results for butterfly specimen. Based on the first calibration point.

Angle	Experimental data		Numerical results					
	u_f	$\bar{\varepsilon}_f{}^*$		k	u_f	$\bar{\varepsilon}^p$	η_0	θ_0
0°	*1.03*	*0.860*	*N&H*	*1.0*	*1.03*	*0.57*	*0.00*	*0.00*
			Xue	*---*	*0.37*	*0.32*	*0.00*	*0.00*
10°	*0.421*	*0.355*	*N&H*	*1.0*	*0.60*	*0.47*	*0.12*	*0.23*
			Xue	*---*	*0.37*	*0.35*	*0.11*	*0.33*
22°	*0,287*	*0.276*	*N&H*	*1.0*	*0.36*	*0.37*	*0.25*	*0.45*
			Xue	*---*	*0.36*	*0.37*	*0.25*	*0.49*
30°	*0,219*	*0.235*	*N&H*	*1.0*	*0.27*	*0.33*	*0.33*	*0.65*
			Xue	*---*	*0.26*	*0.30*	*0.33*	*0.65*
90°	*0,101*	*0.156*	*N&H*	*1.0*	*0.12*	*0.28*	*0.61*	*0.75*
			Xue	*---*	*0.11*	*0.25*	*0.61*	*0.75*

Table 5.4. Numerical results for butterfly specimen. Based on the second calibration point.

Angle	Experimental data		Numerical results					
	u_f	$\bar{\varepsilon}_f{}^*$		k	u_f	$\bar{\varepsilon}^p$	η_0	θ_0
0°	*1.03*	*0.860*	*N&H*	*1.0*	*1.03*	*0.75*	*0.00*	*0.00*
			Xue	*---*	*1.03*	*0.60*	*0.00*	*0.00*
10°	*0.421*	*0.355*	*N&H*	*1.0*	*0.46*	*0.51*	*0.12*	*0.23*
			Xue	*---*	*1.00*	*0.70*	*0.11*	*0.33*
22°	*0.287*	*0.276*	*N&H*	*1.0*	*0.32*	*0.42*	*0.25*	*0.49*
			Xue	*---*	*0.39*	*0.53*	*0.25*	*0.49*
30°	*0.219*	*0.235*	*N&H*	*1.0*	*0.24*	*0.36*	*0.33*	*0.65*
			Xue	*---*	*0.27*	*0.45*	*0.33*	*0.65*
90°	*0.101*	*0.156*	*N&H*	*1.0*	*0.11*	*0.30*	*0.61*	*0.75*
			Xue	*---*	*0.12*	*0.35*	*0.61*	*0.75*

** Reference value of the equivalent strain at fracture, which was obtained using a combined experimental/numerical method with the von Mises model (Bai, 2008).*

5.5.1 Equivalent plastic strain at fracture

In order to discuss the values obtained by each model for the equivalent strain at fracture, in this section, the numerical results determined for this parameter are compared with the fracture criteria proposed by Bai & Wierzbicki (2008). The criteria can be geometrically represented by a three dimensional fracture surface, which defines the boundary between the fracture and no-fracture zone, on the space of equivalent plastic strain *versus* stress triaxiality average and Lode angle. This surface, which is based on boundary limit curves, requires the determination of six parameters that need to be calibrated for each specific material. The three dimensional fracture locus for the 1045 steel has been obtained by Bai and Wierzbicki (2008) that employed the material fracture data points obtained by Bao (2003) to interpolate the surface. This surface can be mathematically represented by the following expression, calibrated by butterfly specimens, (Bai and Wierzbicki, 2008):

$$\hat{\varepsilon}_f\left(\eta,\overline{\theta}\right) = \left[\frac{1}{2}\left(0.7121\,\mathrm{e}^{-1.6968\,\eta} + 0.7121\,\mathrm{e}^{-1.6968\,\eta}\right) - 0.5187\,\mathrm{e}^{-1.9454\,\eta}\right]\overline{\theta}^{2} + \frac{1}{2}\left(0.7121\,\mathrm{e}^{-1.6968\,\eta} - 0.7121\,\mathrm{e}^{-1.6968\,\eta}\right)\overline{\theta} + 0.5187\,\mathrm{e}^{-1.9454\,\eta}. \quad (5.51)$$

The numerical results obtained with both shear mechanisms can be represented in this three dimensional space of equivalent plastic strain *versus* stress triaxiality average and Lode angle. Nevertheless, for the sake of clarity, we will represent the surface by its projections, for different values of the normalized Lode angle, on the space of equivalent plastic strain *versus* stress triaxiality. In Figure 5.14, three projections of the surface that correspond to normalized Lode angle values of 0.0, 0.5 and 1.0 are depicted together with the numerical results, obtained for the first and second calibration points.

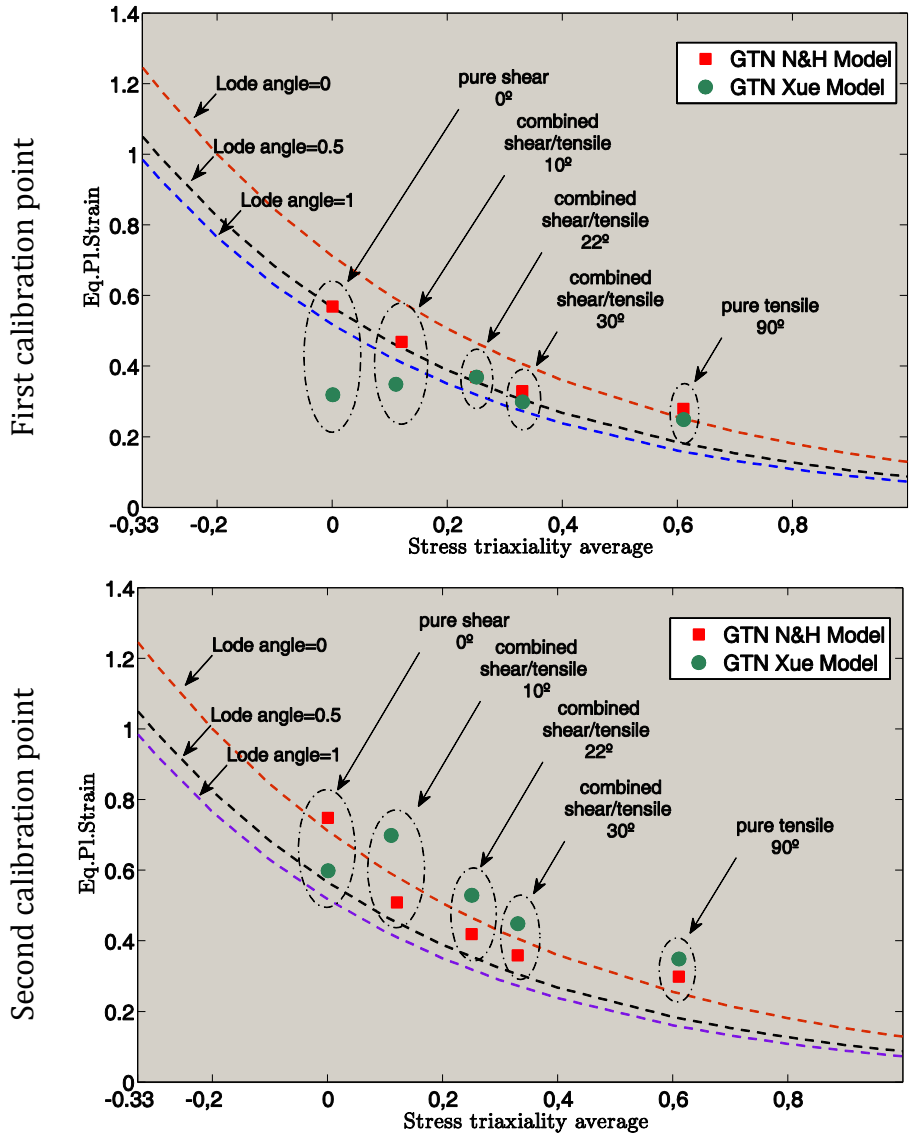

Figure 5.14. Fracture locus for a 1045 steel on the space of equivalent plastic strain *versus* stress triaxiality average.

Based on these results, it can be concluded that the numerical results obtained with the second calibration point agree better with Bai *et al.* (2008) fracture locus than the numerical results obtained with the first calibration point.

5.5.2 Evolution of damage parameter

In this section, the numerical results for the damage evolution are presented and discussed. The butterfly specimen was simulated for several loading conditions until the damage variable, at any critical point of the specimen, reached

the critical value. The numerically predicted displacements are listed in Table 5.5 against the experimentally observed ones for the material properties determined from the first calibration point (see Table 5.1). In Figure 5.15, the evolution of damage (volume void fraction) at the critical point, which may be different for each model, is depicted for each loading condition. The following comments can be made: Under pure shear, the GTN model with Xue's shear mechanism behaves very conservatively, reaching the critical damage value for a small displacement, around 178% less than what is experimentally observed. On the other hand, for the GTN model with N&H shear mechanism under the same loading condition, the critical value was reached for a displacement very similar to the experimental data. For a combination shear/tensile of 10 degree, different critical damage points for both shear mechanisms were verified. The surface of the critical zone was indicated by Xue and the centre of the thickness by N&H (see Figure 5.17). According to the evolution of the damage parameter, regarding these critical points, Xue has predicted the beginning of failure for a displacement 14% less than the experimental data and N&H for a displacement 30% higher (see Figure 5.15). For the other two combinations of loading conditions studied (22° and 30°), both shear mechanisms have reached the critical damage for displacements around the same value and both are higher that the experimentally observed. Under a pure tensile loading (90°), Xue shear mechanism behaves more accurate than N&H mechanism.

Table 5.5. Error between experimental and numerical displacement at fracture. Material properties determined from the first calibration point.

Loading condition	u_f experimental	u_f numerical		Error %	
		N&H	Xue	N&H	Xue
0°	1.03	1.03	0.37	0	-178
10°	0.421	0.60	0.37	30	-14
22°	0.287	0.36	0.36	20	20
30°	0.219	0.27	0.26	19	16
90°	0.101	0.12	0.11	16	8

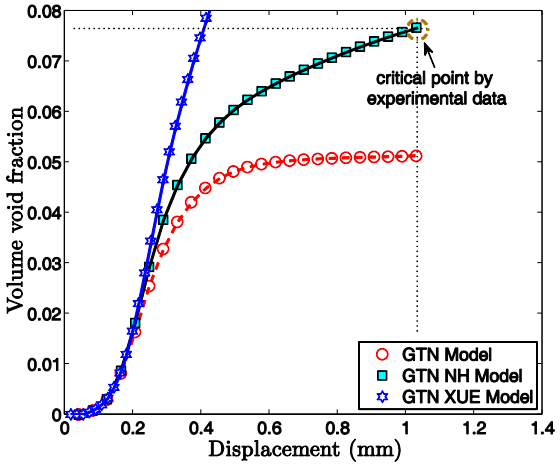

Pure shear 0°

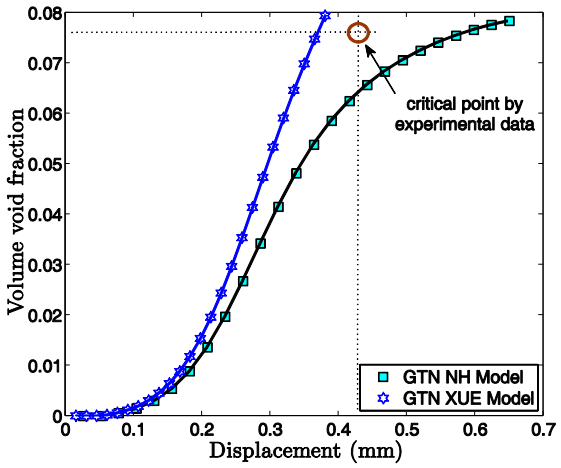

Combined shear/tensile 10°

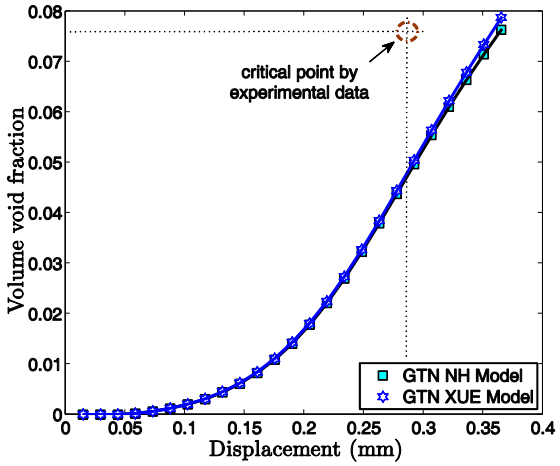

Combined shear/tensile 22°

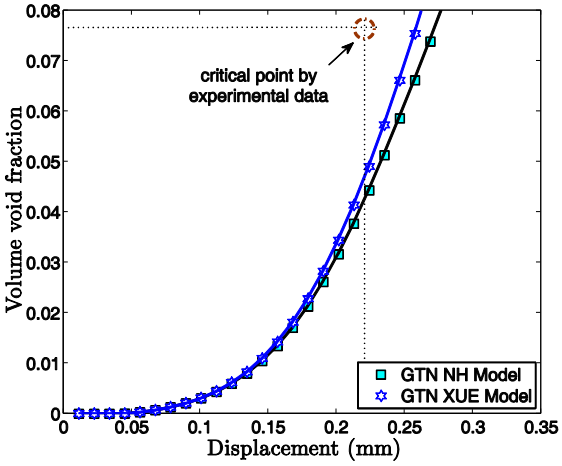

Combined shear/tensile 30°

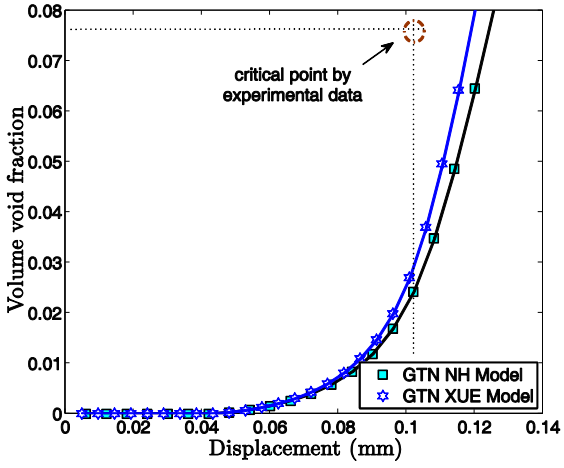

Pure tensile 90°

Figure 5.15. Evolution of the damage parameter. Based on the first calibration point.

Following a similar approach, we will now assess the predictive ability of both models, using the material properties obtained from the second calibration point. Focus will be placed on the evolution of damage and predicted displacement at fracture. For a loading combination of shear/tensile with an angle of 10°, it was found that different critical points are predicted by each shear mechanism. Xue's shear mechanism indicates the surface and N&H 's shear mechanism indicates the centre of the specimen (see Figure 5.18). Xue's shear mechanism, in this loading scenario, behaves very poorly, with a 58% of error in the predicted displacement at fracture.

For the other loading conditions, N&H's shear mechanism has indicated the displacement at fracture very similar to the experimental observation. Table 5.6 presents the values of displacement at fracture predicted by both shear mechanism, and the experimental data.

Table 5.6. Error between experimental and numerical displacement at fracture. Regarding the second calibration point.

Loading condition	u_f experimental	u_f numerical		Error %	
		N&H	Xue	N&H	Xue
0°	1.03	1.03	1.03	0	0
10°	0.421	0.46	1.00	8	58
22°	0.287	0.32	0.39	10	26
30°	0.219	0.24	0.27	9	19
90°	0.101	0.11	0.12	8	16

Figure 5.16 presents the evolution of both damage models, until they reach the critical value. Based on the above numerical results, it can be concluded that the N&H's shear mechanism has presented the best agreement with experimental results when the material properties are obtained from the second calibration point. For this calibration point, the shear mechanism proposed by N&H has got a maximum error of 10%. However, analysing the results of Xue's shear mechanism with both calibration points, it is not possible to claim that one point is better than the other. For the second calibration procedure, the mechanism has got a maximum error of 58% *versus* 178% for the first calibration point. Nevertheless,

for the other loading conditions, the results for the first calibration procedure were in closer agreement with experimental results.

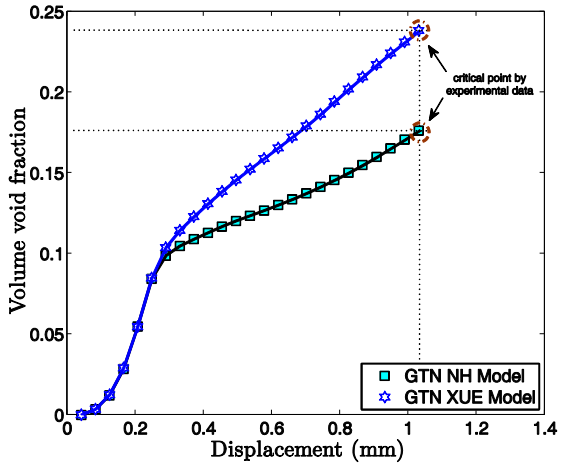

Pure shear 0°

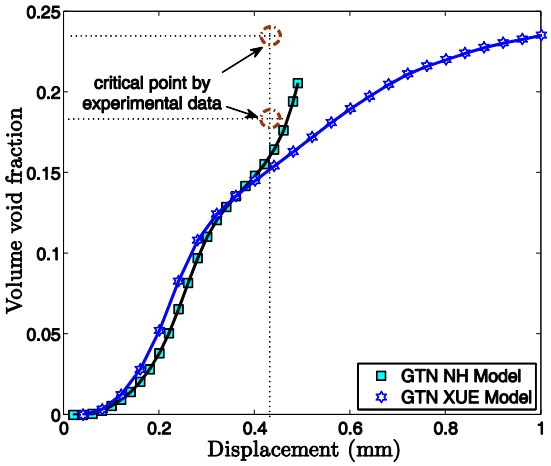

Combined shear/tensile 10°

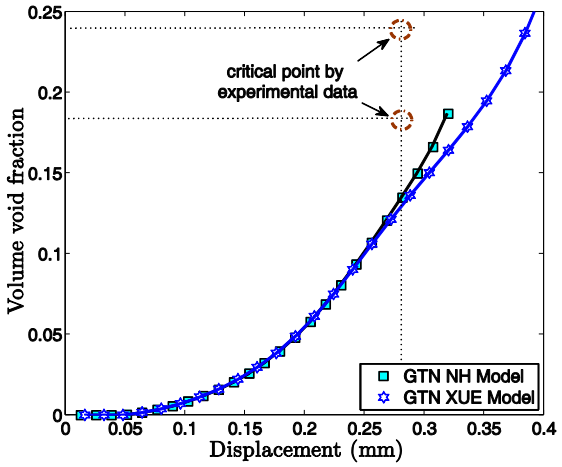

Combined shear/tensile 22°

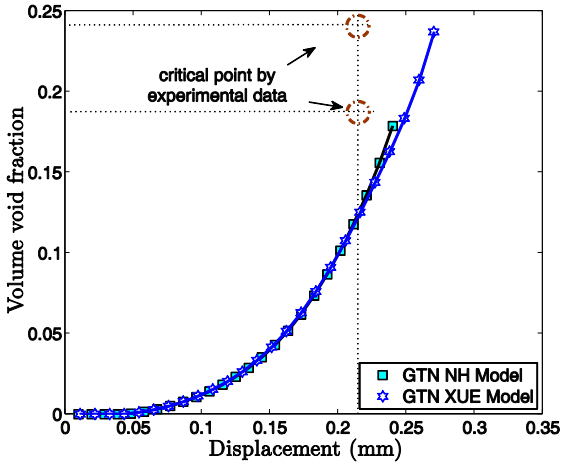

Combined shear/tensile 30°

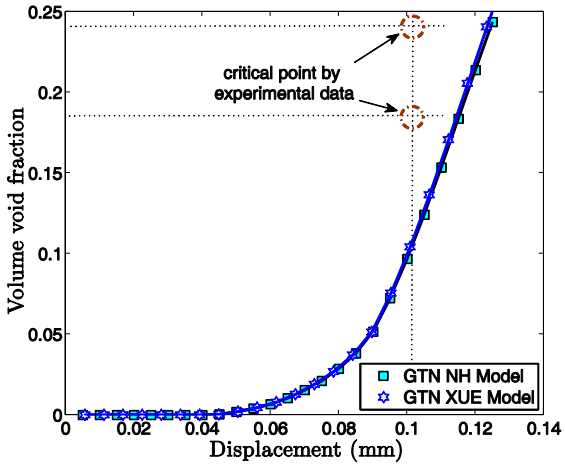

Pure tensile 90°

Figure 5.16. Evolution of the damage parameter. Based on the second calibration point.

5.5.3 Determination of fracture onset

Another important aspect to be analyzed, in order to validate the accuracy of both shear mechanisms using two different calibration points, is the ability to predict the correct fracture location. Reis *et al*. (2010) and Malcher *et al*. (2012) have shown that the shear mechanisms already proposed in literature, fail in the prediction of the correct location to crack formation when combined loading condition is applied. Based on experimental tests performed by Bai (2008), using the butterfly specimen, it can be observed that in pure shear loading condition, the micro crack is initially formed in the surface of the critical zone. However, when combined shear/tensile loading condition is applied, the crack is formed in the middle of the thickness and grows toward the surface of the critical zone. Figure 5.17 and Figure 5.18 present the contour of the damage parameter at fracture for both calibration points.

It can be observed that the damage contour plots obtained with the second calibration procedure were in closer agreement with experimental evidence than the contours obtained with the first calibration. Furthermore, the maximum value of the damage parameter is much localized in a specific zone. Nevertheless, Xue's shear mechanism fails the prediction for combined shear/tensile of 10°, indicating the surface of the specimen as the potential site to fracture onset, which is in disagreement with experimental observation.

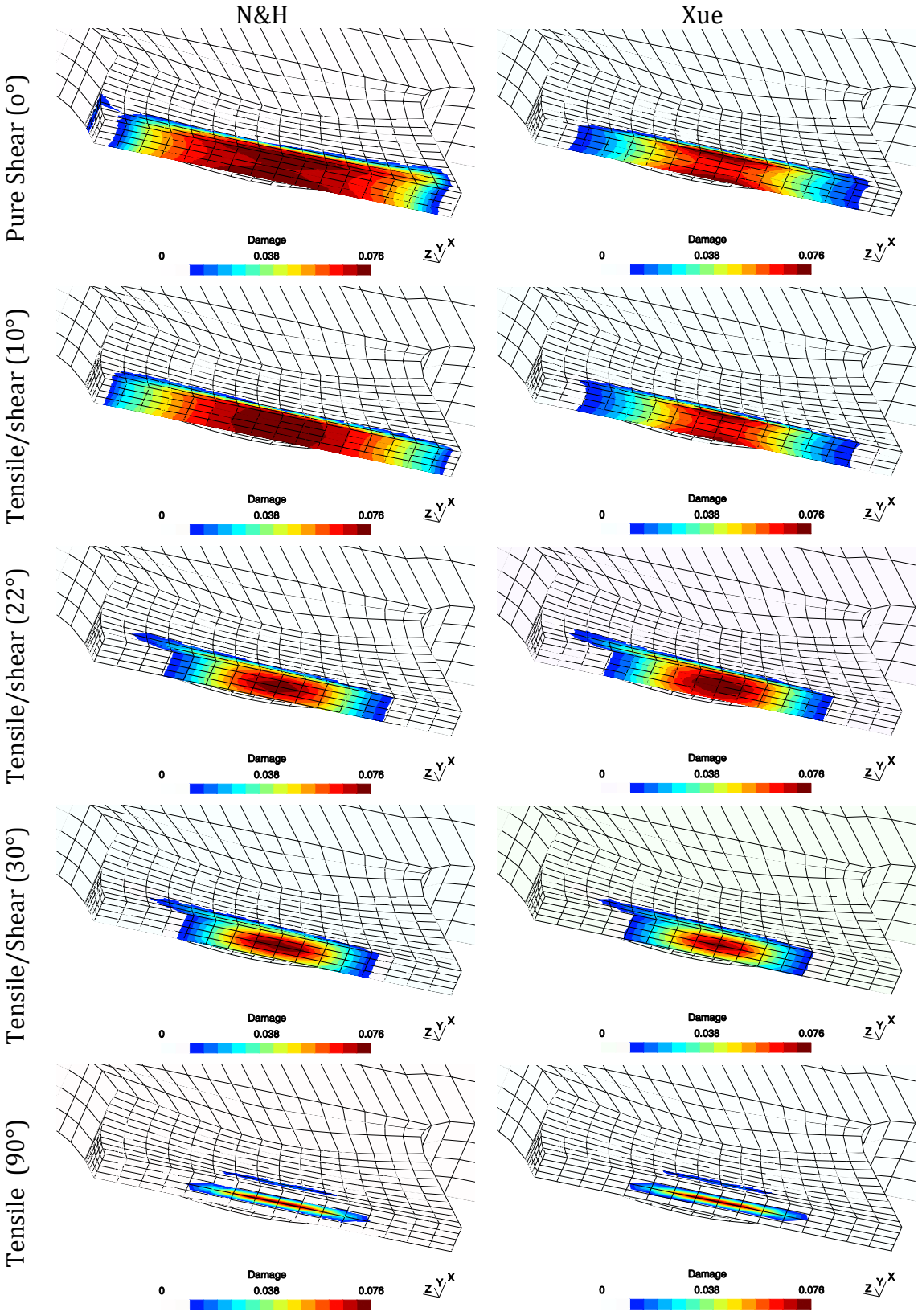

Figure 5.17. Contour of the damage parameter for both shear mechanisms. Based on the first calibration point.

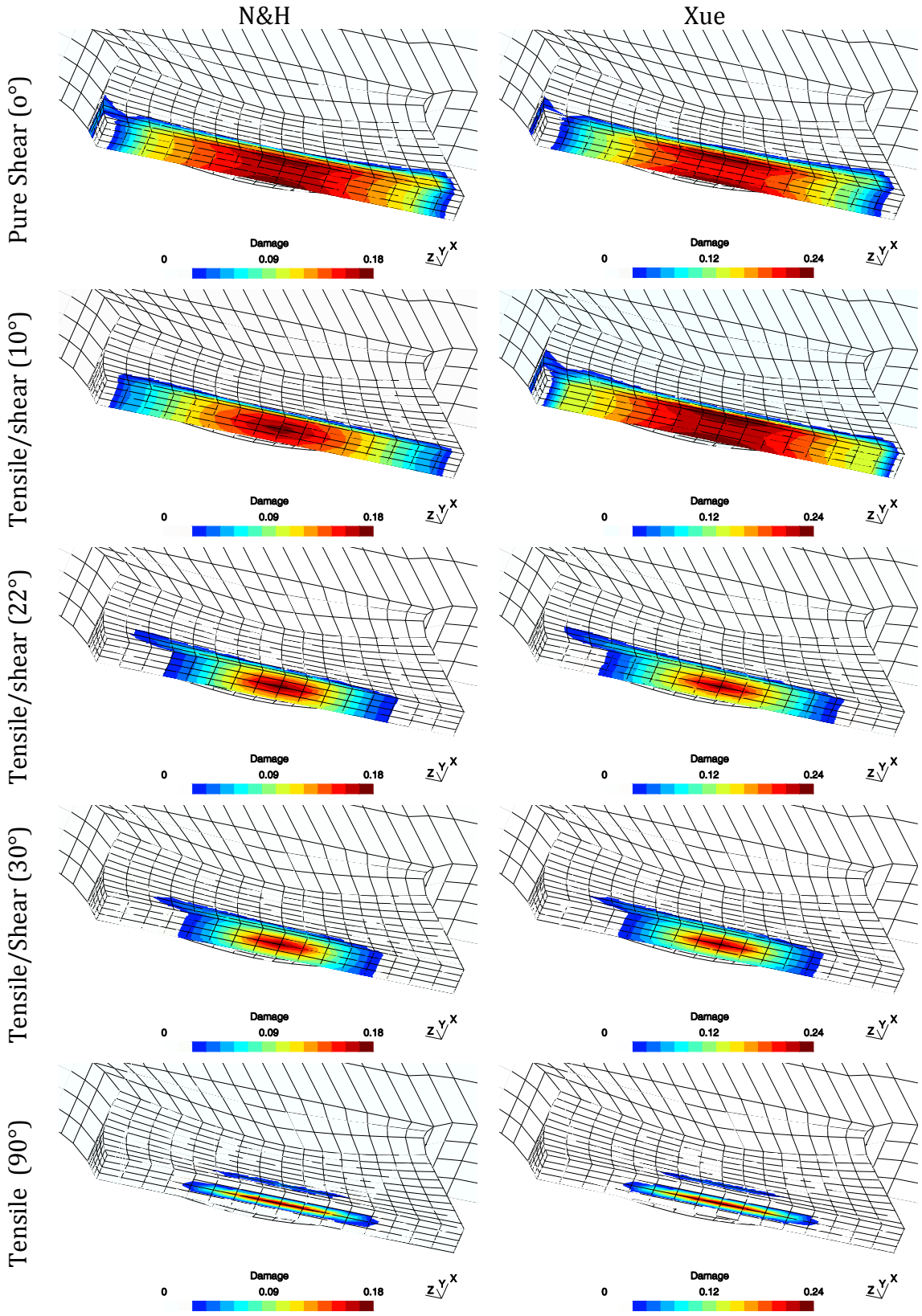

Figure 5.18. Contour of the damage parameter for both shear mechanisms. Based on the second calibration point.

5.6 CONCLUSIONS

In this chapter, an assessment of two different shear mechanisms was performed using the set of material parameters, calibrated in two different points. A specimen that promotes high stress triaxiality as well as a specimen under a pure shear loading condition were chosen to perform the calibration procedure. The material properties obtained from both calibration specimens were then used to simulate the material behaviour under several loading scenarios. The evolution of the equivalent plastic strain, the damage parameter and displacement at fracture were analyzed as well as the ability to predict the correct site to crack initiation. The results obtained, highlighted that for coupled damage models, the specimen chosen for the calibration of the material properties has a great influence on the numerical results. The accuracy of the coupled damage models is strongly dependent on the calibration point and the best performance of these models is found when the external loading condition applied is close to the loading condition selected for the calibration point. For these analyses including all numerical results, the second calibration point has the best agreement with experimental results and can be suggested for use when dominant shear loading conditions are present. In addition, the N&H's shear mechanism is in closer agreement with experimental observation, regarding a combination of 10 degrees between shear and tensile loading, which cannot be observed by Xue's shear mechanism.

CHAPTER 6

An Extended GTN Model for Ductile Fracture under High and Low Stress Triaxiality

In this chapter, an extended GTN model for the prediction of the fracture location under low level of stress triaxiality is proposed. In the new micromechanical damage model, two distinct damage parameters are introduced as internal variables and an effective damage is defined as a sum of both contributions in a post-processed step. The first damage parameter is established according to Gurson's original model and the volume void fraction is defined, based on conservation mass law. This damage contribution is able to capture spherical void growth, which plays the main role when dominant tensile loading conditions are present. In addition, a second damage parameter is proposed to account for shear effect, based on geometrical and phenomenological arguments. This variable is a function of the equivalent plastic strain, Lode angle and stress triaxiality. Regarding its formulation, the shear mechanism is independent of the volume void fraction and requires a new nucleation of micro-defects law to trigger the shear growth contribution. This mechanism is able to capture elongated void growth, which is present in pure shear and combined shear/tensile or shear/compression loading conditions. Both damage parameters are coupled in the constitutive formulation in order to affect the hydrostatic stress component and the deviatoric stress contribution, respectively. This chapter is organized as follows: In the first part, a review of the Gurson model and its most well known version is done. After that, the new formulation is discussed and an implicit numerical integration algorithm is derived, based on the operator split methodology, as well as the calibration of material parameters. Numerical tests are performed for a butterfly specimen using two types of materials, aluminum alloy 2024-T351 and steel 1045, for a wide range of stress triaxiality $-1/3 < \eta < 1/3$. The behavior of the internal variables is analyzed such as, the evolution of both damage parameters, the evolution of the equivalent plastic strain, the force *versus* displacement curve and the contour of the effective damage parameter. The numerical results are

compared with experimental evidence and show that the present formulation performs well, with regard to the prediction of the correct fracture location, the determination of the displacement and the equivalent plastic strain at fracture under low level of stress triaxiality.

6.1 INTRODUCTION

Due to the shortcomings observed on the GTN model in Chapter 4 and the limitations of the enhanced GTN models presented in Chapter 5, in this chapter, a new extension to the GTN model is proposed in order to improve the ability to predict the correct fracture location and determine the internal parameters at fracture. A new independent damage parameter is suggested to capture the elongation of micro-defects and coupled to the constitutive equations to affect only the deviatoric stress component. A nucleation of general micro defects is introduced to trigger the shear mechanism which gives more accuracy to the model in the prediction of ductile failure under mixed loading condition.

The great majority of engineering alloys contains several populations of inclusions corresponding to different length scales. Typically, it is possible to distinguish two main populations: one composed by primary inclusions, which are large particles embedded in the matrix, and one composed of secondary inclusions (or second phase particles), which can be 10-1000 orders of magnitude smaller. The phenomenon of ductile failure is usually induced by primary inclusions and second phase particles where micro-voids nucleate either by decohesion of inclusions (or second phase particles) from the surrounding matrix of by fracture of inclusions. The nucleated damage grows consistently with the applied stress state and the material degrades rapidly with the coalescence of multiple damage sites.

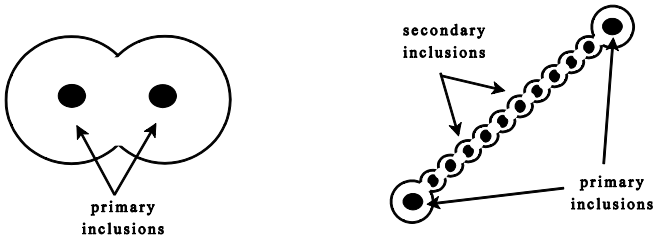

(a) (b)

Figure 6.1. Schematic representation of ductile failure micro mechanisms: (a) internal necking and (b) void sheeting (Adapted from Besson, 2010).

Two ductile failure micro mechanisms have be identified:

(a) Failure by internal necking where large primary voids nucleate, grow and coalesce promoting the necking and failure of the inter-void ligaments (see Figure 6.1a). This mechanism is associated with high triaxiality loading;

(b) Failure by void sheeting where tiny secondary voids are nucleated due to a process of shear localization linking larger voids (see Figure 6.1b). This mechanism is associated with low triaxiality loading.

6.2 EXTENDED CONSTITUTIVE FORMULATION

Due to the limitation of Gurson based models, in the prediction of fracture onset under conditions of low stress triaxiality, several researchers (Barsoum & Faleskog, 2007; McVeigh *et al.*, 2007; Xue, 2008; Nahshon & Hutchinson, 2008) have proposed the introduction of shear effects (see Section 6.3.3) on the formulation. Although the results obtained with the modified GTN models (Xue, 2008; Nahshon & Hutchinson, 2008) have shown improvements in the prediction of damage, it has also been observed (Reis *et al.*, 2011; Malcher *et al.,* 2012), that both models have inherent limitations. In particular, the prediction of the location of fracture, the displacement to fracture and the equivalent plastic strain to fracture, for combined stress states, is not adequate. Therefore, in order to overcome these shortcomings, in this contribution, a new extended GTN model is proposed that incorporates a new nucleation law for second-phase particles, the yield surface is modified to include two distinct damage mechanisms (volumetric void growth and shear damage), a modified Lode angle dependence function is introduced and a new criterion for coalescence is proposed.

6.2.1 Nucleation mechanism

The nucleation of voids associated with the GTN model, described by Equation (5.15), was proposed by Chu & Needleman (1980). This specific form for the nucleation of primary voids is strain rate controlled and was introduced on a purely phenomenological basis. Nevertheless, as described previously, engineering alloys loaded under shear conditions create localization bands due to the nucleation of secondary voids through a void sheeting mechanism. Although, secondary nucleation might be hard to detect in some materials, we will introduce

here a new independent nucleation mechanism that triggers void sheeting and localization. This nucleation mechanism is a result of second-phase particle debonding and cracking.

Following the same approach of Chu & Needleman (1980), we consider a normal distribution of all second-phase particles with potential for nucleation as:

$$\dot{D}^n = \frac{D_{\mathrm{N}}}{s'_N\sqrt{2\pi}} \exp\left[-\frac{1}{2}\left(\frac{\overline{\varepsilon}^p - \varepsilon'_N}{s'_N}\right)^2\right] \dot{\overline{\varepsilon}}^p \quad , \tag{6.1}$$

where D_{N} represents the fraction of all second-phase particles with potential for nucleation, ε'_N and s'_N are the mean strain for second-phase nucleation and its standard deviation. This set of parameters $\{D_{\mathrm{N}}, \varepsilon'_N, s'_N\}$ needs to be calibrated under a pure shear loading condition. The calibration of material parameters will be discussed latter in a specific section.

The extended GTN model, proposed in this chapter, incorporates two independent nucleation mechanisms. The first one, which is the conventional nucleation mechanism of the GTN model (Equation 5.15), triggers the evolution of the void volume fraction. The second, described by Equation (6.1), triggers the evolution of the shear mechanism. The activation of these nucleation mechanisms under pure volumetric and shear conditions is relatively straightforward to establish. Nevertheless, under arbitrary stress states that may include combinations of tensile/shear or compressive/shear is not so easy to define. It is necessary to couple both mechanisms and also establish their relative magnitude. Here, we introduce the Lode angle function (see section 5.2.3), g_0, to combine both nucleation mechanisms. Therefore, Equation (5.15) and Equation (6.1) are re-defined as:

$$\dot{f}^n = (1 - g_0)\frac{f_{\mathrm{N}}}{s_{\mathrm{N}}\sqrt{2\pi}} \exp\left[-\frac{1}{2}\left(\frac{\overline{\varepsilon}^p - \varepsilon_{\mathrm{N}}}{s_{\mathrm{N}}}\right)^2\right] \dot{\overline{\varepsilon}}^p, \tag{6.2}$$

$$\dot{D}^n = g_0 \frac{D_{\mathrm{N}}}{s'_N\sqrt{2\pi}} . \exp\left[-\frac{1}{2}\left(\frac{\overline{\varepsilon}^p - \varepsilon'_N}{s'_N}\right)^2\right] \dot{\overline{\varepsilon}}^p. \tag{6.3}$$

Under pure tensile loading conditions, the function g_0 is equal to zero and only primary nucleation of voids occurs (Equation 6.2). For pure shear loading conditions, the function g_0 is equal to one and only secondary nucleation occurs (Equation 6.3). For combined tensile/shear stress states, both mechanisms are active and the Lode angle function defines the relative importance of each component. Finally, if a combination of shear/compressive conditions is present there is no nucleation of primary voids and secondary nucleation takes place with the function g_0 defining the relative magnitude.

6.2.2 Incorporation of Shear Effects

As mentioned previously, several modified versions of the Gurson model, which include damage growth under low triaxiality straining for shear dominated stress states, have been proposed in the literature (Barsoum & Faleskog, 2007; McVeigh *et al.*, 2007; Xue, 2008; Nahshon & Hutchinson, 2008). Nevertheless, the incorporation of shear effects on the Gurson model has been mainly accomplished through the introduction of additional terms on the evolution of the void volume fraction, $\dot{f}$, as:

$$\dot{f} = \dot{f}^n + \dot{f}^g + \dot{f}^s, \tag{6.4}$$

where the term $\dot{f}^s$ does not represent a physical value of the porosity but ensures the detrimental effect of void distortion and inter-void linking, associated with low triaxiality, in the material. Therefore, the void volume fraction, f, in the modified versions of Gurson´s model, does not represent the plastic volume change of the material as in the original Gurson model. Alternatively, this scalar variable, f, measures the total accumulation of different types of damage in the material in an average sense.

In contrast with this approach, in this work, we use two separate damage variables. The first one is the evolution of the volume void fraction employed in the GTN model, rewritten here with appropriate modifications, as:

$$\dot{f} = \dot{f}^n + \dot{f}^g = (1 - g_0).\frac{f_N}{S_N\sqrt{2\pi}}\exp\left[-\frac{1}{2}\left(\frac{\bar{\varepsilon}^p - \varepsilon_N}{S_N}\right)^2\right]\dot{\bar{\varepsilon}}^p + (1 - f)\dot{\varepsilon}_v^p. \tag{6.5}$$

The second variable is the evolution of damage due to shear effects, which is defined by an independent scalar variable, as:

$$\dot{D} = \dot{D}^{n} + q_6 \dot{D}^{shear} = g_0 \frac{D_{\mathrm{N}}}{s'_N \sqrt{2\pi}} \exp\left[-\frac{1}{2} \left(\frac{\overline{\varepsilon}^{p} - \varepsilon'_N}{s'_N} \right)^2 \right] \dot{\bar{\varepsilon}}^{p} + q_6 \dot{D}^{shear}, \qquad (6.6)$$

where $\dot{D}$ represents the evolution of the shear damage variable, $\dot{D}^{n}$ represents its nucleation, which was introduced in Equation (6.3), and $\dot{D}^{shear}$ is the evolution of shear effects that can be defined based on geometrical considerations (see Equations 5.36 and 5.37) or phenomenological considerations (see Equation 5.38). The parameter q_6 is a numerical constant, calibrated for a specific material, which defines the magnitude of the damage growth rate in shear.

The extended GTN model proposed here has two scalar damage variables: a volumetric damage component characterized by the void volume fraction, f, and a deviatoric damage component described by shear damage, D. Each of these variables will be coupled with a specific component of the stress tensor: the hydrostatic pressure, p, will be related with the void volume fraction, f and the deviatoric component of the stress tensor, $\boldsymbol{S}$, will be associated with the shear damage variable, D. The yield function of the model is therefore, defined by the following equation:

$$\Phi(\boldsymbol{\sigma}, k, f, D) = \frac{J_2(\boldsymbol{S})}{(1-D)} - \frac{1}{3}\left\{ 1 + q_3 f^2 - 2 q_1 f \cosh\left(\frac{q_2 3p}{2\sigma_y} \right) \right\} {\sigma_y}^2. \qquad (6.7)$$

According to the principle of maximum dissipation, the yield function is taken as the dissipation potential of the model. Therefore, the evolution law for the plastic flow, assuming the hypothesis of generalized normality, is given by:

$$\dot{\varepsilon}^{p} = \dot{\gamma} \frac{\partial \Phi}{\partial \boldsymbol{\sigma}} = \dot{\varepsilon}_d^{p} + \dot{\varepsilon}_v^{p} = \dot{\gamma} \frac{\boldsymbol{S}}{(1-D)} + \dot{\gamma} \frac{1}{3} q_1 q_2 f \sigma_y \sinh\left(\frac{q_2 3 p}{2\sigma_y} \right) \boldsymbol{I}, \qquad (6.8)$$

where $\dot{\gamma}$ represents the plastic multiplier, $\boldsymbol{S}$ represents the deviatoric component of the stress tensor and $\boldsymbol{I}$ is a second order identity tensor. From the previous equation, it is possible to observe that each component of the plastic strain rate tensor is affected by a different damage variable. In addition, only the deviatoric

plastic strain rate, $\dot{\varepsilon}_d^p$, was altered, when compared with the Gurson model (Equation 5.16), due to the introduction of a distinct shear damage variable.

***Remark*:** Due to the fact that we have proposed two distinct damage variables in the formulation of the extended GTN model, the evolution of the volumetric plastic strain, $\dot{\varepsilon}_v^p$, predicted by the model (see Equation 6.8) will be different from previously proposed modifications of the Gurson model (Xue, 2008; Nahshon & Hutchinson, 2008). In these models, the volumetric plastic strain is coupled with an effective porosity (or damage variable), f, which includes both the volume void growth and shear damage. In addition, in these models, the deviatoric plastic strain rate, $\dot{\varepsilon}_d^p$, is not affected by the material degradation.

The evolution law for the hardening variable, R, is determined by performing the derivative of the yield function with regard to the hardening force, k:

$$\dot{R} = -\dot{\gamma}\,\frac{\partial \Phi}{\partial k} = \frac{\dot{\gamma}}{(1-f-D)}\left\{q_1 q_2 f p \sinh\left(\frac{3q_2 p}{2\sigma_y}\right) + \frac{2}{3}\sigma_y\left[1 + q_3 f^2 - 2q_1 f \cosh\left(\frac{3q_2 p}{2\sigma_y}\right)\right]\right\}, \tag{6.9}$$

where the term $(1-f-D)$ is introduced to account for the softening effect on the material evolution law. The equivalent plastic strain rate, for the present model, can be determined from:

$$\dot{\bar{\varepsilon}}^p = \sqrt{\frac{2}{3}\dot{\varepsilon}^p : \dot{\varepsilon}^p} = \dot{\gamma}\sqrt{\frac{2}{3}\left\{\frac{\boldsymbol{S}:\boldsymbol{S}}{(1-D)^2} + \frac{1}{3}\left[\sigma_y q_1 q_2 f \sinh\left(\frac{3q_2 p}{2\sigma_y}\right)\right]^2\right\}}. \tag{6.10}$$

It is important to mention that the extended GTN model, described by the previous set of equations, does not change the original model under stress states where shear effects are not present. The extension only modifies the predictions for stress states that include shear, i.e. for problems with a Lode angle function, g_0, different from zero.

6.2.3 Damage Evolution

The evolution law for the volume void fraction, $\dot{f}$, has got two components (see Equation 6.5): nucleation and growth. The most significant contribution to the evolution of spherical voids is the growth mechanism, $\dot{f}^g$, which depends on the

evolution of the volumetric plastic strain, $\dot{\varepsilon}_v^p$, established on Equation (6.8). Therefore, with the substitution of the rate of the volumetric plastic strain, $\dot{\varepsilon}_v^p$, on Equation (6.5) we obtain the evolution law for the void volume fraction, $\dot{f}$, of the model:

$$\dot{f} = \dot{f}^n + \dot{f}^g = (1-g_0)\frac{f_N}{S_N\sqrt{2\pi}}\exp\left[-\frac{1}{2}\left(\frac{\bar{\varepsilon}^p-\varepsilon_N}{S_N}\right)^2\right]\dot{\bar{\varepsilon}}^p + \dot{\gamma}\,\frac{1}{3}f(1-f)\,q_1\,q_2\,\sigma_y\sinh\left(\frac{3\,q_2\,p}{2\,\sigma_y}\right)\boldsymbol{I}. \tag{6.11}$$

Two possible evolution laws for the shear damage, based on geometrical considerations, were described by Equations (5.36) and (5.37). The evolution of damage in the material inevitably reduces the overall elastic properties. However, this effect is small when compared to the influence of damage on the plastic behavior. Therefore, the evolution of damage due to shear effects, employed in this work, will neglect the influence of damage on elasticity as is usually done in this type of model. The shear damage evolution laws are redefined as a function of both the accumulated plastic strain, $\bar{\varepsilon}^p$, and the rate of the accumulated plastic strain, $\dot{\bar{\varepsilon}}^p$, instead of the equivalent strain, ε_{eq}, and equivalent strain rate, $\dot{\varepsilon}_{eq}$:

$$\dot{D}^{shear} = g_0\left(\, q_4 D^{q_5}\bar{\varepsilon}^p\,\dot{\bar{\varepsilon}}^p\right), \tag{6.12}$$

$$\dot{D}^{shear} = g_0\left[\frac{1}{\ln\sqrt{1/\chi}}\left(\frac{3\bar{\varepsilon}^p}{1+3\bar{\varepsilon}^{p\,2}}\right)\dot{\bar{\varepsilon}}^p\right], \qquad \chi = \left(q_4 D\,\frac{\lambda_2}{\lambda_1}\right)^{q_5}. \tag{6.13}$$

In addition, due to the introduction of two separate damage variables, the shear damage evolutions described by Equations (5.36) and (5.37), for the present model, do not depend on the current void volume fraction, f, but on the current value of the shear damage variable, D. With the substitution of the equivalent plastic strain rate, $\dot{\bar{\varepsilon}}^p$, established on Equation (6.10), on the shear damage evolution law based on Xue's work (Equation 6.12), we obtain:

$$\dot{D}^{shear} = \dot{\gamma} g_0 q_4 D^{q_5}\,\bar{\varepsilon}^p\sqrt{\frac{2}{3}\left\{\frac{\boldsymbol{S}:\boldsymbol{S}}{(1-D)^2}+\frac{1}{3}\left[\sigma_y q_1 q_2 f\sinh\left(\frac{3q_2 p}{2\sigma_y}\right)\right]^2\right\}}. \tag{6.14}$$

On the other hand, with the substitution of the equivalent plastic strain rate, $\dot{\bar{\varepsilon}}^p$, established on Equation (6.10), on the shear damage evolution law based on Butcher´s work (Equation 6.13), we obtain:

$$\dot{D}^{shear} = \dot{\gamma} g_0 \frac{1}{\ln\sqrt{1/\chi}} \left(\frac{3\bar{\varepsilon}^p}{1+3\bar{\varepsilon}^{p\,2}} \right) \sqrt{\frac{2}{3}\left\{ \frac{\boldsymbol{S}:\boldsymbol{S}}{(1-D)^2} + \frac{1}{3}\left[\sigma_y q_1 q_2 f \sinh\left(\frac{3q_2 p}{2\sigma_y} \right) \right]^2 \right\}}. \quad (6.15)$$

6.2.4 Modified Lode Angle Dependence Function

The Lode angle dependence functions proposed by Xue (2008) and Nahshon & Hutchinson (2008), described in section 5.2.3, were introduced to generalize a pure shear damage evolution for arbitrary stress states. They critically include the effect of the deviatoric stress tensor through the Lode angle. The relative magnitude of shear and volumetric effects under combined stress states is defined by these functions, whose behavior was presented in Figure 5.6. Nevertheless, in this contribution, we suggest the introduction of the stress triaxiality parameter, η, defined by Equation (3.2) on the definition of the Lode angle dependence function, g_0. This modification, which can be performed on either of the functions described in section 5.2.3, has the following exponential form:

$$g_0'(\xi,\eta) = [g_0(\xi)]^{\frac{1}{|\eta|+k}}, \quad (6.16)$$

where g_0' is the modified function, η represents the stress triaxiality and k is a numerical constant that needs to be calibrated for each material. If either the Lode angle dependence function proposed by Xue or Nahshon & Hutchinson, g_0, is selected; the modified function is expressed by:

$$g_0'(\xi,\eta) = \left[1-\left|\bar{\theta}\right|\right]^{\frac{1}{|\eta|+k}} = \left[1-\left|1-\frac{2}{\pi}\mathrm{acos}(\xi)\right|\right]^{\frac{1}{|\eta|+k}}, \quad (6.17)$$

$$g_0'(\xi,\eta) = [1-\xi^2]^{\frac{1}{|\eta|+k}}. \quad (6.18)$$

Figure 6.2 illustrates the behavior of the original functions (Equations 5.34 and 5.35) on the space of $\{g_0, \xi, \eta\}$ and Figure 6.3 represents the behavior of the modified function (Equations 6.17 and 6.18) on the same space.

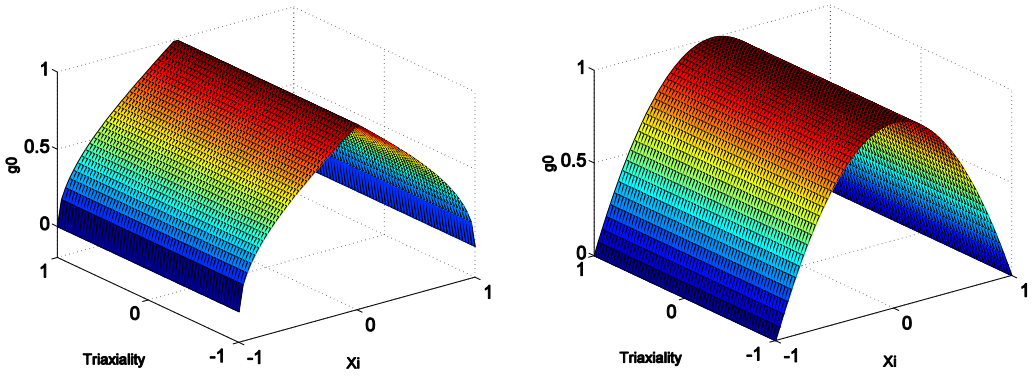

(a) (b)

Figure 6.2. Three dimensional representation of the Lode angle functions, g_0: (a) Xue´s model (b) Nahshon & Hutchinson´s model.

The influence of stress triaxiality will be dominant whenever the value of stress triaxiality is within the range of $[-1/3\,;1/3]$.

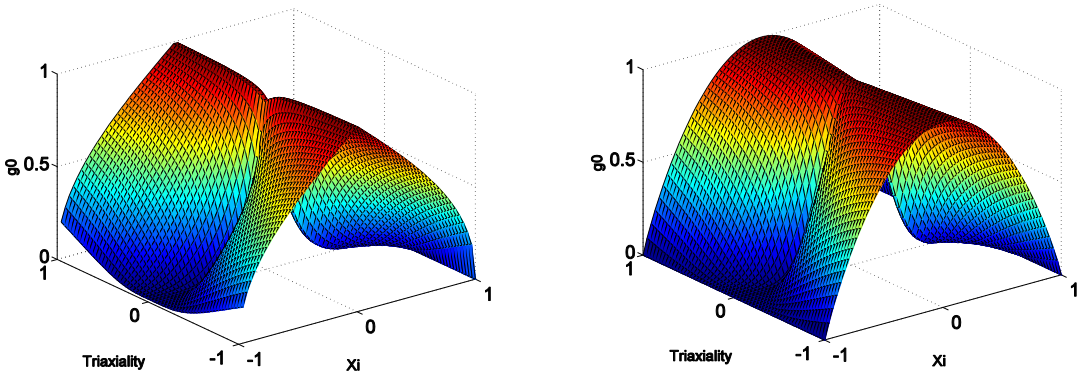

(a) (b)

Figure 6.3. Three dimensional representation of the modified Lode angle dependence function, g_0': (a) Xue´s model (b) Nahshon & Hutchinson´s model.

In order to analyze the influence of the new exponential term on the Lode angle dependence function, let us restrict ourselves, for instance, to the function described by Equation (6.17) that was proposed by Xue (2008). The constant k introduced in the exponent can be better understood through the analysis of

Figures 6.4 and 6.5. Figure 6.4 illustrates the shape of the modified Lode angle function, g_0', when the stress triaxiality is zero, $\eta = 0$, and we assign different values to the constant k. If the constant is equal to one, $k = 1$, the value of the exponent will be equal to 1 (since the stress triaxiality is zero) and we obtain the same evolution for the modified Lode angle function as the original one (see Figure 6.2). For values of constant, k, higher than unity, the modified Lode angle function will be higher than the original function. If the value of the constant, k, is smaller than 1 but higher than zero, the modified Lode angle function will be lower than the original function.

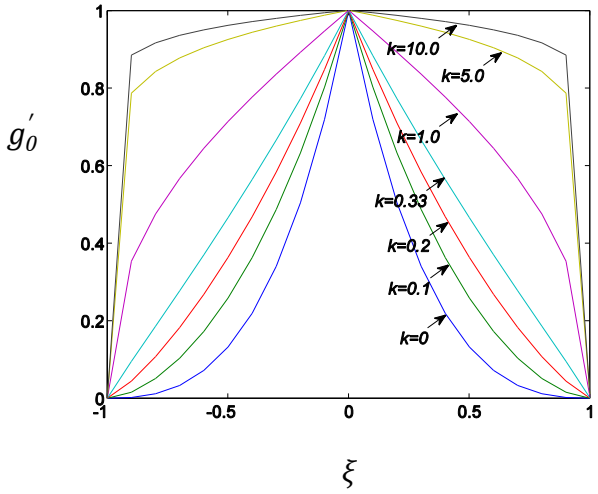

Figure 6.4. Influence of the constant k on the behavior of the function g_0' with regard to the third invariant fixing the stress triaxiality to zero ($\eta = 0$).

Figure 6.5 illustrates the shape of the modified Lode angle function, g_0', when the normalized third invariant is near of zero, or in other words, when dominate shear load is presented, and we assign different values to the constant k. If the constant, k, is equal to zero, it is possible to appreciate the influence of the stress triaxiality, η, on the modified Lode angle function. It can be observed that for high values of the parameter, k, the modified Lode angle function, g_0', is less affected by both third invariant and stress triaxiality. Nevertheless, for low values of the constant, k, the impact of the value of the parameters is very significant. Therefore, we recommend that the range of this value should be defined within the interval $[0.1; 1/3]$.

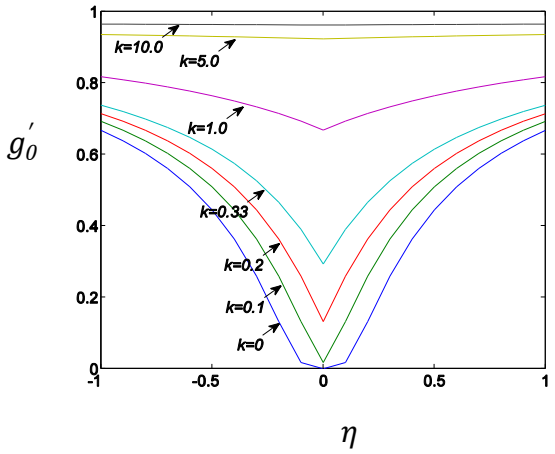

Figure 6.5. Influence of the constant k on the behavior of the function g_0' with regard to stress triaxiality.

Figure 6.6 also presents the influence of the parameter k on the global shape of the function g_0'. In particular, Figure 6.6 (a) represents the original Lode angle function (without the introduction of the dependence of stress triaxiality) proposed by Xue (2008) and the set of Figures 6.6 (b)-(c)-(d) represent the global shape of the modified function for different values of the parameter k. When the value of k is low, we have a stronger dependence on the stress triaxiality and when k is high, the modified function is less dependent on stress triaxiality, recovering in the limit the original Lode angle function.

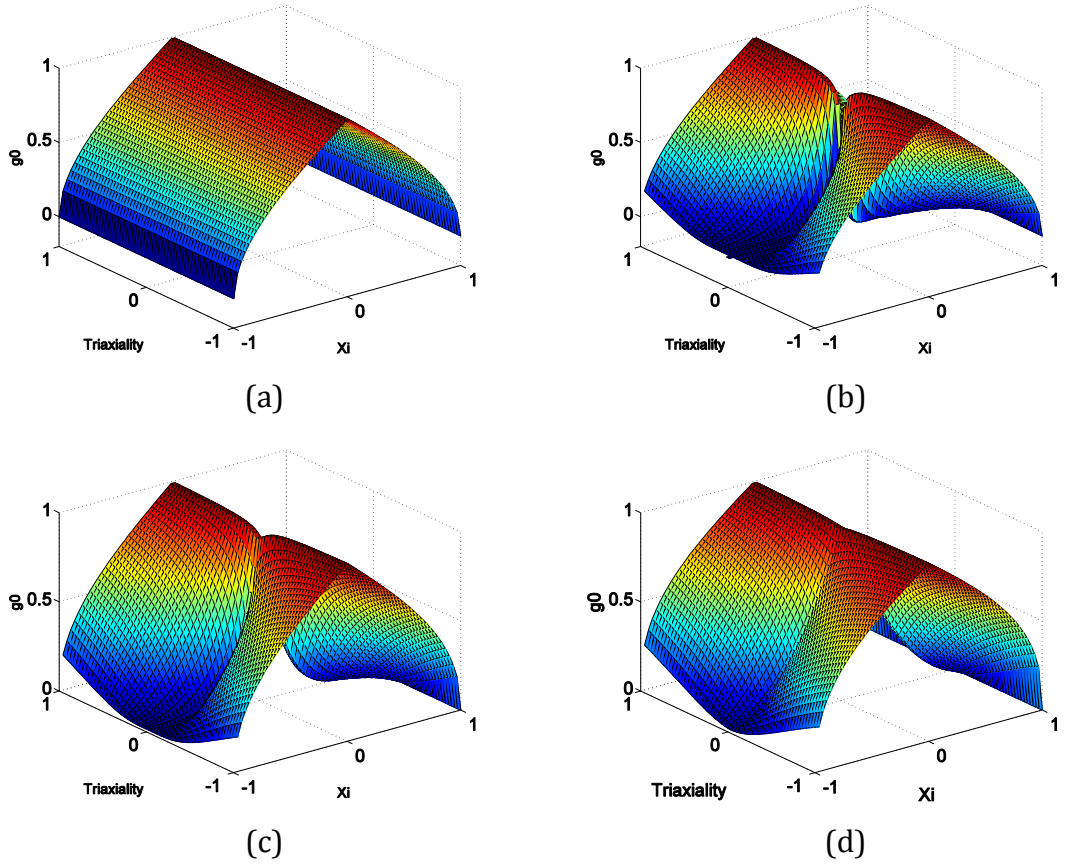

Figure 6.6. Behavior of the modified Lode angle dependence function g_0' for different values of k: (a) without dependence; (b) $k = 0$; (c) $k = 0.1$; (d) $k = 0.4$.

6.2.5 Coalescence Criterion

The definition of a criterion for void coalescence is extremely important for the prediction of fracture onset and for the simulation of crack formation and propagation. The simplest criterion for void coalescence is to assume a constant critical value of the void volume fraction, f_c. Once this value is reached, the mechanism of coalescence accelerates the rate of increase of the void volume fraction, $\dot{f}$, which will lead to final failure. The void coalescence process can be simulated by the function, f^*, introduced by Tvergaard & Needleman (1984) described by Equation (5.13). This criterion has been followed by several authors (Needleman &Tvergaard, 1987; Xia *et al.*, 1995; Faleskog *et al.*, 1998).

Nevertheless, further research on the topic focused on whether the volume fraction of voids could be regarded as a constant for different loading conditions.

Several researchers (Berzerga *et al.*, 1999; Zhang *et al.*, 2000; Pardoen & Hutchinson, 2000; Kim *et al*., 2004) employing unit cell models have shown that the void volume fraction of voids, f_c, is not sufficient to describe the initiation of fracture and established that it depends on several factors, such as the void shape and spacing, stress triaxiality, material hardening, etc. Recently, criterions based on either the effective strain or effective stress has been proposed to trigger the coalescence of voids. In particular, Gao *et al.* (2009) employed the Gologanu-Leblond-Devaux model (1985), with the modification proposed by Pardoen & Hutchinson (2000), to describe void growth and the macroscopic plastic response of cell elements containing non-spherical micro voids. They concluded that when the macroscopic effective strain of the element reaches a critical value, void coalescence occurs. On the other hand, Jackiewicz (2011) has proposed a coalescence criterion based on the assumption that a singular value of the effective stress triggers the coalescence of micro voids in materials.

In the present model, we have used two separate scalar damage variables, namely the void volume fraction, f, and the shear damage variable, D. Therefore, we will have two distinct critical values: the critical void volume fraction, f_c, which is the critical void volume fraction employed in the GTN model, and the critical shear damage value, D_c, which is regarded as a material constant that needs to be obtained. Each of the critical values will have to be determined under different conditions: the critical void volume fraction, f_c, will be obtained from a specimen subjected to tensile dominant loading conditions (associated with high triaxiality) and the critical shear damage value, D_c, will be obtained from a specimen subjected to a pure shear loading condition (associated with low triaxiality). More details will be given on section 6.4.

The coalescence criterion proposed here introduces an effective damage variable, D^{ef}, which is conveniently normalized, to combine both critical damage parameters (f_c and D_c). The determination of fracture onset is established whenever the effective damage variable, D^{ef}, reaches unity.

$$D^{ef} = \begin{cases} \dfrac{D}{D_c} & , \quad g_0' = 1 \\ \left(1 + \dfrac{f_c}{D_c}\right)\left(\dfrac{f}{f_c} + \dfrac{D}{D_c}\right), & 0 < g_0' < 1 \\ \dfrac{f}{f_c} & , \quad g_0' = 0 \end{cases} \tag{6.19}$$

The coalescence criterion based on the effective damage, D^{ef}, has three possible cases:

- Under generalized tension ($g_0' = 0$), where the spherical void growth drives the damage evolution, the effective damage is given by the ratio f/f_c and fracture onset is predicted when the void volume fraction, f, reaches the critical volume fraction, f_c;
- Under generalized shear ($g_0' = 1$), where the distortion of voids and inter-void linking promotes damage evolution, the effective damage variable is given by the ratio D/D_c and fracture is predicted when the shear damage variable, D, attains the critical shear damage, D_c;
- Under combined stress states, both the void growth under hydrostatic tension and shear localization compete with each other and the prediction of fracture onset is a combination of both contributions ($f/f_c + D/D_c$). In addition, in order to account for stress multiaxiality, we will introduce an additional term ($1 + f_c/D_c$) in the definition of the effective damage variable. This term will accelerate the prediction of fracture onset.

The effective damage variable is evaluated in the model in a post processed manner and does not affect the evolution of the two independent scalar damage variables. Critically, the criterion proposed allows fracture initiation at different values of the void volume fraction, f, and at different values of the shear damage variable, D. Furthermore, in the case of axsymmetric uniaxial tension, this criterion (employed in conjunction with the extended GTN model proposed) recovers the original GTN model criterion with critical f_c as a particular case, where $g_0' = 0$ and the damage shear evolution is zero.

In Box 6.1, the basic constitutive equations and evolution laws for the internal variables and damage are summarized:

Box 6.1. GTN's extended modified model including nucleation, growth and shear effects.

(i) Elasto-plastic split of the strain tensor

$$\boldsymbol{\varepsilon} = \boldsymbol{\varepsilon}^e + \boldsymbol{\varepsilon}^p$$

(ii) Elastic law

$$\boldsymbol{\sigma} = \mathbb{D}^e : \boldsymbol{\varepsilon}^e$$

(iii) Yield function

$$\Phi(\boldsymbol{\sigma}, r, f, D) = \frac{J_2}{1-D} - \frac{1}{3}\left[1 + q_3 f^2 - 2q_1 f \cosh\left(\frac{3q_2 p}{2\sigma_y}\right)\right]\sigma_y^2$$

(iv) Plastic flow and evolution equations for R, f and D

$$\dot{\boldsymbol{\varepsilon}}^p = \dot{\gamma}\boldsymbol{N}$$

$$\dot{R} = -\dot{\gamma}\frac{\partial \Phi}{\partial k}$$

$$\dot{f} = (1-g_0)\frac{f_N}{S_N\sqrt{2\pi}}\exp\left[-\frac{1}{2}\left(\frac{\bar{\varepsilon}^p - \varepsilon_N}{S_N}\right)^2\right]\dot{\bar{\varepsilon}}^p + (1-f)\dot{\varepsilon}_v^p$$

$$\dot{D} = g_0\frac{D_{\mathrm{N}}}{s'_N\sqrt{2\pi}}\exp\left[-\frac{1}{2}\left(\frac{\bar{\varepsilon}^p - \varepsilon'_N}{s'_N}\right)^2\right].\dot{\bar{\varepsilon}}^p + [g_0]^{\frac{1}{|\eta|+k}}\ q_6\,\dot{D}^{shear}$$

where,

$$\dot{D}^{shear} = \begin{cases} q_4 D^{q_5}\bar{\varepsilon}^p\dot{\bar{\varepsilon}}^p & ,if\ Xue's\ shear\ mechanism \\ \dfrac{1}{\ln\sqrt{1/\chi}}\left(\dfrac{3\bar{\varepsilon}^p}{1+3\bar{\varepsilon}^{p\,2}}\right)\dot{\bar{\varepsilon}}^p & ,if\ Butcher's\ shear\ mechanism \end{cases}$$

$$g_0 = \begin{cases} 1-|\bar{\theta}|, & if\ Xue's\ Lode\ angle\ function \\ 1-\xi^2\ , & if\ \text{Nahshon's}\ Lode\ angle\ function \end{cases}$$

and,

$$\dot{\bar{\varepsilon}}^p = \sqrt{\frac{2}{3}(\dot{\boldsymbol{\varepsilon}}^p : \dot{\boldsymbol{\varepsilon}}^p)} \qquad\qquad \dot{\varepsilon}_v^p = \mathrm{tr}(\dot{\boldsymbol{\varepsilon}}^p)$$

(v) Loading/unloading criterion

$$\dot{\gamma} \geq 0\,, \qquad \Phi \leq 0\,, \qquad \dot{\gamma}\Phi = 0$$

6.3 NUMERICAL INTEGRATION ALGORITHM

In this section, the numerical solution strategy adopted to perform the numerical simulations is summarized. The algorithm developed is based on operator split methodology which is especially suitable for the numerical integration of the evolution problem and have been widely used in computational plasticity (see Simo & Hughes, 1998; De Souza Neto *et al.*, 2008). The model was implemented in a quasi-static finite element framework based on the infinitesimal strain theory. The extension of the model to the finite strain range was done by adopting the well established multiplicative hyperelasto-plastic framework (Peric´ *et al.*, 1992; Eterovic & Bathe, 1990).

Let us consider what happens to a typical Gauss point of the finite element mesh within pseudo-time interval $[t_n,\ t_{n+1}]$. Given the incremental strain, $\Delta\boldsymbol{\varepsilon}$, and the values of $\boldsymbol{\sigma}_n$, $\boldsymbol{\varepsilon}_n^p$, $\bar{\varepsilon}_n^p$, R_n, f_n and D_n at time t_n, the numerical integration algorithm should obtain the updated values at the end of the interval, $\boldsymbol{\sigma}_{n+1}$, $\boldsymbol{\varepsilon}_{n+1}^p$, $\bar{\varepsilon}_{n+1}^p$, R_{n+1}, f_{n+1} and D_{n+1}, in a manner consistent with the constitutive equations of the model.

6.3.1 The Elastic Trial Step

The first step in the algorithm is the evaluation of the elastic trial state, where the increment is assumed purely elastic with no evolution of internal variables. The elastic trial strain and trial state variables are given by:

$$\boldsymbol{\varepsilon}_{n+1}^{e\,trial} = \boldsymbol{\varepsilon}_n^e + \Delta\boldsymbol{\varepsilon} \quad ; \quad \bar{\varepsilon}_{n+1}^{p\,trial} = \bar{\varepsilon}_n^p \quad ; \quad R_{n+1}^{trial} = R_n$$
$$f_{n+1}^{trial} = f_n \quad ; \quad D_{n+1}^{trial} = D_n \tag{6.20}$$

The corresponding elastic trial stress tensor is computed

$$\boldsymbol{\sigma}_{n+1}^{trial} = \mathbb{D}^e : \boldsymbol{\varepsilon}_{n+1}^{e\,trial}\ , \tag{6.21}$$

where $\mathbb{D}^e$ is the standard isotropic elasticity tensor. Equivalently, in terms of stress deviator and hydrostatic pressure, we have

$$\boldsymbol{S}_{n+1}^{trial} = 2G\boldsymbol{\varepsilon}_{d\,n+1}^{e\,trial}\ , \qquad p_{n+1}^{trial} = K\varepsilon_{v\,n+1}^{e\,trial}, \tag{6.22}$$

where $\boldsymbol{\varepsilon}_{d\,n+1}^{e\,trial}$ is the deviatoric elastic trial strain tensor and $\varepsilon_{v\,n+1}^{e\,trial}$ is the volumetric elastic trial strain. The material constants G and K represent the shear and bulk moduli.

The trial yield stress is defined, in this case, as a function of the internal hardening variable at time t_n:

$$\sigma_y^{trial} = \sigma_y(R_n) = \sigma_0 + k_n = \sigma_0 + HR_n \ , \tag{6.23}$$

where k_n is the thermodynamical force associated with the isotropic hardening internal variable, R_n.

The next step of the algorithm is to check whether $\boldsymbol{\sigma}_{n+1}^{trial}$ lies inside or outside of the trial yield surface. With variables $R, \bar{\varepsilon}^p$, f and D frozen at time t_n we compute:

$$\begin{aligned}\Phi^{trial} = &\frac{J_2^{trial}}{1 - D_{n+1}^{trial}} \\ &- \frac{1}{3}\left[1 + q_3 {f_{n+1}^{trial}}^2 - 2q_1 f_{n+1}^{trial} \cosh\left(\frac{3q_2 p_{n+1}^{trial}}{2\sigma_y^{trial}}\right)\right]\left(\sigma_y^{trial}\right)^2 .\end{aligned} \tag{6.24}$$

If $\Phi^{trial} \leq 0$, the process is indeed elastic within the interval and the elastic trial state coincides with the updated state at t_{n+1}. In other words, there is no plastic flow evolution within the interval and the trial state is equal to real state,

$$(*)_{n+1} = (*)_{n+1}^{trial} \ . \tag{6.25}$$

Otherwise, if $\Phi^{\text{trial}} > 0$, it is necessary to apply the plastic corrector or return mapping algorithm whose derivation is described in the following.

6.3.2 The Plastic Corrector Step or Return Mapping Algorithm

Following a straightforward specialization of standard return mapping procedure for the present constitutive equations, leads to the numerical integration of the evolution equations for $\boldsymbol{\varepsilon}_n^e$, $\bar{\varepsilon}_n^p$, R_n, f_n and D_n having the trial state as the initial condition. The discretization of the elastic strain tensor reads:

$$\boldsymbol{\varepsilon}^{e}_{n+1} = \boldsymbol{\varepsilon}^{e\,trial}_{n+1} - \Delta\gamma\left[\frac{\boldsymbol{S}_{n+1}}{1-D_{n+1}} + \frac{1}{3}\sigma_y q_1 q_2 f_{n+1}\sinh\left(\frac{3q_2 p_{n+1}}{2\sigma_y}\right)\boldsymbol{I}\right]. \tag{6.26}$$

With the application of Hooke's Law to the above expression, it is possible to determine the evolution of the stress tensor:

$$\boldsymbol{\sigma}_{n+1} = \mathbb{D}^{e}\colon\boldsymbol{\varepsilon}^{e}_{n+1} - 2G\Delta\gamma\frac{\boldsymbol{S}_{n+1}}{1-D_{n+1}} - \frac{1}{3}\Delta\gamma K\sigma_y q_1 q_2 f_{n+1}\sinh\left(\frac{3q_2 p_{n+1}}{2\sigma_y}\right)\boldsymbol{I}. \tag{6.27}$$

Equation (6.27) can be split into a deviatoric and a hydrostatic contribution. The updating relation for each component is given by:

$$\boldsymbol{S}_{n+1} = \frac{\boldsymbol{S}^{trial}_{n+1}}{\left[1+\left(\frac{2G\Delta\gamma}{1-D_{n+1}}\right)\right]}, \tag{6.28}$$

$$p_{n+1}\,\boldsymbol{I} = \left[p^{trial}_{n+1} - \frac{1}{3}\Delta\gamma K\sigma_y q_1 q_2 f_{n+1}\sinh\left(\frac{3q_2 p_{n+1}}{2\sigma_y}\right)\right]\boldsymbol{I}\ . \tag{6.29}$$

Furthermore, the discrete counterparts of the other variables of the problem read:

$$R_{n+1} = R^{trial}_{n+1} + \frac{\Delta\gamma}{(1-f_{n+1}-D_{n+1})}\left\{q_1 q_2 f_{n+1} p_{n+1}\sinh\left(\frac{3q_2 p_{n+1}}{2\sigma_y}\right) + \frac{2}{3}\sigma_y\left[1+q_3 {f_{n+1}}^{2} - 2q_1 f_{n+1}\cosh\left(\frac{3q_2 p_{n+1}}{2\sigma_y}\right)\right]\right\}$$

$$f_{n+1} = f^{trial}_{n+1} + (1-g_{0\,n+1})\frac{f_N}{S_N\sqrt{2\pi}}\exp\left[-\frac{1}{2}\left(\frac{\bar{\varepsilon}^{p}_{n+1}-\varepsilon_N}{S_N}\right)^{2}\right]\Delta\bar{\varepsilon}^{p} + (1-f_{n+1})\Delta\gamma\sigma_y q_1 q_2 f_{n+1}\sinh\left(\frac{3q_2 p_{n+1}}{2\sigma_y}\right) \tag{6.30}$$

$$D_{n+1} = D^{trial}_{n+1} + g_{0\,n+1}\frac{D_N}{S'_N\sqrt{2\pi}}\exp\left[-\frac{1}{2}\left(\frac{\bar{\varepsilon}^{p}_{n+1}-\varepsilon'_N}{S'_N}\right)^{2}\right]\Delta\bar{\varepsilon}^{p} + q_6\Delta D^{shear},$$

where the incremental shear damage component, ΔD^{shear}, can be either defined by Equation (6.14) or (6.15). Due to the fact that the Lode angle dependence function proposed by Nahshon & Hutchinson (2008) is continuous and does not have singular points (see Figure 6.2), it is more convenient for numerical implementation. Therefore, in our derivations, we will use this function.

Furthermore, the updating relation for the equivalent plastic strain can be obtained from:

$$\bar{\varepsilon}_{n+1}^{p} = \bar{\varepsilon}_{n+1}^{p\,trial} + \Delta\gamma \sqrt{\frac{2}{3}\left\{\frac{\boldsymbol{S}_{n+1}^{trial} : \boldsymbol{S}_{n+1}^{trial}}{\left[1+\left(\frac{2G\Delta\gamma}{1-D_{n+1}}\right)\right]^{2}(1-D_{n+1})^{2}} + \frac{1}{3}\left[\sigma_y q_1 q_2 f_{n+1} \sinh\left(\frac{3q_2 p_{n+1}}{2\sigma_y}\right)\right]^{2}\right\}}. \tag{6.31}$$

The above equations must be complemented by the so-called consistency condition that guarantees that the stress state at the end of the plastic step lies on the updated yield surface:

$$\Phi_{n+1} = \frac{J_{2\,n+1}^{trial}}{\left[1+\left(\frac{2G\Delta\gamma}{1-D_{n+1}}\right)\right]^{2}(1-D_{n+1})} - \frac{1}{3}\left[1 + {q_3 f_{n+1}}^{2} - 2q_1 f_{n+1} \cosh\left(\frac{3q_2 p_{n+1}}{2\sigma_y}\right)\right]\sigma_y^2. \tag{6.32}$$

Since it is possible to express the deviatoric stress tensor, $\boldsymbol{S}_{n+1}$, as a function of the plastic multiplier, $\Delta\gamma$, the shear damage, D_{n+1}, and the trial stress state, $\boldsymbol{S}_{n+1}^{trial}$, (Equation 6.28) it is possible to eliminate the deviatoric stress tensor from the initial system of equations, which is composed by ten equations in the three-dimensional case. The return mapping scheme can therefore be reduced to a set of only five coupled non-linear equations, which need to be solved for the unknowns p_{n+1}, R_{n+1}, f_{n+1}, D_{n+1} and $\Delta\gamma$, for any stress state. After the solution of the system, all other variables need to be conveniently updated. The overall algorithm for numerical integration is summarized in Box 6.2.

Box 6.2. Fully implicit Elastic predictor/Return mapping algorithm.

(i) Evaluate the elastic trial state: Given the incremental strain $\Delta\boldsymbol{\varepsilon}$ and the state variables at t_n:

$$\boldsymbol{\varepsilon}_{n+1}^{e\,trial} = \boldsymbol{\varepsilon}_n^e + \Delta\boldsymbol{\varepsilon} \quad ; \quad \bar{\varepsilon}_{n+1}^{p\,trial} = \bar{\varepsilon}_n^p \quad ; \quad R_{n+1}^{trial} = R_n$$

$$f_{n+1}^{trial} = f_n \quad ; \quad D_{n+1}^{trial} = D_n \quad ; \quad \boldsymbol{S}_{n+1}^{trial} = 2G\boldsymbol{\varepsilon}_{n+1}^{e\,trial}$$

$$p_{n+1}^{trial} = K\varepsilon_{v\,n+1}^{e\,trial} \quad ; \quad \sigma_y^{trial} = \sigma_y\left(R_{n+1}^{trial}\right)$$

(ii) Check plastic admissibility:

IF $\Phi^{trial} = \frac{J_2^{trial}}{1-D_{n+1}^{trial}} - \frac{1}{3}\left[1 + q_3 {f_{n+1}^{trial}}^2 - 2q_1 f_{n+1}^{trial}\cosh\left(\frac{3q_2 p_{n+1}^{trial}}{2\sigma_y^{trial}}\right)\right]\left(\sigma_y^{trial}\right)^2 \leq 0$

THEN

Set $(\cdot)_{n+1} = (\cdot)_{n+1}^{trial}$ ***(elastic step)*** and go to *(v)*

ELSE go to (iii)

(iii) Return mapping ***(plastic step)***: *Solve the system of equations for* $\Delta\gamma, p_{n+1}, f_{n+1}, R_{n+1}$ and D_{n+1}

$$\begin{Bmatrix} \dfrac{J_{2\,n+1}^{trial}}{\left[1+\left(\frac{2G.\Delta\gamma}{1-D_{n+1}}\right)\right]^2(1-D_{n+1})} - \dfrac{1}{3}\left[1 + q_3 {f_{n+1}}^2 - 2q_1 f_{n+1}\cosh\left(\dfrac{3q_2 p_{n+1}}{2\sigma_y}\right)\right]\sigma_y^2 \\ p_{n+1} - p_{n+1}^{trial} + \Delta\gamma K\sigma_y q_1 q_2 f_{n+1}\sinh\left(\dfrac{3q_2 p_{n+1}}{2\sigma_y}\right) \\ f_{n+1} - f_{n+1}^{trial} - \Delta f^n - \Delta f^g \\ R_{n+1} - R_{n+1}^{trial} - \Delta R \\ D_{n+1} - D_{n+1}^{trial} - \Delta D^n - q_6\Delta D^{shear} \end{Bmatrix} = \begin{Bmatrix} 0 \\ 0 \\ 0 \\ 0 \\ 0 \end{Bmatrix}$$

where,

$$\Delta f^n = (1 - g_{0\,n+1})\frac{f_N}{S_N\sqrt{2\pi}}\exp\left[-\frac{1}{2}\left(\frac{\bar{\varepsilon}_{n+1}^p - \varepsilon_N}{S_N}\right)^2\right]\Delta\bar{\varepsilon}^p$$

$$\Delta f^g = (1 - f_{n+1})\Delta\gamma\sigma_y q_1 q_2 f_{n+1}\sinh\left(\frac{3q_2 p_{n+1}}{2\sigma_y}\right)$$

$$\Delta R = \frac{\Delta\gamma}{(1 - f_{n+1} - D_{n+1})}\left\{q_1 q_2 f_{n+1} p_{n+1}\sinh\left(\frac{3q_2 p_{n+1}}{2\sigma_y}\right) + \frac{2}{3}\sigma_y\left[1 + q_3 {f_{n+1}}^2 - 2q_1 f_{n+1}\cosh\left(\frac{3q_2 p_{n+1}}{2\sigma_y}\right)\right]\right\}$$

$$\Delta D^n = g_{0\,n+1}\frac{D_N}{S_N'\sqrt{2\pi}}\exp\left[-\frac{1}{2}\left(\frac{\bar{\varepsilon}_{n+1}^p - \varepsilon_N'}{S_N'}\right)^2\right]\Delta\bar{\varepsilon}^p$$

continue Box 6.2.

$$\Delta D^{shear} = \begin{cases} [g_{0\,n+1}]^{\left(\frac{1}{|\eta_{n+1}|+k}\right)} q_4\, D_{n+1}^{q_5}\, \bar{\varepsilon}_{n+1}^{p} \Delta\bar{\varepsilon}^{p} & ,if\ Xue's\ mechanism \\ [g_{0\,n+1}]^{\left(\frac{1}{|\eta_{n+1}|+k}\right)} \dfrac{1}{\ln\sqrt{1/\chi}} \left(\dfrac{3\bar{\varepsilon}_{n+1}^{p}}{1+3\bar{\varepsilon}_{n+1}^{p\,2}}\right) \Delta\bar{\varepsilon}^{p} & ,if\ Butcher's\ mechanism \end{cases}$$

$$g_{0\,n+1} = (1-\xi_{n+1}^{2})$$

$$\chi = \begin{cases} \left(\dfrac{4}{\pi} D_{n+1} \dfrac{\lambda_2}{\lambda_1}\right)^{\frac{1}{2}}, & if\ 2D\ problem \\ \left(\dfrac{6}{\pi} D_{n+1} \dfrac{\lambda_2}{\lambda_1}\right)^{\frac{1}{3}}, & if\ 3D\ problem \end{cases}$$

(iv) Update the other state variables:

$$\boldsymbol{\varepsilon}_{n+1}^{e} = \boldsymbol{\varepsilon}_{n+1}^{e\,trial} - \Delta\gamma \left[\frac{\boldsymbol{S}_{n+1}^{trial}}{\left[1+\left(\frac{2G.\Delta\gamma}{1-D_{n+1}}\right)\right](1-D_{n+1})} + \frac{1}{3}\sigma_y q_1 q_2 f_{n+1} \sinh\left(\frac{3q_2 p_{n+1}}{2\sigma_y}\right) \boldsymbol{I} \right]$$

$$\boldsymbol{S}_{n+1} = \frac{\boldsymbol{S}_{n+1}^{trial}}{\left[1+\left(\frac{2G\Delta\gamma}{1-D_{n+1}}\right)\right]}$$

$$\boldsymbol{\sigma}_{n+1} = \boldsymbol{S}_{n+1} + p_{n+1}\boldsymbol{I}$$

$$\Delta\bar{\varepsilon}^{p} = \Delta\gamma \sqrt{\frac{2}{3}\left\{ \frac{\boldsymbol{S}_{n+1}^{trial} : \boldsymbol{S}_{n+1}^{trial}}{\left[1+\left(\frac{2G\Delta\gamma}{1-D_{n+1}}\right)\right]^{2}(1-D_{n+1})^{2}} + \frac{1}{3}\left[\sigma_y q_1 q_2 f_{n+1} \sinh\left(\frac{3q_2 p_{n+1}}{2\sigma_y}\right)\right]^{2} \right\}}$$

$$\bar{\varepsilon}_{n+1}^{p} = \bar{\varepsilon}_{n+1}^{p\,trial} + \Delta\bar{\varepsilon}^{p}$$

(v) Exit

The previous set of discrete equations needs to be solved for the unknowns p_{n+1}, R_{n+1}, f_{n+1}, D_{n+1} and $\Delta\gamma$. The Newton-Raphson (NR) method will be used for solving the return mapping system of equations due to the asymptotic rate of quadratic convergence of the method. Let us rewrite the non-linear scalar system of residual equations, in the following form:

$$\begin{Bmatrix} r_{\Delta\gamma} \\ r_p \\ r_f \\ r_R \\ r_D \end{Bmatrix} = \begin{Bmatrix} \dfrac{J_{2_{n+1}}^{trial}}{\left[1+\left(\dfrac{2G\Delta\gamma}{1-D_{n+1}}\right)\right]^2 (1-D_{n+1})} - \dfrac{1}{3}\left[1+{q_3 f_{n+1}}^2 - 2q_1 f_{n+1}\cosh\left(\dfrac{3q_2 p_{n+1}}{2\sigma_y}\right)\right]\sigma_y^2 \\ p_{n+1} - p_{n+1}^{trial} + \Delta\gamma K \sigma_y q_1 q_2 f_{n+1}\sinh\left(\dfrac{3q_2 p_{n+1}}{2\sigma_y}\right) \\ f_{n+1} - f_{n+1}^{trial} - \Delta f^n - \Delta f^g \\ R_{n+1} - R_{n+1}^{trial} - \Delta R \\ D_{n+1} - D_{n+1}^{trial} - \Delta D^n - q_6 \Delta D^{shear} \end{Bmatrix}. \quad (6.33)$$

To obtain a new guess for each variable of the problem, it is necessary to solve a linearized system of equations given by:

$$\begin{bmatrix} \dfrac{\partial r_{\Delta\gamma}}{\partial\Delta\gamma} & \dfrac{\partial r_{\Delta\gamma}}{\partial p_{n+1},} & \dfrac{\partial r_{\Delta\gamma}}{\partial f_{n+1}} & \dfrac{\partial r_{\Delta\gamma}}{\partial R_{n+1}} & \dfrac{\partial r_{\Delta\gamma}}{\partial D_{n+1}} \\ \dfrac{\partial r_p}{\partial\Delta\gamma} & \dfrac{\partial r_p}{\partial p_{n+1},} & \dfrac{\partial r_p}{\partial f_{n+1}} & \dfrac{\partial r_p}{\partial R_{n+1}} & \dfrac{\partial r_p}{\partial D_{n+1}} \\ \dfrac{\partial r_f}{\partial\Delta\gamma} & \dfrac{\partial r_f}{\partial p_{n+1},} & \dfrac{\partial r_f}{\partial f_{n+1}} & \dfrac{\partial r_f}{\partial R_{n+1}} & \dfrac{\partial r_f}{\partial D_{n+1}} \\ \dfrac{\partial r_R}{\partial\Delta\gamma} & \dfrac{\partial r_R}{\partial p_{n+1},} & \dfrac{\partial r_R}{\partial f_{n+1}} & \dfrac{\partial r_R}{\partial R_{n+1}} & \dfrac{\partial r_R}{\partial D_{n+1}} \\ \dfrac{\partial r_D}{\partial\Delta\gamma} & \dfrac{\partial r_D}{\partial p_{n+1},} & \dfrac{\partial r_D}{\partial f_{n+1}} & \dfrac{\partial r_D}{\partial R_{n+1}} & \dfrac{\partial r_D}{\partial D_{n+1}} \end{bmatrix}^j \begin{bmatrix} \delta\Delta\gamma \\ \delta p_{n+1} \\ \delta f_{n+1} \\ \delta R_{n+1} \\ \delta D_{n+1} \end{bmatrix}^{j+1} = -\begin{bmatrix} r_{\Delta\gamma} \\ r_p \\ r_f \\ r_R \\ r_D \end{bmatrix}^j. \quad (6.34)$$

In the above system, the terms in the matrix are composed by the derivative of each residual equation (see Equation 6.33) with regard to each variable of the problem (p_{n+1}, R_{n+1}, f_{n+1}, D_{n+1} and $\Delta\gamma$) at iteration *j*. The matrix is multiplied by a vector with the incremental values of each variable at iteration, $j + 1$. The vector on the right hand side represents the residual of each variable at iteration *j*. After solving the system for the unknowns and obtaining a new guess for each variable, the convergence needs to be checked. More details of the linearization procedure for the present model can be found in Appendix "E". The overall algorithm for numerical integration is summarized in Box 6.3 in pseudo-code format.

Box 6.3. The Newton-Raphson algorithm for solution of the return mapping system of equations.

1) Initialize iteration counter, $k := 0$, set initial guess for $\Delta\gamma^{(0)} = 0$, $p_{n+1}^{(0)} = p_n^{(0)}$, $f_{n+1}^{(0)} = f_n^{(0)}$, $R_{n+1}^{(0)} = R_n^{(0)}$ and $D_{n+1}^{(0)} = D_n^{(0)}$ corresponding residual:

$$\begin{Bmatrix} r_{\Delta\gamma} \\ r_p \\ r_f \\ r_R \\ r_D \end{Bmatrix} = \begin{Bmatrix} \dfrac{J_{2\,n+1}^{trial}}{\left[1+\left(\dfrac{2G\Delta\gamma}{1-D_{n+1}}\right)\right]^2(1-D_{n+1})} - \dfrac{1}{3}\left[1+q_3 {f_{n+1}}^2 - 2q_1 f_{n+1}\cosh\left(\dfrac{3q_2 p_{n+1}}{2\sigma_y}\right)\right]\sigma_y^2 \\ p_{n+1} - p_{n+1}^{trial} + \Delta\gamma K\sigma_y q_1 q_2 f_{n+1}\sinh\left(\dfrac{3q_2 p_{n+1}}{2\sigma_y}\right) \\ f_{n+1} - f_{n+1}^{trial} - \Delta f^n - \Delta f^g \\ R_{n+1} - R_{n+1}^{trial} - \Delta R \\ D_{n+1} - D_{n+1}^{trial} - \Delta D^n - q_6\Delta D^{shear} \end{Bmatrix}$$

2) Perform Newton-Raphson iteration

$$\begin{bmatrix} \dfrac{\partial r_{\Delta\gamma}}{\partial\Delta\gamma} & \dfrac{\partial r_{\Delta\gamma}}{\partial p_{n+1},} & \dfrac{\partial r_{\Delta\gamma}}{\partial f_{n+1}} & \dfrac{\partial r_{\Delta\gamma}}{\partial R_{n+1}} & \dfrac{\partial r_{\Delta\gamma}}{\partial D_{n+1}} \\ \dfrac{\partial r_p}{\partial\Delta\gamma} & \dfrac{\partial r_p}{\partial p_{n+1},} & \dfrac{\partial r_p}{\partial f_{n+1}} & \dfrac{\partial r_p}{\partial R_{n+1}} & \dfrac{\partial r_p}{\partial D_{n+1}} \\ \dfrac{\partial r_f}{\partial\Delta\gamma} & \dfrac{\partial r_f}{\partial p_{n+1},} & \dfrac{\partial r_f}{\partial f_{n+1}} & \dfrac{\partial r_f}{\partial R_{n+1}} & \dfrac{\partial r_f}{\partial D_{n+1}} \\ \dfrac{\partial r_R}{\partial\Delta\gamma} & \dfrac{\partial r_R}{\partial p_{n+1},} & \dfrac{\partial r_R}{\partial f_{n+1}} & \dfrac{\partial r_R}{\partial R_{n+1}} & \dfrac{\partial r_R}{\partial D_{n+1}} \\ \dfrac{\partial r_D}{\partial\Delta\gamma} & \dfrac{\partial r_D}{\partial p_{n+1},} & \dfrac{\partial r_D}{\partial f_{n+1}} & \dfrac{\partial r_D}{\partial R_{n+1}} & \dfrac{\partial r_D}{\partial D_{n+1}} \end{bmatrix}^j \begin{bmatrix} \delta\Delta\gamma \\ \delta p_{n+1} \\ \delta f_{n+1} \\ \delta R_{n+1} \\ \delta D_{n+1} \end{bmatrix}^{j+1} = -\begin{bmatrix} r_{\Delta\gamma} \\ r_p \\ r_f \\ r_R \\ r_D \end{bmatrix}^j .$$

New guess for p_{n+1}, R_{n+1}, f_{n+1}, D_{n+1} and $\Delta\gamma$***:***

$$\Delta\gamma^{(j+1)} = \Delta\gamma^{(j)} + \delta\Delta\gamma^{(j+1)} \quad ; \quad {p_{n+1}}^{(j+1)} = {p_{n+1}}^{(j)} + \delta {p_{n+1}}^{(j+1)}$$

$${R_{n+1}}^{(j+1)} = {R_{n+1}}^{(j)} + \delta {R_{n+1}}^{(j+1)} \quad ; \quad {D_{n+1}}^{(j+1)} = {D_{n+1}}^{(j)} + \delta {D_{n+1}}^{(j+1)}$$

$${f_{n+1}}^{(j+1)} = {f_{n+1}}^{(j)} + \delta {f_{n+1}}^{(j+1)}$$

3) Check for convergence

$$\tilde{\Phi} = \frac{J_{2\,n+1}^{trial}}{\left[1+\left(\dfrac{2G\Delta\gamma}{1-D_{n+1}}\right)\right]^2(1-D_{n+1})} - \frac{1}{3}\left[1+q_3 {f_{n+1}}^2 - 2q_1 f_{n+1}\cosh\left(\frac{3q_2 p_{n+1}}{2\sigma_y}\right)\right]\sigma_y^2$$

IF $\left\|\tilde{\Phi}\right\| \le \epsilon_{tol}$ THEN RETURN to Box 6.2.

4) GO TO (*2*)

6.3.3 The Consistent Tangent Operator

Under the elastic loading condition, the tangent operator for this constitutive formulation is the standard linear elasticity tensor. Nevertheless, for the plastic step, the elasto-plastic tangent operator is obtained by the linearization procedure of the system of residual equations described in section 6.3.2. Hence, the first step for determining the operator is to differentiate the stress tensor update expression:

$$\boldsymbol{\sigma}_{n+1} = \frac{\boldsymbol{s}_{n+1}^{trial}}{\left[1+\left(\frac{2G\Delta\gamma}{1-D_{n+1}}\right)\right]} + p_{n+1}\,\boldsymbol{I}\,. \tag{6.35}$$

After some algebraic manipulation, the differentiation of Equation 6.35 can be expressed by:

$$\begin{aligned} \mathrm{d}\boldsymbol{\sigma}_{n+1} = {} & \frac{2G}{\left[1+\left(\frac{2G\Delta\gamma}{1-D_{n+1}}\right)\right]}\mathrm{d}\boldsymbol{\varepsilon}_{d\,n+1}^{e\,trial} \\ & - \left\{\frac{2G}{\left[1+\left(\frac{2G\Delta\gamma}{1-D_{n+1}}\right)\right]}\right\}^2 \boldsymbol{\varepsilon}_{d\,n+1}^{e\,trial}\frac{1}{1-D_{n+1}}\mathrm{d}\Delta\gamma \\ & - \left\{\frac{2G}{\left[1+\left(\frac{2G\Delta\gamma}{1-D_{n+1}}\right)\right]}\right\}^2 \boldsymbol{\varepsilon}_{d\,n+1}^{e\,trial}\frac{\Delta\gamma}{(1-D_{n+1})^2}\mathrm{d}D_{n+1} + \mathrm{d}p_{n+1}\boldsymbol{I}. \end{aligned} \tag{6.36}$$

The terms $\mathrm{d}\Delta\gamma$, $\mathrm{d}D_{n+1}$ and $\mathrm{d}p_{n+1}$ can be obtained by the linearization procedure of the residual system of equations. Furthermore, the elasto-plastic operator can be determined by:

$$\mathbb{D}^{ep} = \frac{\mathrm{d}\boldsymbol{\sigma}_{n+1}}{\mathrm{d}\boldsymbol{\varepsilon}_{n+1}^{e\,trial}}\,. \tag{6.37}$$

The linearized system of residual equations for the plastic corrector algorithm at the converged state results in the following identity:

$$\begin{bmatrix} \frac{\partial r_{\Delta\gamma}}{\partial \Delta\gamma} & \frac{\partial r_{\Delta\gamma}}{\partial p_{n+1},} & \frac{\partial r_{\Delta\gamma}}{\partial f_{n+1}} & \frac{\partial r_{\Delta\gamma}}{\partial R_{n+1}} & \frac{\partial r_{\Delta\gamma}}{\partial D_{n+1}} \\ \frac{\partial r_p}{\partial \Delta\gamma} & \frac{\partial r_p}{\partial p_{n+1},} & \frac{\partial r_p}{\partial f_{n+1}} & \frac{\partial r_p}{\partial R_{n+1}} & \frac{\partial r_p}{\partial D_{n+1}} \\ \frac{\partial r_f}{\partial \Delta\gamma} & \frac{\partial r_f}{\partial p_{n+1},} & \frac{\partial r_f}{\partial f_{n+1}} & \frac{\partial r_f}{\partial R_{n+1}} & \frac{\partial r_f}{\partial D_{n+1}} \\ \frac{\partial r_R}{\partial \Delta\gamma} & \frac{\partial r_R}{\partial p_{n+1},} & \frac{\partial r_R}{\partial f_{n+1}} & \frac{\partial r_R}{\partial R_{n+1}} & \frac{\partial r_R}{\partial D_{n+1}} \\ \frac{\partial r_D}{\partial \Delta\gamma} & \frac{\partial r_D}{\partial p_{n+1},} & \frac{\partial r_D}{\partial f_{n+1}} & \frac{\partial r_D}{\partial R_{n+1}} & \frac{\partial r_D}{\partial D_{n+1}} \end{bmatrix} \begin{bmatrix} \mathrm{d}\Delta\gamma \\ \mathrm{d}p_{n+1} \\ \mathrm{d}f_{n+1} \\ \mathrm{d}R_{n+1} \\ \mathrm{d}D_{n+1} \end{bmatrix} = - \begin{bmatrix} \frac{\partial r_{\Delta\gamma}}{\partial \boldsymbol{\varepsilon}_{d\ n+1}^{e\ trial}} \mathrm{d}\boldsymbol{\varepsilon}_{d\ n+1}^{e\ trial} \\ \frac{\partial r_p}{\partial \boldsymbol{\varepsilon}_{v\ n+1}^{e\ trial}} \mathrm{d}\boldsymbol{\varepsilon}_{v\ n+1}^{e\ trial} \\ \frac{\partial r_f}{\partial \boldsymbol{\varepsilon}_{d\ n+1}^{e\ trial}} \mathrm{d}\boldsymbol{\varepsilon}_{d\ n+1}^{e\ trial} \\ 0 \\ \frac{\partial r_D}{\partial \boldsymbol{\varepsilon}_{d\ n+1}^{e\ trial}} \mathrm{d}\boldsymbol{\varepsilon}_{d\ n+1}^{e\ trial} \end{bmatrix}. \quad (6.38)$$

In order to determine the terms $\mathrm{d}\Delta\gamma$, $\mathrm{d}D_{n+1}$, $\mathrm{d}f_{n+1}$, $\mathrm{d}R_{n+1}$ and $\mathrm{d}p_{n+1}$, the inversion of the above system of derivatives is required and can be re-written as:

$$\begin{bmatrix} \mathrm{d}\Delta\gamma \\ \mathrm{d}p_{n+1} \\ \mathrm{d}f_{n+1} \\ \mathrm{d}R_{n+1} \\ \mathrm{d}D_{n+1} \end{bmatrix} = - \begin{bmatrix} C_{1,1} & C_{1,2} & C_{1,3} & C_{1,4} & C_{1,5} \\ C_{2,1} & C_{2,2} & C_{2,3} & C_{2,4} & C_{2,5} \\ C_{3,1} & C_{3,2} & C_{3,3} & C_{3,4} & C_{3,5} \\ C_{4,1} & C_{4,2} & C_{4,3} & C_{4,4} & C_{4,5} \\ C_{5,1} & C_{5,2} & C_{5,3} & C_{5,4} & C_{5,5} \end{bmatrix} . \begin{bmatrix} \frac{\partial r_{\Delta\gamma}}{\partial \boldsymbol{\varepsilon}_{d\ n+1}^{e\ trial}} \mathrm{d}\boldsymbol{\varepsilon}_{d\ n+1}^{e\ trial} \\ \frac{\partial r_p}{\partial \boldsymbol{\varepsilon}_{v\ n+1}^{e\ trial}} \mathrm{d}\boldsymbol{\varepsilon}_{v\ n+1}^{e\ trial} \\ \frac{\partial r_f}{\partial \boldsymbol{\varepsilon}_{d\ n+1}^{e\ trial}} \mathrm{d}\boldsymbol{\varepsilon}_{d\ n+1}^{e\ trial} \\ 0 \\ \frac{\partial r_D}{\partial \boldsymbol{\varepsilon}_{d\ n+1}^{e\ trial}} \mathrm{d}\boldsymbol{\varepsilon}_{d\ n+1}^{e\ trial} \end{bmatrix}, \quad (6.39)$$

where the matrix **C** results from the inversion matrix of the linearized residual equations in order to each variable of the problem. After some algebraic manipulation, the term $\mathrm{d}\Delta\gamma$, $\mathrm{d}D_{n+1}$ and $\mathrm{d}p_{n+1}$ can be written as:

$$\mathrm{d}\Delta\gamma = -C_{1,1} \frac{\partial r_{\Delta\gamma}}{\partial \boldsymbol{\varepsilon}_{d\ n+1}^{e\ trial}} - C_{1,2} \frac{\partial r_p}{\partial \boldsymbol{\varepsilon}_{v\ n+1}^{e\ trial}} - C_{1,3} \frac{\partial r_f}{\partial \boldsymbol{\varepsilon}_{d\ n+1}^{e\ trial}} - C_{1,5} \frac{\partial r_D}{\partial \boldsymbol{\varepsilon}_{d\ n+1}^{e\ trial}}$$

$$\mathrm{d}D_{n+1} = -C_{5,1} \frac{\partial r_{\Delta\gamma}}{\partial \boldsymbol{\varepsilon}_{d\ n+1}^{e\ trial}} - C_{5,2} \frac{\partial r_p}{\partial \boldsymbol{\varepsilon}_{v\ n+1}^{e\ trial}} - C_{5,3} \frac{\partial r_f}{\partial \boldsymbol{\varepsilon}_{d\ n+1}^{e\ trial}} - C_{5,5} \frac{\partial r_D}{\partial \boldsymbol{\varepsilon}_{d\ n+1}^{e\ trial}} \quad (6.40)$$

$$\mathrm{d}p_{n+1} = -C_{2,1} \frac{\partial r_{\Delta\gamma}}{\partial \boldsymbol{\varepsilon}_{d\ n+1}^{e\ trial}} - C_{2,2} \frac{\partial r_p}{\partial \boldsymbol{\varepsilon}_{v\ n+1}^{e\ trial}} - C_{2,3} \frac{\partial r_f}{\partial \boldsymbol{\varepsilon}_{d\ n+1}^{e\ trial}} - C_{2,5} \frac{\partial r_D}{\partial \boldsymbol{\varepsilon}_{d\ n+1}^{e\ trial}}.$$

Substituting the above expressions into Equation 6.36, the close form for the tangent operator can be determined. More details about how to obtain the derivative of each residual equation in function of the elastic strain tensor can be found in Appendix "E".

6.4 CALIBRATION PROCEDURE

In order to determine the materials parameters for the proposed constitutive model, two calibration points are required. The first point will be characterized by a specimen at a high level of stress triaxiality, where a conventional smooth bar specimen is used. For this specimen, the hardening law, $\sigma_y(R)$, for the undamaged material is determined as well as the set of parameters for the nucleation of micro voids $[f_N, S_N, \varepsilon_N]$. The second calibration point will be characterized by a specimen under a pure shear loading condition, where the numerical parameter, q_6, is determined as well as the set of parameters for the nucleation of micro defects under shear $[D_N, S'_N, \varepsilon'_N]$. Here, a butterfly specimen is used under pure shear loading condition.

The new constitutive model will be assessed for two different materials. One of them, strongly and the other weakly dependent on the Lode angle, such as: the aluminum alloy 2024-T351 and the steel 1045, respectively. Furthermore, for both materials, the numerical tests are conducted for three different loading conditions: pure shear, shear/tensile and shear/compression loading conditions. The numerical tests presented here have been performed with Xue's shear mechanism.

6.4.1 Geometry and mesh definition

In order to obtain the material properties for the first calibration point, a classical smooth bar specimen is used where the geometry employed is depicted in Figure 6.7:

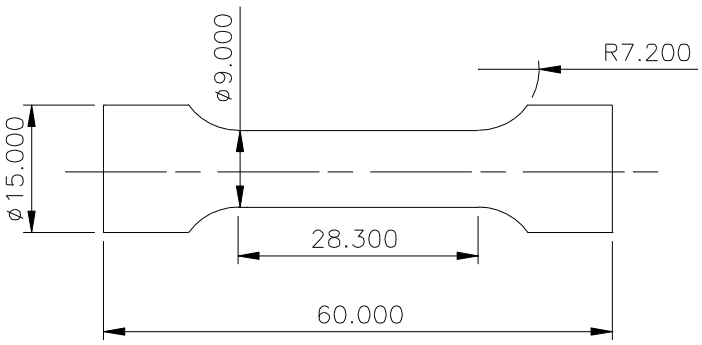

Figure 6.7. Geometry for the smooth bar specimen (dimension in mm). Specimen reproduced from Teng (2008).

In order to trigger necking, a dimensional reduction of 5% in the central diameter of the specimen is used. However, different gauges sections are taken regarding the experimental data (see Teng, 2008). For the aluminum alloy and steel, gauges sections of 25.4 mm and 20.6 mm are used, respectively. The standard eight-nodded axsymmetric quadrilateral element, with four Gauss integration points, is adopted. The initial mesh discretization for both cases is illustrated in Figure 6.8, where only one symmetric quarter of the problem, with the appropriate symmetric boundary conditions imposed to the relevant edges, is modeled. A total number of 1800 elements have been used in the discretization of both smooth bar specimens, amounting to a total of 5581 nodes.

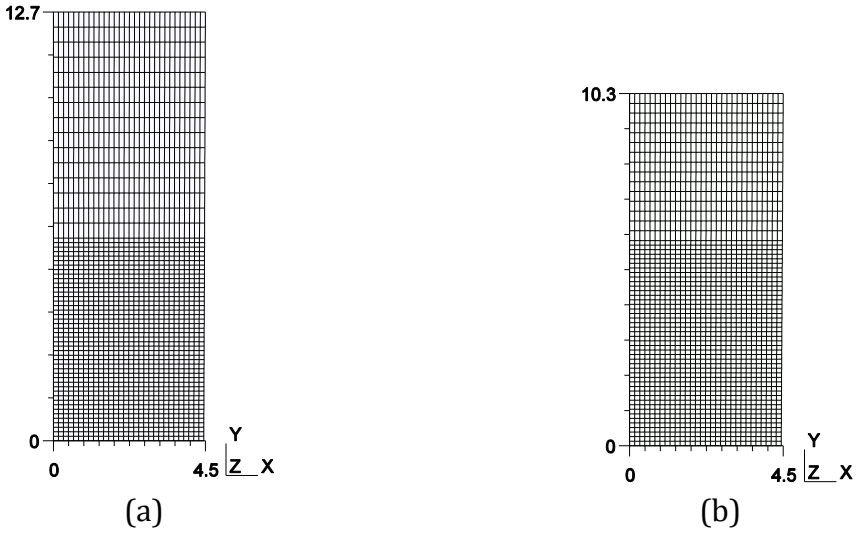

Figure 6.8. Finite elements meshes for (a) aluminum alloy and (b) steel, regarding the gauge section.

For the second calibration point and for the numerical assessment of the behavior of the constitutive model proposed, a butterfly specimen is used. The specimen was initially designed by Bai (2008) and the geometry and general dimensions can be found in Figure 6.9.

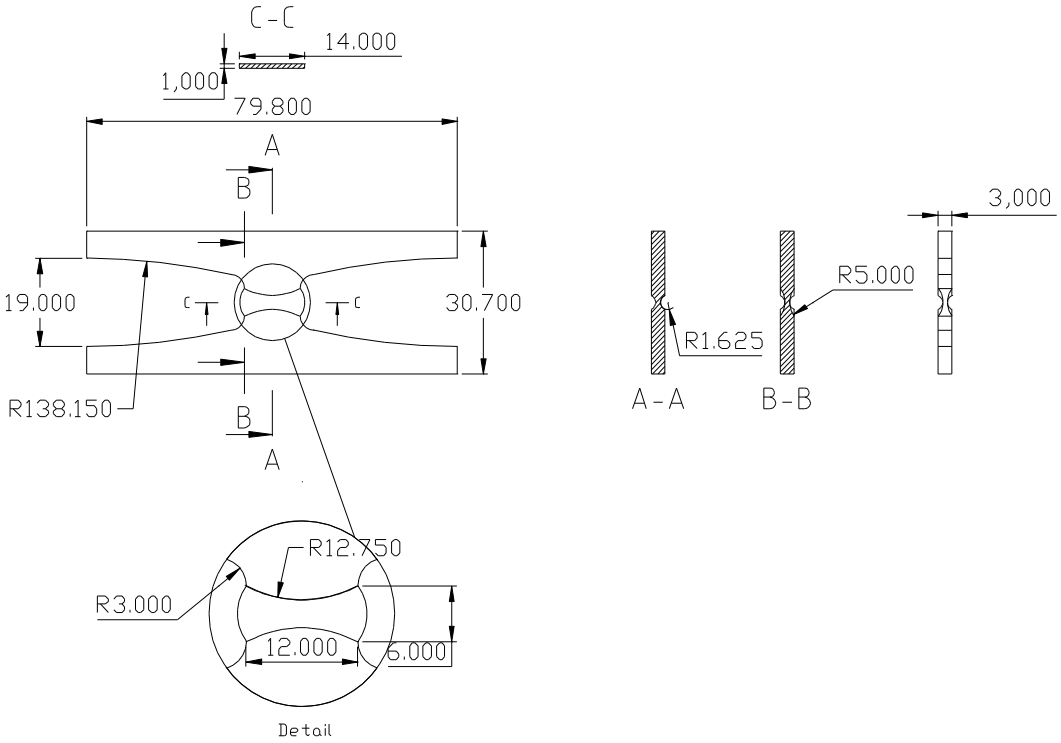

Figure 6.9. Geometry of the butterfly specimen (dimension in mm). Reproduced from Bai (2008).

In this case, a three dimensional finite element mesh of 3.392 twenty nodded elements, with eight Gauss integration points, is used amounting to 17.465 nodes (see Figure 6.10).

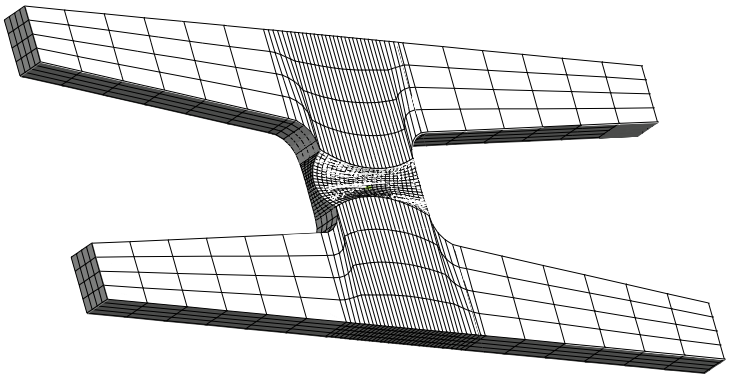

Figure 6.10. Finite element mesh for the butterfly specimen.

6.4.2 First Calibration Point: smooth bar under tensile loading condition

In the present section, the stress-strain curves and the parameters required for simulating the micro void nucleation mechanism of the GTN model are calibrated by a tensile test on a cylindrical smooth bars. Through experimental tests conducted on both materials (see Teng 2008 and Bai 2008), the reaction *versus* displacement curves were determined as well as the stress-strain curves for an elasto-plastic model of von Mises type. An inverse method is adopted in order to calibrate the material parameters for the proposed coupled damage model by forcing the numerical solution of the reaction *versus* displacement curve to be, as close as possible to the experimental one. Figure 6.11a and Figure 6.12a show reaction curves obtained by the proposed model after the application of inverse method. A good agreement between the experimental and numerical results can be observed. Furthermore, the critical volume void fraction is also determined at the point where the model attains the displacement to fracture, experimentally observed (see Figure 6.11b and Figure 6.12b). The critical values obtained are $f_c = 0.06$ and $f_c = 0.076$, for the aluminum alloy 2024-T351 and the steel 1045, respectively.

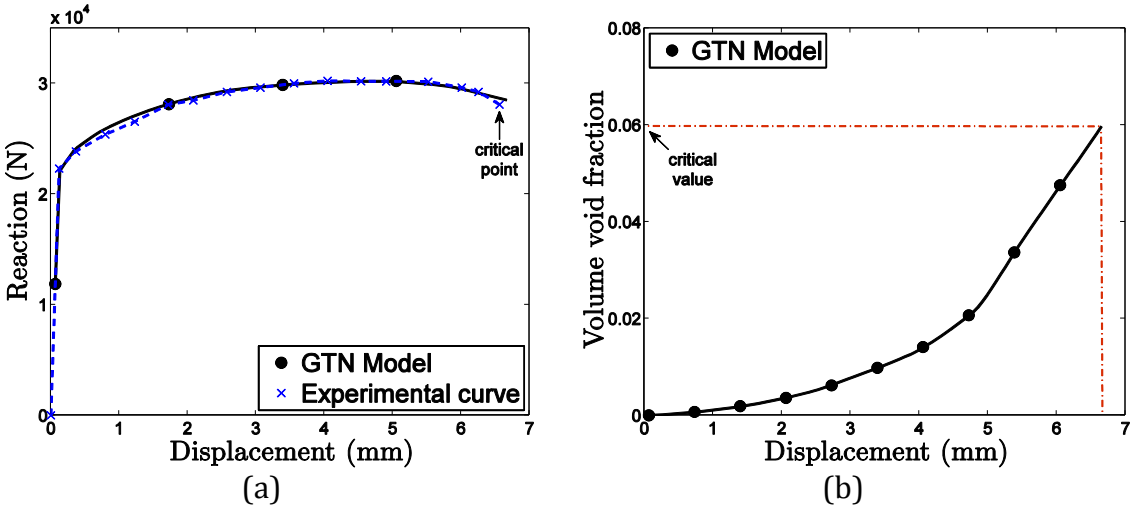

Figure 6.11. (a) Reaction *versus* displacement curve for GTN model and experimental results of the aluminum alloy 2024-T351. (b) Critical volume void fraction parameter calibrated for the material.

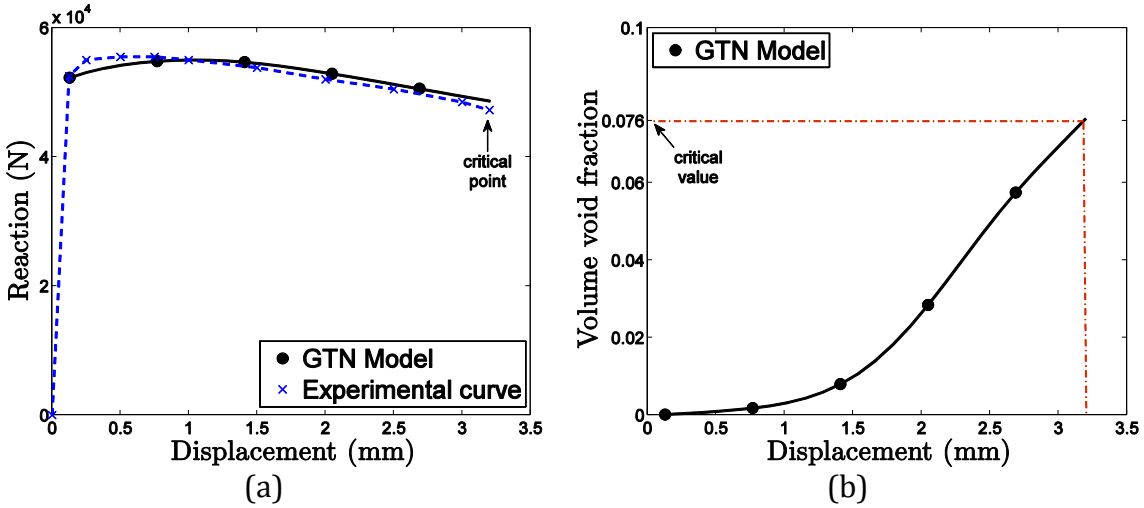

Figure 6.12. (a) Reaction *versus* displacement curve for GTN model and experimental results of the steel 1045. (b) Critical volume void fraction parameter calibrated for the material.

The results of the calibration procedure, in terms of stress-strain curve, can also be observed in Figure 6.13, where both curves, for uncoupled and coupled damage models, were determined.

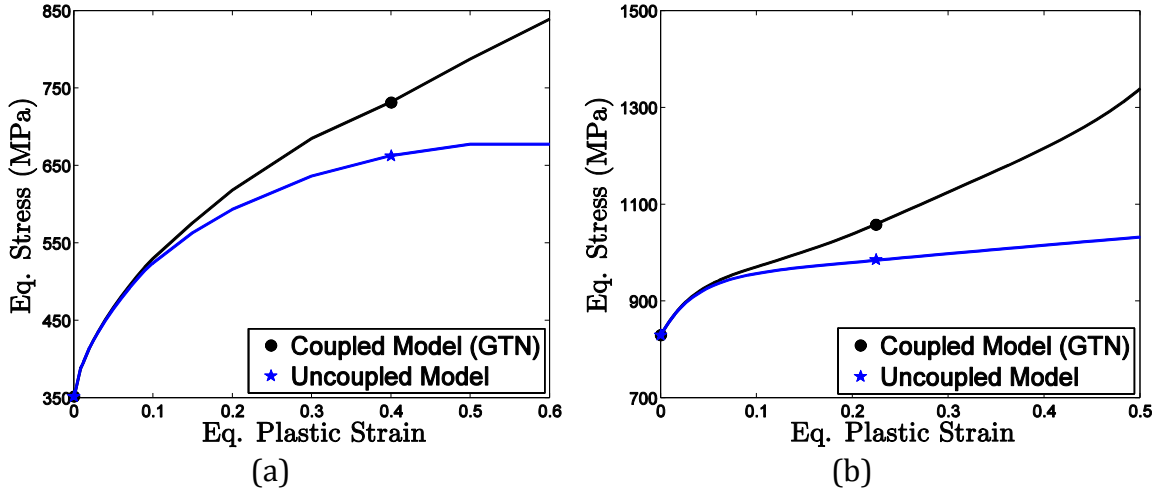

Figure 6.13. Stress-strain curves determined for an uncoupled and coupled models for: (a) aluminum alloy 2024-T351 and (b) steel 1045.

The material properties and other parameters related to the micro void nucleation mechanism obtained by employing an inverse method are listed in Table 6.1.

Table 6.1: Materials properties for the aluminum alloy 2024-T351 and the steel 1045 and materials parameter related to the nucleation of micro-void.

Material	f_N	S_N	ε_N	q_1	q_2	q_3	f_c	E (MPa)	υ
Aluminum alloy *2024-T351*	*0.04*	*0.2*	*0.1*	*1.5*	*1.0*	*2.25*	*0.060*	*72.400*	*0.33*
Steel *1045*	*0.05*	*0.2*	*0.1*	*1.5*	*1.0*	*2.25*	*0.076*	*220.000*	*0.33*

6.4.3 Second Calibration Point: pure shear loading condition.

From this calibration point, the parameters related to the micro defects nucleation mechanism are determined as well as the critical value for the shear damage variable, D_c. Furthermore, details related to the determination of the numerical parameter, q_6, are described. The butterfly specimen is used under a pure shear loading condition and the displacement to fracture, experimentally determined for both materials by Bai (2008), is imposed to the specimen. An inverse method is also adopted, for the calibration of the parameters by forcing the numerical results to be as close as possible to the experimental data.

The behavior of the parameter q_6 can be better understood by looking at Figure 6.14, where the evolution of the effective damage parameter, included in the definition of the shear mechanism proposed by Xue, is observed for different values of q_6. According to the value of the numerical parameter, a different critical shear damage value, D_c, is also established. Figure 6.15 represents the critical shear damage as a function of the value of q_6.

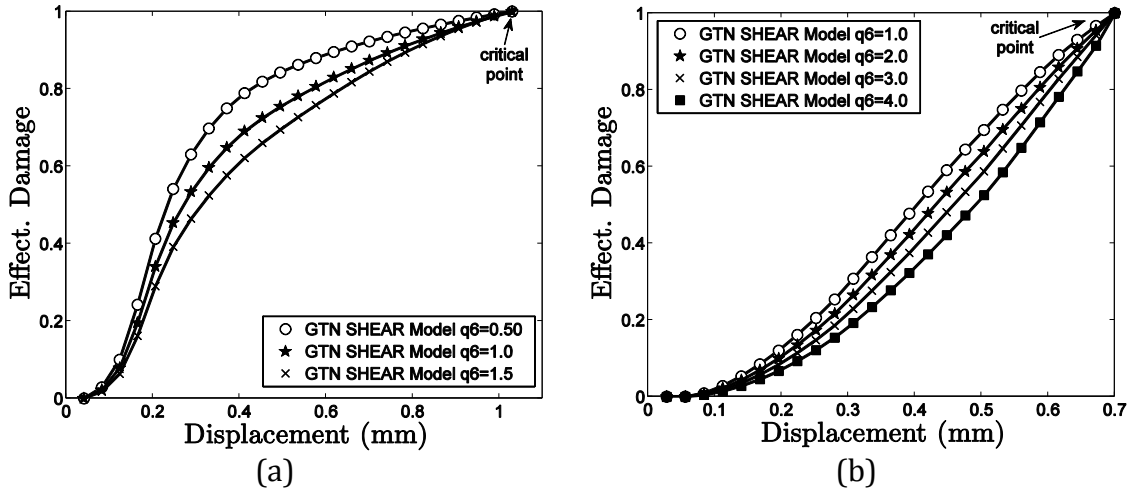

Figure 6.14. Evolution of the shear damage parameter according to the value of q_6 selected for: (a) steel 1045 and (b) aluminum alloy 2024-T351.

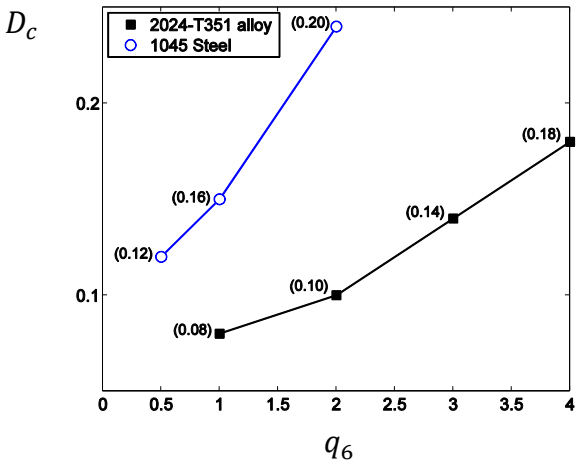

Figure 6.15. Representation of the critical shear damage, D_c, as a function of the numerical parameter, q_6.

Table 6.2 lists the best material parameters obtained after conducting the inverse numerical procedure. The parameters will be used during all numerical simulations.

Table 6.2: Materials parameters for the aluminum alloy 2024-T351 and the steel 1045, related to the nucleation and growth of micro-defects.

Material	d_N	S_N	ε_N	k	q_6	D_c
Aluminum alloy *2024-T351*	*0.08*	*0.15*	*0.10*	*0.10*	*1.00*	*0.08*
Steel *1045*	*0.10*	*0.15*	*0.10*	*0.10*	*1.00*	*0.16*

6.5 NUMERICAL RESULTS

In order to perform a systematic assessment of the new constitutive formulation at a low level of stress triaxiality, several numerical tests are performed using the butterfly specimen and the implicit algorithm described in section 6.3. Three different loading conditions are enforced: pure shear (0°), shear/tensile (10°) and shear/compression (-5°), for two materials: aluminum alloy 2024-T351 and steel 1045. The behavior of some parameters such as the equivalent plastic strain and the displacement at fracture together with the ability to predict the correct fracture location are evaluated. Finally, the numerical results obtained by the new formulation are compared with the results obtained by the GTN models improved with the shear mechanism proposed by as Xue (2008) and by Nahshon & Hutchinson (2008).

6.5.1 Evolution of equivalent plastic strain and damage parameters

The experimental results obtained by Bai (2008), which will be used as reference for comparison, are listed in Table 6.3. In particular, the displacement at fracture, u_f, the equivalent strain at fracture, $\bar{\varepsilon}_f$, and the location of crack initiation are listed for each loading condition and material.

Table 6.3. Reference values for different loading scenarios of two materials.

Angle	Aluminum alloy 2024-T351			Steel 1045		
	u_f	$\bar{\varepsilon}_f$	Fracture location	u_f	$\bar{\varepsilon}_f$	Fracture location
0°	0.70	0.22	Surface of the critical zone	1.03	0.50	Surface of the critical zone
10°	0.50	0.26	Middle of the critical zone	0.42	0.36	Middle of the critical zone
-5°	1.00	0.22	Surface of the critical zone	1.71	0.60	Surface of the critical zone

All the numerical results obtained with the new model, which will be presented in this section, were conducted following the same approach. For each simulation, the butterfly specimen was subjected to a prescribed displacement that matches with the respective critical one experimentally observed that is listed in Table 6.3. The evolution of the damage variables and of the equivalent plastic strain for each loading condition and material are presented in Figures 6.16, 6.17, 6.18 and 6.19. For a pure shear loading condition, we can observe in Figures 6.16a and 6.17a, for the steel 1045 and the aluminum alloy, respectively, that there is an evolution of the shear damage parameter with the applied displacement and the volume void fraction does not grow and remains equal to zero. Hence, the introduction of the new damage variable allows the prediction of failure with the GTN original model and, in this case, plays the main damage role.

Under a combined shear/tensile loading with an angle of 10°, it is possible to observe in Figures 6.16c and 6.17c an evolution of both the shear damage variable and the void volume fraction variable. For this loading case, the prediction of crack initiation is established when the, previously defined, effective damage variable reaches unity (see Equation 6.19). Due to the presence of a multi axial stress state,

an additional factor is introduced by the term $(1 + f_c/D_c)$ in Equation (6.19), to accelerate the prediction of fracture.

In Figures 6.16e and 6.17e we have a combined shear/compression loading condition and, the shear damage parameter also plays a dominant role in the prediction of fracture. In this case, there is a crack closure effect and the degradation of material occurs due to the formation of shear bands, which can be captured by the proposed shear mechanism. The volume void fraction, in this case, is reduce to zero due to a negative hydrostatic pressure.

In Figures 6.16b, 6.16d and 6.16f, the evolution of equivalent plastic strain parameter is shown for different numerical parameter, q_6, using the steel 1045. We can observe that the numerical parameter does not have a strong influence over the evolution of this internal variable. However, it is expected that the parameter q_6 affects the evolution of the shear damage variable and effective damage, which can be seem in Figure 6.18 that presents the evolution of the effective damage parameter for different values of q_6, for both combined loading conditions and pure shear, for the 1045 steel. According to the value of the numerical parameter, the failure condition is established. From the analysis of Figure 6.15, for $q_6 = 0.5$, $q_6 = 1.0$ and $q_6 = 1.5$, the failure condition is met when the shear damage variable is equal to $D_c = 0.12$, $D_c = 0.16$ and $D_c = 0.20$, respectively. Based on the results presented in Figure 6.18, we can observe that when $q_6 = 1.0$, for the 1045 steel, the constitutive formulation predicts a crack formation closer to experimental evidence.

For the aluminum alloy 2024-T351, the evolution of equivalent plastic strain is represented by Figures 6.17b, 6.17d and 6.17e and a similar behavior is also observed, since the numerical constant, q_6, has a small impact in the evolution. For this material, it is possible to conduct a similar analysis for the value of the constant q_6, though the examination of Figures 6.15 and 6.19, and conclude that $q_6 = 1.0$ also predicts failure closer to experimental evidence than the other values (see Figure 6.19). The set of all results can also be analyzed in Table 6.3 and Table 6.4 which list all the numerical results and expected values, experimentally observed, for the equivalent plastic strain and displacement at fracture.

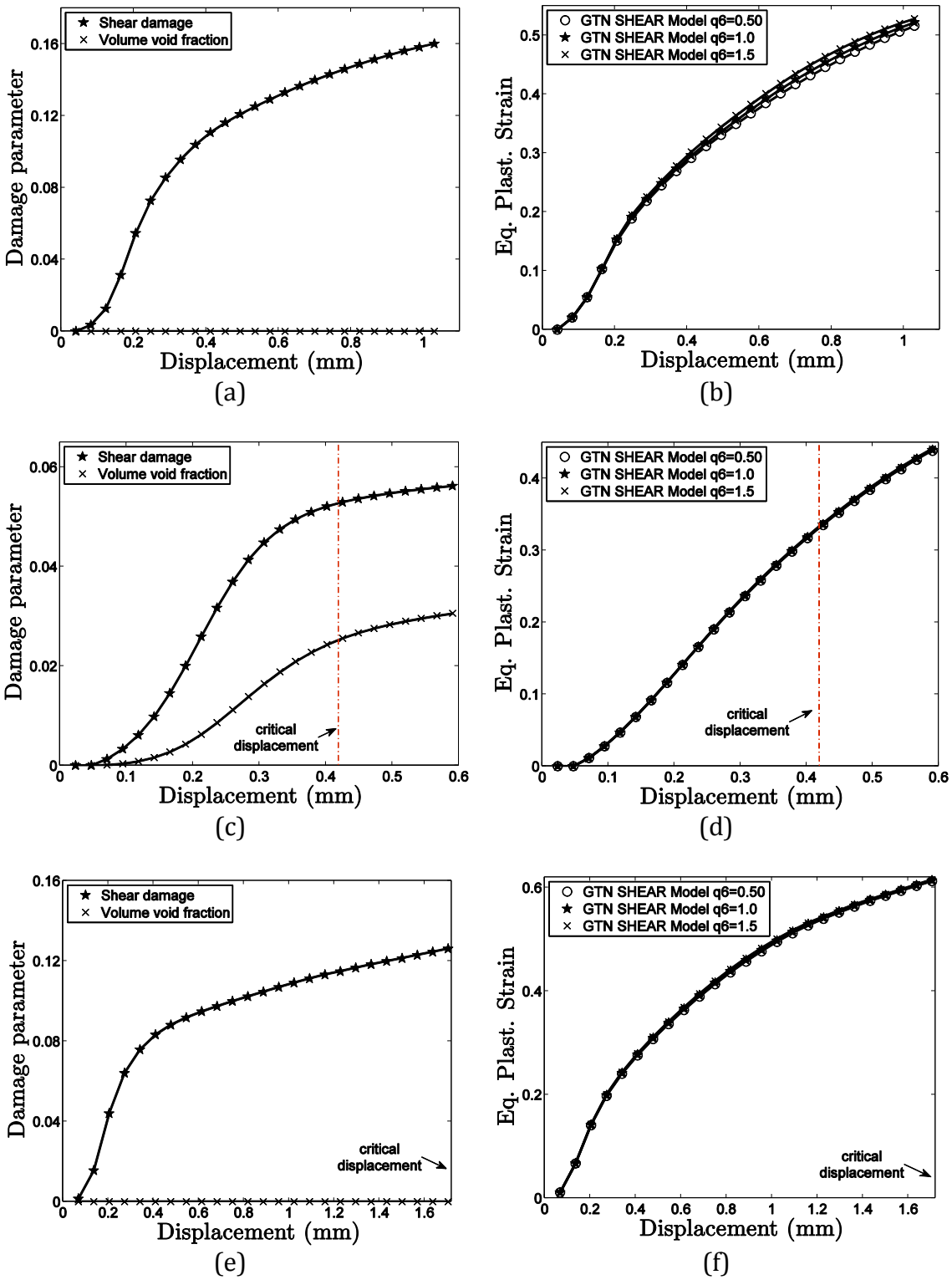

Figure 6.16. Evolution of damage parameter and evolution of equivalent plastic strain for the 1045 steel. (a) and (b) pure shear – (0°), (c) and (d) shear/tensile – (10°) and (e) and (f) shear/compression – (-5°) loading conditions.

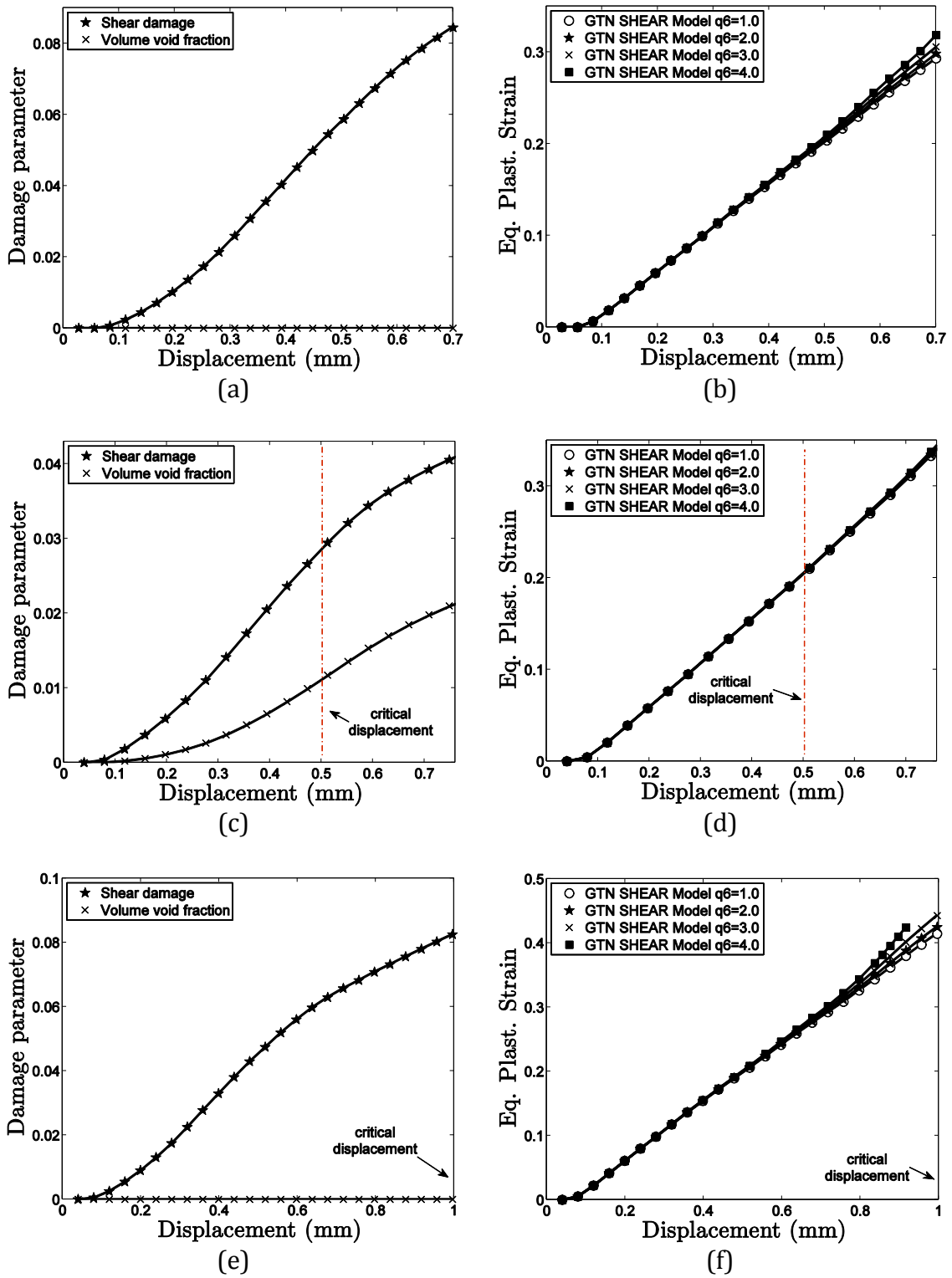

Figure 6.17. Evolution of damage parameter and evolution of equivalent plastic strain for 2024-T351 alloy. (a) and (b) pure shear – (0°), (c) and (d) shear/tensile – (10°) and (e) and (f) shear/compression – (-5°) loading conditions.

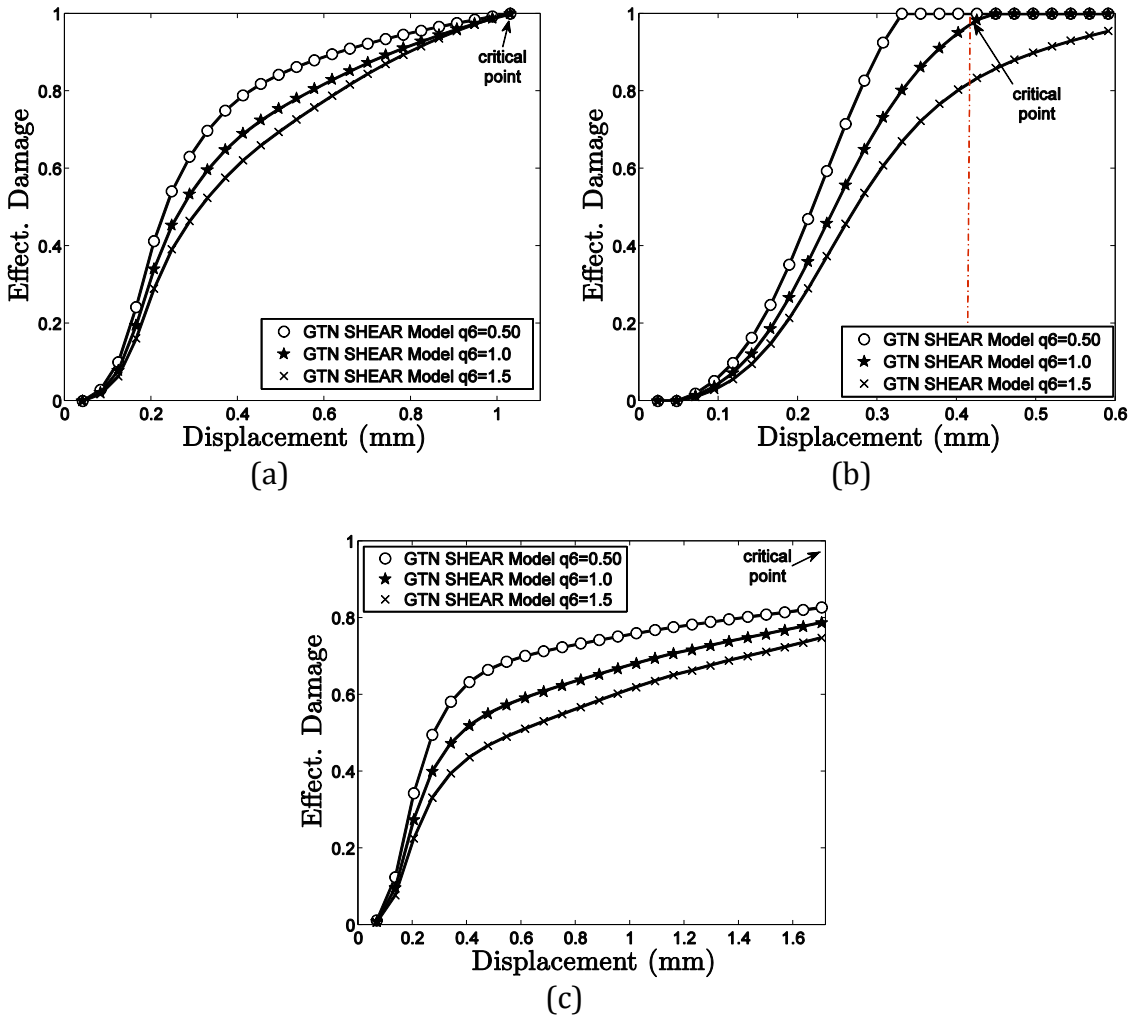

Figure 6.18. Evolution of effective damage parameter for the 1045 steel, under: (a) pure shear – (0°), (b) shear/tensile - (10°) and (c) shear/compression - (-5°) loading conditions.

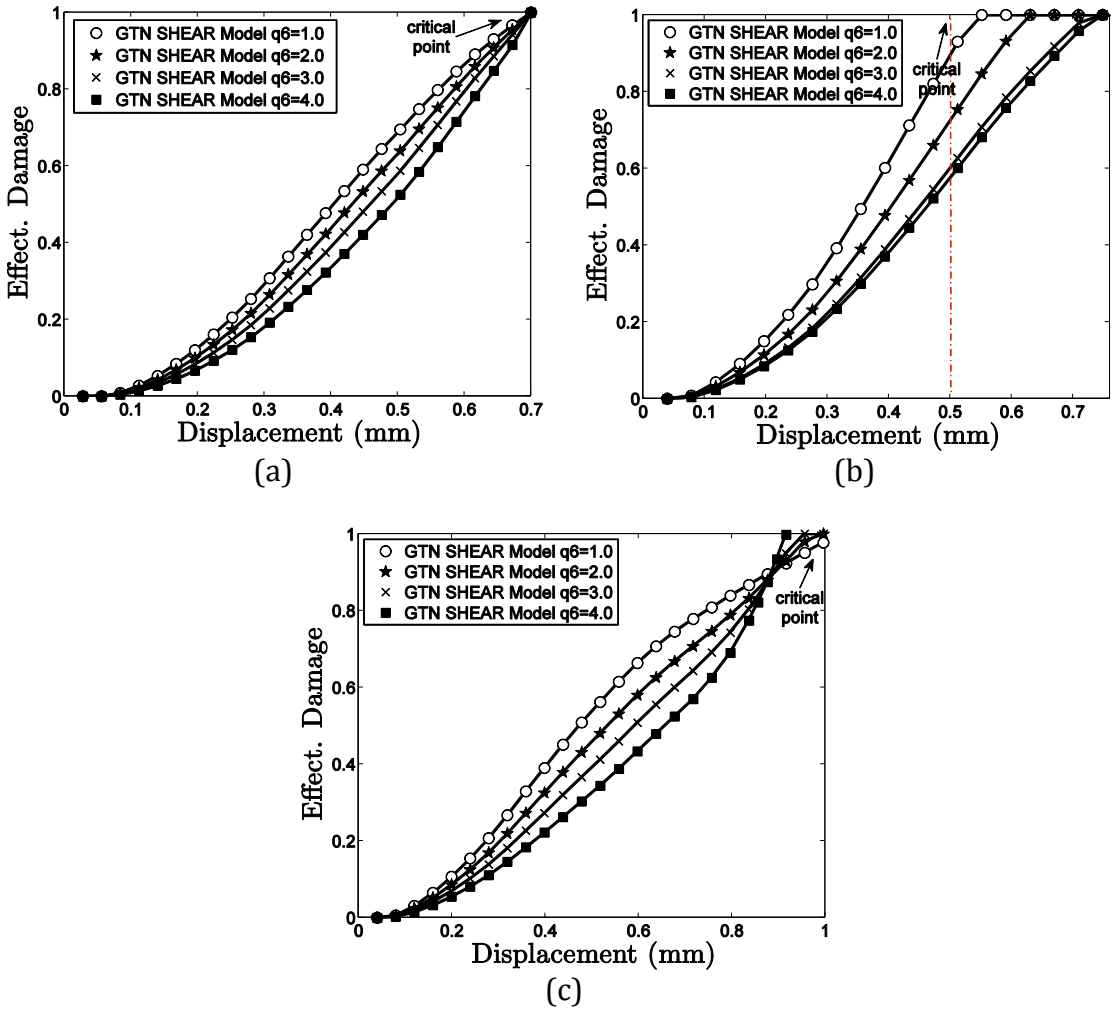

Figure 6.19. Evolution of effective damage parameter for 2024-T351 alloy. (a) pure shear - (0°), (b) shear/tensile - (10°) and (c) shear/compression - (-5°) loading conditions.

Based on numerical results presented, we can conclude that the new formulation has the ability to predict the correct moment to crack formation by appropriately calibrating the numerical constants and parameters of the model. Both the equivalent plastic strain and the displacement, calculated by present formulation, are in close agreement with the experimental data for both loading conditions and materials applied (see Table 6.4 and Table 6.5).

Table 6.4: Numerical results for butterfly specimen using the 1045 steel under different loading conditions.

Angle	Experimental data		Numerical results						
	u_f	$\bar{\varepsilon}_f$	q_6	u_f	$\bar{\varepsilon}^p$	η_{av}	θ_{av}	f	d
0º	*1.03*	*0.50*	0.5	1.03	0.516	0.022	0.061	0.000	0.122
			1.0	*1.03*	*0.522*	*0.022*	*0.060*	*0.000*	*0.160*
			1.5	1.03	0.528	0.021	0.057	0.000	0.204
10º	*0.42*	*0.36*	0.5	0.33	0.257	0.241	0.477	0.018	0.045
			1.0	*0.44*	*0.353*	*0.245*	*0.485*	*0.026*	*0.053*
			1.5	0.59	0.440	0.257	0.507	0.030	0.061
-5º	*1.71*	*0.60*	0.5	1.71	0.611	-0.066	-0.173	0.000	0.100
			1.0	*1.71*	*0.612*	*-0.065*	*-0.173*	*0.000*	*0.126*
			1.5	1.71	0.616	-0.065	-0.173	0.000	0.153

Table 6.5: Numerical results for butterfly specimen using the aluminum alloy 2024-T351 under different loading conditions.

Angle	Experimental data		Numerical results						
	u_f	$\bar{\varepsilon}_f$	q_6	u_f	$\bar{\varepsilon}^p$	η_{av}	θ_{av}	f	d
0º	*0.70*	*0.22*	*1.0*	*0.70*	*0.292*	*0.018*	*0.048*	*0.000*	*0.084*
			2.0	0.70	0.298	0.017	0.048	0.000	0.107
			3.0	0.70	0.305	0.017	0.047	0.000	0.137
			4.0	0.70	0.318	0.017	0.046	0.000	0.179
10º	*0.50*	*0.26*	*1.0*	*0.55*	*0.230*	*0.250*	*0.486*	*0.013*	*0.032*
			2.0	0.63	0.271	0.254	0.492	0.017	0.039
			3.0	0.75	0.336	0.257	0.494	0.021	0.051
			4.0	0.75	0.337	0.264	0.502	0.021	0.056
-5º	*1.00*	*0.22*	*1.0*	*1.00*	*0.414*	*-0.066*	*-0.176*	*0.000*	*0.084*
			2.0	0.98	0.424	-0.065	-0.173	0.000	0.110
			3.0	0.95	0.432	-0.064	-0.169	0.000	0.140
			4.0	0.93	0.455	-0.063	-0.165	0.000	0.190

6.5.2 Prediction of the correct fracture location

Another important feature to be analyzed, in order to validate the new constitutive formulation, is the ability to predict the correct fracture location. Based on experimental tests performed by Bai (2008), using the butterfly specimen, it can be observed that under a pure shear loading condition, the micro crack is initiated in the surface of the critical zone. However, when combined shear/tensile loading condition is applied, the crack is formed in the middle of the thickness and grows toward the surface of the critical zone. Under a combined shear/compression loading (-5°), the surface of the critical zone is also the location of crack formation.

Figures 6.20 and 6.21 present the contour of effective damage for the steel 1045 and the aluminum alloy 2024-T351, respectively, at fracture. It is possible to conclude that the new damage formulation has the ability to predict the correct fracture location in all loading conditions.

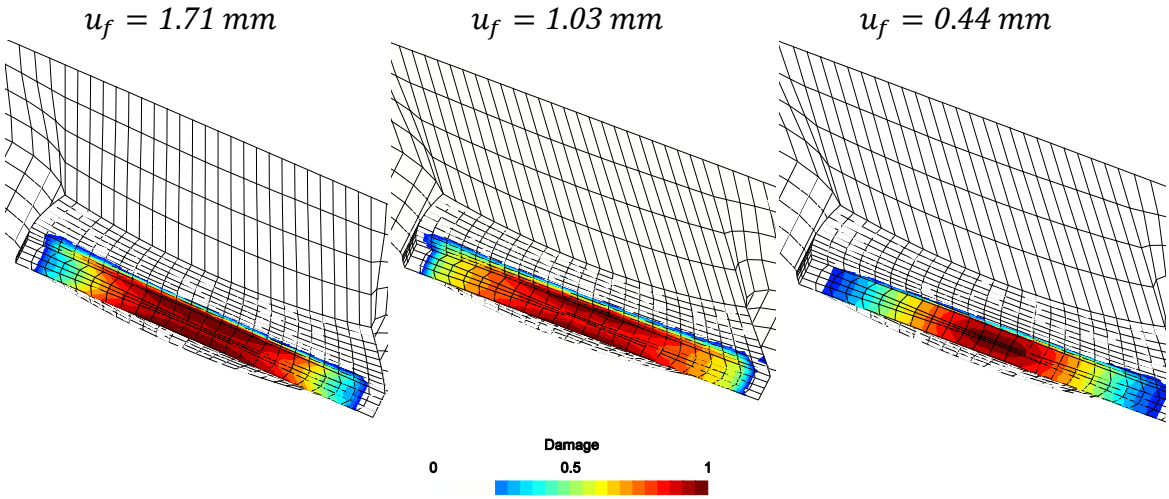

Figure 6.20. Effective damage contour for the butterfly specimen using the 1045 steel, under: (a) shear/compression - (-5°), (b) pure shear - (0°) and (c) shear/tensile - (-10°) loading conditions.

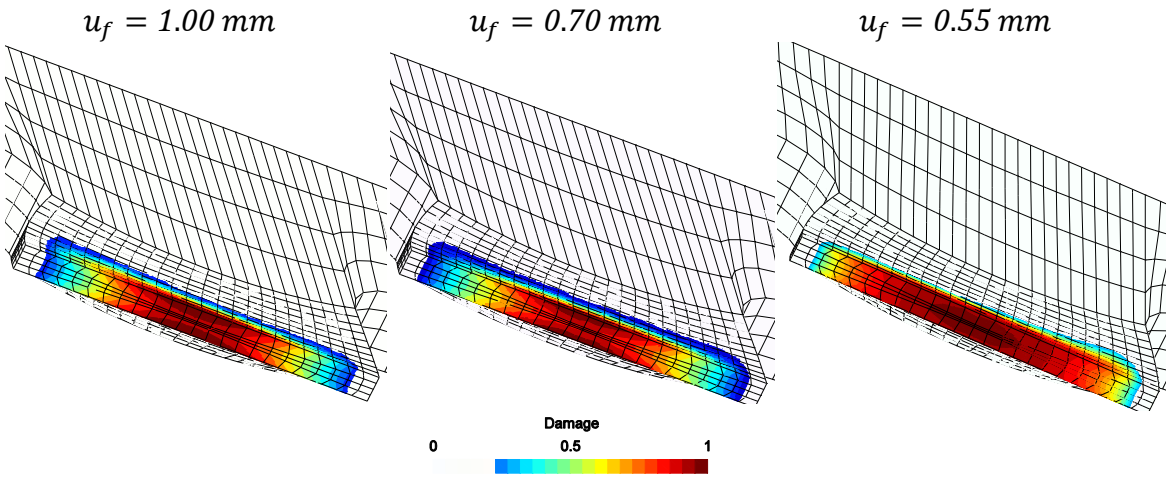

Figure 6.21. Effective damage contour for the butterfly specimen using the aluminum 2024-T351 alloy, under: (a) shear/compression - (-5°), (b) pure shear - (0°) and (c) shear/tensile - (-10°) loading conditions.

The predictive ability of the new model, in terms of fracture location, can also be compared against two recent extensions of the GTN model, which were presented in Chapter 5 of this thesis. The accuracy of the three models in the prediction of the fracture location is evaluated here for a combined shear tensile loading of 10° for the steel 1045. Figure 6.22a illustrates the contour of the damage parameter for Nahshon & Hutchinson shear mechanism (Nahshon & Hutchinson, 2008), Figure 22b for Xue shear mechanism (Xue, 2008) and Figure 6.22c for the new model. We can observe that only the new model predicts the initiation of failure in agreement with experimental evidence. The prediction of the GTN model extended with Xue's shear mechanism is in complete disagreement with experimental evidence and the prediction of the GTN model extended with Nahshon & Hutchison shear mechanism is somewhat spread along the critical section, which may suggest a certain vagueness to the model.

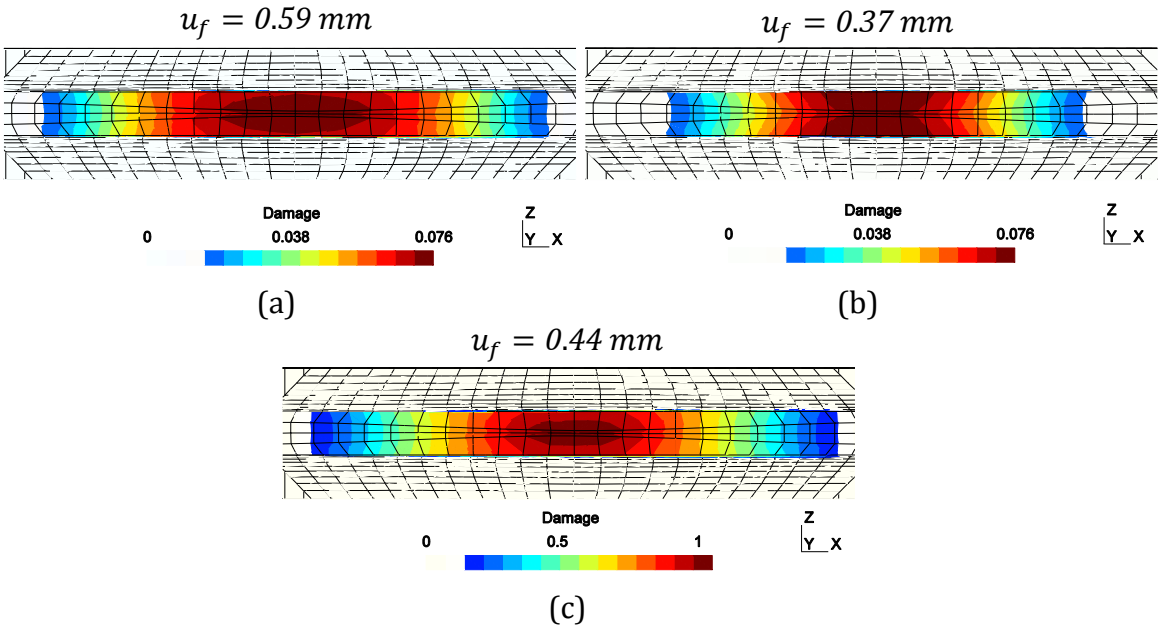

Figure 6.22. Damage parameter contour for the butterfly specimen using the 1045 steel. (a) Nahshon & Hutchinson shear mechanism, (b) Xue shear mechanism and (c) new model. Section AA at the critical zone.

6.5.3 Representation in the three dimensional fracture locus

In order to qualitatively judge the constitutive model, we can represent the numerical results, listed in Tables 6.4 and 6.5, within the so-called three dimensional fracture locus, originally proposed by Bai (2008). For the 1045 steel, Bai (2008) proposed a surface represented by the interpolation of the equivalent plastic strain, stress triaxiality and Lode angle. The fracture locus for the steel 1045 was calibrated by classical specimens in different loading condition, see Bao (2004) and Bai (2008). Figure 6.23 represents the projection of the three dimensional fracture locus on the space of equivalent plastic strain *versus* stress triaxiality. We can observe that the numerical results, obtained by the new model, have a good agreement with the calibrated curve for different levels of the Lode angle. In the same Figure, the numerical results obtained by the Nahshon & Hutchinson and Xue formulations are also plotted, using only pure shear and combined shear/tensile loading conditions. In both cases, these formulations do not present an uniform behavior in the prediction of results. Nahshon & Hutchinson's model is more accurate than Xue's model under pure shear loading condition and Xue agrees better with experimental results under combined loading conditions. However, the new model is in agreement with the fracture surface for both conditions.

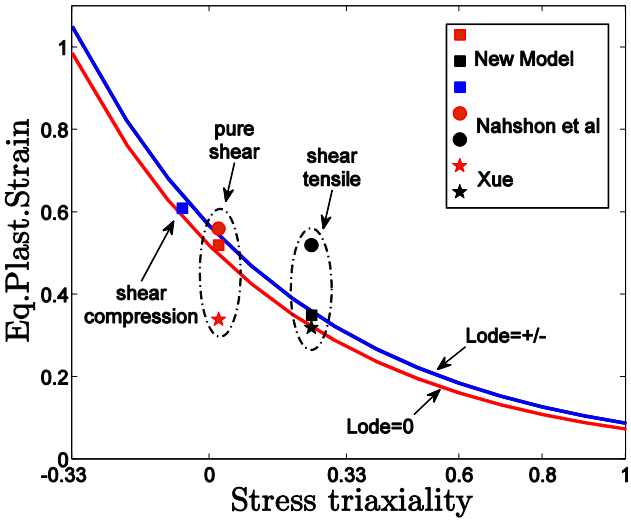

Figure 6.23. Projection of three dimensional fracture *loci* for steel 1045.

6.6 CONCLUSIONS

In this chapter, a new formulation was proposed to improve the original GTN model, regarding the ability to predict ductile fracture under a low level of stress triaxiality. Firstly, a new shear mechanism was proposed that is a function of the equivalent plastic strain, stress triaxiality and Lode angle. This mechanism can capture the elongation of micro-defects, when shear loading condition is present. Furthermore, a new micro-defects nucleation mechanism was proposed which is responsible for triggering the evolution of the shear damage parameter, since the new mechanism is independent on the volume void fraction. Then, the new damage parameter was coupled in GTN constitutive formulation in such a way that only affects the deviatoric stress contribution. Thus, the new model has two independent damage parameters: first one affecting only the hydrostatic stress component and the other affecting the deviatoric stress component.

Numerical tests were conducted, with an implicit integration algorithm, in order to evaluate the formulation ability to predict the crack formation. A butterfly specimen was employed and two different materials: the steel 1045 and the aluminum alloy 2024-T351 were used. In all loading conditions, the model behaves well, either in the determination of the correct level of equivalent plastic strain and displacement at fracture, or in prediction of the location of crack formation.

The introduction of two damage parameters affecting separate components of the stress tensor stress critically affects the evolution of internal variables and

allows more accurate values at the time of crack formation. Furthermore, the introduction of a new micro-defects nucleation mechanism facilitates the calibration model and thus an improved performance for a wide range of stress triaxiality. The introduction of the stress triaxiality dependence in the evolution of shear damage parameter also enhanced the prediction of the fracture location under combined loading conditions, since this parameter influences the behavior of material under low stress triaxiality. An effective damage variable is determined in post-processed step as a function of both volume void fraction and shear damage parameter. A penalization factor is introduced in order to accelerate the damage evolution due to the presence of multi axial loading conditions.

In spite of the best performance of this formulation when compared to the models available in the literature, the introduction of more parameters that need to be calibrated requires special attention. In particular, two calibration points are required to fully define the model. A calibration point at high triaxiality, which was already required in GTN original model, and now a new point at low triaxiality, to obtain the parameters that govern the new shear damage evolution law. In summary, the new model was formulated in order to perform well in all loading conditions and for different materials. From the results presented, it is possible to conclude that the objective was achieved for the cases tested.

CHAPTER 7

An Enhanced Micromechanical Constitutive Model for the Prediction of the Loading History Effect with Ductile Fracture

7.1 INTRODUCTION

The loading history to which a material is subjected is an effect that has been studied for several decades by numerous researchers, such as Muschenborn and Sonne (1975), Graf and Hosford (1994) and Stoughton (2000), among others, in order to characterize ductile fracture under proportional and non-proportional loading conditions. This effect has an important impact on the mechanical behavior of ductile materials, which has been clearly observed on strain-based forming limit diagrams, since the material response is not unique under non-proportinal loading conditions (Stoughton, 2000; Cao et al, 2000; Chow et al, 2001; Bai et al, 2007). In addition, the material parameters used in fracture models are commonly calibrated based on monotonic tests. Therefore, under more complex loading conditions, several researchers (Johnson and Cook, 1985; Bao, 2003; Bao et al, 2004; Bai et al, 2006) have shown that this calibration strategy, leads to an incorrect prediction when complex loading conditions are present.

In this chapter, the extended GTN model proposed in Chapter 6 is enhanced with a kinematic hardening rule in order to improve its predictive ability when subjected to more complex loading scenarios. Firstly, the set of equations that govern the evolution of the internal variables of the model are described with emphasis on the nonlinear kinematic hardening law employed. Then, the numerical treatment required for the implementation of the constitutive model within an implicit quasi-static finite element framework is described in detail. The performance of the enhanced model was analyzed using the “butterfly” specimen and with the aluminum alloy 2024-T351. Details of the calibration procedure carried out within the context of this study are also described in detail. Three

numerical tests with complex external loading conditions were conducted: *i)* pure shear (+0º) followed by combined shear/tensile (+30º) loading condition; *ii)* compression (-90º) followed by traction (+90º) and finally *iii)* a reversal shear loading (−0º followed by +0º). At the end of each numerical simulation the behavior of the internal variables was analyzed. In particular, the evolution of both damage parameters, the evolution of the equivalent plastic strain, the reaction *versus* displacement curve and the contours of the effective damage parameter. Finally, the numerical results obtained with the enhanced model were compared with experimental data. As observed in the present work, the new model is able to capture the onset of fracture in close agreement with experimental evidence when the specimen is subjected to complex external loading conditions.

7.2 CONSTITUTIVE MODEL WITH A MIXED HARDENING RULE

In order to evaluate the effect of the loading history on the mechanical behavior of ductile materials and thus measure its internal degradation, the so-called Bauschinger effect was incorporated in the extended GTN model (see Lemaitre, 2001). This important effect recognizes that the yield stress of a metal is different in opposite directions (for example traction and compression), when the plastic regime is reached. In order to capture this behavior, phenomenological models introduce the so-called kinematic hardening. Figure 7.1 shows schematically the effect of Bauschinger for a traction/compression loading condition, as well as, the isotropic hardening effect. In Figure 7.1, σ_y represents the initial yield stress of the material, R is the thermodynamic force associated with the isotropic hardening and β represent the so-called backstress tensor.

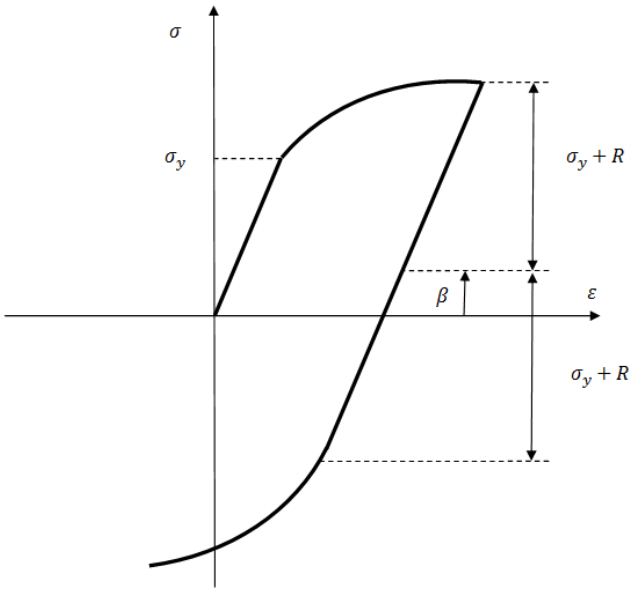

Figure 7.1. Stress-strain curve including mixed isotropic and kinematic hardening.

In this work, the evolution law for the backstress tensor employed was the one proposed by Prager (see De Souza Neto, 2008), which considers a nonlinear kinematic hardening, according to:

$$\dot{\boldsymbol{\beta}} = \frac{2}{3} H^K(R)\dot{\boldsymbol{\varepsilon}}^p, \tag{7.1}$$

where $\dot{\boldsymbol{\beta}}$ represents the rate of growth for the backstress, $\dot{\boldsymbol{\varepsilon}}^p$ is the rate of the equivalent plastic strain and H^K is the kinematic hardening modulos that is determined by the function:

$$H^K(R) = \frac{d\bar{\beta}(R)}{dR}, \tag{7.2}$$

where $\bar{\beta}(R)$ represents a scalar function of the backstress with relation to the internal variable associated with the isotropic hardening. It can be mentioned that other evolution equations for the backstress are suggested in literature, such as the Armstrong and Frederick model (see De Souza Neto et al, 2008), Morz model (see Lemaitre 2001), among of others.

Thus, a new yield function for the extended GTN model can be established as follow:

$$\Phi(\boldsymbol{\sigma},\boldsymbol{\beta},r,f,D)=\frac{J_2(\boldsymbol{\eta})}{1-D}-\frac{1}{3}\left[1+q_3f^2-2q_1f\cosh\left(\frac{3q_2p}{2\sigma_y}\right)\right]\sigma_y^2\ , \tag{7.3}$$

where $\boldsymbol{\eta}$ represents the so-called reference tensor, that can be determined as:

$$\boldsymbol{\eta}=\boldsymbol{S}-\boldsymbol{\beta}\ , \tag{7.4}$$

where $\boldsymbol{S}$ represents the deviatoric stress tensor and J_2 is now the second invariant of the reference tensor. The governing equations of the extended GTN model with mixed nonlinear isotropic and kinematic hardening are summarized in Box 7.1.

Box 7.1. Extended GTN model with nonlinear isotropic and kinematic hardening.

(i) Elasto-plastic split of the strain tensor

$$\boldsymbol{\varepsilon}=\boldsymbol{\varepsilon}^e+\boldsymbol{\varepsilon}^p$$

(ii) Elastic law

$$\boldsymbol{\sigma}=\mathbb{D}^e:\boldsymbol{\varepsilon}^e$$

(iii) Yield function

$$\Phi(\boldsymbol{\sigma},\boldsymbol{\beta},r,f,D)=\frac{J_2(\boldsymbol{\eta})}{1-D}-\frac{1}{3}\left[1+q_3f^2-2q_1f\cosh\left(\frac{3q_2p}{2\sigma_y}\right)\right]\sigma_y^2$$

(iv) Plastic flow and evolution equations for $\boldsymbol{\beta}$, R, f and D.

$$\dot{\boldsymbol{\varepsilon}}^p=\dot{\gamma}\left[\frac{\boldsymbol{\eta}}{(1-D)}+\frac{1}{3}\sigma_y q_1q_2f\sinh\left(\frac{3q_2p}{2\sigma_y}\right)\boldsymbol{I}\right]$$

$$\dot{\boldsymbol{\beta}}=\frac{2}{3}H^K(R)\dot{\boldsymbol{\varepsilon}}^p$$

$$\dot{R}=\frac{\dot{\gamma}}{(1-f-D)}\left\{q_1q_2fp\sinh\left(\frac{3q_2p}{2\sigma_y}\right)+\frac{2}{3}\sigma_y\left[1+q_3f^2-2q_1f\cosh\left(\frac{3q_2p}{2\sigma_y}\right)\right]\right\}$$

$$\dot{f}=(1-g_0)\frac{f_N}{S_N\sqrt{2\pi}}\exp\left[-\frac{1}{2}\left(\frac{\bar{\varepsilon}^p-\varepsilon_N}{S_N}\right)^2\right]\dot{\bar{\varepsilon}}^p+(1-f)\dot{\varepsilon}_v^p$$

continue Box 7.1.

$$\dot{D} = g_0 \frac{D_{\mathrm{N}}}{s'_N\sqrt{2\pi}} \exp\left[-\frac{1}{2}\left(\frac{\overline{\varepsilon}^p - \varepsilon'_N}{s'_N}\right)^2\right]\dot{\overline{\varepsilon}}^p + q_6\dot{D}^s[g_0(\xi)]^{\frac{1}{|\Gamma|+k}}$$

where,

$$\dot{D}^s = q_4 D^{q_5}\overline{\varepsilon}^p\dot{\overline{\varepsilon}}^p \qquad\qquad g_0 = 1-\xi^2$$

and,

$$\dot{\overline{\varepsilon}}^p = \dot{\gamma}\sqrt{\frac{2}{3}\left\{\frac{\boldsymbol{\eta}:\boldsymbol{\eta}}{(1-D)^2} + \frac{1}{3}\left[\sigma_y q_1 q_2 f \sinh\left(\frac{3q_2 p}{2\sigma_y}\right)\right]^2\right\}} \qquad \dot{\varepsilon}_v^p = \dot{\gamma}\sigma_y q_1 q_2 f \sinh\left(\frac{3q_2 p}{2\sigma_y}\right)$$

(v) Loading/unloading criterion

$$\dot{\gamma} \geq 0\,, \qquad \Phi \leq 0\,, \qquad \dot{\gamma}\Phi = 0$$

7.3 NUMERICAL TREATMENT

In this section, the numerical strategy employed to derive the integration algorithm for the extended GTN model with mixed isotropic and kinematic hardening is presented. A finite strain algorithm to extend the infinitesimal theory is introduced for the kinematic hardening evolution (see De Souza Neto et al, 2008).

7.3.1 Return Mapping Algorithm for Small Strains

Analogously to what was done in previous chapters, for the present model, the stress update procedure is also based on the so-called operator split concept (see Simo & Hughes, 1998; De Souza Neto et al., 2008), which consists in splitting the problem in two parts: an elastic predictor, where the problem is assumed to be elastic and, a plastic corrector, in which the system of residual equations comprising the elasticity law, plastic consistency and the rate equations is solved, taking the results of the elastic predictor stage as initial conditions. It is important to highlight that in the present formulation, an additional evolution equation is introduced in the plastic corrector to represent the evolution of the backstress tensor (see Equation 7.1). Box 7.2 summarizes the overall return mapping

algorithm for the extended GTN model with isotropic and kinematic nonlinear hardening at infinitesimal strains.

Box 7.2. Fully implicit Elastic predictor/Return mapping algorithm.

(i) Evaluate the elastic trial state: Given the incremental strain $\Delta\boldsymbol{\varepsilon}$ and the state variables at t_n:

$$\boldsymbol{\varepsilon}_{n+1}^{e\,trial} = \boldsymbol{\varepsilon}_n^e + \Delta\boldsymbol{\varepsilon} \quad ; \quad \bar{\varepsilon}_{n+1}^{p\,trial} = \bar{\varepsilon}_n^p \quad ; \quad R_{n+1}^{trial} = R_n$$

$$f_{n+1}^{trial} = f_n \quad ; \quad D_{n+1}^{trial} = D_n \quad ; \quad \boldsymbol{S}_{n+1}^{trial} = 2G\boldsymbol{\varepsilon}_{n+1}^{e\,trial}$$

$$p_{n+1}^{trial} = K\varepsilon_{v\,n+1}^{e\,trial} \quad ; \quad \boldsymbol{\beta}_{n+1}^{trial} = \boldsymbol{\beta}_n \quad ; \quad \sigma_y^{trial} = \sigma_y\left(R_{n+1}^{trial}\right)$$

$$\boldsymbol{\eta}_{n+1}^{trial} = \boldsymbol{S}_{n+1}^{trial} - \boldsymbol{\beta}_{n+1}^{trial}$$

(ii) Check plastic admissibility:

IF $\Phi^{trial} = \frac{J_2^{trial}(\boldsymbol{\eta}_{n+1}^{trial})}{1-D_{n+1}^{trial}} - \frac{1}{3}\left[1 + q_3 f_{n+1}^{trial\,2} - 2q_1 f_{n+1}^{trial}\cosh\left(\frac{3q_2 p_{n+1}^{trial}}{2\sigma_y^{trial}}\right)\right]\sigma_y^{trial\,2} \leq 0$

THEN set $(\cdot)_{n+1} = (\cdot)_{n+1}^{trial}$ ***(elastic step)*** and go to *(v)*

ELSE go to (iii)

(iii) Return mapping ***(plastic step)***: *Solve the system of equations below for* $\Delta\gamma$,p_{n+1},f_{n+1}, R_{n+1} and D_{n+1}, *using Newton-Raphson method:*

$$\begin{Bmatrix} \frac{J_{2\,n+1}}{(1-D_{n+1})} - \frac{1}{3}\left[1 + q_3 {f_{n+1}}^2 - 2q_1 f_{n+1}\cosh\left(\frac{3q_2 p_{n+1}}{2\sigma_y}\right)\right]\sigma_y^2 \\ p_{n+1} - p_{n+1}^{trial} + \Delta\gamma K\sigma_y q_1 q_2 f_{n+1}\sinh\left(\frac{3q_2 p_{n+1}}{2\sigma_y}\right) \\ f_{n+1} - f_{n+1}^{trial} - \Delta f^n - \Delta f^g \\ R_{n+1} - R_{n+1}^{trial} - \Delta R \\ D_{n+1} - D_{n+1}^{trial} - \Delta D^n - q_6\Delta D^s \end{Bmatrix} = \begin{Bmatrix} 0 \\ 0 \\ 0 \\ 0 \\ 0 \end{Bmatrix}$$

where,

$$J_{2\,n+1} = \frac{1}{2\left[1 + \frac{2G\Delta\gamma}{(1-D_{n+1})} + \frac{2H^K\Delta\gamma}{3(1-D_{n+1})}\right]^2}\left\{\boldsymbol{\eta}_{n+1}^{trial} : \boldsymbol{\eta}_{n+1}^{trial} + \frac{1}{3}\left[\Delta\gamma\frac{2}{3}H^K\sigma_y q_1 q_2 f_{n+1}\sinh\left(\frac{3q_2 p_{n+1}}{2\sigma_y}\right)\right]^2\right\}$$

$$\Delta D^n = g_0\frac{D_N}{S'_N\sqrt{2\pi}}\exp\left[-\frac{1}{2}\left(\frac{\bar{\varepsilon}_{n+1}^p - \varepsilon'_N}{S'_N}\right)^2\right]\Delta\bar{\varepsilon}^p$$

continue Box 7.2.

$$\Delta D^s = [g_0]^{\left(1/|\Gamma_{n+1}|+k\right)} q_4 D^{q_5}\, \bar{\varepsilon}^p \Delta\bar{\varepsilon}^p$$

$$g_0 = (1-\xi_{n+1}^2)$$

$$\Delta f^n = (1-g_0)\frac{f_N}{S_N\sqrt{2\pi}}\exp\left[-\frac{1}{2}\left(\frac{\bar{\varepsilon}_{n+1}^p - \varepsilon_N}{S_N}\right)^2\right]\Delta\bar{\varepsilon}^p$$

$$\Delta f^g = (1-f_{n+1})\Delta\gamma\sigma_y q_1 q_2 f_{n+1}\sinh\left(\frac{3q_2 p_{n+1}}{2\sigma_y}\right)$$

$$\Delta R = \frac{\Delta\gamma}{(1-f_{n+1}-D_{n+1})}\left\{q_1 q_2 f_{n+1} p_{n+1}\sinh\left(\frac{3q_2 p_{n+1}}{2\sigma_y}\right) + \frac{2}{3}\sigma_y\left[1+q_3 {f_{n+1}}^2 - 2q_1 f_{n+1}\cosh\left(\frac{3q_2 p_{n+1}}{2\sigma_y}\right)\right]\right\}$$

(iv) Update the others state variables:

$$\boldsymbol{\eta}_{n+1} = \frac{\boldsymbol{\eta}_{n+1}^{trial} - \Delta\gamma\frac{2}{9}H^K\sigma_y q_1 q_2 f_{n+1}\sinh\left(\frac{3q_2 p_{n+1}}{2\sigma_y}\right)\boldsymbol{I}}{\left[1+\frac{2G\Delta\gamma}{(1-D_{n+1})}+\frac{2H^K\Delta\gamma}{3(1-D_{n+1})}\right]}$$

$$\boldsymbol{S}_{n+1} = \boldsymbol{S}_{n+1}^{trial} - \frac{2G\Delta\gamma}{(1-D_{n+1})}\boldsymbol{\eta}_{n+1}$$

$$\boldsymbol{\beta}_{n+1} = \boldsymbol{\eta}_{n+1} + \boldsymbol{S}_{n+1}$$

$$\boldsymbol{\varepsilon}_{n+1}^e = \boldsymbol{\varepsilon}_{n+1}^{e\,trial} - \Delta\gamma\left[\frac{\boldsymbol{\eta}_{n+1}}{(1-D_{n+1})} + \frac{1}{3}\sigma_y q_1 q_2 f_{n+1}\sinh\left(\frac{3q_2 p_{n+1}}{2\sigma_y}\right)\boldsymbol{I}\right]$$

$$\Delta\bar{\varepsilon}^p = \Delta\gamma\sqrt{\frac{2}{3}\left\{\frac{\boldsymbol{\eta}_{n+1}:\boldsymbol{\eta}_{n+1}}{(1-D_{n+1})^2} + \frac{1}{3}\left[\sigma_y q_1 q_2 f_{n+1}\sinh\left(\frac{3q_2 p_{n+1}}{2\sigma_y}\right)\right]^2\right\}}$$

*(v)*Exit

7.3.2 Finite Strain Extension of Infinitesimal Theory

In this section, an overall integration scheme for an exponential map-based numerical integration algorithm for finite strain is presented, for mixed isotropic and kinematic hardening, that maintains the small-strain scheme (Box 7.2). The

integration scheme adopted was proposed by De Souza Net et al (2008) and is based on the use of logarithmic strains and the multiplicative elasto-plastic splitting. The computational implementation starts from retrieving the elastic logarithmic strain, $\boldsymbol{\varepsilon}_n^e$, at pseudo-time t_n, and computing the corresponding elastic Cauchy-Green tensor, with the expression:

$$\boldsymbol{B}_n^e = exp[2\boldsymbol{\varepsilon}_n^e]\,, \tag{7.5}$$

where $\boldsymbol{B}_n^e$ represents the elastic left Cauchy-Green tensor. Then, it is necessary to computer the trial state and the elastic trial left Cauchy-Green tensor, $\boldsymbol{B}_{n+1}^{e\,trial}$, is obtained by:

$$\boldsymbol{B}_{n+1}^{e\,trial} = \boldsymbol{F}_{n+1}^{e\,trial}\left(\boldsymbol{F}_{n+1}^{e\,trial}\right)^T = \boldsymbol{F}_{\Delta}\boldsymbol{B}_n^e(\boldsymbol{F}_{\Delta})^{\boldsymbol{T}}\ , \tag{7.6}$$

where $\boldsymbol{F}_{n+1}^{e\,trial}$ represents the elastic trial deformation gradient and $\boldsymbol{F}_{\Delta}$ is the incremental deformation gradient. Based on the elastic trial left Cauchy-Green tensor, $\boldsymbol{B}_{n+1}^{e\,trial}$, the elastic trial logarithmic strain tensor is calculated as follows:

$$\boldsymbol{\varepsilon}_{n+1}^{e\,trial} = \frac{1}{2}\ln\left[\boldsymbol{B}_{n+1}^{e\,trial}\right] \tag{7.7}$$

With regard to the inclusion of the kinematic hardening effect, the so-called trial backstress tensor, $\boldsymbol{\beta}_{n+1}^{trial}$, needs to be computed. In order to do so, the incremental elastic rotation needs to be determined by the relation:

$$\Lambda_{\Delta} = \boldsymbol{R}_{n+1}^{e\,trial}(\boldsymbol{R}_n^e)^T\ , \tag{7.8}$$

where Λ_{Δ} represents the incremental elastic rotation, $\boldsymbol{R}_{n+1}^{e\,trial}$ is the elastic trial rotation tensor and $\boldsymbol{R}_n^e$ is the elastic rotation tensor at pseudo-time t_n. Thus, knowing the backstress tensor at t_n, $\boldsymbol{\beta}_n$, the trial backstress tensor, $\boldsymbol{\beta}_{n+1}^{trial}$, is determined by:

$$\boldsymbol{\beta}_{n+1}^{trial} = \Lambda_{\Delta}\boldsymbol{\beta}_n(\Lambda_{\Delta})^T \tag{7.9}$$

Having determined the elastic trial logarithmic strain tensor, the trial backstress tensor and knowing the values of the internal variable at pseudo-time t_n, the return mapping algorithm derived for infinitesimal strains (see Box 7.2) can

be used to update the so-called Kirchhoff stress tensor, $\boldsymbol{\tau_{n+1}}$, and the other state variables. In order to update the Cauchy stress tensor, the following relation is employed:

$$\boldsymbol{\sigma}_{n+1} = det[\boldsymbol{F}_{n+1}]^{-1}\boldsymbol{\tau}_{n+1} \ , \tag{7.10}$$

where $\boldsymbol{\sigma}_{n+1}$ represents the Cauchy stress tensor, $\boldsymbol{\tau}_{n+1}$ is the Kirchhoff stress tensor and $\boldsymbol{F}_{n+1}$ is the gradient deformation at pseudo-time t_{n+1}. The elastic gradient deformation can be determined as:

$$\boldsymbol{F}^{e}_{n+1} = \boldsymbol{V}^{e}_{n+1}\boldsymbol{R}^{e}_{n+1} \ , \tag{7.11}$$

where $\boldsymbol{V}^{e}_{n+1}$ represents the elastic left stretch tensor, that can be computed by:

$$\boldsymbol{V}^{e}_{n+1} = exp[\boldsymbol{\varepsilon}^{e}_{n+1}] \ , \tag{7.12}$$

and $\boldsymbol{R}^{e}_{n+1}$ represents the elastic rotation gradient, which is equal to the trial state $\boldsymbol{R}^{e}_{n+1} = \boldsymbol{R}^{e\,trial}_{n+1}$. Box 7.3 contents a brief summary of the numerical integration algorithm for the general multiplicative finite strain elasto-plasticity model with kinematic hardening.

Box 7.3. Finite Strain Extension of the small strain algorithm

i) Given incremental displacement Δu, update the deformation gradient:

$$\boldsymbol{F}_{\Delta} := \boldsymbol{I} + \nabla_n[\Delta\boldsymbol{u}]$$

$$\boldsymbol{F_{n+1}} := \boldsymbol{F}_{\Delta}\boldsymbol{F_n}$$

ii) Compute elastic trial state

$$\boldsymbol{F}^{e\,trial}_{n+1} := \boldsymbol{F}_{\Delta}\boldsymbol{F}^{e}_{n}$$

$$\boldsymbol{B}^{e\,trial}_{n+1} := \boldsymbol{F}^{e\,trial}_{n+1}\left(\boldsymbol{F}^{e\,trial}_{n+1}\right)^{T}$$

$$\boldsymbol{\varepsilon}^{e\,trial}_{n+1} := \ln\left[\boldsymbol{V}^{e\,trial}_{n+1}\right] = \frac{1}{2}\ln\left[\boldsymbol{B}^{e\,trial}_{n+1}\right]$$

$$\Lambda_{\Delta} := \boldsymbol{R}^{e\,trial}_{n+1}(\boldsymbol{R}^{e}_{n})^{T}$$

$$\boldsymbol{\beta}^{trial}_{n+1} := \Lambda_{\Delta}\boldsymbol{\beta}_{n}\Lambda^{\mathrm{T}}_{\Delta}$$

continue Box 7.3.

$$\boldsymbol{\beta}_{n+1}^{trial} := \Lambda_{\Delta} \boldsymbol{\beta}_n \Lambda_{\Delta}^{\mathrm{T}}$$

$$\overline{\boldsymbol{\varepsilon}}_{n+1}^{p\ trial} := \overline{\boldsymbol{\varepsilon}}_n^{p}$$

iii) Use small strain algorithm to update the Kirchhoff stress tensor, the backstress tensor and other state variables.

iv) Update Cauchy stress tensor and the elastic deformation gradient:

$$\boldsymbol{\sigma}_{n+1} := det[\boldsymbol{F}_{\boldsymbol{n+1}}]^{-1} \boldsymbol{\tau}_{\boldsymbol{n+1}}$$

$$\boldsymbol{V}_{n+1}^{e} := exp[\boldsymbol{\varepsilon}_{n+1}^{e}]$$

$$\boldsymbol{R}_{n+1}^{e} := \boldsymbol{R}_{n+1}^{e\ trial}$$

$$\boldsymbol{F}_{n+1}^{e} = \boldsymbol{V}_{n+1}^{e} \boldsymbol{R}_{n+1}^{e}$$

v) End.

7.3.3 Consistent Tangent Operator

In this section, the consistent tangent operator for the present model will be obtained following a similar procedure to the one employed in previous chapters. Hence, the first step for determining the operator is to differentiate the stress tensor update expression with regard to the elastic trial strain tensor, $\boldsymbol{\varepsilon}_{n+1}^{e\ trial}$:

$$\boldsymbol{\sigma}_{n+1} = \boldsymbol{\sigma}_{n+1}^{trial} - 2G\Delta\gamma \frac{\boldsymbol{\eta}_{n+1}}{(1 - D_{n+1})} - p_{n+1}\boldsymbol{I} \ , \tag{7.13}$$

where $\boldsymbol{\sigma}_{n+1}$ represents the update stress tensor. Therefore, the tangent operator can be computed through:

$$\mathbb{D}^{ep} = \frac{\mathrm{d}\boldsymbol{\sigma}_{n+1}}{\mathrm{d}\boldsymbol{\varepsilon}_{n+1}^{e\ trial}} \ . \tag{7.14}$$

Performing similar mathematical operations and algebraic manipulation, the following expression can be obtained:

$$\mathrm{d}\boldsymbol{\sigma}_{n+1} = \frac{2G}{\left[1+\left(\frac{2G\Delta\gamma}{1-D_{n+1}}\right)\right]}\mathrm{d}\boldsymbol{\varepsilon}_{d\ n+1}^{e\ trial} - 2G\frac{\boldsymbol{\eta}_{n+1}}{(1-D_{n+1})}\mathrm{d}\Delta\gamma - 2G\Delta\gamma\frac{\boldsymbol{\eta}_{n+1}}{(1-D_{n+1})^2}\mathrm{d}D_{n+1} - 2G\Delta\gamma\frac{\mathrm{d}\boldsymbol{\eta}_{n+1}}{(1-D_{n+1})} + \mathrm{d}p_{n+1}\boldsymbol{I}. \tag{7.15}$$

The terms $\mathrm{d}\Delta\gamma$, $\mathrm{d}D_{n+1}$ and $\mathrm{d}p_{n+1}$ represent the derivative of $\Delta\gamma$, D_{n+1} and p_{n+1} with regard to the elastic strain tensor, $\boldsymbol{\varepsilon}_{n+1}^{e\ trial}$. They can be obtained by the linearization procedure of the residual system of equations. However, the term $\mathrm{d}\boldsymbol{\eta}_{n+1}$, that represents the derivative of $\boldsymbol{\eta}_{n+1}$ with regard to the elastic strain tensor, has to be computed by the differentiation of the update relative tensor expression.

$$\mathrm{d}\boldsymbol{\eta}_{n+1} = \frac{\mathrm{d}\boldsymbol{\eta}_{n+1}^{trial} - \Delta\gamma\frac{1}{3}H^K q_1 q_2 q_2 f_{n+1}\cosh\left(\frac{3q_2 p_{n+1}}{2\sigma_y}\right)\mathrm{d}p_{n+1}\otimes\boldsymbol{I}}{\left[1+\frac{2G\Delta\gamma}{(1-D_{n+1})}+\frac{2H^K\Delta\gamma}{3(1-D_{n+1})}\right]} - \frac{\left[\boldsymbol{\eta}_{n+1}^{trial} - \Delta\gamma\frac{2}{9}H^K\sigma_y q_1 q_2 f_{n+1}\sinh\left(\frac{3q_2 p_{n+1}}{2\sigma_y}\right)\boldsymbol{I}\right]}{\left[1+\frac{2G\Delta\gamma}{(1-D_{n+1})}+\frac{2H^K\Delta\gamma}{3(1-D_{n+1})}\right]^2}\left[\frac{2G\mathrm{d}\Delta\gamma}{(1-D_{n+1})} + \frac{2G\Delta\gamma}{(1-D_{n+1})^2}\mathrm{d}D_{n+1} + \frac{2H^K\Delta\gamma}{3(1-D_{n+1})^2}\mathrm{d}D_{n+1}\right] \tag{7.16}$$

The final expression for the consistent tangent operator of the extended GTN model including kinematic hardening can be found in Appendix E. The extension, of the small strain consistent tangent operator, to the finite strains regime is more complex than the isotropic counterpart. The additional degree of complexity is due to the fact that the elastic trial state of the backstress tensor, $\boldsymbol{\beta}_{n+1}^{trial}$, (Equation 7.9) is not fixed. It is a function of the backstress tensor, $\boldsymbol{\beta}_n$, at instant t_n and the incremental elastic rotation Λ_Δ. The incremental elastic rotation, which is given by Equation (7.8), is a function itself of the elastic trial deformation gradient, $\boldsymbol{F}_{n+1}^{e\ trial}$. Therefore, the derivative of the Kirchhoff stress tensor with respect to the deformation gradient, for the spatial tangent modulus, is given by:

$$\frac{\partial \boldsymbol{\tau}_{n+1}}{\partial \boldsymbol{F}_{n+1}} = \mathbb{D}^{ep} : \frac{\partial \boldsymbol{\varepsilon}_{n+1}^{e\,trial}}{\partial \boldsymbol{B}_{n+1}^{e\,trial}} : \frac{\partial \boldsymbol{B}_{n+1}^{e\,trial}}{\partial \boldsymbol{F}_{n+1}} + \mathbb{D}^{\beta} : \frac{\partial \boldsymbol{\beta}_{n+1}^{trial}}{\partial \boldsymbol{F}_{n+1}^{e\,trial}} : \frac{\partial \boldsymbol{F}_{n+1}^{e\,trial}}{\partial \boldsymbol{F}_{n+1}} \tag{7.17}$$

where $\mathbb{D}^{ep}$ is the standard infinitesimal elasto-plastic consistent tangent operator (see Equation 7.14) and $\mathbb{D}^{\beta}$ represents a fourth-order tensor that is the tangent relation between the updated Kirchhoff stress tensor and the trial backstress:

$$\mathbb{D}^{\beta} = \frac{\partial \boldsymbol{\tau}_{n+1}}{\partial \boldsymbol{\beta}_{n+1}^{trial}} \tag{7.18}$$

More details about the linearization of the extended GTN model with kinematic hardening can be found in Appendix E.

7.4 CALIBRATION STRATEGY AND MESH DEFINITION

The determination of the material parameters, which are indispensable for using the extended GTN model with mixed isotropic and kinematic hardening, follows the same calibration procedure described in the previous chapter (see Chapter 6). In the present chapter only the experimental results for the aluminum alloy 2024-T351 are employed (see Bai, 2008) and only two experimental tests need to be conducted to determine all the parameters required by the extended model. As already described previously (Chapter 6), a so-called high stress triaxiality point is adopted, which is experimentally accomplished with a cylindrical smooth bar specimen subjected to a pure tensile loading condition. With this calibration point the parameters for the micro voids nucleation mechanism $[f_N, S_N, \varepsilon_N]$ and hardening curve $\sigma_y(R)$ are determined. Regarding the so-called low stress triaxiality calibration point, a butterfly specimen subjected to pure shear loading is used in the experimental test. At this point, all parameters required for the micro defects nucleation mechanism (under shear) $[D_N, S'_N, \varepsilon'_N]$ and the constants k and q_6 are determined. Table 7.1 shows the parameters determined for the aluminum alloy 2024-T351 based on both calibration points.

Table 7.1: Materials properties for the aluminum alloy 2024-T351, regarding the first and second calibration points.

Calibration point	f_N/d_N	S_N/S'_N	$\varepsilon_N/\varepsilon'_N$	q_1/k	q_2/q_6	q_3	f_c/D_c	E (MPa)	υ
Traction	0.04	0.2	0.1	1.5	1.0	2.25	0.060	72.400	0.33
Shear	0.08	0.15	0.10	0.10	1.00	-	0.08	-	-

The same specimen, the so-called butterfly specimen, was employed in the calibration and during the simulation of the various loading scenarios. The specimen was discretized with a three dimensional finite element mesh of 3.392 twenty nodded elements, with eight Gauss integration points, amounting to 17.465 nodes.

The numerical studies were conducted for three cases that can be described as follows: Case 1) pure shear (+0º) followed by combined shear/tensile (+30º) loading condition; Case 2) compression (-90º) followed by traction (+90º) and finally Case 3) a reversal shear loading (−0º followed by +0º). Figure 7.2 schematically represents the three loading scenarios studied with the extended GTN model.

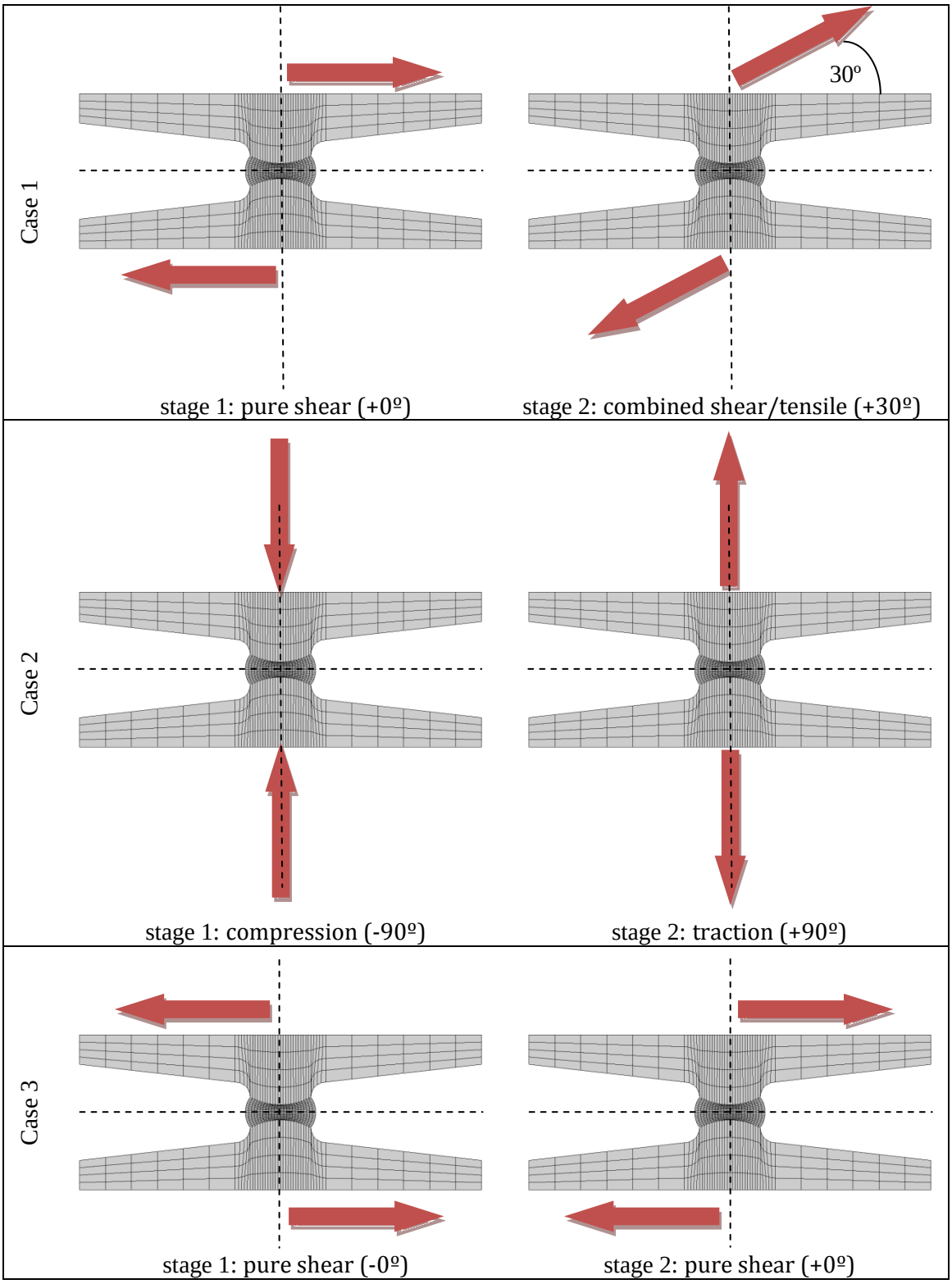

Figure 7.2. Schematic representation of the types of loads under study.

7.5 NUMERICAL RESULTS

For the cases under study, the following results are quantitatively analyzed: the reaction *versus* displacement curve, the evolution of effective damage

parameter and the rate of evolution for the equivalent plastic strain. In all cases, the numerical results obtained by the extended GTN model are compared with experimental results found by Bai (see Bai, 2008). Furthermore, the ability to predict the location of fracture onset is analyzed when the loading history effect needs to be accounted in the plastic flow rule for ductile materials.

7.5.1 Reaction *versus* displacement curve

Figure 7.3 presents numerical and experimental results determined for the reaction *versus* displacement curve, for each case.

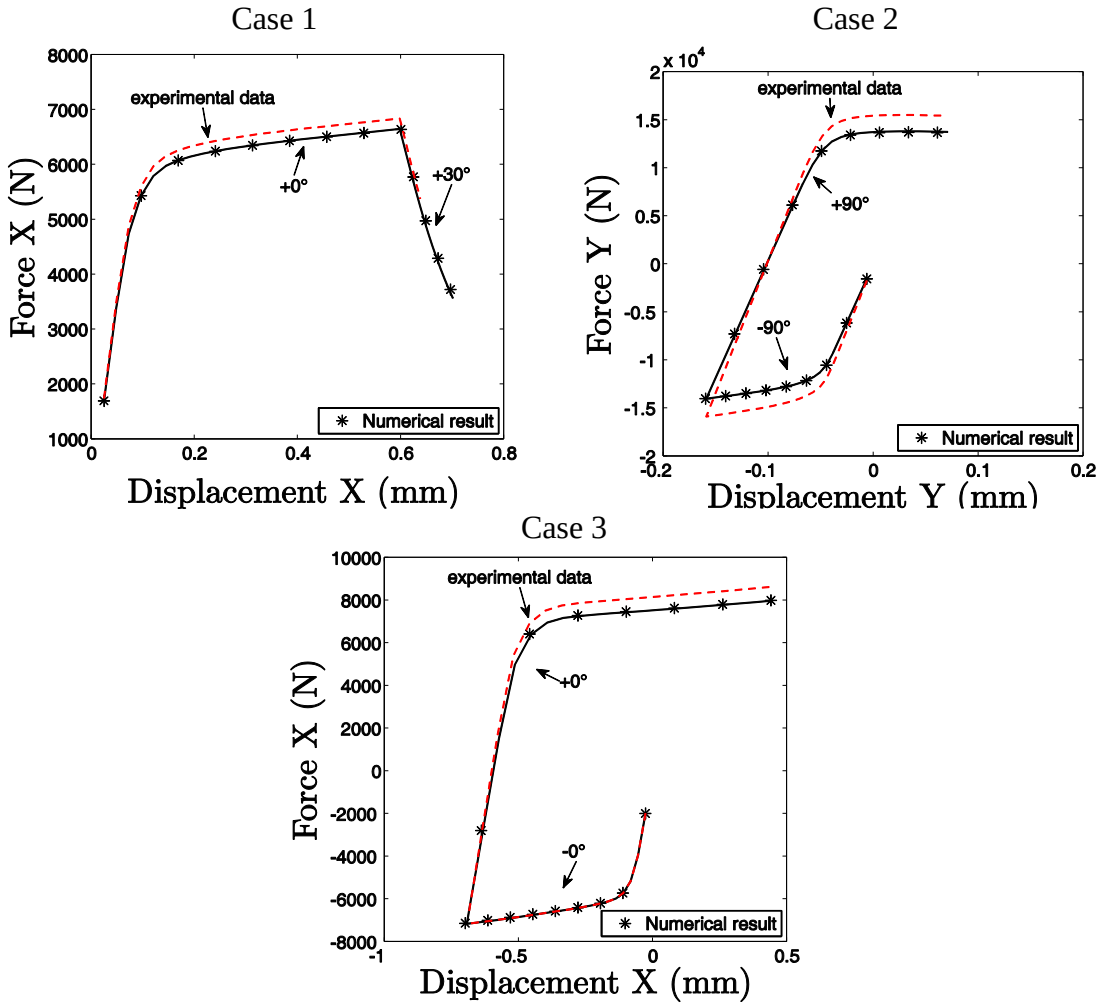

Figure 7.3. Reaction curve determined by numerical simulation, regarding cases 1, 2 e 3, with the extended GTN model.

Based on the analysis of the results presented in Figure 7.3, it is possible to conclude that there is a good agreement between experimental and numerical results using the proposed model. The small differences observed in the figure, can be justified by the use of the evolution law proposed by Prager for the backstress

tensor, which grows in a direction collinear to the plastic flow rule of the material. According to some researchers, in some cases (see Jiang, 1996; Stoughton, 2000; Lemaitre, 2001), due to non-proportionality of the loading applied, the evolution of the backstress and the plastic flow rule do not follow the same direction. In these cases, a more sophisticated evolution law needs to be considered, such as: the Morz model (see Lemaitre, 2001) and the Armstrong and Frederick model (see De Souza Neto et al, 2008).

7.5.2 Evolution of the effective damage parameter

The evolution of the effective damage parameter, D^{ef}, which was introduced in Equation (6.19) of Chapter 6, is presented in Figure 7.4. For each loading scenario, the effective damage evolution obtained from the numerical simulation is plotted against the applied displacement. From the results, it is possible to conclude, that the critical damage ($D^{ef} = 1$) is reached for displacements at fracture, which are in close agreement with experimental evidence.

The biggest difference between the numerical and experimental results for the so-called displacement at fracture is observed for the first case. For this loading scenario, the displacement at fracture predicted but the extended GTN model is around $u_f = 0.85\ mm$, and the experimentally observed is around $u_f = 0.72\ mm$. For the other two cases (cases 2 and Case 3), the numerical and experimental results have a 5% of difference. Table 7.2 presents the critical displacement values obtained with the proposed model and the experimentally determined values obtained by Bai (see Bai, 2008).

Table 7.2. Critical displacement at fracture for all cases.

	u_f numerical [mm]	u_f experimental [mm]
Case 1	0.85	0.72
Case 2	0.80	0.84
Case 3	0.48	0.51

Figure 7.4 illustrates the evolution of the effective damage and the determination of the critical displacement at fracture, regarding cases 1, 2 and 3.

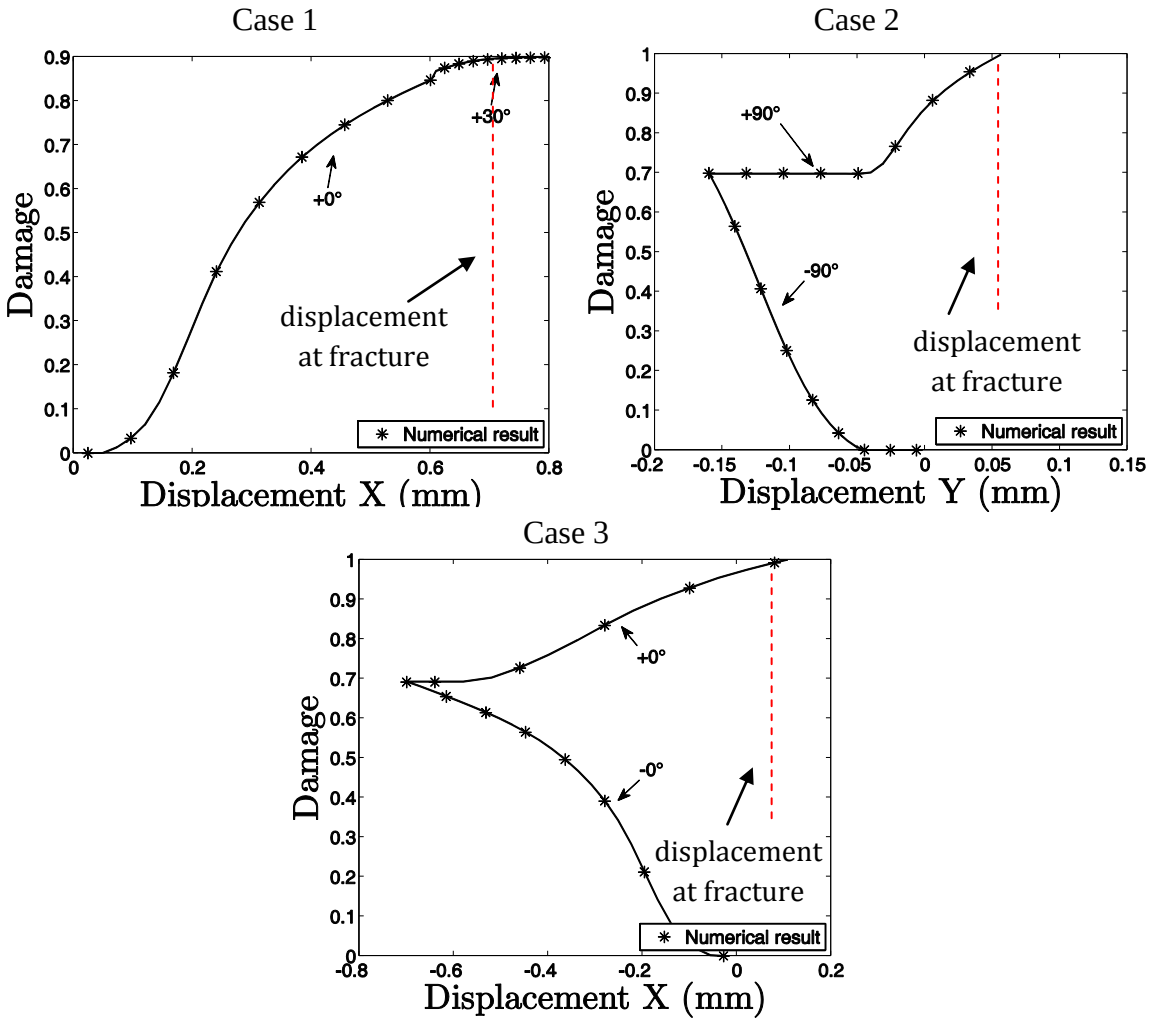

Figure 7.4. Evolution of effective damage for all cases 1, 2 and 3.

7.5.4 Effective damage contour

The predictive ability of the model, regarding the correct prediction of the potential site for ductile crack initiation, is the last feature to judge. In this evaluation, the numerical results obtained by the extended model are compared with experimental data reported by Bai (see Bai, 2008). Figure 7.5 shows the contour of the effective damage parameter for the three cases under analysis.

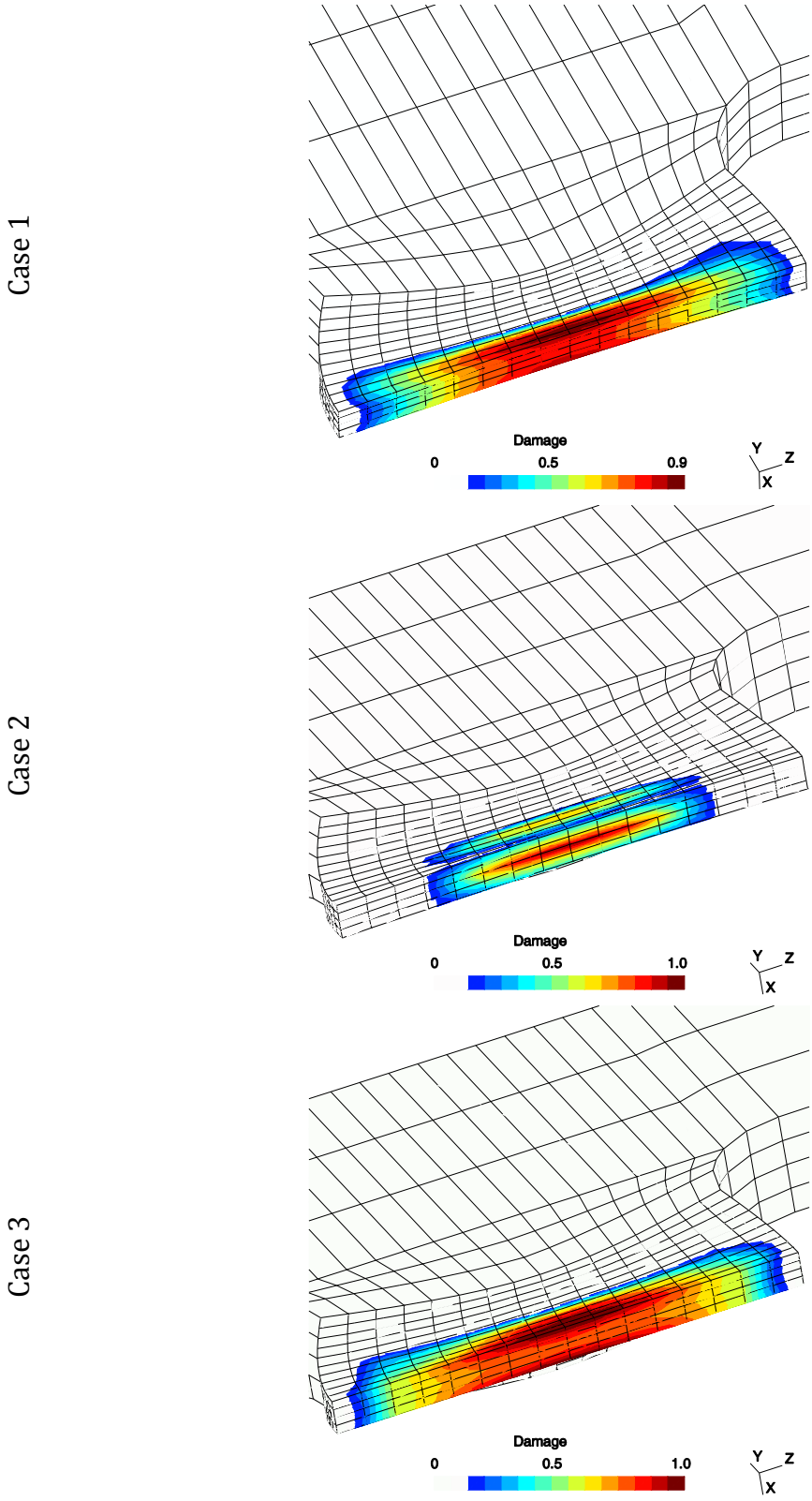

Figure 7.5. Contour of the effective damage parameter.

From the results obtained for cases 1 and 3, it is possible to observe that the crack starts at the surface of the critical region of the specimen. Nevertheless, for the second case, it is observed that crack initiation occurs at the center of thickness of the critical region of the specimen. According to experimental observations, reported by Bai (Bai, 2008), in all cases, the numerical prediction of the potential site to crack initiation was in agreement with the experimental evidences.

7.6 CONCLUSIONS

In this chapter, the extended GTN model proposed in Chapter 6 was improved with an evolution law for the backstress tensor proposed by Prager (De Souza Net et al, 2008), in order to increase its predictive ability under combined loading. The set of equations that govern the behavior of the model, including nonlinear kinematic hardening, was presented and the integration algorithm developed was described in detail. An assessment of the model was then conducted for three loading conditions, such as (case 1) pure shear (+0 °) followed by combined shear / tensile (+30 °) loading, (case 2) compression (-90 °) followed by traction (+90 °) and finally (case 3) the reversal shear loading (Followed by +0 ° -0 °). The evolution of the reaction curve of the material, the evolution of the damage parameter and predictive ability of the model were then evaluated. In all loading cases the numerical model has shown good results when compared to experimental results available in the literature (see Bai, 2008). Thus, it can be concluded that the mechanical behavior for ductile materials, in the presence of proportional and non proportional loadings, may be represented by the proposed model, which introduces two damage variables and the effect of both isotropic and kinematic hardening, through nonlinear evolution laws.

As a further development to the extended GTN model, the addition of more complex evolution laws for the backstress tensor is suggested, in order to improve the prediction of the numerical critical displacement at fracture. The evolution law for the backstress tensor proposed by Armostrong and Frederick (see De Souza Neto et al, 2008), which assumes no collinearity between the backstress tensor and the plastic flow rule, and the model suggested by Morz (see Lemaitre, 2001), which assumes multi yield surface, might be able to increase the predictive ability of the proposed extended model.

CHAPTER 8

Final Remarks

8.1 CONCLUSIONS

The study of the mechanical behavior of metallic materials is a topic of great importance and, in recent years, has been subjected to numerous studies regarding the formulation of mathematical models capable of describing the mechanical behavior in the most realistic way possible. The introduction of new effects, both in the plastic flow rule of the material and in the evolution law for internal variables like damage, are among the topics more discussed and improved in the last decade. These scientific developments bring to the industry, in general, competitive gains in relation to the development of more efficient and durable mechanical components as well as the improvement of manufacturing processes. Coupled with the development of new constitutive models for materials, the numerical techniques used to simulate the real behavior of structures, the materials characterization, the simulation of manufacturing processes, among others, have also been enhanced and spread by industries such as: automobile, aerospace, naval, among others.

Thus, in this thesis, we have investigated many different elasto-plastic formulations with damage as internal variable, and propose improvements to increase their accuracy, with regard to their ability to predict the loss of stiffness and the fracture initiation in ductile materials. Among other advances, we attempted to discuss the importance of the third invariant of the deviatoric stress tensor in the mechanical behavior of metallic materials and introduce this effect in the plastic flow rule. It was also found that the predictive behavior of many different constitutive models, such as: Lemaitre's model, Bai's model and Gurson's model (in GTN version), as well as some recent extensions of the GTN model, is limited regarding the ability to predict failure in predominant shear loading conditions. An extended GTN model, which includes calibration points in the so-

called high and low stress triaxiality zone, distinct mechanisms for nucleation of defects regarding shear and tensile predominant loading conditions, as well as two internal variables for damage evolution that are combined to provide an effective damage scalar variable which triggers the coalescence mechanism, has been proposed. Finally, we have addressed the influence of the loading history effect on the predictive ability of the model, i.e., the study of proportional and non-proportional loads. To this end, the so-called Bauschinger effect was added, through the coupling of kinematic hardening in accordance with what was proposed by Prager. In following paragraphs, the advances made in each chapter of the thesis are described in detail.

Chapter 3

In this chapter, an implicit numerical integration algorithm for an elasto-plastic model developed by Bai et al. (see Bai, 2008) was studied and proposed. The constitutive model introduces in the hardening law of the material, the effect of hydrostatic pressure by the so-called stress triaxiality, and the effect of the third invariant of the deviatoric stress tensor by the so-called Lode angle. Regarding the development of the numerical algorithm, the operator split methodology (see Simo et al, 1998) was used and its implementation was done in a quasi-static academic finite element framework. Some numerical tests for different specimens and two engineering metallic materials (aluminum alloy and steel 1045) were conduced, regarding the demonstration of the robustness of the proposed algorithm, as well as validation of the predictive gain, when both pressure and Lode angle effects are coupled in the plastic flow rule. The quadratic convergence of the numerical model was shown by the so-called isoerror maps, as well as by the convergence of the local and global problem. Considering the mechanical behavior of engineering materials and the introduction of the effects under study, the numerical results depicted more accurately the experimental data. It also verified a distinct mechanical behavior for the aluminum alloy and the steel, regarding the effect of the third invariant. In this direction, a material classification was proposed according to the sensitivity to the stress triaxiality and the Lode angle, such as:

strongly dependent (aluminum alloy) and weakly dependent (steel 1045) on the pressure and the third invariant.

Chapter 4

In order to evaluate several approaches for determining ductile fracture onset, in this chapter, an attempt was made to make a qualitative and quantitative comparison of the numerical results predicted according to the Bai's model (2008), Lemaitre's model (1985) and Gurson' model, in the GTN version model with a shear mechanism coupled (1984). For this, we tested specimens under low and high stress triaxiality, based on an aluminum alloy. For Bai's model, an implicit integration algorithm proposed in the previous chapter was used. However, for the Lemaitre's model, we used the integration algorithm, with only one scalar equation for the plastic multiplier, suggested by De Souza Neto et al (2002). In the GTN version of Gurson's model, with the shear mechanism proposed by Xue (2008) coupled, an implicit algorithm based on operator split methodology was developed. All algorithms were implemented in a quasi-static finite element academic framework. The numerical results were evaluated through several parameters such as: the reaction curve obtained for each model, the evolution of the equivalent plastic strain, the evolution of damage variable, the numerical displacement at fracture as well as the ability to predict the potential location for ductile fracture initiation. It has been shown that several models are unable to achieve a good predictive capacity when applied to a large range of stress triaxiality. It was found that the GTN's model with the shear mechanism coupled does not behave well under mixed tensile/shear loading conditions. Lemaitre's model has predicted a very high level of plastic strain at fracture, when used in predominantly shear loading conditions. For Bai's model, there was a good response when used under high stress triaxiality, but due to lack of an internal variable of damage, it has a limited range of application. Finally, it can be concluded that both elasto-plastic and damage models have a great dependence of the calibration condition. It was also observed that when the load condition under study is far from the loading condition used for calibration of the material parameters, the predictive ability of models is compromised.

Chapter 5

In this chapter, the evaluation of various shear mechanisms proposed to improve the GTN's model, under predominant shear loading conditions, was conducted. The effect of the calibration condition was also assessed as regards the predictive fracture onset ability of models. For this purpose, two independent calibration points were used to determine the material parameters: one of them at high and the other at low level of stress triaxiality. It was found that, in general, the shear mechanisms evaluated do not have a good predictive capacity for both pure shear and shear/tensile combined loading conditions. By using the material parameters calibrated for high stress triaxiality, it was found that Xue's shear mechanism behaved rather conservative in predicting fracture onset, when a pure shear loading condition was applied. Regarding the same loading and calibration conditions, the mechanism proposed by Nahshon & Hutchinson showed excellent predictive ability. For combined loading, both Xue and Nahshon & Hutchinson shear mechanisms showed predictive ability in disagreement with experimental observations. Regarding the material parameters obtained by the second calibration point (in low stress triaxiality), the performance of all mechanisms was in accordance with the experimental observations, when predominant shear loading conditions was used, but under combined loading conditions, limitations were observed in predicting the correct displacement at fracture. Thus, after the numerical tests performed, it is possible to conclude that there is a procedure for improving the GTN's model performance under predominantly shear and the response of the constitutive formulation. Since the models, with internal damage variable coupled, are strongly dependent on the relationship between the calibration condition used to determined the material parameters and the real loading condition under study, they can be calibrated close to the loading condition.

Chapter 6

Based on information from the performance of the constitutive models evaluated in the previous chapters, this chapter, attempted to develop a constitutive formulation that enhances the capability of predicting fracture initiation for ductile materials, with regard to the determination of the correct displacement at the fracture, the correct level of the expected equivalent plastic strain at fracture, and the correct determination of the potential site for fracture initiation. For this goal, a model based on the micromechanic of defects, such as the GTN's model was adopted, and the geometric deduction of the evolution law for the shear mechanism proposed by Xue. Thus, a new coupling of the so-called deviatoric damage variable was proposed. The deviatoric stress component was affected by only the so-called shear damage (or deviatoric damage) and the volumetric component of the stress tensor by the so-called volume void fraction that plays a volumetric damage role. With this proposition, a better relationship between the internal damage variables and the components of the stress tensor was observed. In order to reduce the dependence of the model with respect to the calibration condition employed, a new nucleation mechanism for the shear damage was created, based on the concept that the defects are generated in a different manner and speed for predominant tensile or shear loading conditions. Thus, the new model, here called as extended GTN model, requires two calibration points combined to determine all material parameters: one under high and other under low level of stress triaxiality. A so-called effective damage variable has also been suggested, with the aim of combining the two independent internal damage variables and determine clearly the correct fracture initiation under general loading conditions. An implicit numerical integration algorithm for the extended GTN model is proposed and implemented within a quasi-static finite element framework. The model was then tested under different loading conditions and a good performance was observed for all situations employed. Finally, it can be concluded that the extended GTN model is a more reliable formulation that can be applied for wide range of stress triaxiality.

Chapter 7

In this chapter, the influence of the loading history in the correct prediction of fracture was studied. To reach this goal, the effect of the so-called kinematic hardening, as proposed by Prager, was added into the extended GTN model. An implicit integration based on the operator split methodology was suggested and implemented in a academic finite element tool. In this case, an extension of the integration algorithm developed for small deformation to large deformation was also carried out. The method suggested by De Souza Neto et al (2008) was used. The extended GTN model with isotropic and kinematic hardening was tested under three different loading conditions, such as: pure shear followed by combined shear/traction, compression followed by traction and reversible shear. In all loading cases, the reaction curves obtained, the evolution of the effective damage and the determination of the potential site to fracture initiation were studied. In general, the numerical results presented reasonable agreement with the experimental data found in literature. It was observed, differences around 10% between the reaction forces determined numerically and the experimental observations.

8.2 SUGGESTIONS FOR FUTURE WORK

After the studies and advances proposed to improve the predictive ability of the elasto-plastic models and damage models, based mainly on the micromechanics of defects, in this section, some suggestions for future work are made:

Elasto-plastic model with the influence of J_3 in the equivalent stress

In this case, the study of the influence of the third invariant of the deviatoric stress tensor in the mechanical behavior of the material is recommended. For some researchers the third invariant has an influence in the shape of the yield surface. Thus, the development of a new yield function, which has the so-called equivalent stress as a function of both J_2 and J_3, could be an interesting possibility.

This suggestion has the goal, in addition to the inclusion of the influence of the effect of the third invariant, of facilitating the process of determining the numerical model.

$$q(J_2, J_3) - \sigma_y(\bar{\varepsilon}^p) = 0$$

Reducing the dependence of the calibration point in Lemaitre's model

As evaluated in Chapter 4, Lemaitre's model also has a large dependence of the relationship between the calibration procedure and the real loading condition under study. Thus, it is suggested to develop an improvement in Lemaitre's damage evolution law to contemplate the influence of two calibration points: one under high and other under low level of stress triaxiality. This influence can be included, for example, by having two denominators of damage: one for predominant tensile loading, S_1, (using the smooth bar specimen under tensile loading) and other for predominant shear loading conditions, S_2.

$$\dot{D} = \frac{\dot{\gamma}}{1 - D}\left[\frac{-Y}{S(S_1, S_2)}\right]^s$$

Coupling other evolution laws for backstress tensor

In assessing the effect of loading history, it is suggested as future study, the coupling with other evolution laws for the backstress tensor, knowing that the Prager proposition, used in this thesis, considers the principle of co linearity between the evolution of backstress tensor and the plastic flow rule of the material. This condition may not satisfy the saturation level of the internal variable. Thus, the Armstrong and Frederick model could be a suggestion for implementation and evaluation.

$$\dot{\boldsymbol{\beta}} = \frac{2}{3} H^K(R)\dot{\boldsymbol{\varepsilon}}^p - \dot{\gamma} b \boldsymbol{\beta}$$

APPENDIX A

Determine the flow vector and plastic flow rule for Bai & Wierzbicki elasto-plastic model

a) Define the yield function for the specific model:

$$\Phi = q - \sigma_y(\bar{\varepsilon}^p)\left[1 - C_\eta(\eta - \eta_0)\right]\left[C_\theta^s + (C_\theta^{ax} - C_\theta^s)\left(\mu - \frac{\mu^{m+1}}{m+1}\right)\right] \tag{a.1}$$

where, q is the von Mises equivalent stress, $\sigma_y(\bar{\varepsilon}^p)$ is the isotropic hardening rule, $\bar{\varepsilon}^p$ is the accumulated plastic strain, η is the stress triaxiality, μ is the parameter responsible for introducing Lode angle dependence. C_η, η_0, C_θ^s, C_θ^{ax} and m are experimental parameters.

We can define functions $A(\eta)$ and $B(\mu)$ according to Equations (a.2) and (a.3), and re-write Equation (a.1) as follow:

$$A(\eta) = \left[1 - C_\eta(\eta - \eta_0)\right] \tag{a.2}$$

$$B(\mu) = \left[C_\theta^s + (C_\theta^{ax} - C_\theta^s)\left(\mu - \frac{\mu^{m+1}}{m+1}\right)\right] \tag{a.3}$$

$$\Phi = q - \sigma_y(\bar{\varepsilon}^p)\, A(\eta)B(\mu) \tag{a.4}$$

Remark: *The von Mises equivalent stress, stress triaxiality and parameter μ can be defined as:*

$$q = \sqrt{3J_2} = \sqrt{\frac{3}{2}\boldsymbol{S}:\boldsymbol{S}} = \sqrt{\frac{3}{2}}\|\boldsymbol{S}\| \tag{a.5}$$

$$\eta = \frac{p}{q} = \frac{\frac{1}{3}tr(\boldsymbol{\sigma})}{q} \tag{a.6}$$

$$\mu = \frac{cos(\pi/6)}{1 - cos(\pi/6)}\left[\frac{1}{cos(\theta - \pi/6)} - 1\right] = 6.4641[sec(\theta - \pi/6) - 1] \tag{a.7}$$

$$\xi = \left(\frac{r}{q}\right)^3 = \frac{27}{2}\frac{det(\boldsymbol{S})}{q^3} = \cos(3\theta) \tag{a.8}$$

b) The flow vector is defined as a derivative of the yield function in relation to the stress tensor, as:

$$\boldsymbol{N} \equiv \frac{\partial \Phi}{\partial \boldsymbol{\sigma}} \tag{a.9}$$

After some algebraic manipulation, we can re-write the above equation as:

$$\boldsymbol{N} = \frac{\partial[q]}{\partial \boldsymbol{\sigma}} - \sigma_y(\bar{\varepsilon}^p)\left\{\frac{\partial[A(\eta)]}{\partial \boldsymbol{\sigma}}B(\mu) + A(\eta)\frac{\partial[B(\mu)]}{\partial \boldsymbol{\sigma}}\right\} \tag{a.10}$$

In order to determine the closed equation for the flow vector, we have to determine the derivative of the von Mises equivalent stress, function $A(\eta)$ and $B(\mu)$ in relation to the stress tensor. The procedure to determine the required derivatives are described below:

$$\frac{\partial[q]}{\partial \boldsymbol{\sigma}} = \frac{1}{2q}\left[\frac{3}{2}\left(2\,\boldsymbol{S}{:}\frac{\partial \boldsymbol{S}}{\partial \boldsymbol{\sigma}}\right)\right] \tag{a.11}$$

The derivative of the deviatoric stress tensor in relation to the stress tensor is determined as:

$$\frac{\partial \boldsymbol{S}}{\partial \boldsymbol{\sigma}} = \mathbb{I} - \frac{1}{3}\boldsymbol{I}\otimes\boldsymbol{I} \tag{a.12}$$

where, $\mathbb{I}$ represents the fourth order identity tensor and $\boldsymbol{I}$ represents the second order identity tensor.

Substituting Equation (a.12) in to Equation (a.11) and after some algebraic manipulation, we have:

$$\frac{\partial[q]}{\partial \boldsymbol{\sigma}} = \frac{3}{2q}\boldsymbol{S} \tag{a.13}$$

Proof.: $\boldsymbol{S}:\left(\mathbb{I} - \frac{1}{3}\boldsymbol{I}\otimes\boldsymbol{I}\right) = \boldsymbol{S}$

$$\boldsymbol{S} = \boldsymbol{S}:\left(\mathbb{I} - \frac{1}{3}I\otimes I\right) = \boldsymbol{S}:\mathbb{I} - \frac{1}{3}\boldsymbol{S}:\boldsymbol{I}\otimes\boldsymbol{I}$$

$$\boldsymbol{S}:\boldsymbol{I} = tr(\boldsymbol{S}) = 0 \tag{a.14}$$

$$\boldsymbol{S} = \boldsymbol{S}:\mathbb{I} = \boldsymbol{S}$$

The derivative of function $A(\eta)$ can be obtained according to Equation (a.15):

$$\frac{\partial[A(\eta)]}{\partial \boldsymbol{\sigma}} = -C_\eta \frac{\partial[\eta]}{\partial \boldsymbol{\sigma}} \tag{a.15}$$

We have to determine the derivative of the stress triaxiality in relation to the stress tensor. After some algebraic manipulations, the derivative of the stress triaxiality can be written as:

$$\frac{\partial[\eta]}{\partial \boldsymbol{\sigma}} = \frac{\partial[p]}{\partial \boldsymbol{\sigma}}\frac{1}{q} - \frac{\eta}{q}\frac{\partial[q]}{\partial \boldsymbol{\sigma}} = \frac{1}{3q}\boldsymbol{I} - \frac{3\eta}{2q^2}\boldsymbol{S} \tag{a.16}$$

where, $\partial[p]/\partial\boldsymbol{\sigma} = (1/3)\boldsymbol{I}$.

Substituting Equation (a.16) in to Equation (a.15), we can obtain the derivative of function $A(\eta)$ in relation to the stress tensor:

$$\frac{\partial[A(\eta)]}{\partial \boldsymbol{\sigma}} = -C_\eta\left[\frac{1}{3q}\boldsymbol{I} - \frac{3\eta}{2q^2}\boldsymbol{S}\right] = C_\eta\left[\frac{3\eta}{2q^2}\boldsymbol{S} - \frac{1}{3q}\boldsymbol{I}\right] \tag{a.17}$$

The derivative of the function $B(\mu)$ can be obtained according Equation (a.18):

$$\frac{\partial[B(\mu)]}{\partial \boldsymbol{\sigma}} = (C_\theta^{ax} - C_\theta^{s})(1-\mu^m)\frac{\partial[\mu]}{\partial \boldsymbol{\sigma}} \tag{a.18}$$

We have to determine the derivative of the parameter μ. Then, the closed form can be obtained according the equation below:

$$\frac{\partial[\mu]}{\partial \boldsymbol{\sigma}} = \frac{cos(\pi/6)}{1-cos(\pi/6)}\frac{\tan(\theta-\pi/6)}{cos(\theta-\pi/6)}\frac{\partial[\theta]}{\partial \boldsymbol{\sigma}} \tag{a.19}$$

where, $\partial[\theta]/\partial\boldsymbol{\sigma}$ represents derivative of the Lode angle in relation to stress tensor and can be determined according Equation (a.20):

$$\frac{\partial[\theta]}{\partial \boldsymbol{\sigma}} = \frac{\partial\left[\frac{1}{3}\arccos(\xi)\right]}{\partial \boldsymbol{\sigma}} = -\frac{1}{3}\frac{1}{\sqrt{1-\xi^2}}\frac{\partial[\xi]}{\partial \boldsymbol{\sigma}} \tag{a.20}$$

where, $\partial[\xi]/\partial\boldsymbol{\sigma}$ represents derivative of the normalized third invariant in relation to stress tensor and can also be determined according Equation (a.21):

$$\frac{\partial[\xi]}{\partial \boldsymbol{\sigma}} = \frac{\partial\left[\left(\frac{r}{q}\right)^3\right]}{\partial \boldsymbol{\sigma}} = 3\xi\left(\frac{\partial[r]}{\partial \boldsymbol{\sigma}}\frac{1}{r} - \frac{\partial[q]}{\partial \boldsymbol{\sigma}}\frac{1}{q}\right) \tag{a.21}$$

where, $\partial[r]/\partial\boldsymbol{\sigma}$ represents derivative of the third invariant of the stress tensor in relation to stress tensor. The derivative of $[r]$ can be obtained according Equation (a.22).

$$\frac{\partial[r]}{\partial \boldsymbol{\sigma}} = \frac{\partial\left[\sqrt[3]{\frac{27}{2}det(\boldsymbol{S})}\right]}{\partial \boldsymbol{\sigma}} = \frac{9}{2r^2}\frac{\partial[det(\boldsymbol{S})]}{\partial \boldsymbol{\sigma}} \tag{a.22}$$

The derivative of the deviatoric stress tensor determinant in relation to stress tensor can be written as:

$$\frac{\partial[det(\boldsymbol{S})]}{\partial \boldsymbol{\sigma}} = \frac{\partial[det(\boldsymbol{S})]}{\partial \boldsymbol{S}} : \frac{\partial \boldsymbol{S}}{\partial \boldsymbol{\sigma}} = \boldsymbol{S}^2 - \frac{1}{3}tr(\boldsymbol{S}^2)\boldsymbol{I} - I_1\boldsymbol{S} \tag{a.23}$$

where, $\partial[det(\boldsymbol{S})]/\partial\boldsymbol{S} = \boldsymbol{S}^2 - I_1\boldsymbol{S} + I_2\boldsymbol{I}$, and I_1 and I_2 represents the first and second invariants of the stress tensor. Then, we can define a new second order

tensor $\boldsymbol{M}$, in order to re-write the derivative of the deviatoric stress tensor determinant in relation to the stress tensor, as:

$$\boldsymbol{M} = \boldsymbol{S}^2 - \frac{1}{3} tr(\boldsymbol{S}^2)\boldsymbol{I} \tag{a.24}$$

Substituting Equation (a.24) in to Equation (a.23), we have:

$$\frac{\partial[det(\boldsymbol{S})]}{\partial \boldsymbol{\sigma}} = \boldsymbol{M} - I_1 \boldsymbol{S} \tag{a.25}$$

However, substituting Equation (a.25) in to Equation (a.22), and the result together with Equation (a.13) in to Equation (a.21), we have the derivative of the normalized third invariant in relation to stress tensor. Preceding the substitution of the results since Equation (a.21) until Equation (a.18), we can determine a closed equation for the derivative of parameter $B(\mu)$ in relation to stress tensor, as:

$$\frac{\partial[B(\mu)]}{\partial \boldsymbol{\sigma}} = D\xi \left[\left(\frac{3}{2q^2} + \frac{9I_1}{2r^3} \right) \boldsymbol{S} - \frac{9}{2r^3} \boldsymbol{M} \right] \tag{a.26}$$

where, D is defined as:

$$D(\theta) = (C_\theta^{ax} - C_\theta^{s})(1 - \mu^m) \frac{\cos(\pi/6)}{1 - \cos(\pi/6)} \frac{\tan(\theta - \pi/6)}{\cos(\theta - \pi/6)} \frac{1}{\sin 3\theta} \tag{a.27}$$

In order to determine the closed form for the flow vector, we have to substitute Equations (a.13), (a.17) and (a.26) in to Equation (a.10). Thus, after some algebraic manipulation, the flow vector can be calculated as:

$$\boldsymbol{N} = \frac{3}{2q} \alpha \boldsymbol{S} + \frac{3}{2q} \lambda \boldsymbol{M} + \frac{1}{3} \beta \boldsymbol{I} \tag{a.28}$$

where α, β and λ are parameter defined according Equation (a.29), (a.30) and (a.31).

$$\alpha = 1 - \frac{\sigma_y(\bar{\varepsilon}^p)}{q} \left[C_\eta B \eta + AD\xi \left(1 + 3I_1 \frac{q^2}{r^3} \right) \right] \tag{a.29}$$

$$\beta = \frac{\sigma_y(\bar{\varepsilon}^p) C_\eta B}{q} \tag{a.30}$$

$$\lambda = \frac{3\sigma_y(\bar{\varepsilon}^p) AD}{q^2} \tag{a.31}$$

c) The plastic flow rule:

The evolution of the plastic strain can be defined according Equation (a.32), as:

$$\Delta\varepsilon^p \equiv \Delta\gamma \boldsymbol{N} = \Delta\gamma \left[\frac{3}{2q}\alpha \boldsymbol{S} + \frac{3}{2q}\ \lambda \boldsymbol{M} + \frac{1}{3}\beta \boldsymbol{I}\right] \tag{a.32}$$

where, $\Delta\varepsilon^p$ is the incremental plastic strain, $\Delta\gamma$ is the plastic multiplier and $\boldsymbol{N}$ is the flow vector defined according Equation (a.28). The equivalent plastic strain can also be determined through Equation (a.33):

$$\Delta\bar{\varepsilon}^p = \sqrt{\frac{2}{3}(\Delta\varepsilon^p : \Delta\varepsilon^p)} \tag{a.33}$$

Substituting Equation (a.32) in to Equation (a.33) and after some algebraic manipulation, we can obtain:

$$\Delta\bar{\varepsilon}^p = \Delta\gamma \sqrt{\alpha^2 + \frac{2}{9}\beta^2 + \lambda^2 \frac{\boldsymbol{M}:\boldsymbol{M}}{\boldsymbol{S}:\boldsymbol{S}} + 2.\alpha.\lambda \frac{\boldsymbol{S}:\boldsymbol{M}}{\boldsymbol{S}:\boldsymbol{S}}} \tag{a.34}$$

APPENDIX B

Linearization procedure for Bai & Wierzbicki elasto-plastic model

a) Defining the yield function for Bai & Wierzbicki elasto-plastic model according Equation (b.1) below:

$$\Phi = q - \sigma_y(\bar{\varepsilon}^p)\, A(\eta)B(\mu)$$

$$\Phi = q - \sigma_y(\bar{\varepsilon}^p)\left[1 - C_\eta(\eta - \eta_0)\right]\left[C_\theta^s + (C_\theta^{ax} - C_\theta^s)\left(\mu - \frac{\mu^{m+1}}{m+1}\right)\right] \tag{b.1}$$

where q is the equivalent stress, $\sigma_y(\bar{\varepsilon}^p)$ is the yield stress that is a function of the accumulated plastic strain $\bar{\varepsilon}^p$, $A(\eta)$ is the parameter that introduce the pressure effect on the hardening rule through the triaxiality ratio, η, and $B(\mu)$ is the parameter that introduce the Lode dependence on the hardening rule.

b) The flow vector, plastic flow rule and evolution for the equivalent plastic strain

The flow vector

$$\boldsymbol{N} = \frac{3}{2q}\alpha\boldsymbol{S} + \frac{3}{2q}\,\lambda\boldsymbol{M} + \frac{1}{3}\beta\boldsymbol{I} \tag{b.2}$$

where, $\boldsymbol{N}$ represents the flow vector, $\boldsymbol{S}$ is the deviatoric stress tensor, $\boldsymbol{I}$ is the second order identity tensor and α, λ and β are parameters defined according below:

$$\alpha = 1 - \frac{\sigma_y(\bar{\varepsilon}^p)}{q}\left[C_\eta B\eta + AD\xi\left(1 + 3I_1\frac{q^2}{r^3}\right)\right] \tag{b.3}$$

$$\beta = \frac{\sigma_y(\bar{\varepsilon}^p) C_\eta B}{q} \tag{b.4}$$

$$\lambda = \frac{3\sigma_y(\bar{\varepsilon}^p) AD}{q^2} \tag{b.5}$$

$$D(\theta) = (C_\theta^{ax} - C_\theta^s)(1 - \mu^m) \frac{\cos(\pi/6)}{1 - \cos(\pi/6)} \frac{\tan(\theta - \pi/6)}{\cos(\theta - \pi/6)} \frac{1}{\sin 3\theta} \tag{b.6}$$

The plastic flow rule

The evolution of the plastic strain tensor is defined as follow:

$$\Delta\varepsilon^p = \Delta\gamma \left(\frac{3}{2q} \alpha \boldsymbol{S} + \frac{3}{2q}\, \lambda \boldsymbol{M} + \frac{1}{3} \beta \boldsymbol{I} \right) \tag{b.7}$$

where, $\Delta\varepsilon^p$ is the increment of the plastic strain and $\Delta\gamma$ is the plastic multiplier.

Evolution of the equivalent plastic strain

The evolution of the equivalent plastic strain is defined as follow:

$$\Delta\bar{\varepsilon}^p = \Delta\gamma \sqrt{\alpha^2 + \frac{2}{9}\beta^2 + \lambda^2 \frac{\boldsymbol{M}:\boldsymbol{M}}{\boldsymbol{S}:\boldsymbol{S}} + 2.\alpha.\lambda \frac{\boldsymbol{S}:\boldsymbol{M}}{\boldsymbol{S}:\boldsymbol{S}}} \tag{b.8}$$

where, $\Delta\bar{\varepsilon}^p$ is the increment of the accumulated plastic strain.

c) Determining the residual system of equations

The update equation for the stress tensor can be determined as:

$$\boldsymbol{\sigma}_{n+1} = \mathbf{D^e} : \left(\boldsymbol{\varepsilon}_{n+1}^{e\,trial} - \Delta\boldsymbol{\varepsilon}^p \right) = \boldsymbol{\sigma}_{n+1}^{trial} - \Delta\gamma \mathbf{D^e} : \boldsymbol{N}_{n+1} \tag{b.9}$$

where, $\boldsymbol{\sigma}_{n+1}$ is the stress tensor at time t_{n+1}, $\boldsymbol{\sigma}_{n+1}^{trial}$ is the trial stress tensor at time t_{n+1} and $\mathbf{D^e}$ is the elasticity matrix.

Then, the residual system of equations can be determined by the update equation for the stress tensor (Equation b.9), update equation for the equivalent plastic strain (Equation b.8) and the complementary Equation (Equation b.1), as:

$$\begin{cases} \boldsymbol{r}_{\sigma} = \boldsymbol{\sigma}_{n+1} - \boldsymbol{\sigma}_{n+1}^{trial} + \Delta\gamma \mathbf{D}: \boldsymbol{N}_{n+1} \\ r_{\bar{\varepsilon}^p} = \bar{\varepsilon}_{n+1}^{p} - \bar{\varepsilon}_{n+1}^{p\ trial} - \Delta\gamma \sqrt{\alpha^2 + \frac{2}{9}\beta^2 + \lambda^2 \frac{\boldsymbol{M}:\boldsymbol{M}}{\boldsymbol{S}:\boldsymbol{S}} + 2.\alpha.\lambda \frac{\boldsymbol{S}:\boldsymbol{M}}{\boldsymbol{S}:\boldsymbol{S}}} \\ r_{\Delta\gamma} = q_{n+1} - \sigma_y\left(\bar{\varepsilon}_{n+1}^{p}\right) A_{n+1} B_{n+1} \end{cases} \tag{b.10}$$

d) Write the nonlinear residual system of equation in the linearized form

Equation (b.10) can be written in the linearized form according Equation (b.11), as:

$$\begin{bmatrix} \frac{\partial \boldsymbol{r}_{\sigma}}{\partial \boldsymbol{\sigma}_{n+1}} & \frac{\partial \boldsymbol{r}_{\sigma}}{\partial \bar{\varepsilon}_{n+1}^{p}} & \frac{\partial \boldsymbol{r}_{\sigma}}{\partial \Delta\gamma} \\ \frac{\partial r_{\bar{\varepsilon}^p}}{\partial \boldsymbol{\sigma}_{n+1}} & \frac{\partial r_{\bar{\varepsilon}^p}}{\partial \bar{\varepsilon}_{n+1}^{p}} & \frac{\partial r_{\bar{\varepsilon}^p}}{\partial \Delta\gamma} \\ \frac{\partial r_{\Delta\gamma}}{\partial \boldsymbol{\sigma}_{n+1}} & \frac{\partial r_{\Delta\gamma}}{\partial \bar{\varepsilon}_{n+1}^{p}} & \frac{\partial r_{\Delta\gamma}}{\partial \Delta\gamma} \end{bmatrix}^{k} \cdot \begin{bmatrix} \delta\boldsymbol{\sigma}_{n+1} \\ \delta\bar{\varepsilon}_{n+1}^{p} \\ \delta\Delta\gamma \end{bmatrix}^{k+1} = -\begin{bmatrix} \boldsymbol{r}_{\sigma}\left(\boldsymbol{\sigma}_{n+1}, \bar{\varepsilon}_{n+1}^{p}, \Delta\gamma\right) \\ r_{\bar{\varepsilon}^p}\left(\boldsymbol{\sigma}_{n+1}, \bar{\varepsilon}_{n+1}^{p}, \Delta\gamma\right) \\ r_{\Delta\gamma}\left(\boldsymbol{\sigma}_{n+1}, \bar{\varepsilon}_{n+1}^{p}, \Delta\gamma\right) \end{bmatrix}^{k} \tag{b.11}$$

where, $\partial(\,)/\partial\boldsymbol{\sigma}_{n+1}$, $\partial(\,)/\partial\bar{\varepsilon}_{n+1}^{p}$ and $\partial(\,)/\partial\Delta\gamma$ represent the derivative of each residual equation in relation to each variable of the problem. After some algebraic manipulations, Equation (b.11) can be re-written as:

$$\begin{bmatrix} \mathbb{I} + \Delta\gamma \mathbf{D}^{e}: \frac{\partial \boldsymbol{N}_{n+1}}{\partial \boldsymbol{\sigma}_{n+1}} & \Delta\gamma \frac{\partial \boldsymbol{N}_{n+1}}{\partial \bar{\varepsilon}_{n+1}^{p}} & \mathbf{D}^{e}: \boldsymbol{N}_{n+1} \\ -\Delta\gamma \frac{\partial \sqrt{(*)}}{\partial \boldsymbol{\sigma}_{n+1}} & 1 - \Delta\gamma \frac{\partial \sqrt{(*)}}{\partial \bar{\varepsilon}_{n+1}^{p}} & -\sqrt{(*)} \\ \boldsymbol{N}_{n+1} & -A_{n+1}B_{n+1}H & 0 \end{bmatrix}^{k} \cdot \begin{bmatrix} \delta\boldsymbol{\sigma}_{n+1} \\ \delta\bar{\varepsilon}_{n+1}^{p} \\ \delta\Delta\gamma \end{bmatrix}^{k+1} = -\begin{bmatrix} r_{\sigma}\left(\boldsymbol{\sigma}_{n+1}, \bar{\varepsilon}_{n+1}^{p}, \Delta\gamma\right) \\ r_{\bar{\varepsilon}^p}\left(\boldsymbol{\sigma}_{n+1}, \bar{\varepsilon}_{n+1}^{p}, \Delta\gamma\right) \\ r_{\Delta\gamma}\left(\boldsymbol{\sigma}_{n+1}, \bar{\varepsilon}_{n+1}^{p}, \Delta\gamma\right) \end{bmatrix}^{k} \tag{b.15}$$

where, $\frac{\partial \boldsymbol{N}_{n+1}}{\partial \sigma_{n+1}}$, $\frac{\partial \boldsymbol{N}_{n+1}}{\partial \bar{\varepsilon}_{n+1}^{p}}$ represent the derivative of the flow vector in relation to stress tensor and accumulated plastic strain, respectively. The terms $\frac{\partial \sqrt{(*)}}{\partial \boldsymbol{\sigma}_{n+1}}$ and $\frac{\partial \sqrt{(*)}}{\partial \bar{\varepsilon}_{n+1}^{p}}$ represent the derivative of the auxiliary square root in relation to stress tensor and accumulated plastic strain.

$$\sqrt{(*)} = \sqrt{\alpha^2 + \frac{2}{9}\beta^2 + \lambda^2 \frac{\boldsymbol{M}:\boldsymbol{M}}{\boldsymbol{S}:\boldsymbol{S}} + 2.\alpha.\lambda \frac{\boldsymbol{S}:\boldsymbol{M}}{\boldsymbol{S}:\boldsymbol{S}}} \tag{b.16}$$

In order to determine the derivative of the flow vector in relation to stress tensor and equivalent plastic strain, we have:

$$\frac{\partial \boldsymbol{N}_{n+1}}{\partial \boldsymbol{\sigma}_{n+1}} = \frac{\partial \left[\frac{3}{2q_{n+1}} \alpha_{n+1} \boldsymbol{S}_{n+1}\right]}{\partial \boldsymbol{\sigma}_{n+1}} + \frac{\partial \left[\frac{3}{2q_{n+1}} \lambda_{n+1} \boldsymbol{M}_{n+1}\right]}{\partial \boldsymbol{\sigma}_{n+1}} + \frac{\partial \left[\frac{1}{3} \beta_{n+1} \boldsymbol{I}\right]}{\partial \boldsymbol{\sigma}_{n+1}} \tag{b.17}$$

where:

$$\frac{\partial \left[\frac{3}{2q} \alpha \boldsymbol{S}\right]}{\partial \boldsymbol{\sigma}} = \frac{3}{2}\left[\frac{1}{q}\left(\frac{\partial \alpha}{\partial \boldsymbol{\sigma}}\right) \otimes \boldsymbol{S} + \frac{\alpha}{q}\left(\frac{\partial \boldsymbol{S}}{\partial \boldsymbol{\sigma}}\right) - \frac{\alpha}{q^2}\left(\frac{\partial q}{\partial \boldsymbol{\sigma}}\right) \otimes \boldsymbol{S}\right] \tag{b.18}$$

$$\frac{\partial \left[\frac{3}{2q} \lambda \boldsymbol{M}\right]}{\partial \boldsymbol{\sigma}} = \frac{3}{2}\left[\frac{1}{q}\left(\frac{\partial \lambda}{\partial \boldsymbol{\sigma}}\right) \otimes \boldsymbol{M} + \frac{\lambda}{q}\left(\frac{\partial \boldsymbol{M}}{\partial \boldsymbol{\sigma}}\right) - \frac{\lambda}{q^2}\left(\frac{\partial q}{\partial \boldsymbol{\sigma}}\right) \otimes \boldsymbol{M}\right] \tag{b.19}$$

$$\frac{\partial \left[\frac{1}{3} \beta \boldsymbol{I}\right]}{\partial \boldsymbol{\sigma}} = \frac{1}{3}\left(\frac{\partial \beta}{\partial \boldsymbol{\sigma}}\right) \otimes \boldsymbol{I} \tag{b.20}$$

$$\frac{\partial \boldsymbol{N}_{n+1}}{\partial \bar{\varepsilon}^p_{n+1}} = \frac{\partial \left[\frac{3}{2q_{n+1}} \alpha_{n+1} \boldsymbol{S}_{n+1}\right]}{\partial \bar{\varepsilon}^p_{n+1}} + \frac{\partial \left[\frac{3}{2q_{n+1}} \lambda_{n+1} \boldsymbol{M}_{n+1}\right]}{\partial \bar{\varepsilon}^p_{n+1}} + \frac{\partial \left[\frac{1}{3} \beta_{n+1} \boldsymbol{I}\right]}{\partial \bar{\varepsilon}^p_{n+1}} \tag{b.21}$$

where,

$$\frac{\partial\left[\frac{3}{2q}\alpha\boldsymbol{S}\right]}{\partial\varepsilon^{p}}=\frac{3}{2q}\left(\frac{\partial\alpha}{\partial\varepsilon^{p}}\right)\boldsymbol{S} \tag{b.22}$$

$$\frac{\partial\left[\frac{3}{2q}\lambda\boldsymbol{M}\right]}{\partial\varepsilon^{p}}=\frac{3}{2q}\left(\frac{\partial\lambda}{\partial\varepsilon^{p}}\right)\boldsymbol{M} \tag{b.23}$$

$$\frac{\partial\left[\frac{1}{3}\beta\boldsymbol{I}\right]}{\partial\varepsilon^{p}}=\frac{1}{3}\left(\frac{\partial\beta}{\partial\varepsilon^{p}}\right)\boldsymbol{I} \tag{b.24}$$

In order to determine the derivative of $\sqrt{(*)}$ in relation to stress tensor and equivalent plastic strain, we have:

$$\frac{\partial\left[\sqrt{(*)}\right]}{\partial\boldsymbol{\sigma}}=\frac{1}{2\sqrt{(*)}}\left[2\alpha\left(\frac{\partial\alpha}{\partial\boldsymbol{\sigma}}\right)+\frac{4}{9}\beta\left(\frac{\partial\beta}{\partial\boldsymbol{\sigma}}\right)+\frac{\partial}{\partial\boldsymbol{\sigma}}\left(\lambda^{2}\frac{\boldsymbol{M}:\boldsymbol{M}}{\boldsymbol{S}:\boldsymbol{S}}\right)+2\frac{\partial}{\partial\boldsymbol{\sigma}}\left(\alpha\lambda\frac{\boldsymbol{S}:\boldsymbol{M}}{\boldsymbol{S}:\boldsymbol{S}}\right)\right] \tag{b.25}$$

where,

$$\frac{\partial}{\partial\boldsymbol{\sigma}}\left(\lambda^{2}\frac{\boldsymbol{M}:\boldsymbol{M}}{\boldsymbol{S}:\boldsymbol{S}}\right)=2\lambda\left(\frac{\partial\lambda}{\partial\boldsymbol{\sigma}}\right)\frac{\boldsymbol{M}:\boldsymbol{M}}{\boldsymbol{S}:\boldsymbol{S}}+2\left[\boldsymbol{M}:\left(\frac{\partial\boldsymbol{M}}{\partial\boldsymbol{\sigma}}\right)\right]\frac{\lambda^{2}}{\boldsymbol{S}:\boldsymbol{S}}-2\left[\underline{\boldsymbol{S}}:\left(\frac{\partial\boldsymbol{S}}{\partial\boldsymbol{\sigma}}\right)\right]\left(\lambda^{2}\frac{\boldsymbol{M}:\boldsymbol{M}}{\boldsymbol{S}:\boldsymbol{S}}\right) \tag{b.26}$$

$$\begin{aligned}2\frac{\partial}{\partial\boldsymbol{\sigma}}\left(\alpha\lambda\frac{\boldsymbol{S}:\boldsymbol{M}}{\boldsymbol{S}:\boldsymbol{S}}\right)=2\Bigg[&\lambda\left(\frac{\partial\alpha}{\partial\boldsymbol{\sigma}}\right)\frac{\boldsymbol{S}:\boldsymbol{M}}{\boldsymbol{S}:\boldsymbol{S}}+\alpha\left(\frac{\partial\lambda}{\partial\boldsymbol{\sigma}}\right)\frac{\boldsymbol{S}:\boldsymbol{M}}{\boldsymbol{S}:\boldsymbol{S}}+\frac{\alpha\lambda}{\boldsymbol{S}:\boldsymbol{S}}\left(\frac{\partial\boldsymbol{S}}{\partial\boldsymbol{\sigma}}:\boldsymbol{M}+\boldsymbol{S}:\frac{\partial\boldsymbol{M}}{\partial\boldsymbol{\sigma}}\right)\\&-2\alpha\lambda\frac{\boldsymbol{S}:\boldsymbol{M}}{(\boldsymbol{S}:\boldsymbol{S})^{2}}\left(\boldsymbol{S}:\frac{\partial\boldsymbol{S}}{\partial\boldsymbol{\sigma}}\right)\Bigg]\end{aligned} \tag{b.27}$$

$$\frac{\partial\left[\sqrt{(*)}\right]}{\partial\varepsilon^p}=\frac{1}{2\sqrt{(*)}}\Big[2\alpha\left(\frac{\partial\alpha}{\partial\varepsilon^p}\right)+\frac{4}{9}\beta\left(\frac{\partial\beta}{\partial\varepsilon^p}\right)+2\lambda\left(\frac{\partial\lambda}{\partial\varepsilon^p}\right)\frac{\boldsymbol{M}:\boldsymbol{M}}{\boldsymbol{S}:\boldsymbol{S}}+2\lambda\left(\frac{\partial\alpha}{\partial\varepsilon^p}\right)\frac{\boldsymbol{S}:\boldsymbol{M}}{\boldsymbol{S}:\boldsymbol{S}}$$
$$+2\alpha\left(\frac{\partial\lambda}{\partial\varepsilon^p}\right)\frac{\boldsymbol{S}:\boldsymbol{M}}{\boldsymbol{S}:\boldsymbol{S}}\Big] \tag{b.28}$$

Other required derivatives can be defined as following:

$$\frac{\partial q}{\partial\boldsymbol{\sigma}}=\frac{3}{2q}\boldsymbol{S} \tag{b.29}$$

$$\frac{\partial S}{\partial\boldsymbol{\sigma}}=\mathbb{I}-\frac{1}{3}\boldsymbol{I}\otimes\boldsymbol{I} \tag{b.30}$$

$$\frac{\partial M}{\partial\boldsymbol{\sigma}}=\left[\left(\frac{\partial\boldsymbol{S}^2}{\partial\boldsymbol{S}}\right)-\frac{1}{3}\left(\frac{\partial tr\boldsymbol{S}^2}{\partial\boldsymbol{S}}\right)\otimes\boldsymbol{I}\right]:\frac{\partial\boldsymbol{S}}{\partial\boldsymbol{\sigma}} \tag{b.31}$$

$$\left(\frac{\partial\boldsymbol{S}^2}{\partial\boldsymbol{\sigma}}\right)=\left(\frac{\partial\boldsymbol{S}^2}{\partial\boldsymbol{S}}\right):\left(\frac{\partial\boldsymbol{S}}{\partial\boldsymbol{\sigma}}\right) \tag{b.32}$$

$$\left(\frac{\partial\boldsymbol{S}^2}{\partial\boldsymbol{S}}\right)=2\boldsymbol{S} \tag{b.33}$$

$$\left(\frac{\partial tr\boldsymbol{S}^2}{\partial\boldsymbol{\sigma}}\right)=2\boldsymbol{S}^T:\frac{\partial\boldsymbol{S}}{\partial\boldsymbol{\sigma}} \tag{b.34}$$

$$\frac{\partial \alpha}{\partial \boldsymbol{\sigma}} = \sigma_y(\bar{\varepsilon}^p)\frac{1}{q^2}\left[C_\eta B\eta + AD\xi\left(1 + 3I_1\frac{q^2}{r^3}\right)\right]\left(\frac{\partial q}{\partial \boldsymbol{\sigma}}\right)$$
$$-\frac{\sigma_y(\bar{\varepsilon}^p)}{q}\left[C_\eta\left(\frac{\partial B}{\partial \boldsymbol{\sigma}}\eta + B\frac{\partial \eta}{\partial \boldsymbol{\sigma}}\right)\right.$$
$$+\left(\frac{\partial A}{\partial \boldsymbol{\sigma}}D\xi + A\frac{\partial D}{\partial \boldsymbol{\sigma}}\xi + AD\frac{\partial \xi}{\partial \boldsymbol{\sigma}}\right)\left(1 + 3I_1\frac{q^2}{r^3}\right) \tag{b.35}$$
$$\left. + 3AD\xi\left(\frac{\partial I_1}{\partial \boldsymbol{\sigma}}\frac{q^2}{r^3} + \frac{2I_1 q}{r^3}\frac{\partial q}{\partial \boldsymbol{\sigma}} - \frac{3I_1 q^2}{r^4}\frac{\partial r}{\partial \boldsymbol{\sigma}}\right)\right]$$

$$\frac{\partial \beta}{\partial \boldsymbol{\sigma}} = \sigma_y(\bar{\varepsilon}^p)C_\eta\left[\left(\frac{\partial B}{\partial \boldsymbol{\sigma}}\right)\frac{1}{q} - \frac{B}{q^2}\left(\frac{\partial q}{\partial \boldsymbol{\sigma}}\right)\right] \tag{b.36}$$

$$\frac{\partial \lambda}{\partial \boldsymbol{\sigma}} = 3\sigma_y(\bar{\varepsilon}^p)\left[\left(\frac{\partial A}{\partial \boldsymbol{\sigma}}\right)\frac{D}{q^2} + \left(\frac{\partial D}{\partial \boldsymbol{\sigma}}\right)\frac{A}{q^2} - \frac{2AD}{q^3}\left(\frac{\partial q}{\partial \boldsymbol{\sigma}}\right)\right] \tag{b.37}$$

$$\frac{\partial \alpha}{\partial \varepsilon^p} = \frac{-H}{q}\left[C_\eta B\eta + AD\xi\left(1 + 3I_1\frac{q^2}{r^3}\right)\right] \tag{b.38}$$

$$\frac{\partial \beta}{\partial \varepsilon^p} = \frac{HC_\eta B}{q} \tag{b.39}$$

$$\frac{\partial \lambda}{\partial \varepsilon^p} = \frac{3HAD}{q^2} \tag{b.40}$$

$$\frac{\partial[A(\eta)]}{\partial \boldsymbol{\sigma}} = -C_\eta \left[\frac{1}{3q}\boldsymbol{I} - \frac{3\eta}{2q^2}\boldsymbol{S}\right] = C_\eta \left[\frac{3\eta}{2q^2}\boldsymbol{S} - \frac{1}{3q}\boldsymbol{I}\right] \tag{b.41}$$

$$\frac{\partial[B(\mu)]}{\partial \boldsymbol{\sigma}} = D\xi \left[\left(\frac{3}{2q^2} + \frac{9I_1}{2r^3}\right)\boldsymbol{S} - \frac{9}{2r^3}\boldsymbol{M}\right] \tag{b.42}$$

where, D is defined as:

$$D(\theta) = (C_\theta^{ax} - C_\theta^{s})(1-\mu^m)\frac{\cos(\pi/6)}{1-\cos(\pi/6)}\frac{\tan(\theta-\pi/6)}{\cos(\theta-\pi/6)}\frac{1}{\sin 3\theta} \tag{b.43}$$

$$\begin{aligned}\frac{\partial[D(\theta)]}{\partial \boldsymbol{\sigma}} = \frac{\cos\pi/6}{1-\cos\pi/6}\frac{(C_\theta^{ax} - C_\theta^{s})}{3\sin^2(3\theta)}\Bigg[&m\gamma^{m+1}\frac{\cos\pi/6}{1-\cos\pi/6}\frac{\tan^2(\theta-\pi/6)}{\cos^2(\theta-\pi/6)} \\ &-(1-\gamma^m)\frac{(1-2\tan^2(\theta-\pi/6))}{\cos(\theta-\pi/6)} \\ &+(1-\gamma^m)\frac{\tan(\theta-\pi/6)}{\cos(\theta-\pi/6)}\frac{\cos(3\theta)}{\sin(3\theta)}\Bigg]\left(\frac{\partial\xi}{\partial\boldsymbol{\sigma}}\right)\end{aligned} \tag{b.44}$$

APPENDIX C

Determine the flow vector and plastic flow rule for GTN model with shear mechanism

a) Define the yield function for the specific model:

$$\Phi(\boldsymbol{\sigma}, k, f) = \left(\frac{\sigma_{eq}}{\sigma_0}\right)^2 + 2q_1 f \cosh\left(\frac{q_2 tr\boldsymbol{\sigma}}{2\sigma_0}\right) - 1 - q_3 f^2 \quad \text{(c.1)}$$

where, σ_{eq} is the von Mises equivalent stress, σ_0 is the isotropic hardening rule which can be defined as $\sigma_0 = k - \sigma_{y0}$, k represents the isotropic hardening state variable, f represents the effective porosity and q_1 , q_2 and q_3 are material constants. Equation (c.1) can be re-written as:

$$\Phi(\boldsymbol{\sigma}, k, f) = J_2(\boldsymbol{S}) - \frac{1}{3}\left\{1 + q_3 f^2 - 2q_1 f \cosh\left(\frac{q_2 3p}{2\sigma_0}\right)\right\}{\sigma_0}^2 \quad \text{(c.2)}$$

where, J_2 represents the second invariant of the deviatoric stress tensor and p is the pressure which can be defined as $p = \frac{1}{3} tr\boldsymbol{\sigma}$.

The evolution of the porosity can be verified below, which we have the mechanisms of nucleation, growth of volumetric void and shear:

$$\dot{f} = \dot{f}_n + \dot{f}_g + \dot{D}_{shear} \quad \text{(c.3)}$$

where, $\dot{f}_n$ represents the volumetric void nucleation mechanism, $\dot{f}_g$ represents the volumetric void growth mechanism and $\dot{D}_{shear}$ represents the shear mechanism.

The evolutions of the volume void nucleation, growth of void and shear mechanisms can be obtained by Equations (c.4 – c.6), respectively.

$$\dot{f}_n = \frac{f_N}{s_N\sqrt{2\pi}} \exp\left[-\frac{1}{2}\left(\frac{\overline{\varepsilon}^p - \varepsilon_N}{s_N}\right)^2\right] \dot{\overline{\varepsilon}}^p \tag{c.4}$$

where, f_N represents the volume fraction of all second-phase particles with potential for microvoid nucleation, ε_N and s_N are the mean strain for void nucleation and its standard deviation. The term $\overline{\varepsilon}^p$ represents the equivalent plastic strain and $\dot{\overline{\varepsilon}}^p$ is the evolution of the accumulated plastic strain.

$$\dot{f}_g = (1-f)\dot{\varepsilon}_v^p \tag{c.5}$$

where, $\dot{\varepsilon}_v^p$ represents the incremental plastic volumetric strain. Then, the evolution law for the shear mechanism can be defined according Xue (2008) or Nahshon *et al.* (2008), as:

$$\dot{D}_{shear} = \begin{cases} q_4\left(1-\left|\bar{\theta}\right|\right) f^{q_5}\, \bar{\varepsilon}^p \dot{\overline{\varepsilon}}^p \,, & for\ Xue's\ mechanism \\ kf(1-\xi^2)\dot{\overline{\varepsilon}}^p \,, & for\ Nahshon's\ mechanism \end{cases} \tag{c.6}$$

where, q_4, q_5 and k are constants. The terms $\bar{\theta}$ and ξ represent the normalized Lode angle and normalized third invariant, respectively.

b) The flow vector is defined as:

$$\boldsymbol{N} \equiv \frac{\partial \Phi}{\partial \boldsymbol{\sigma}} = \frac{\partial [J_2(\boldsymbol{S})]}{\partial \boldsymbol{\sigma}} - \frac{1}{3}\frac{\partial\left[\left\{1 + q_3 f^2 - 2q_1 f \cosh\left(\frac{q_2 3p}{2\sigma_0}\right)\right\}{\sigma_0}^2\right]}{\partial \boldsymbol{\sigma}} \tag{c.7}$$

In order to determine the closed equation for the flow vector, we have to determine the following derivative:

$$\frac{\partial [J_2(\boldsymbol{S})]}{\partial \boldsymbol{\sigma}} = \frac{\partial\left[\frac{1}{2}\boldsymbol{S}:\boldsymbol{S}\right]}{\partial \boldsymbol{\sigma}} = \boldsymbol{S}:\frac{\partial \boldsymbol{S}}{\partial \boldsymbol{\sigma}} = \boldsymbol{S} \tag{c.8}$$

The derivative of the second term of Equation (c.7) can be determined as:

$$\frac{\partial\left[\left\{1+q_3f^2-2q_1f\cosh\left(\frac{q_2 3p}{2\sigma_0}\right)\right\}{\sigma_0}^2\right]}{\partial\boldsymbol{\sigma}}=-2q_1f{\sigma_0}^2\frac{\partial\left[\cosh\left(\frac{q_2 3p}{2\sigma_0}\right)\right]}{\partial\boldsymbol{\sigma}} \tag{c.9}$$

Remark: The derivative of $(\partial\cosh(x)/\partial x)$ *is equal to* $\sinh(x)$.

Thus, after some algebraic manipulation, the above derivative can be written as:

$$\frac{\partial\left[\left\{1+q_3f^2-2q_1f\cosh\left(\frac{q_2 3p}{2\sigma_0}\right)\right\}{\sigma_0}^2\right]}{\partial\boldsymbol{\sigma}}=-q_1q_2f\sigma_0\sinh\left(\frac{q_2 3p}{2\sigma_0}\right)\boldsymbol{I} \tag{c.10}$$

However, the flow vector for GTN´s model can be obtained as:

$$\boldsymbol{N}=\boldsymbol{S}+\frac{1}{3}q_1q_2f\sigma_0\sinh\left(\frac{q_2 3p}{2\sigma_0}\right)\boldsymbol{I} \tag{c.11}$$

c) The plastic flow rule:

The incremental plastic strain can be defined according Equation (c.12), as:

$$\dot{\varepsilon}^p\equiv\dot{\gamma}.\boldsymbol{N}=\dot{\gamma}.\left[\boldsymbol{S}+\frac{1}{3}q_1q_2f\sigma_0\sinh\left(\frac{q_2 3p}{2\sigma_0}\right)\boldsymbol{I}\right] \tag{c.12}$$

where, $\dot{\varepsilon}^p$ represents the incremental plastic strain and $\dot{\gamma}$ is the plastic multiplier. Thus, the incremental plastic volumetric strain can be obtained by Equation below:

$$\dot{\varepsilon}_v^p=\dot{\gamma}q_1q_2f\sigma_0\sinh\left(\frac{q_2 3p}{2\sigma_0}\right) \tag{c.13}$$

The evolution of the isotropic hardening variable is defined as:

$$\dot{R}=-\dot{\gamma}\frac{\partial\Phi}{\partial k} \tag{c.14}$$

where, $\dot{R}$ represents the evolution of the isotropic hardening variable, k is the isotropic hardening state variable which can be defined as $k=H\,R$ and H is the hardening modulus. After some algebraic manipulation, the above derivative of the yield function in relation to the isotropic hardening state variable can be written as:

$$\frac{\partial \Phi}{\partial k} = -\left\{q_1 q_2 f p \sinh\left(\frac{q_2 3p}{2\sigma_0}\right) + \frac{2}{3}\left[1 + q_3 f^2 - 2q_1 f \cosh\left(\frac{q_2 3p}{2\sigma_0}\right)\right]\sigma_0\right\} \tag{c.15}$$

Substituting the above result into Equation (c.14) we can obtain:

$$\dot{R} = \dot{\gamma}\frac{\left\{q_1 q_2 f p \sinh\left(\frac{q_2 3p}{2\sigma_0}\right) + \frac{2}{3}\left[1 + q_3 f^2 - 2q_1 f \cosh\left(\frac{q_2 3p}{2\sigma_0}\right)\right]\sigma_0\right\}}{(1-f)} \tag{c.16}$$

The term $(1-f)$ into the denominator of the equation (c.18) is responsible for introduce the softening effect into the GTN´s model.

The accumulated plastic strain can be determined by Equation (c.19):

$$\dot{\bar{\varepsilon}}^p = \sqrt{\frac{2}{3}(\dot{\varepsilon}^p : \dot{\varepsilon}^p)} \tag{c.17}$$

Substituting Equation (c.12) into Equation (c.17) and after some algebraic manipulation, we can obtain:

$$\dot{\bar{\varepsilon}}^p = \dot{\gamma}.\sqrt{\frac{2}{3}\left\{\boldsymbol{S}:\boldsymbol{S} + \frac{1}{3}\left[q_1 q_2 f \sigma_0 \sinh\left(\frac{q_2 3p}{2\sigma_0}\right)\right]^2\right\}} \tag{c.18}$$

d) The stress tensor:

The updated stress tensor can be obtained as:

$$\boldsymbol{\sigma}_{n+1} = \boldsymbol{\sigma}_{n+1}^{trial} - \mathbf{D}:\Delta\boldsymbol{\varepsilon}_{n+1}^{p} \tag{c.19}$$

Substituting Equation (c.12) into Equation (c.19), we have:

$$\boldsymbol{\sigma}_{n+1} = \boldsymbol{\sigma}_{n+1}^{trial} - \mathbf{D}:\Delta\gamma\left[\boldsymbol{S}_{n+1} + \frac{1}{3}q_1 q_2 f_{n+1}\sigma_0 \sinh\left(\frac{q_2 3p_{n+1}}{2\sigma_0}\right)\boldsymbol{I}\right] \tag{c.20}$$

We can split the trial stress tensor into deviatoric and volumetric parts as:

$$\boldsymbol{\sigma}_{n+1} = \boldsymbol{S}_{n+1}^{trial} + p_{n+1}^{trial}\boldsymbol{I} - \mathbf{D}\colon \Delta\gamma\left[\boldsymbol{S}_{n+1} + \frac{1}{3}q_1 q_2 f_{n+1}\sigma_0 \sinh\left(\frac{q_2 3p_{n+1}}{2\sigma_0}\right)\boldsymbol{I}\right] \qquad \text{(c.21)}$$

Then, after some algebraic manipulations, the updated deviatoric and volumetric parts of the stress tensor can be obtained as:

$$\boldsymbol{S}_{n+1} = \frac{\boldsymbol{S}_{n+1}^{trial}}{(1 + 2G\Delta\gamma)} \qquad \text{(c.22)}$$

$$p_{n+1}\boldsymbol{I} = \left[p_{n+1}^{trial} - \frac{1}{3}\Delta\gamma K q_1 q_2 f_{n+1}\sigma_0 . \sinh\left(\frac{q_2 3p_{n+1}}{2\sigma_0}\right)\right]\boldsymbol{I} \qquad \text{(c.23)}$$

Using above equations, the evolution of the accumulated plastic strain and the updated form for the yield function can be determined as:

$$\Delta\varepsilon_{n+1}^{p} = \Delta\gamma\left[\frac{\boldsymbol{S}_{n+1}^{trial}}{(1 + 2G\Delta\gamma)} + \frac{1}{3}q_1 q_2 f_{n+1}\sigma_0 \sinh\left(\frac{q_2 3p_{n+1}}{2\sigma_0}\right)\boldsymbol{I}\right] \qquad \text{(c.24)}$$

$$\Delta\bar{\varepsilon}_{n+1}^{p} = \Delta\gamma\sqrt{\frac{2}{3}\left\{\frac{\boldsymbol{S}_{n+1}^{trial}\colon \boldsymbol{S}_{n+1}^{trial}}{(1 + 2G\Delta\gamma)^2} + \frac{1}{3}\left[q_1 q_2 f_{n+1}\sigma_0 \sinh\left(\frac{q_2 3p_{n+1}}{2\sigma_0}\right)\right]^2\right\}} \qquad \text{(c.25)}$$

$$\Phi(\boldsymbol{\sigma}, k, f) = \frac{1}{2}\frac{\boldsymbol{S}_{n+1}^{trial}\colon \boldsymbol{S}_{n+1}^{trial}}{(1 + 2G\Delta\gamma)^2} - \frac{1}{3}\left\{1 + q_3 {f_{n+1}}^2 - 2q_1 f_{n+1}\cosh\left(\frac{q_2 3p_{n+1}}{2\sigma_0}\right)\right\}{\sigma_0}^2 \qquad \text{(c.26)}$$

APPENDIX D

Linearization procedure for GTN's model with shear mechanism

a) Constitutive model

Define the yield function

The yield function for GTN´s model can be defined according the equation below:

$$\Phi(\boldsymbol{\sigma}, k, f) = \frac{1}{2}\frac{\boldsymbol{S}_{n+1}^{trial} : \boldsymbol{S}_{n+1}^{trial}}{(1+2G\Delta\gamma)^2} - \frac{1}{3}\left\{1 + {q_3 f_{n+1}}^2 - 2q_1 f_{n+1}\cosh\left(\frac{q_2 3p_{n+1}}{2\sigma_0}\right)\right\}{\sigma_0}^2 \tag{d.1}$$

where, σ_0 is the isotropic hardening rule which can be defined as $\sigma_0 = k - \sigma_{y0}$, k represents the isotropic hardening state variable, f represents the porosity and q_1, q_2 and q_3 are material constants.

The flow vector

$$\boldsymbol{N} \equiv \frac{\partial \Phi}{\partial \sigma} = \left[\frac{\boldsymbol{S}_{n+1}^{trial}}{(1+2G\Delta\gamma)} + \frac{1}{3}q_1 q_2 f_{n+1}\sigma_0 \sinh\left(\frac{q_2 3p_{n+1}}{2\sigma_0}\right)\boldsymbol{I}\right] \tag{d.2}$$

where, $\boldsymbol{N}$ represents the flow vector, $\boldsymbol{S}$ is the deviatoric stress tensor, $\boldsymbol{I}$ is the second order identity tensor

The plastic flow rule

Plastic strain:

$$\Delta\varepsilon^p = \Delta\gamma\left[\frac{\boldsymbol{S}_{n+1}^{trial}}{(1+2G\Delta\gamma)} + \frac{1}{3}q_1 q_2 f_{n+1}\sigma_0 \sinh\left(\frac{q_2 3p_{n+1}}{2\sigma_0}\right)\boldsymbol{I}\right] \tag{d.3}$$

where, $\Delta\varepsilon^p$ represents the increment of the plastic strain and $\Delta\gamma$ is the plastic multiplier.

Accumulated plastic strain:

$$\Delta\bar{\varepsilon}^{p} = \Delta\gamma\sqrt{\frac{2}{3}\left\{\frac{\boldsymbol{S}_{n+1}^{trial}:\boldsymbol{S}_{n+1}^{trial}}{(1+2G\Delta\gamma)^{2}}+\frac{1}{3}\left[q_1 q_2 f_{n+1}\sigma_0 \sinh\left(\frac{q_2 3p_{n+1}}{2\sigma_0}\right)\right]^{2}\right\}} \tag{d.4}$$

where, $\Delta\bar{\varepsilon}^{p}$ represents the increment of the accumulated plastic strain.

Evolution of the isotropic hardening variable

$$\begin{aligned}\Delta R = \frac{\Delta\gamma}{(1-f_{n+1})}\Bigg\{&q_1 q_2 f_{n+1} p_{n+1}\sinh\left(\frac{q_2 3p_{n+1}}{2\sigma_0}\right)\\ &+\frac{2}{3}\left[1+q_3 {f_{n+1}}^{2}-2q_1 f_{n+1}\cosh\left(\frac{q_2 3p_{n+1}}{2\sigma_0}\right)\right]\sigma_0\Bigg\}\end{aligned} \tag{d.5}$$

The term $(1-f_{n+1})$ into the denominator of Equation (d.5) is responsible for introduce the softening effect into the GTN´s model.

Evolution of the porosity

The evolution of the damage variable which is called here for porosity or volume void fraction, can be defined as:

$$\begin{aligned}\Delta f = &\frac{f_{\mathrm{N}}}{s_{\mathrm{N}}\sqrt{2\pi}}\exp\left[-\frac{1}{2}\left(\frac{\bar{\varepsilon}_{n+1}^{p}-\varepsilon_{\mathrm{N}}}{s_{\mathrm{N}}}\right)^{2}\right]\Delta\bar{\varepsilon}^{p}\\ &+(1-f_{n+1})\Delta\gamma q_1 q_2 f_{n+1}\sigma_0.\sinh\left(\frac{q_2 3p_{n+1}}{2\sigma_0}\right)+\Delta D_s\end{aligned} \tag{d.6}$$

where, ΔD_s represents the increment of the shear contribution and can be determined as:

$$\Delta D_s = \begin{cases} q_4 g_0 {f_{n+1}}^{q_5}\,\bar{\varepsilon}_{n+1}^{p}\Delta\bar{\varepsilon}^{p}, & for\ Xue's\ mechanism \\ k f_{n+1} g_0 \Delta\bar{\varepsilon}^{p}, & for\ Nahshon's\ mechanism \end{cases} \tag{d.7}$$

Update stress tensor

$$\boldsymbol{\sigma}_{n+1} = \boldsymbol{\sigma}_{n+1}^{trial} - \mathbf{D}\colon \Delta\gamma \left[\boldsymbol{S}_{n+1} + \frac{1}{3} q_1 q_2 f_{n+1} \sigma_0 \sinh\left(\frac{q_2 3 p_{n+1}}{2\sigma_0}\right) \boldsymbol{I} \right] \tag{d.8}$$

The updated equations for deviatoric and volumetric parts of the stress tensor can be obtained as:

$$\boldsymbol{S}_{n+1} = \frac{\boldsymbol{S}_{n+1}^{trial}}{(1 + 2G\Delta\gamma)} \tag{d.9}$$

and,

$$p_{n+1}\boldsymbol{I} = \left[p_{n+1}^{trial} - \frac{1}{3} \Delta\gamma K q_1 q_2 f_{n+1} \sigma_0 \sinh\left(\frac{q_2 3 p_{n+1}}{2\sigma_0}\right) \right] \boldsymbol{I} \tag{d.10}$$

where, $\boldsymbol{\sigma}_{n+1}$ is the stress tensor at time t_{n+1}, $\boldsymbol{\sigma}_{n+1}^{trial}$ is the trial stress tensor at time t_{n+1} and **D** is the elasticity matrix.

b) Return mapping algorithm

The system of equations below needs to be solved for $\Delta\gamma$, p_{n+1}, f_{n+1} and R_{n+1} , by Newton_Raphson method.

$$\begin{cases} \Phi(\boldsymbol{\sigma}, k, f) = \dfrac{1}{2} \dfrac{\boldsymbol{S}^{trial} : \boldsymbol{S}^{trial}}{(1 + 2G\Delta\gamma)^2} - \dfrac{1}{3} \left\{ 1 + q_3 f^2 - 2 q_1 f \cosh\left(\dfrac{q_2 3p}{2\sigma_0}\right) \right\} {\sigma_0}^2 \\ p_{n+1} = p_{n+1}^{trial} - \Delta\gamma K q_1 q_2 f_{n+1} \sigma_0 \sinh\left(\dfrac{q_2 3 p_{n+1}}{2\sigma_0}\right) \\ f_{n+1} = f_{n+1}^{trial} + \dfrac{f_{\mathrm{N}}}{s_{\mathrm{N}}\sqrt{2\pi}} \exp\left[-\dfrac{1}{2} \left(\dfrac{\bar{\varepsilon}_{n+1}^{p} - \varepsilon_{\mathrm{N}}}{s_{\mathrm{N}}} \right)^2 \right] \Delta\bar{\varepsilon}_{n+1}^{p} + (1 - f) \Delta\varepsilon_{v\,n+1}^{p} + \Delta D_s \\ R_{n+1} = R_{n+1}^{trial} + \Delta R_{n+1} \end{cases} \tag{d.11}$$

The equivalent plastic strain can be determined as:

$$\bar{\varepsilon}_{n+1}^{p} = \bar{\varepsilon}_{n+1}^{p\,trial} + \Delta\bar{\varepsilon}_{n+1}^{p} \tag{d.12}$$

Linearization procedure:

Define the residual system of equations:

$$\begin{cases} r_{\Delta\gamma} = \dfrac{1}{2}\dfrac{\boldsymbol{S}^{trial}:\boldsymbol{S}^{trial}}{(1+2G\Delta\gamma)^2} - \dfrac{1}{3}\left\{1 + q_3 f^2 - 2q_1 f\cosh\left(\dfrac{q_2 3p}{2\sigma_0}\right)\right\}{\sigma_0}^2 \\ r_p = p_{n+1} - p_{n+1}^{trial} + \Delta\gamma K q_1 q_2 f_{n+1}\sigma_0 \sinh\left(\dfrac{q_2 3p_{n+1}}{2\sigma_0}\right) \\ r_f = f_{n+1}^{trial} + \dfrac{f_{\mathrm{N}}}{s_{\mathrm{N}}\sqrt{2\pi}}\exp\left[-\dfrac{1}{2}\left(\dfrac{\bar{\varepsilon}_{n+1}^{p} - \varepsilon_{\mathrm{N}}}{s_{\mathrm{N}}}\right)^2\right]\Delta\bar{\varepsilon}_{n+1}^{p} + (1-f)\Delta\varepsilon_{v\,n+1}^{p} + \Delta D_s \\ r_R = R_{n+1} - R_{n+1}^{trial} - \Delta R_{n+1} \end{cases} \tag{d.13}$$

Newton Raphson: using N-R method, the following linearized system of equations needs to be solver for $\Delta\gamma$, p_{n+1}, f_{n+1} and R_{n+1}

$$\begin{bmatrix} \dfrac{\partial r_{\Delta\gamma}}{\partial\Delta\gamma} & \dfrac{\partial r_{\Delta\gamma}}{\partial p_{n+1}} & \dfrac{\partial r_{\Delta\gamma}}{\partial f_{n+1}} & \dfrac{\partial r_{\Delta\gamma}}{\partial R_{n+1}} \\ \dfrac{\partial r_p}{\partial\Delta\gamma} & \dfrac{\partial r_p}{\partial p_{n+1}} & \dfrac{\partial r_p}{\partial f_{n+1}} & \dfrac{\partial r_p}{\partial R_{n+1}} \\ \dfrac{\partial r_f}{\partial\Delta\gamma} & \dfrac{\partial r_f}{\partial p_{n+1}} & \dfrac{\partial r_f}{\partial f_{n+1}} & \dfrac{\partial r_f}{\partial R_{n+1}} \\ \dfrac{\partial r_R}{\partial\Delta\gamma} & \dfrac{\partial r_R}{\partial p_{n+1}} & \dfrac{\partial r_R}{\partial f_{n+1}} & \dfrac{\partial r_R}{\partial R_{n+1}} \end{bmatrix}^k \cdot \begin{bmatrix} \delta\Delta\gamma \\ \delta p_{n+1} \\ \delta f_{n+1} \\ \delta R_{n+1} \end{bmatrix}^{k+1} = -\begin{bmatrix} r_{\Delta\gamma}(\Delta\gamma, p, f, R) \\ r_p(\Delta\gamma, p, f, R) \\ r_f(\Delta\gamma, p, f, R) \\ r_R(\Delta\gamma, p, f, R) \end{bmatrix}^k \tag{d.14}$$

We can represent above system of equation as:

$$\left[\frac{\partial r}{\partial(x)_{n+1}}\right]^k . [\delta x]^{k+1} = -[r(x)]^k \tag{d.15}$$

After some algebraic manipulation, the derivative of each residual equation in relation to each variable of the problem can be obtained as:

$$\frac{\partial r_{\Delta\gamma}}{\partial\Delta\gamma} = -\left[\frac{2G}{(1+2G\Delta\gamma)}\right]^3 \frac{1}{2}\boldsymbol{\varepsilon}_{d\,n+1}^{e\,trial}:\boldsymbol{\varepsilon}_{d\,n+1}^{e\,trial} \tag{d.16}$$

$$\frac{\partial r_{\Delta\gamma}}{\partial p_{n+1}} = q_1 q_2 f_{n+1}\sigma_0 \sinh\left(\frac{q_2 3p_{n+1}}{2\sigma_0}\right) \tag{d.17}$$

$$\frac{\partial r_{\Delta\gamma}}{\partial f_{n+1}} = -\frac{2}{3}{\sigma_0}^2\left[q_3 f_{n+1} - q_1 \cosh\left(\frac{q_2 3p_{n+1}}{2\sigma_0}\right)\right] \tag{d.18}$$

$$\begin{aligned}\frac{\partial r_{\Delta\gamma}}{\partial R_{n+1}} = &-\frac{2}{3}\sigma_0 H\left[1 + q_3 f_{n+1}^2 - 2q_1 f_{n+1}\cosh\left(\frac{q_2 3p_{n+1}}{2\sigma_0}\right)\right] \\ &- q_1 q_2 f_{n+1} p_{n+1} H \sinh\left(\frac{q_2 3p_{n+1}}{2\sigma_0}\right)\end{aligned} \tag{d.19}$$

$$\frac{\partial r_p}{\partial \Delta\gamma} = q_1 q_2 f_{n+1}\sigma_0 K \sinh\left(\frac{q_2 3p_{n+1}}{2\sigma_0}\right) \tag{d.20}$$

$$\frac{\partial r_p}{\partial p_{n+1}} = 1 + \frac{3}{2}\Delta\gamma K q_1 q_2 q_2 f_{n+1}\cosh\left(\frac{q_2 3p_{n+1}}{2\sigma_0}\right) \tag{d.21}$$

$$\frac{\partial r_p}{\partial f_{n+1}} = \Delta\gamma K q_1 q_2 \sigma_0 \sinh\left(\frac{q_2 3p_{n+1}}{2\sigma_0}\right) \tag{d.22}$$

$$\frac{\partial r_p}{\partial R_{n+1}} = H\Delta\gamma K q_1 q_2 f_{n+1}\left[\sinh\left(\frac{q_2 3p_{n+1}}{2\sigma_0}\right) - \frac{q_2 3p_{n+1}}{2\sigma_0}\cosh\left(\frac{q_2 3p_{n+1}}{2\sigma_0}\right)\right] \tag{d.23}$$

$$\begin{aligned}\frac{\partial r_f}{\partial \Delta\gamma} = &-\left(f_{n+1} - {f_{n+1}}^2\right) q_1 q_2 \sigma_0 \sinh\left(\frac{q_2 3p_{n+1}}{2\sigma_0}\right) \\ &- \frac{f_N}{s_N\sqrt{2\pi}}\exp\left[-\frac{1}{2}\left(\frac{\bar{\varepsilon}^p_{n+1} - \varepsilon_N}{s_N}\right)^2\right]\left[1\right. \\ &\left. - \Delta\bar{\varepsilon}^p_{n+1}\frac{1}{s_N}\left(\frac{\bar{\varepsilon}^p_{n+1} - \varepsilon_N}{s_N}\right)\right]\frac{\partial \Delta\bar{\varepsilon}^p_{n+1}}{\partial\Delta\gamma} + \frac{\partial \Delta D_s}{\partial\Delta\gamma}\end{aligned} \tag{d.24}$$

$$\frac{\partial r_f}{\partial p_{n+1}} = -\left(f_{n+1} - {f_{n+1}}^2\right)\frac{3\Delta\gamma}{2} q_1 q_2 q_2 \cosh\left(\frac{q_2 3p_{n+1}}{2\sigma_0}\right) - \frac{f_N}{s_N\sqrt{2\pi}} \exp\left[-\frac{1}{2}\left(\frac{\bar{\varepsilon}^p_{n+1} - \varepsilon_N}{s_N}\right)^2\right]\left[1 - \Delta\bar{\varepsilon}^p_{n+1}\frac{1}{s_N}\left(\frac{\bar{\varepsilon}^p_{n+1} - \varepsilon_N}{s_N}\right)\right]\frac{\partial\Delta\bar{\varepsilon}^p_{n+1}}{\partial p_{n+1}} + \frac{\partial\Delta D_s}{\partial p_{n+1}} \quad \text{(d.25)}$$

$$\frac{\partial r_f}{\partial f_{n+1}} = 1 - (1 - 2f_{n+1})\,\Delta\gamma q_1 q_2 \sigma_0 \sinh\left(\frac{q_2 3p_{n+1}}{2\sigma_0}\right) - \frac{f_N}{s_N\sqrt{2\pi}} \exp\left[-\frac{1}{2}\left(\frac{\bar{\varepsilon}^p_{n+1} - \varepsilon_N}{s_N}\right)^2\right]\left[1 - \Delta\bar{\varepsilon}^p_{n+1}\frac{1}{s_N}\left(\frac{\bar{\varepsilon}^p_{n+1} - \varepsilon_N}{s_N}\right)\right]\frac{\partial\Delta\bar{\varepsilon}^p_{n+1}}{\partial f_{n+1}} + \frac{\partial\Delta D_s}{\partial f_{n+1}} \quad \text{(d.26)}$$

$$\frac{\partial r_f}{\partial R_{n+1}} = -\left(f_{n+1} - {f_{n+1}}^2\right)\Delta\gamma q_1 q_2 H\left[\sinh\left(\frac{q_2 3p_{n+1}}{2\sigma_0}\right) - \frac{q_2 3p_{n+1}}{2\sigma_0}\cosh\left(\frac{q_2 3p_{n+1}}{2\sigma_0}\right)\right] - \frac{f_N}{s_N\sqrt{2\pi}} \exp\left[-\frac{1}{2}\left(\frac{\bar{\varepsilon}^p_{n+1} - \varepsilon_N}{s_N}\right)^2\right]\left[1 - \Delta\bar{\varepsilon}^p_{n+1}\frac{1}{s_N}\left(\frac{\bar{\varepsilon}^p_{n+1} - \varepsilon_N}{s_N}\right)\right]\frac{\partial\Delta\bar{\varepsilon}^p_{n+1}}{\partial R_{n+1}} + \frac{\partial\Delta D_s}{\partial R_{n+1}} \quad \text{(d.27)}$$

$$\frac{\partial r_R}{\partial \Delta\gamma} = -\frac{1}{(1-f_{n+1})}\left\{q_1 q_2 f_{n+1} p_{n+1} \sinh\left(\frac{q_2 3 p_{n+1}}{2\sigma_0}\right) + \frac{2}{3}\left[1 + q_3 f_{n+1}^2 - 2 q_1 f_{n+1} \cosh\left(\frac{q_2 3 p_{n+1}}{2\sigma_0}\right)\right]\sigma_0\right\} \tag{d.28}$$

$$\frac{\partial r_R}{\partial p_{n+1}} = -\frac{\Delta\gamma}{(1-f_{n+1})}\left[q_1 q_2 \left(\frac{q_2 3 p_{n+1}}{2\sigma_0}\right) f_{n+1} \cosh\left(\frac{q_2 3 p_{n+1}}{2\sigma_0}\right) - q_1 q_2 f_{n+1} \sinh\left(\frac{q_2 3 p_{n+1}}{2\sigma_0}\right)\right] \tag{d.29}$$

$$\frac{\partial r_R}{\partial f_{n+1}} = -\frac{\Delta\gamma}{(1-f_{n+1})^2}\left\{(1-f_{n+1})\left[q_1 q_2 p_{n+1} \sinh\left(\frac{q_2 3 p_{n+1}}{2\sigma_0}\right)\right] + \frac{2\sigma_0}{3}\left[2 f_{n+1} - 2\cosh\left(\frac{q_2 3 p_{n+1}}{2\sigma_0}\right)\right] + \left[q_1 q_2 f_{n+1} p_{n+1} \sinh\left(\frac{q_2 3 p_{n+1}}{2\sigma_0}\right) + \frac{2\sigma_0}{3}\left(1 + q_3 f_{n+1}^2 - 2 q_1 f_{n+1} \cosh\left(\frac{q_2 3 p_{n+1}}{2\sigma_0}\right)\right)\right]\right\} \tag{d.30}$$

$$\frac{\partial r_R}{\partial R_{n+1}} = 1 - \frac{\Delta\gamma}{(1-f_{n+1})}\left\{-q_1 q_2 q_2 \frac{3 {p_{n+1}}^2 H f_{n+1}}{2 {\sigma_0}^2} \cosh\left(\frac{q_2 3 p_{n+1}}{2\sigma_0}\right) + \frac{2H}{3}\left[1 + q_3 f_{n+1}^2 - 2 q_1 f_{n+1} \cosh\left(\frac{q_2 3 p_{n+1}}{2\sigma_0}\right)\right] - q_1 q_2 \frac{2 p_{n+1} H f_{n+1}}{\sigma_0} \sinh\left(\frac{q_2 3 p_{n+1}}{2\sigma_0}\right)\right\} \tag{d.31}$$

$$\frac{\partial \Delta D_s}{\partial \Delta \gamma} = \begin{cases} q_4 g_0 {f_{n+1}}^{q_5} \left(\bar{\varepsilon}^p_{n+1} + \Delta \bar{\varepsilon}^p\right) \dfrac{\partial \Delta \bar{\varepsilon}^p_{n+1}}{\partial \Delta \gamma}, & Xue \\ k f_{n+1} g_0 \dfrac{\partial \Delta \bar{\varepsilon}^p_{n+1}}{\partial \Delta \gamma}, & Nahshon \end{cases} \tag{d.32}$$

$$\frac{\partial \Delta D_s}{\partial p_{n+1}} = \begin{cases} q_4 g_0 {f_{n+1}}^{q_5} \left(\bar{\varepsilon}^p_{n+1} + \Delta \bar{\varepsilon}^p\right) \dfrac{\partial \Delta \bar{\varepsilon}^p_{n+1}}{\partial p_{n+1}}, & Xue \\ k f_{n+1} g_0 \dfrac{\partial \Delta \bar{\varepsilon}^p_{n+1}}{\partial p_{n+1}}, & Nahshon \end{cases} \tag{d.33}$$

$$\frac{\partial \Delta D_s}{\partial f_{n+1}} = \begin{cases} q_4 q_5 g_0 {f_{n+1}}^{(q_5-1)} \bar{\varepsilon}^p_{n+1} \Delta \bar{\varepsilon}^p + q_4 g_0 {f_{n+1}}^{q_5} \left(\bar{\varepsilon}^p_{n+1} + \Delta \bar{\varepsilon}^p\right) \dfrac{\partial \Delta \bar{\varepsilon}^p_{n+1}}{\partial f_{n+1}}, & Xue \\ k g_0 \Delta \bar{\varepsilon}^p + k f_{n+1} g_0 \dfrac{\partial \Delta \bar{\varepsilon}^p_{n+1}}{\partial f_{n+1}}, & Nahshon \end{cases} \tag{d.34}$$

$$\frac{\partial \Delta D_s}{\partial R_{n+1}} = \begin{cases} q_4 g_0 {f_{n+1}}^{q_5} \left(\bar{\varepsilon}^p_{n+1} + \Delta \bar{\varepsilon}^p\right) \dfrac{\partial \Delta \bar{\varepsilon}^p_{n+1}}{\partial R_{n+1}}, & Xue \\ \dfrac{\partial \Delta \bar{\varepsilon}^p_{n+1}}{\partial R_{n+1}}, & Nahshon \end{cases} \tag{d.35}$$

$$\frac{\partial \Delta \bar{\varepsilon}^p_{n+1}}{\partial \Delta \gamma} = \sqrt{\zeta} - \frac{\Delta \gamma}{\sqrt{\zeta}} \frac{4G}{3} \frac{\boldsymbol{S}^{trial} : \boldsymbol{S}^{trial}}{(1 + 2G\Delta\gamma)^3} \tag{d.35}$$

$$\frac{\partial \Delta \bar{\varepsilon}^p_{n+1}}{\partial p_{n+1}} = \frac{\Delta \gamma}{\sqrt{\zeta}} \frac{1}{3} q_1 q_1 q_2 q_2 q_2 f^2_{n+1} \sinh\left(\frac{q_2 3 p_{n+1}}{2\sigma_0}\right) \cosh\left(\frac{q_2 3 p_{n+1}}{2\sigma_0}\right) \tag{d.36}$$

$$\frac{\partial \Delta \bar{\varepsilon}^p_{n+1}}{\partial f_{n+1}} = \frac{\Delta \gamma}{\sqrt{\zeta}} \frac{2}{9} q_1 q_1 q_2 q_2 f_{n+1} {\sigma_0}^2 \sinh\left(\frac{q_2 3 p_{n+1}}{2\sigma_0}\right) \sinh\left(\frac{q_2 3 p_{n+1}}{2\sigma_0}\right) \tag{d.37}$$

$$\frac{\partial \Delta\bar{\varepsilon}^{p}_{n+1}}{\partial R_{n+1}} = \frac{\Delta\gamma}{\sqrt{\zeta}}\frac{2}{9}q_1 q_1 q_2 q_2 f^{2}_{n+1} H\sigma_0 \sinh\left(\frac{q_2 3p_{n+1}}{2\sigma_0}\right)\left[\sinh\left(\frac{q_2 3p_{n+1}}{2\sigma_0}\right) - \left(\frac{q_2 3p_{n+1}}{2\sigma_0}\right)\cosh\left(\frac{q_2 3p_{n+1}}{2\sigma_0}\right)\right] \tag{d.38}$$

where,

$$\sqrt{\zeta} = \sqrt{\frac{2}{3}\left\{\frac{\boldsymbol{S}^{trial}:\boldsymbol{S}^{trial}}{(1+2G\Delta\gamma)^2} + \frac{1}{3}\left[q_1 q_2 f\sigma_0 \sinh\left(\frac{q_2 3p}{2\sigma_0}\right)\right]^2\right\}} \tag{d.39}$$

Consistent tangent operator

The consistent tangent operator for GTN´s model can be obtained through the differentiating the stress update equation (c.21) which gives:

$$d\boldsymbol{\sigma}_{n+1} = \frac{2G}{(1+2G\Delta\gamma)}d\boldsymbol{\varepsilon}^{e\ trial}_{d\ n+1} - \left[\frac{2G}{(1+2G\Delta\gamma)}\right]^2 \boldsymbol{\varepsilon}^{e\ trial}_{d\ n+1}d\Delta\gamma + dp_{n+1}\boldsymbol{I} \tag{d.40}$$

The system of equations of the plastic corrector phase is differentiated at the converged state resulting in the expression:

$$\begin{bmatrix} \frac{\partial r_{\Delta\gamma}}{\partial\Delta\gamma} & \frac{\partial r_{\Delta\gamma}}{\partial p_{n+1}} & \frac{\partial r_{\Delta\gamma}}{\partial f_{n+1}} & \frac{\partial r_{\Delta\gamma}}{\partial R_{n+1}} \\ \frac{\partial r_p}{\partial\Delta\gamma} & \frac{\partial r_p}{\partial p_{n+1}} & \frac{\partial r_p}{\partial f_{n+1}} & \frac{\partial r_p}{\partial R_{n+1}} \\ \frac{\partial r_f}{\partial\Delta\gamma} & \frac{\partial r_f}{\partial p_{n+1}} & \frac{\partial r_f}{\partial f_{n+1}} & \frac{\partial r_f}{\partial R_{n+1}} \\ \frac{\partial r_R}{\partial\Delta\gamma} & \frac{\partial r_R}{\partial p_{n+1}} & \frac{\partial r_R}{\partial f_{n+1}} & \frac{\partial r_R}{\partial R_{n+1}} \end{bmatrix} \cdot \begin{bmatrix} d\Delta\gamma \\ dp_{n+1} \\ df_{n+1} \\ dR_{n+1} \end{bmatrix} = \begin{bmatrix} -\frac{\partial r_{\Delta\gamma}}{\partial \boldsymbol{\varepsilon}^{e\ trial}_{d\ n+1}} : d\boldsymbol{\varepsilon}^{e\ trial}_{d\ n+1} \\ -\frac{\partial r_p}{\partial \varepsilon^{e\ trial}_{v\ n+1}} d\varepsilon^{e\ trial}_{v\ n+1} \\ -\frac{\partial r_f}{\partial \boldsymbol{\varepsilon}^{e\ trial}_{d\ n+1}} : d\boldsymbol{\varepsilon}^{e\ trial}_{d\ n+1} \\ 0 \end{bmatrix} \tag{d.41}$$

The inversion of the above equations can be written as:

$$\begin{bmatrix} d\Delta\gamma \\ dp_{n+1} \\ df_{n+1} \\ dR_{n+1} \end{bmatrix} = \begin{bmatrix} \frac{\partial r_{\Delta\gamma}}{\partial \Delta\gamma} & \frac{\partial r_{\Delta\gamma}}{\partial p_{n+1}} & \frac{\partial r_{\Delta\gamma}}{\partial f_{n+1}} & \frac{\partial r_{\Delta\gamma}}{\partial R_{n+1}} \\ \frac{\partial r_p}{\partial \Delta\gamma} & \frac{\partial r_p}{\partial p_{n+1}} & \frac{\partial r_p}{\partial f_{n+1}} & \frac{\partial r_p}{\partial R_{n+1}} \\ \frac{\partial r_f}{\partial \Delta\gamma} & \frac{\partial r_f}{\partial p_{n+1}} & \frac{\partial r_f}{\partial f_{n+1}} & \frac{\partial r_f}{\partial R_{n+1}} \\ \frac{\partial r_R}{\partial \Delta\gamma} & \frac{\partial r_R}{\partial p_{n+1}} & \frac{\partial r_R}{\partial f_{n+1}} & \frac{\partial r_R}{\partial R_{n+1}} \end{bmatrix}^{-1} \begin{bmatrix} -\frac{\partial r_{\Delta\gamma}}{\partial \boldsymbol{\varepsilon}_{d\,n+1}^{e\,trial}} : d\boldsymbol{\varepsilon}_{d\,n+1}^{e\,trial} \\ -\frac{\partial r_p}{\partial \varepsilon_{v\,n+1}^{e\,trial}} d\varepsilon_{v\,n+1}^{e\,trial} \\ -\frac{\partial r_f}{\partial \boldsymbol{\varepsilon}_{d\,n+1}^{e\,trial}} : d\boldsymbol{\varepsilon}_{d\,n+1}^{e\,trial} \\ 0 \end{bmatrix} \tag{d.42}$$

or,

$$\begin{bmatrix} d\Delta\gamma \\ dp_{n+1} \\ df_{n+1} \\ dR_{n+1} \end{bmatrix} = \begin{bmatrix} C_{11} & C_{12} & C_{13} & C_{14} \\ C_{21} & C_{22} & C_{23} & C_{24} \\ C_{31} & C_{32} & C_{33} & C_{34} \\ C_{41} & C_{42} & C_{43} & C_{44} \end{bmatrix} \begin{bmatrix} -\frac{\partial r_{\Delta\gamma}}{\partial \underline{\boldsymbol{\varepsilon}}_{d\,n+1}^{e\,trial}} : d\underline{\boldsymbol{\varepsilon}}_{d\,n+1}^{e\,trial} \\ -\frac{\partial r_p}{\partial \varepsilon_{v\,n+1}^{e\,trial}} d\varepsilon_{v\,n+1}^{e\,trial} \\ -\frac{\partial r_f}{\partial \underline{\boldsymbol{\varepsilon}}_{d\,n+1}^{e\,trial}} : d\varepsilon_{d\,n+1}^{e\,trial} \\ 0 \end{bmatrix} \tag{d.43}$$

Thus, through the above system, we can remove the expression for $d\Delta\gamma$ and dp_{n+1}.

$$d\Delta\gamma = -C_{11} \frac{\partial r_{\Delta\gamma}}{\partial \boldsymbol{\varepsilon}_{d\,n+1}^{e\,trial}} : d\boldsymbol{\varepsilon}_{d\,n+1}^{e\,trial} - C_{12} \frac{\partial r_p}{\partial \varepsilon_{v\,n+1}^{e\,trial}} d\varepsilon_{v\,n+1}^{e\,trial} - C_{13} \frac{\partial r_f}{\partial \boldsymbol{\varepsilon}_{d\,n+1}^{e\,trial}} : d\boldsymbol{\varepsilon}_{d\,n+1}^{e\,trial} \tag{d.44}$$

and,

$$dp_{n+1} = -C_{21} \frac{\partial r_{\Delta\gamma}}{\partial \boldsymbol{\varepsilon}_{d\,n+1}^{e\,trial}} : d\boldsymbol{\varepsilon}_{d\,n+1}^{e\,trial} - C_{22} \frac{\partial r_p}{\partial \varepsilon_{v\,n+1}^{e\,trial}} d\varepsilon_{v\,n+1}^{e\,trial} - C_{23} \frac{\partial r_f}{\partial \boldsymbol{\varepsilon}_{d\,n+1}^{e\,trial}} : d\boldsymbol{\varepsilon}_{d\,n+1}^{e\,trial} \tag{d.45}$$

Substituting the above equations into the expressions (d.40) and after some algebraic manipulation, the consistent tangent operator for GTN´s model can be obtained as:

$$\mathbf{D}^{ep} = \frac{d\boldsymbol{\sigma}_{n+1}}{d\boldsymbol{\varepsilon}_{n+1}^{e\,trial}}$$
$$= \frac{2G}{(1+2G\Delta\gamma)}\left(\mathbb{I} - \frac{1}{3}\boldsymbol{I}\otimes\boldsymbol{I}\right)$$
$$+ \left[\frac{2G}{(1+2G\Delta\gamma)}\right]^2 \boldsymbol{\varepsilon}_{d\,n+1}^{e\,trial} \otimes \left[\left(C_{11}\frac{\partial r_{\Delta\gamma}}{\partial \boldsymbol{\varepsilon}_{d\,n+1}^{e\,trial}} + C_{13}\frac{\partial r_f}{\partial \boldsymbol{\varepsilon}_{d\,n+1}^{e\,trial}}\right)\right.$$
$$\left. + C_{12}\frac{\partial r_p}{\partial \varepsilon_{v\,n+1}^{e\,trial}}\boldsymbol{I}\right] \qquad \text{(d.46)}$$
$$- \boldsymbol{I}\otimes\left[\left(C_{21}\frac{\partial r_{\Delta\gamma}}{\partial \boldsymbol{\varepsilon}_{d\,n+1}^{e\,trial}} + C_{23}\frac{\partial r_f}{\partial \boldsymbol{\varepsilon}_{d\,n+1}^{e\,trial}}\right) + C_{22}\frac{\partial r_p}{\partial \varepsilon_{v\,n+1}^{e\,trial}}\boldsymbol{I}\right]$$

where,

$$\frac{\partial r_{\Delta\gamma}}{\partial \boldsymbol{\varepsilon}_{d\,n+1}^{e\,trial}} = \left(\frac{2G}{1+2G\Delta\gamma}\right)^2 \boldsymbol{\varepsilon}_{d\,n+1}^{e\,trial} : d\boldsymbol{\varepsilon}_{d\,n+1}^{e\,trial} \qquad \text{(d.47)}$$

$$\frac{\partial r_p}{\partial \varepsilon_{v\,n+1}^{e\,trial}} = -K \qquad \text{(d.48)}$$

$$\frac{\partial r_f}{\partial \boldsymbol{\varepsilon}_{d\,n+1}^{e\,trial}} = \frac{2\Delta\gamma}{3\sqrt{\zeta}}\left(\frac{2G}{1+2\Delta\gamma}\right)^2 \boldsymbol{\varepsilon}_{d\,n+1}^{e\,trial} : d\boldsymbol{\varepsilon}_{d\,n+1}^{e\,trial} \qquad \text{(d.49)}$$

$$d\boldsymbol{\varepsilon}_{d\,n+1}^{e\,trial} = \left(\mathbb{I} - \frac{1}{3}\boldsymbol{I}\otimes\boldsymbol{I}\right) : d\boldsymbol{\varepsilon}_{n+1}^{e\,trial} \qquad \text{(d.50)}$$

APPENDIX E

Linearization procedure for extended GTN's model

The yield function for the extended GTN model is defined as:

$$\Phi(\boldsymbol{\sigma}, k, f, D) = \frac{J_2(\boldsymbol{S})}{(1-D)} - \frac{1}{3}\left\{1 + q_3 f^2 - 2q_1 f \cosh\left(\frac{q_2 3p}{2\sigma_y}\right)\right\}{\sigma_y}^2 \ , \qquad \text{(e.1)}$$

where the evolution equation for the volume void fraction is:

$$\dot{f} = \dot{f}^n + \dot{f}^g \ . \qquad \text{(e.2)}$$

The terms $\dot{f}^n$ and $\dot{f}^g$ represent respectively the evolution of the nucleation and growth mechanisms and mathematically represented by:

$$\begin{aligned} \dot{f}^n &= \|\bar{\theta}\| \frac{f_N}{S_N\sqrt{2\pi}} \exp\left[-\frac{1}{2}\left(\frac{\bar{\varepsilon}^p - \varepsilon_N}{S_N}\right)^2\right] \dot{\bar{\varepsilon}}^p \\ \dot{f}^g &= (1-f)\dot{\varepsilon}_v^p \ . \end{aligned} \qquad \text{(e.3)}$$

Then, the evolution of the shear damage is represented by:

$$\dot{D} = \dot{D}^n + \dot{D}^s \ , \qquad \text{(e.4)}$$

where $\dot{D}^n$ and $\dot{D}^s$ are mathematically represented by:

$$\begin{aligned} \dot{D}^n &= \left(1 - \|\bar{\theta}\|\right) \frac{D_N}{S_N\sqrt{2\pi}} \exp\left[-\frac{1}{2}\left(\frac{\bar{\varepsilon}^p - \varepsilon_N}{S_N}\right)^2\right] \dot{\bar{\varepsilon}}^p \\ \dot{D}^s &= q_4 D^{q_5}\left[q_7\left(1 - \|\bar{\theta}\|\right)^{\frac{q_6}{\|\eta\| - q_6}}\right] \bar{\varepsilon}^p \dot{\bar{\varepsilon}}^p = q_4 D^{q_5} g_0 \bar{\varepsilon}^p \dot{\bar{\varepsilon}}^p \ , \end{aligned} \qquad \text{(e.5)}$$

where $g_0 = q_7\left(1 - \|\bar{\theta}\|\right)^{\frac{q_6}{\|\eta\| - q_6}}$.

The flow vector can be obtained as:

$$\boldsymbol{N} \equiv \frac{\partial \Phi}{\partial \boldsymbol{\sigma}} = \frac{\boldsymbol{S}}{1-D} + \frac{1}{3}\sigma_y q_1 q_2 f \sinh\left(\frac{3q_2 p}{2\sigma_y}\right)\boldsymbol{I} \ . \qquad \text{(e.6)}$$

The plastic flow rule can be computed as:

$$\dot{\varepsilon}^p = \dot{\gamma}\boldsymbol{N} = \dot{\gamma}\left[\frac{\boldsymbol{S}}{1-D} + \frac{1}{3}\sigma_y q_1 q_2 f \sinh\left(\frac{3q_2 p}{2\sigma_y}\right)\boldsymbol{I}\right], \tag{e.7}$$

$$\dot{\bar{\varepsilon}}^p = \sqrt{\frac{2}{3}\dot{\varepsilon}^p : \dot{\varepsilon}^p}\,\dot{\bar{\varepsilon}}^p = \dot{\gamma}\sqrt{\frac{2}{3}\left\{\frac{\boldsymbol{S}:\boldsymbol{S}}{(1-D)^2} + \frac{1}{3}\left[\sigma_y q_1 q_2 f \sinh\left(\frac{3q_2 p}{2\sigma_y}\right)\right]^2\right\}}. \tag{e.8}$$

Evolution equation for $\dot{R}$ is determined by:

$$\dot{R} = -\dot{\gamma}\frac{\partial \Phi}{\partial k}, \tag{e.9}$$

where $\sigma_y = \sigma_0 + k = \sigma_0 + RH$, and:

$$\begin{gathered}\dot{R} = \dot{\gamma}\left\{q_1 q_2 f p \sinh\left(\frac{3q_2 p}{2\sigma_y}\right) + \frac{2}{3}\sigma_y\left[1 + q_3 f^2 - 2q_1 f \cosh\left(\frac{3q_2 p}{2\sigma_y}\right)\right]\right\}, \\ \dot{R} = \frac{\dot{R}}{1-f-D}.\end{gathered} \tag{e.10}$$

Updating the strain tensor

$$\begin{gathered}\boldsymbol{\varepsilon}^e_{n+1} = {\boldsymbol{\varepsilon}^e_{n+1}}^{trial} - \Delta\varepsilon^p \\ \boldsymbol{\varepsilon}^e_{n+1} = {\boldsymbol{\varepsilon}^e_{n+1}}^{trial} - \Delta\gamma\left[\frac{\boldsymbol{S}_{n+1}}{1-d_{n+1}} + \frac{1}{3}\sigma_y q_1 q_2 f_{n+1}\sinh\left(\frac{3q_2 p_{n+1}}{2\sigma_y}\right)\boldsymbol{I}\right] \\ \Delta\varepsilon^p_v = \Delta\gamma\sigma_y q_1 q_2 f_{n+1}\sinh\left(\frac{3q_2 p_{n+1}}{2\sigma_y}\right).\end{gathered} \tag{e.11}$$

Updating the stress tensor

$$\begin{gathered}\boldsymbol{\sigma}_{n+1} = \mathbb{D}^e : \boldsymbol{\varepsilon}^e_{n+1} \\ \boldsymbol{\sigma}_{n+1} = \mathbb{D}^e : {\boldsymbol{\varepsilon}^e_{n+1}}^{trial} - 2G\Delta\gamma\frac{\boldsymbol{S}_{n+1}}{1-D_{n+1}} - \frac{1}{3}\Delta\gamma K\sigma_y q_1 q_2 f_{n+1}\sinh\left(\frac{3q_2 p_{n+1}}{2\sigma_y}\right)\boldsymbol{I}.\end{gathered} \tag{e.12}$$

The deviatoric and hydrostatic contributions are determined as:

$$\boldsymbol{S}_{n+1} = \mathbb{D}^e : \boldsymbol{\varepsilon}^e_{n+1}{}^{trial} - 2G\Delta\gamma \frac{\boldsymbol{S}_{n+1}}{1 - D_{n+1}}$$

$$\boldsymbol{\sigma}^{trial}_{n+1} = \boldsymbol{S}^{trial}_{n+1} + p^{trial}_{n+1}\boldsymbol{I} = 2G\,\boldsymbol{\varepsilon}^e_{d\,n+1}{}^{trial} + K\boldsymbol{\varepsilon}^e_{v\,n+1}{}^{trial}$$

$$\boldsymbol{S}_{n+1} = \frac{\boldsymbol{S}^{trial}_{n+1}}{\left[1 + \left(\frac{2G\Delta\gamma}{1 - D_{n+1}}\right)\right]} \qquad \text{(e.13)}$$

$$p_{n+1}\,\boldsymbol{I} = \left[p^{trial}_{n+1} - \frac{1}{3}\Delta\gamma K\sigma_y q_1 q_2 f_{n+1} \sinh\left(\frac{3q_2 p_{n+1}}{2\sigma_y}\right)\right]\boldsymbol{I}\ .$$

Updating other elasto-plastic variables

$$J_{2\,n+1} = \frac{J_{2\,n+1}^{trial}}{\left[1 + \left(\frac{2G\Delta\gamma}{1 - D_{n+1}}\right)\right]^2}$$

$$\bar{\theta}_{n+1} = 1 - \frac{6\theta_{n+1}}{\pi}$$

$$\theta_{n+1} = 1 - \frac{2}{\pi}\arccos\xi_{n+1}$$

$$\xi_{n+1} = \frac{27}{2}\frac{\det \boldsymbol{S}_{n+1}}{(q_{n+1})^3} \qquad \text{(e.14)}$$

$$q_{n+1} = \frac{q_{n+1}{}^{trial}}{\left[1 + \left(\frac{2G\Delta\gamma}{1 - D_{n+1}}\right)\right]}$$

$$\det \boldsymbol{S}_{n+1} = \left[1 + \left(\frac{2G\Delta\gamma}{1 - D_{n+1}}\right)\right]^3 \det \boldsymbol{S}_{n+1}{}^{trial}$$

$$\xi_{n+1} = \xi_{n+1}{}^{trial} \Rightarrow \theta_{n+1} = \theta_{n+1}{}^{trial} \Rightarrow \bar{\theta}_{n+1} = \bar{\theta}^{trial}_{n+1}\ .$$

Brief summary of the extended GTN model with isotropic hardening

i) Elasto-plastic split of the strain tensor

$$\boldsymbol{\varepsilon} = \boldsymbol{\varepsilon}^e + \boldsymbol{\varepsilon}^p$$

ii) Elastic law

$$\boldsymbol{\sigma} = \mathbb{D}^e : \boldsymbol{\varepsilon}^e$$

iii) Yield function

$$\Phi(\boldsymbol{\sigma}, f, d, R) = \frac{J_{2_{n+1}}^{trial}}{\left[1 + \left(\frac{2G\Delta\gamma}{1 - D_{n+1}}\right)\right]^2 (1 - D_{n+1})} - \frac{1}{3}\left[1 + {q_3 f_{n+1}}^2 - 2q_1 f_{n+1} \cosh\left(\frac{3q_2 p_{n+1}}{2\sigma_y}\right)\right]\sigma_y^2$$

iv) Plastic flow and evolution equations for R, f and d

$$\Delta\varepsilon^p = \Delta\gamma\left[\frac{\boldsymbol{S}_{n+1}^{trial}}{\left[1 + \left(\frac{2G\Delta\gamma}{1 - D_{n+1}}\right)\right](1 - D_{n+1})} + \frac{1}{3}\sigma_y q_1 q_2 f_{n+1} \sinh\left(\frac{3q_2 p_{n+1}}{2\sigma_y}\right)\boldsymbol{I}\right]$$

$$\Delta R = \frac{\Delta\gamma}{(1 - f - D)}\left\{q_1 q_2 f_{n+1} p_{n+1} \sinh\left(\frac{3q_2 p_{n+1}}{2\sigma_y}\right) + \frac{2}{3}\sigma_y\left[1 + {q_3 f_{n+1}}^2 - 2q_1 f_{n+1} \cosh\left(\frac{3q_2 p_{n+1}}{2\sigma_y}\right)\right]\right\}$$

$$\Delta f = \Delta f^n + \Delta f^g$$

$$\Delta f^n = \left\|\bar{\theta}_{n+1}^{trial}\right\| \frac{f_N}{S_N\sqrt{2\pi}} \exp\left[-\frac{1}{2}\left(\frac{\bar{\varepsilon}^p{}_{n+1} - \varepsilon_N}{S_N}\right)^2\right]\Delta\bar{\varepsilon}^p$$

$$\Delta f^g = (1 - f_{n+1})\Delta\gamma\sigma_y q_1 q_2 f_{n+1} \sinh\left(\frac{3q_2 p_{n+1}}{2\sigma_y}\right)$$

$$\Delta D = \Delta D^n + \Delta D^s$$

$$\Delta D^n = \left(1 - \left\|\bar{\theta}_{n+1}^{trial}\right\|\right) \frac{d_N}{S_N\sqrt{2\pi}} \exp\left[-\frac{1}{2}\left(\frac{\bar{\varepsilon}^p - \varepsilon_N}{S_N}\right)^2\right]\Delta\bar{\varepsilon}^p$$

$$\Delta D^s = q_4 {D_{n+1}}^{q_5}\left[q_7\left(1 - \left\|\bar{\theta}_{n+1}\right\|\right)^{\frac{q_6}{\|\eta_{n+1}\| - q_6}}\right]\bar{\varepsilon}^p\Delta\bar{\varepsilon}^p$$

$$\Delta\bar{\varepsilon}^p = \Delta\gamma\sqrt{\frac{2}{3}\left\{\frac{\boldsymbol{S}_{n+1}^{trial} : \boldsymbol{S}_{n+1}^{trial}}{\left[1 + \left(\frac{2G\Delta\gamma}{1 - D_{n+1}}\right)\right]^2 (1 - D_{n+1})^2} + \frac{1}{3}\left[\sigma_y q_1 q_2 f_{n+1} \sinh\left(\frac{3q_2 p_{n+1}}{2\sigma_y}\right)\right]^2\right\}}$$

Residual equations for the extended model:

$$r_{\Delta\gamma} = \frac{J_{2_{n+1}}^{trial}}{\left[1+\left(\frac{2G\Delta\gamma}{1-D_{n+1}}\right)\right]^2 (1-D_{n+1})} - \frac{1}{3}\left[1 + q_3 {f_{n+1}}^2 - 2q_1 f_{n+1}\cosh\left(\frac{3q_2 p_{n+1}}{2\sigma_y}\right)\right]\sigma_y^2, \quad \text{(e.15)}$$

$$r_p = p_{n+1} - p_n + \Delta\gamma K \sigma_y q_1 q_2 f_{n+1}\sinh\left(\frac{3q_2 p_{n+1}}{2\sigma_y}\right), \quad \text{(e.16)}$$

$$r_f = f_{n+1} - f_n - \Delta f^n - \Delta f^g \ , \quad \text{(e.17)}$$

$$\begin{aligned} r_R = R_{n+1} - R_n - \frac{\Delta\gamma}{(1-f_{n+1}-D_{n+1})}\Bigg\{ & q_1 q_2 f_{n+1} p_{n+1}\sinh\left(\frac{3q_2 p_{n+1}}{2\sigma_y}\right) \\ & + \frac{2}{3}\sigma_y\left[1 + q_3 {f_{n+1}}^2 - 2q_1 f_{n+1}\cosh\left(\frac{3q_2 p_{n+1}}{2\sigma_y}\right)\right]\Bigg\}, \end{aligned} \quad \text{(e.18)}$$

$$r_d = D_{n+1} - D_n - \Delta D^n - \Delta D^s \ . \quad \text{(e.19)}$$

Residual system of nonlinear equation in the linearized form:

$$\begin{bmatrix} \frac{\partial r_{\Delta\gamma}}{\partial\Delta\gamma} & \frac{\partial r_{\Delta\gamma}}{\partial p} & \frac{\partial r_{\Delta\gamma}}{\partial f} & \frac{\partial r_{\Delta\gamma}}{\partial R} & \frac{\partial r_{\Delta\gamma}}{\partial D} \\ \frac{\partial r_p}{\partial\Delta\gamma} & \frac{\partial r_p}{\partial p} & \frac{\partial r_p}{\partial f} & \frac{\partial r_p}{\partial R} & \frac{\partial r_p}{\partial D} \\ \frac{\partial r_f}{\partial\Delta\gamma} & \frac{\partial r_f}{\partial p} & \frac{\partial r_f}{\partial f} & \frac{\partial r_f}{\partial R} & \frac{\partial r_f}{\partial D} \\ \frac{\partial r_R}{\partial\Delta\gamma} & \frac{\partial r_R}{\partial p} & \frac{\partial r_R}{\partial f} & \frac{\partial r_R}{\partial R} & \frac{\partial r_R}{\partial D} \\ \frac{\partial r_D}{\partial\Delta\gamma} & \frac{\partial r_D}{\partial p} & \frac{\partial r_D}{\partial f} & \frac{\partial r_D}{\partial R} & \frac{\partial r_D}{\partial D} \end{bmatrix}^k \begin{bmatrix} \delta\Delta\gamma \\ \delta p \\ \delta f \\ \delta R \\ \delta D \end{bmatrix}^{k+1} = -\begin{bmatrix} r_{\Delta\gamma} \\ r_p \\ r_f \\ r_R \\ r_D \end{bmatrix}^k , \quad \text{(e.20)}$$

where:

$$\frac{\partial r_{\Delta\gamma}}{\partial \Delta\gamma} = -\frac{8G^3 \boldsymbol{\varepsilon}_{d\,n+1}^{e\,trial} : \boldsymbol{\varepsilon}_{d\,n+1}^{e\,trial}}{(1-D_{n+1})^2\left[1+\left(\frac{2G\Delta\gamma}{1-D_{n+1}}\right)\right]^3}$$

$$\frac{\partial r_{\Delta\gamma}}{\partial p} = q_1 q_2 f_{n+1}\sigma_y \sinh\left(\frac{3q_2 p_{n+1}}{2\sigma_y}\right)$$

$$\frac{\partial r_{\Delta\gamma}}{\partial f} = -\frac{2}{3}{\sigma_y}^2\left[q_3 f_{n+1} - q_1 \cosh\left(\frac{3q_2 p_{n+1}}{2\sigma_y}\right)\right]$$

$$\frac{\partial r_{\Delta\gamma}}{\partial R} = -\frac{2}{3}\sigma_y H\left[1+{q_3 f_{n+1}}^2 - 2q_1 f_{n+1}\cosh\left(\frac{3q_2 p_{n+1}}{2\sigma_y}\right)\right] \qquad \text{(e.21)}$$

$$-q_1 q_2 f_{n+1} p_{n+1} H \sinh\left(\frac{3q_2 p_{n+1}}{2\sigma_y}\right)$$

$$\frac{\partial r_{\Delta\gamma}}{\partial D} = J_{2_{n+1}}^{trial}\left\{\frac{1}{(1-D_{n+1})^2\left[1+\left(\frac{2G\Delta\gamma}{1-D_{n+1}}\right)\right]^2} - \frac{4G\Delta\gamma}{(1-D_{n+1})^3\left[1+\left(\frac{2G\Delta\gamma}{1-D_{n+1}}\right)\right]^3}\right\},$$

and,

$$\frac{\partial r_p}{\partial \Delta\gamma} = K\sigma_y q_1 q_2 f_{n+1}\sinh\left(\frac{3q_2 p_{n+1}}{2\sigma_y}\right)$$

$$\frac{\partial r_p}{\partial p} = 1 + \frac{3}{2}\Delta\gamma K q_1 (q_2)^2 f_{n+1}\cosh\left(\frac{3q_2 p_{n+1}}{2\sigma_y}\right)$$

$$\frac{\partial r_p}{\partial f} = \Delta\gamma K\sigma_y q_1 q_2 \sinh\left(\frac{3q_2 p_{n+1}}{2\sigma_y}\right) \qquad \text{(e.22)}$$

$$\frac{\partial r_p}{\partial R} = \Delta\gamma K q_1 q_2 f_{n+1} H\left[\sinh\left(\frac{3q_2 p_{n+1}}{2\sigma_y}\right) - \frac{3q_2 p_{n+1}}{2\sigma_y}\cosh\left(\frac{3q_2 p_{n+1}}{2\sigma_y}\right)\right]$$

$$\frac{\partial r_p}{\partial D} = 0\ ,$$

and,

$$\frac{\partial r_f}{\partial \Delta\gamma} = -\frac{\partial \Delta f^n}{\partial \Delta\gamma} - \frac{\partial \Delta f^g}{\partial \Delta\gamma}$$

$$\frac{\partial r_f}{\partial p} = -\frac{\partial \Delta f^n}{\partial p} - \frac{\partial \Delta f^g}{\partial p}$$

$$\frac{\partial r_f}{\partial f} = 1 - \frac{\partial \Delta f^n}{\partial f} - \frac{\partial \Delta f^g}{\partial f} \qquad \text{(e.23)}$$

$$\frac{\partial r_f}{\partial R} = -\frac{\partial \Delta f^n}{\partial R} - \frac{\partial \Delta f^g}{\partial R}$$

$$\frac{\partial r_f}{\partial D} = -\frac{\partial \Delta f^n}{\partial D} - \frac{\partial \Delta f^g}{\partial D} \ ,$$

where:

$$\frac{\partial \Delta f^n}{\partial(\blacksquare)} = \left\|\bar{\theta}_{n+1}^{trial}\right\| \frac{f_N}{S_N\sqrt{2\pi}} \exp\left[-\frac{1}{2}\left(\frac{\bar{\varepsilon}^p{}_{n+1} - \varepsilon_N}{S_N}\right)^2\right]\left[1 - \frac{\Delta\bar{\varepsilon}^p}{S_N}\left(\frac{\bar{\varepsilon}^p{}_{n+1} - \varepsilon_N}{S_N}\right)\right]\frac{\partial \Delta\bar{\varepsilon}^p}{\partial(\blacksquare)}, \qquad \text{(e.24)}$$

and,

$$\frac{\partial \Delta f^g}{\partial \Delta\gamma} = (1 - f_{n+1})\sigma_y q_1 q_2 f_{n+1} \sinh\left(\frac{3q_2 p_{n+1}}{2\sigma_y}\right)$$

$$\frac{\partial \Delta f^g}{\partial p} = (1 - f_{n+1})\frac{3\Delta\gamma}{2} q_1 (q_2)^2 f_{n+1} \cosh\left(\frac{3q_2 p_{n+1}}{2\sigma_y}\right)$$

$$\frac{\partial \Delta f^g}{\partial f} = -\Delta\gamma\sigma_y q_1 q_2 f_{n+1} \sinh\left(\frac{3q_2 p_{n+1}}{2\sigma_y}\right) + (1 - f_{n+1})\Delta\gamma\sigma_y q_1 q_2 \sinh\left(\frac{3q_2 p_{n+1}}{2\sigma_y}\right) \qquad \text{(e.25)}$$

$$\frac{\partial \Delta f^g}{\partial R} = (1 - f_{n+1})\Delta\gamma H q_1 q_2 f_{n+1}\left[\sinh\left(\frac{3q_2 p_{n+1}}{2\sigma_y}\right) - \frac{3q_2 p_{n+1}}{2\sigma_y}\cosh\left(\frac{3q_2 p_{n+1}}{2\sigma_y}\right)\right]$$

$$\frac{\partial \Delta f^g}{\partial D} = 0 \ ,$$

and,

$$\frac{\partial r_R}{\partial \Delta\gamma} = -\frac{1}{(1-f_{n+1}-D_{n+1})}\left\{q_1 q_2 f_{n+1} p_{n+1} \sinh\left(\frac{3q_2 p_{n+1}}{2\sigma_y}\right) + \frac{2}{3}\left[1+q_3 {f_{n+1}}^2 - 2q_1 f_{n+1}\cosh\left(\frac{3q_2 p_{n+1}}{2\sigma_y}\right)\right]\sigma_y\right\}$$

$$\frac{\partial r_R}{\partial p} = -\frac{\Delta\gamma}{(1-f_{n+1}-D_{n+1})}\left\{\frac{3q_1(q_2)^2}{2\sigma_y} f_{n+1} p_{n+1}\cosh\left(\frac{3q_2 p_{n+1}}{2\sigma_y}\right) - q_1 q_2 f_{n+1}\sinh\left(\frac{3q_2 p_{n+1}}{2\sigma_y}\right)\right\}$$

$$\begin{aligned}\frac{\partial r_R}{\partial f} = &-\frac{\Delta\gamma}{(1-f_{n+1}-D_{n+1})^2}\left\{q_1 q_2 f_{n+1} p_{n+1}\sinh\left(\frac{3q_2 p_{n+1}}{2\sigma_y}\right) + \frac{2}{3}\sigma_y\left[1+q_3 {f_{n+1}}^2 - 2q_1 f_{n+1}\cosh\left(\frac{3q_2 p_{n+1}}{2\sigma_y}\right)\right]\right\} \\ &-\frac{\Delta\gamma}{(1-f_{n+1}-D_{n+1})}\left\{q_1 q_2 p_{n+1}\sinh\left(\frac{3q_2 p_{n+1}}{2\sigma_y}\right) + \frac{2}{3}\sigma_y\left[2q_3 f_{n+1} - 2q_1\cosh\left(\frac{3q_2 p_{n+1}}{2\sigma_y}\right)\right]\right\}\end{aligned} \qquad \text{(e.26)}$$

$$\frac{\partial r_R}{\partial R} = 1 - \frac{\Delta\gamma}{(1-f_{n+1}-D_{n+1})}\left\{-\frac{3q_1(q_2)^2}{2(\sigma_y)^2} f_{n+1}(p_{n+1})^2 H\cosh\left(\frac{3q_2 p_{n+1}}{2\sigma_y}\right) + \frac{2H}{3}\left[1+q_3 {f_{n+1}}^2 - 2q_1 f_{n+1}\cosh\left(\frac{3q_2 p_{n+1}}{2\sigma_y}\right)\right] + 2q_1 q_2 f_{n+1} p_{n+1}\frac{H}{\sigma_y}\sinh\left(\frac{3q_2 p_{n+1}}{2\sigma_y}\right)\right\}$$

$$\frac{\partial r_R}{\partial d} = -\frac{\Delta\gamma}{(1-f_{n+1}-D_{n+1})^2}\left\{q_1 q_2 f_{n+1} p_{n+1}\sinh\left(\frac{3q_2 p_{n+1}}{2\sigma_y}\right) + \frac{2}{3}\left[1+q_3 {f_{n+1}}^2 - 2q_1 f_{n+1}\cosh\left(\frac{3q_2 p_{n+1}}{2\sigma_y}\right)\right]\sigma_y\right\},$$

and,

$$\frac{\partial r_D}{\partial \Delta\gamma} = -\frac{\partial \Delta D^n}{\partial \Delta\gamma} - \frac{\partial \Delta D^s}{\partial \Delta\gamma}$$

$$\frac{\partial r_D}{\partial p} = -\frac{\partial \Delta D^n}{\partial p} - \frac{\partial \Delta D^s}{\partial p}$$

$$\frac{\partial r_D}{\partial f} = -\frac{\partial \Delta D^n}{\partial f} - \frac{\partial \Delta D^s}{\partial f}$$

$$\frac{\partial r_D}{\partial R} = -\frac{\partial \Delta D^n}{\partial R} - \frac{\partial \Delta D^s}{\partial R} \qquad \text{(e.27)}$$

$$\frac{\partial r_D}{\partial D} = 1 - \frac{\partial \Delta D^n}{\partial D} - \frac{\partial \Delta D^s}{\partial D},$$

where:

$$\frac{\partial \Delta D^n}{\partial(\blacksquare)} = \left\| 1 - \bar{\theta}_{n+1}^{trial} \right\| \frac{D_N}{S_N\sqrt{2\pi}} \exp\left[-\frac{1}{2}\left(\frac{\bar{\varepsilon}^p{}_{n+1} - \varepsilon_N}{S_N} \right)^2 \right] \left[1 - \frac{\Delta\bar{\varepsilon}^p}{S_N}\left(\frac{\bar{\varepsilon}^p{}_{n+1} - \varepsilon_N}{S_N} \right) \right] \frac{\partial \Delta\bar{\varepsilon}^p}{\partial(\blacksquare)} \qquad \text{(e.28)}$$

and,

$$\frac{\partial \Delta D^g}{\partial \Delta\gamma} = q_4 D_{n+1}{}^{q_5} \frac{\partial g_0}{\partial \Delta\gamma} \bar{\varepsilon}^p \Delta\bar{\varepsilon}^p + q_4 D_{n+1}{}^{q_5} g_0(\bar{\varepsilon}^p + \Delta\bar{\varepsilon}^p) \frac{\partial \Delta\bar{\varepsilon}^p}{\partial \Delta\gamma}$$

$$\frac{\partial \Delta D^g}{\partial p} = q_4 D_{n+1}{}^{q_5} \frac{\partial g_0}{\partial p} \bar{\varepsilon}^p \Delta\bar{\varepsilon}^p + q_4 D_{n+1}{}^{q_5} g_0(\bar{\varepsilon}^p + \Delta\bar{\varepsilon}^p) \frac{\partial \Delta\bar{\varepsilon}^p}{\partial p}$$

$$\frac{\partial \Delta D^g}{\partial f} = q_4 D_{n+1}{}^{q_5} g_0(\bar{\varepsilon}^p + \Delta\bar{\varepsilon}^p) \frac{\partial \Delta\bar{\varepsilon}^p}{\partial f}$$

$$\frac{\partial \Delta D^g}{\partial R} = q_4 D_{n+1}{}^{q_5} g_0(\bar{\varepsilon}^p + \Delta\bar{\varepsilon}^p) \frac{\partial \Delta\bar{\varepsilon}^p}{\partial R} \qquad \text{(e.29)}$$

$$\frac{\partial \Delta D^g}{\partial D} = q_4 q_5 D_{n+1}{}^{(q_5-1)} g_0 \bar{\varepsilon}^p \Delta\bar{\varepsilon}^p + q_4 D_{n+1}{}^{q_5} \frac{\partial g_0}{\partial d} \bar{\varepsilon}^p \Delta\bar{\varepsilon}^p + q_4 D_{n+1}{}^{q_5} g_0(\bar{\varepsilon}^p + \Delta\bar{\varepsilon}^p) \frac{\partial \Delta\bar{\varepsilon}^p}{\partial D}$$

and,

$$\frac{\partial \Delta\bar{\varepsilon}^p}{\partial \Delta\gamma} = \sqrt{\alpha} - \Delta\gamma \frac{4G}{3\sqrt{\alpha}} \frac{\boldsymbol{S}_{n+1}^{trial} : \boldsymbol{S}_{n+1}^{trial}}{\left[1 + \left(\frac{2G\Delta\gamma}{1 - D_{n+1}}\right)\right]^3 (1 - D_{n+1})^3}$$

$$\frac{\partial \Delta\bar{\varepsilon}^p}{\partial p} = \Delta\gamma \frac{1}{3\sqrt{\alpha}} \left[(q_1)^2 (q_2)^3 (f_{n+1})^2 \sigma_y \sinh\left(\frac{3q_2 p_{n+1}}{2\sigma_y}\right) \cosh\left(\frac{3q_2 p_{n+1}}{2\sigma_y}\right) \right]$$

$$\frac{\partial \Delta\bar{\varepsilon}^p}{\partial f} = \Delta\gamma \frac{2}{9\sqrt{\alpha}} \left\{ (q_1)^2 (q_2)^3 f_{n+1} (\sigma_y)^2 \left[\sinh\left(\frac{3q_2 p_{n+1}}{2\sigma_y}\right) \right]^2 \right\}$$

$$\frac{\partial \Delta\bar{\varepsilon}^p}{\partial R} = \Delta\gamma \frac{2}{9\sqrt{\alpha}} (q_1)^2 (q_2)^3 (f_{n+1})^2 \sigma_y H \sinh\left(\frac{3q_2 p_{n+1}}{2\sigma_y}\right) \left[\sinh\left(\frac{3q_2 p_{n+1}}{2\sigma_y}\right) - \frac{3q_2 p_{n+1}}{2\sigma_y} \cosh\left(\frac{3q_2 p_{n+1}}{2\sigma_y}\right) \right] \tag{e.30}$$

$$\frac{\partial \Delta\bar{\varepsilon}^p}{\partial D} = \Delta\gamma \frac{1}{3\sqrt{\alpha}} \boldsymbol{S}_{n+1}^{trial} : \boldsymbol{S}_{n+1}^{trial} \left\{ \frac{2}{(1 - D_{n+1})^3 \left[1 + \left(\frac{2G\Delta\gamma}{1 - D_{n+1}}\right)\right]^2} - \frac{4G\Delta\gamma}{(1 - D_{n+1})^4 \left[1 + \left(\frac{2G\Delta\gamma}{1 - D_{n+1}}\right)\right]^3} \right\}$$

and,

$$\frac{\partial g_0}{\partial \Delta\gamma} = g_0 \ln\left(1 - \left\|\bar{\theta}_{n+1}^{trial}\right\|\right) \left[-\frac{q_6}{(\|\eta_{n+1}\| + q_6)^2} \frac{\eta_{n+1}}{\|\eta_{n+1}\|} \frac{p_{n+1}}{q_{n+1}^{trial}} \frac{2G}{(1 - D_{n+1})} \right]$$

$$\frac{\partial g_0}{\partial p} = g_0 \ln\left(1 - \left\|\bar{\theta}_{n+1}^{trial}\right\|\right) \left\{ -\frac{q_6}{(\|\eta_{n+1}\| + q_6)^2} \frac{\eta_{n+1}}{\|\eta_{n+1}\|} \frac{1}{q_{n+1}^{trial}} \left[1 + \left(\frac{2G\Delta\gamma}{1 - D_{n+1}}\right)\right] \right\} \tag{e.31}$$

$$\frac{\partial g_0}{\partial D} = g_0 \ln\left(1 - \left\|\bar{\theta}_{n+1}^{trial}\right\|\right) \left[-\frac{q_6}{(\|\eta_{n+1}\| + q_6)^2} \frac{\eta_{n+1}}{\|\eta_{n+1}\|} \frac{p_{n+1}}{q_{n+1}^{trial}} \frac{2G\Delta\gamma}{(1 - D_{n+1})^2} \right]$$

The Consistent tangent operator can be determined by the derivative of the above equation in relation to the elastic trial strain:

$$\boldsymbol{\sigma}_{n+1} = \frac{\boldsymbol{S}_{n+1}^{trial}}{\left[1 + \left(\frac{2G\Delta\gamma}{1 - D_{n+1}}\right)\right]} + p_{n+1}\boldsymbol{I} \ . \tag{e.32}$$

Thus,

$$\begin{aligned} \mathrm{d}\boldsymbol{\sigma}_{n+1} = {} & \frac{2G}{\left[1 + \left(\frac{2G\Delta\gamma}{1 - D_{n+1}}\right)\right]}\mathrm{d}\boldsymbol{\varepsilon}_{d\,n+1}^{e\,trial} - \left\{\frac{2G}{\left[1 + \left(\frac{2G\Delta\gamma}{1 - D_{n+1}}\right)\right]}\right\}^2 \boldsymbol{\varepsilon}_{d\,n+1}^{e\,trial}\frac{1}{1 - D_{n+1}}\mathrm{d}\Delta\gamma \\ & - \left\{\frac{2G}{\left[1 + \left(\frac{2G\Delta\gamma}{1 - D_{n+1}}\right)\right]}\right\}^2 \boldsymbol{\varepsilon}_{d\,n+1}^{e\,trial}\frac{\Delta\gamma}{(1 - D_{n+1})^2}\mathrm{d}D + \mathrm{d}p_{n+1}\boldsymbol{I} \ . \end{aligned} \tag{e.33}$$

The deviatoric contribution is obtained as:

$$\begin{aligned} \mathrm{d}\boldsymbol{S}_{n+1} = {} & \frac{2G}{\left[1 + \left(\frac{2G\Delta\gamma}{1 - D_{n+1}}\right)\right]}\mathrm{d}\boldsymbol{\varepsilon}_{d\,n+1}^{e\,trial} - \left\{\frac{2G}{\left[1 + \left(\frac{2G\Delta\gamma}{1 - D_{n+1}}\right)\right]}\right\}^2 \boldsymbol{\varepsilon}_{d\,n+1}^{e\,trial}\frac{1}{1 - D_{n+1}}\mathrm{d}\Delta\gamma \\ & - \left\{\frac{2G}{\left[1 + \left(\frac{2G\Delta\gamma}{1 - D_{n+1}}\right)\right]}\right\}^2 \boldsymbol{\varepsilon}_{d\,n+1}^{e\,trial}\frac{\Delta\gamma}{(1 - D_{n+1})^2}\mathrm{d}D \ . \end{aligned} \tag{e.34}$$

The derivative of $\Delta\gamma$, p_{n+1} and D_{n+1} in relation to the elastic trial strain are determined by the solution of the system of equation:

$$\begin{bmatrix} \mathrm{d}\Delta\gamma \\ \mathrm{d}p_{n+1} \\ \mathrm{d}f_{n+1} \\ \mathrm{d}R_{n+1} \\ \mathrm{d}D_{n+1} \end{bmatrix} = \begin{bmatrix} \frac{\partial r_{\Delta\gamma}}{\partial\Delta\gamma} & \frac{\partial r_{\Delta\gamma}}{\partial p} & \frac{\partial r_{\Delta\gamma}}{\partial f} & \frac{\partial r_{\Delta\gamma}}{\partial R} & \frac{\partial r_{\Delta\gamma}}{\partial D} \\ \frac{\partial r_p}{\partial\Delta\gamma} & \frac{\partial r_p}{\partial p} & \frac{\partial r_p}{\partial f} & \frac{\partial r_p}{\partial R} & \frac{\partial r_p}{\partial D} \\ \frac{\partial r_f}{\partial\Delta\gamma} & \frac{\partial r_f}{\partial p} & \frac{\partial r_f}{\partial f} & \frac{\partial r_f}{\partial R} & \frac{\partial r_f}{\partial D} \\ \frac{\partial r_R}{\partial\Delta\gamma} & \frac{\partial r_R}{\partial p} & \frac{\partial r_R}{\partial f} & \frac{\partial r_R}{\partial R} & \frac{\partial r_R}{\partial D} \\ \frac{\partial r_D}{\partial\Delta\gamma} & \frac{\partial r_D}{\partial p} & \frac{\partial r_D}{\partial f} & \frac{\partial r_D}{\partial R} & \frac{\partial r_D}{\partial D} \end{bmatrix}^{-1} \begin{bmatrix} -\frac{\partial r_{\Delta\gamma}}{\partial \boldsymbol{\varepsilon}_{d\,n+1}^{e\,trial}}\mathrm{d}\boldsymbol{\varepsilon}_{d\,n+1}^{e\,trial} \\ -\frac{\partial r_p}{\partial \boldsymbol{\varepsilon}_{v\,n+1}^{e\,trial}}\mathrm{d}\boldsymbol{\varepsilon}_{v\,n+1}^{e\,trial} \\ -\frac{\partial r_f}{\partial \boldsymbol{\varepsilon}_{d\,n+1}^{e\,trial}}\mathrm{d}\boldsymbol{\varepsilon}_{d\,n+1}^{e\,trial} \\ 0 \\ -\frac{\partial r_D}{\partial \boldsymbol{\varepsilon}_{d\,n+1}^{e\,trial}}\mathrm{d}\boldsymbol{\varepsilon}_{d\,n+1}^{e\,trial} \end{bmatrix} . \tag{e.35}$$

The above system written in the inverse model can be computed as:

$$\begin{bmatrix} \mathrm{d}\Delta\gamma \\ \mathrm{d}p_{n+1} \\ \mathrm{d}f_{n+1} \\ \mathrm{d}R_{n+1} \\ \mathrm{d}D_{n+1} \end{bmatrix} = \begin{bmatrix} C_{1,1} & C_{1,2} & C_{1,3} & C_{1,4} & C_{1,5} \\ C_{2,1} & C_{2,2} & C_{2,3} & C_{2,4} & C_{2,5} \\ C_{3,1} & C_{3,2} & C_{3,3} & C_{3,4} & C_{3,5} \\ C_{4,1} & C_{4,2} & C_{4,3} & C_{4,4} & C_{4,5} \\ C_{5,1} & C_{5,2} & C_{5,3} & C_{5,4} & C_{5,5} \end{bmatrix} \begin{bmatrix} -\dfrac{\partial r_{\Delta\gamma}}{\partial \boldsymbol{\varepsilon}_{d\,n+1}^{e\,trial}} \mathrm{d}\boldsymbol{\varepsilon}_{d\,n+1}^{e\,trial} \\ -\dfrac{\partial r_{p}}{\partial \boldsymbol{\varepsilon}_{v\,n+1}^{e\,trial}} \mathrm{d}\boldsymbol{\varepsilon}_{v\,n+1}^{e\,trial} \\ -\dfrac{\partial r_{f}}{\partial \boldsymbol{\varepsilon}_{d\,n+1}^{e\,trial}} \mathrm{d}\boldsymbol{\varepsilon}_{d\,n+1}^{e\,trial} \\ 0 \\ -\dfrac{\partial r_{D}}{\partial \boldsymbol{\varepsilon}_{d\,n+1}^{e\,trial}} \mathrm{d}\boldsymbol{\varepsilon}_{d\,n+1}^{e\,trial} \end{bmatrix}. \tag{e.36}$$

So,

$$\begin{aligned} \mathrm{d}\Delta\gamma &= -C_{1,1}\frac{\partial r_{\Delta\gamma}}{\partial \boldsymbol{\varepsilon}_{d\,n+1}^{e\,trial}} - C_{1,2}\frac{\partial r_{p}}{\partial \boldsymbol{\varepsilon}_{v\,n+1}^{e\,trial}} - C_{1,3}\frac{\partial r_{f}}{\partial \boldsymbol{\varepsilon}_{d\,n+1}^{e\,trial}} - C_{1,5}\frac{\partial r_{D}}{\partial \boldsymbol{\varepsilon}_{d\,n+1}^{e\,trial}} \\ \mathrm{d}p_{n+1} &= -C_{2,1}\frac{\partial r_{\Delta\gamma}}{\partial \boldsymbol{\varepsilon}_{d\,n+1}^{e\,trial}} - C_{2,2}\frac{\partial r_{p}}{\partial \boldsymbol{\varepsilon}_{v\,n+1}^{e\,trial}} - C_{2,3}\frac{\partial r_{f}}{\partial \boldsymbol{\varepsilon}_{d\,n+1}^{e\,trial}} - C_{2,5}\frac{\partial r_{D}}{\partial \boldsymbol{\varepsilon}_{d\,n+1}^{e\,trial}} \\ \mathrm{d}D_{n+1} &= -C_{5,1}\frac{\partial r_{\Delta\gamma}}{\partial \boldsymbol{\varepsilon}_{d\,n+1}^{e\,trial}} - C_{5,2}\frac{\partial r_{p}}{\partial \boldsymbol{\varepsilon}_{v\,n+1}^{e\,trial}} - C_{5,3}\frac{\partial r_{f}}{\partial \boldsymbol{\varepsilon}_{d\,n+1}^{e\,trial}} - C_{5,5}\frac{\partial r_{D}}{\partial \boldsymbol{\varepsilon}_{d\,n+1}^{e\,trial}}, \end{aligned} \tag{e.37}$$

where:

$$\frac{\partial r_{\Delta\gamma}}{\partial \boldsymbol{\varepsilon}_{d\,n+1}^{e\,trial}} = \left\{\frac{2G}{\left[1+\left(\frac{2G\Delta\gamma}{1-D_{n+1}}\right)\right]}\right\}^2 \frac{1}{1-D_{n+1}}\boldsymbol{\varepsilon}_{d\,n+1}^{e\,trial} : \mathbb{I}^d$$

$$\frac{\partial r_p}{\partial \boldsymbol{\varepsilon}_{v\,n+1}^{e\,trial}} = -k$$

$$\begin{aligned}\frac{\partial r_f}{\partial \boldsymbol{\varepsilon}_{d\,n+1}^{e\,trial}} = &-\frac{\partial\left\|\bar{\theta}_{n+1}^{trial}\right\|}{\partial \boldsymbol{\varepsilon}_{d\,n+1}^{e\,trial}}\frac{f_N}{S_N\sqrt{2\pi}}\exp\left[-\frac{1}{2}\left(\frac{\bar{\varepsilon}^p{}_{n+1}-\varepsilon_N}{S_N}\right)^2\right]\Delta\bar{\varepsilon}^p \\ &-\left\|\bar{\theta}_{n+1}^{trial}\right\|\frac{f_N}{S_N\sqrt{2\pi}}\exp\left[-\frac{1}{2}\left(\frac{\bar{\varepsilon}^p{}_{n+1}-\varepsilon_N}{S_N}\right)^2\right]\left[1\right. \\ &\left.-\frac{\Delta\bar{\varepsilon}^p}{S_N}\left(\frac{\bar{\varepsilon}^p{}_{n+1}-\varepsilon_N}{S_N}\right)\right]\frac{\partial\Delta\bar{\varepsilon}^p}{\partial \boldsymbol{\varepsilon}_{d\,n+1}^{e\,trial}}\end{aligned} \tag{e.38}$$

$$\begin{aligned}\frac{\partial r_d}{\partial \boldsymbol{\varepsilon}_{d\,n+1}^{e\,trial}} = &\frac{\partial\left\|\bar{\theta}_{n+1}^{trial}\right\|}{\partial \boldsymbol{\varepsilon}_{d\,n+1}^{e\,trial}}\frac{d_N}{S_N\sqrt{2\pi}}\exp\left[-\frac{1}{2}\left(\frac{\bar{\varepsilon}^p{}_{n+1}-\varepsilon_N}{S_N}\right)^2\right]\Delta\bar{\varepsilon}^p \\ &-\left\|1-\bar{\theta}_{n+1}^{trial}\right\|\frac{d_N}{S_N\sqrt{2\pi}}\exp\left[-\frac{1}{2}\left(\frac{\bar{\varepsilon}^p{}_{n+1}-\varepsilon_N}{S_N}\right)^2\right]\left[1\right. \\ &\left.-\frac{\Delta\bar{\varepsilon}^p}{S_N}\left(\frac{\bar{\varepsilon}^p{}_{n+1}-\varepsilon_N}{S_N}\right)\right]\frac{\partial\Delta\bar{\varepsilon}^p}{\partial \boldsymbol{\varepsilon}_{d\,n+1}^{e\,trial}} \\ &-q_4 d_{n+1}{}^{q_5}\left[\frac{\partial g_0}{\partial \boldsymbol{\varepsilon}_{d\,n+1}^{e\,trial}}\bar{\varepsilon}^p\Delta\bar{\varepsilon}^p + g_0(\bar{\varepsilon}^p+\Delta\bar{\varepsilon}^p)\frac{\partial\Delta\bar{\varepsilon}^p}{\partial \boldsymbol{\varepsilon}_{d\,n+1}^{e\,trial}}\right]\end{aligned}$$

and,

$$\frac{\partial\Delta\bar{\varepsilon}^p}{\partial \boldsymbol{\varepsilon}_{d\,n+1}^{e\,trial}} = \frac{2\Delta\gamma}{3\sqrt{\alpha}}\left\{\frac{2G}{\left[1+\left(\frac{2G\Delta\gamma}{1-D_{n+1}}\right)\right]}\right\}^2 \boldsymbol{\varepsilon}_{d\,n+1}^{e\,trial} : \mathbb{I}^d \tag{e.39}$$

$$\frac{\partial\left\|\bar{\theta}_{n+1}^{trial}\right\|}{\partial \boldsymbol{\varepsilon}_{d\,n+1}^{e\,trial}} = \frac{\bar{\theta}_{n+1}^{trial}}{\left\|\bar{\theta}_{n+1}^{trial}\right\|}\left(\frac{2}{\pi\sqrt{1-\xi_{n+1}{}^2}}\right)\frac{\xi_{n+1}}{\partial \boldsymbol{\varepsilon}_{d\,n+1}^{e\,trial}} \tag{e.40}$$

$$\frac{\xi_{n+1}}{\partial \boldsymbol{\varepsilon}_{d\,n+1}^{e\,trial}} = \frac{27}{2}\left[\frac{\det \boldsymbol{\varepsilon}_{d\,n+1}^{e\,trial}}{\left(\sqrt{\frac{3}{2}\boldsymbol{\varepsilon}_{d\,n+1}^{e\,trial}:\boldsymbol{\varepsilon}_{d\,n+1}^{e\,trial}}\right)^3}\left(\boldsymbol{\varepsilon}_{d\,n+1}^{e\,trial}\right)^{-1} - \frac{9}{2}\frac{\det \boldsymbol{\varepsilon}_{d\,n+1}^{e\,trial}}{\left(\sqrt{\frac{3}{2}\boldsymbol{\varepsilon}_{d\,n+1}^{e\,trial}:\boldsymbol{\varepsilon}_{d\,n+1}^{e\,trial}}\right)^5}\boldsymbol{\varepsilon}_{d\,n+1}^{e\,trial}\right] : \mathbb{I}^d \tag{e.41}$$

$$\frac{\partial g_0}{\partial \boldsymbol{\varepsilon}^{e\ trial}_{d\ n+1}} = -\frac{q_6 q_7}{\|\eta_{n+1}\| + q_6}\left(1 - \|\bar{\theta}^{trial}_{n+1}\|\right)\frac{\partial \|\bar{\theta}^{trial}_{n+1}\|}{\partial \boldsymbol{\varepsilon}^{e\ trial}_{d\ n+1}}$$
$$+ g_0 \ln\left(1 - \|\bar{\theta}^{trial}_{n+1}\|\right)\left\{-\frac{q_6}{(\|\eta_{n+1}\| + q_6)^2}\frac{\eta_{n+1}}{\|\eta_{n+1}\|}\frac{3p_{n+1}}{2\left(q^{trial}_{n+1}\right)^3}\frac{(2G)^3}{\left[1 + \left(\frac{2G\Delta\gamma}{1 - D_{n+1}}\right)\right.}\right. \tag{e.42}$$

Regarding the introduction of the kinematic hardening in the extended model, the yield function can be rewritten as:

$$\Phi(\boldsymbol{\sigma}, \boldsymbol{\beta}, r, f, D) = \frac{J_2(\boldsymbol{\eta})}{1 - D} - \frac{1}{3}\left[1 + q_3 f^2 - 2q_1 f \cosh\left(\frac{3q_2 p}{2\sigma_y}\right)\right]\sigma_y^2 \tag{e.43}$$

where $J_2(\boldsymbol{\eta})$ represents the second invariant of the relative stress tensor: $\boldsymbol{\eta} = \boldsymbol{S} - \boldsymbol{\beta}$. In this case, the system of the following nonlinear equations needs to be solve:

$$\left\{\begin{array}{c} \frac{J_{2\ n+1}}{(1 - D_{n+1})} - \frac{1}{3}\left[1 + q_3 {f_{n+1}}^2 - 2q_1 f_{n+1}\cosh\left(\frac{3q_2 p_{n+1}}{2\sigma_y}\right)\right]\sigma_y^2 \\ p_{n+1} - p^{trial}_{n+1} + \Delta\gamma K \sigma_y q_1 q_2 f_{n+1}\sinh\left(\frac{3q_2 p_{n+1}}{2\sigma_y}\right) \\ f_{n+1} - f^{trial}_{n+1} - \Delta f^n - \Delta f^g \\ R_{n+1} - R^{trial}_{n+1} - \Delta R \\ D_{n+1} - D^{trial}_{n+1} - \Delta D^n - q_6 \Delta D^s \end{array}\right\} = \tag{e.44}$$

where $J_{2\ n+1}$ is computed as:

$$J_{2\ n+1} = \frac{1}{2\left[1 + \frac{2G\Delta\gamma}{(1 - D_{n+1})} + \frac{2H^K\Delta\gamma}{3(1 - D_{n+1})}\right]^2}\left\{\boldsymbol{\eta}^{trial}_{n+1} : \boldsymbol{\eta}^{trial}_{n+1}\right.$$
$$\left. + \frac{1}{3}\left[\Delta\gamma\frac{2}{3}H^K\sigma_y q_1 q_2 f_{n+1}\sinh\left(\frac{3q_2 p_{n+1}}{2\sigma_y}\right)\right]^2\right\} \tag{e.45}$$

The other terms as defined similarly to the original extended model. The relative stress tensor and the plastic flow rule are computed as:

$$\boldsymbol{\eta}_{n+1} = \frac{\boldsymbol{\eta}^{trial}_{n+1} - \Delta\gamma\frac{2}{9}H^K\sigma_y q_1 q_2 f_{n+1}\sinh\left(\frac{3q_2 p_{n+1}}{2\sigma_y}\right)\boldsymbol{I}}{\left[1 + \frac{2G\Delta\gamma}{(1 - D_{n+1})} + \frac{2H^K\Delta\gamma}{3(1 - D_{n+1})}\right]} \tag{e.46}$$

and,

$$\boldsymbol{\varepsilon}_{n+1}^{e} = \boldsymbol{\varepsilon}_{n+1}^{e\,trial} - \Delta\gamma\left[\frac{\boldsymbol{\eta}_{n+1}}{(1-D_{n+1})} + \frac{1}{3}\sigma_y q_1 q_2 f_{n+1}\sinh\left(\frac{3q_2 p_{n+1}}{2\sigma_y}\right)\boldsymbol{I}\right]$$
$$\Delta\bar{\varepsilon}^{p} = \Delta\gamma\sqrt{\frac{2}{3}\left\{\frac{\boldsymbol{\eta}_{n+1}:\boldsymbol{\eta}_{n+1}}{(1-D_{n+1})^2} + \frac{1}{3}\left[\sigma_y q_1 q_2 f_{n+1}\sinh\left(\frac{3q_2 p_{n+1}}{2\sigma_y}\right)\right]^2\right\}} \tag{e.47}$$

Regarding the linearization procedure, the following linearized system of equations needs to be solved by Newton Raphson method:

$$\begin{bmatrix} \frac{\partial r_{\Delta\gamma}}{\partial\Delta\gamma} & \frac{\partial r_{\Delta\gamma}}{\partial p} & \frac{\partial r_{\Delta\gamma}}{\partial f} & \frac{\partial r_{\Delta\gamma}}{\partial R} & \frac{\partial r_{\Delta\gamma}}{\partial D} \\ \frac{\partial r_p}{\partial\Delta\gamma} & \frac{\partial r_p}{\partial p} & \frac{\partial r_p}{\partial f} & \frac{\partial r_p}{\partial R} & \frac{\partial r_p}{\partial D} \\ \frac{\partial r_f}{\partial\Delta\gamma} & \frac{\partial r_f}{\partial p} & \frac{\partial r_f}{\partial f} & \frac{\partial r_f}{\partial R} & \frac{\partial r_f}{\partial D} \\ \frac{\partial r_R}{\partial\Delta\gamma} & \frac{\partial r_R}{\partial p} & \frac{\partial r_R}{\partial f} & \frac{\partial r_R}{\partial R} & \frac{\partial r_R}{\partial D} \\ \frac{\partial r_D}{\partial\Delta\gamma} & \frac{\partial r_D}{\partial p} & \frac{\partial r_D}{\partial f} & \frac{\partial r_D}{\partial R} & \frac{\partial r_D}{\partial D} \end{bmatrix}^{k} \begin{bmatrix} \delta\Delta\gamma \\ \delta p \\ \delta f \\ \delta R \\ \delta D \end{bmatrix}^{k+1} = -\begin{bmatrix} r_{\Delta\gamma} \\ r_p \\ r_f \\ r_R \\ r_D \end{bmatrix}^{k}, \tag{e.48}$$

where:

$$\frac{\partial r_{\Delta\gamma}}{\partial\Delta\gamma} = -\frac{1}{\left[1 + \frac{2G\Delta\gamma}{(1-D)} + \frac{2H^k\Delta\gamma}{3(1-D)}\right]}\left[\frac{2\Delta\gamma}{(1-D)} + \frac{2\Delta\gamma}{3(1-D)}\right]$$
$$\left\{\boldsymbol{\eta}_{n+1}^{trial}:\boldsymbol{\eta}_{n+1}^{trial} + \frac{1}{3}\left[\Delta\gamma\frac{2}{3}H^K\sigma_y q_1 q_2 f_{n+1}\sinh\left(\frac{3q_2 p_{n+1}}{2\sigma_y}\right)\right]^2\right\}\frac{1}{(1-D)}$$
$$+\frac{1}{2\left[1 + \frac{2G\Delta\gamma}{(1-D_{n+1})} + \frac{2H^K\Delta\gamma}{3(1-D_{n+1})}\right]^2} \tag{e.49}$$
$$\left\{\frac{2}{3}\Delta\gamma\left[\frac{2}{3}H^K\sigma_y q_1 q_2 f_{n+1}\sinh\left(\frac{3q_2 p_{n+1}}{2\sigma_y}\right)\right]^2\right\}\frac{1}{(1-D)}$$

$$\frac{\partial r_{\Delta\gamma}}{\partial p} = \frac{1}{2\left[1+\frac{2G\Delta\gamma}{(1-D_{n+1})}+\frac{2H^K\Delta\gamma}{3(1-D_{n+1})}\right]^2}$$

$$\left\{\frac{2}{3}\left[\left(\frac{2}{3}\Delta\gamma H^K\sigma_y q_1 q_2 f_{n+1}\right)^2\cosh\left(\frac{3q_2p_{n+1}}{2\sigma_y}\right)\sinh\left(\frac{3q_2p_{n+1}}{2\sigma_y}\right)\right]\right\}\frac{1}{(1-D)} \qquad \text{(e.50)}$$

$$+q_1q_2f_{n+1}\sigma_y\sinh\left(\frac{3q_2p_{n+1}}{2\sigma_y}\right)$$

$$\frac{\partial r_{\Delta\gamma}}{\partial f} = \frac{1}{2\left[1+\frac{2G\Delta\gamma}{(1-D_{n+1})}+\frac{2H^K\Delta\gamma}{3(1-D_{n+1})}\right]^2}$$

$$\left\{\frac{2}{3}\left[\left(\frac{2}{3}\Delta\gamma H^K\sigma_y q_1 q_2\sinh\left(\frac{3q_2p_{n+1}}{2\sigma_y}\right)\right)^2 f_{n+1}\right]\right\}\frac{1}{(1-D)} \qquad \text{(e.51)}$$

$$-\frac{2}{3}{\sigma_y}^2\left[q_3f_{n+1}-q_1\cosh\left(\frac{3q_2p_{n+1}}{2\sigma_y}\right)\right]$$

$$\frac{\partial r_{\Delta\gamma}}{\partial R} = -\frac{1}{2\left[1+\frac{2G\Delta\gamma}{(1-D_{n+1})}+\frac{2H^K\Delta\gamma}{3(1-D_{n+1})}\right]^2}$$

$$\left\{\frac{2}{3}\left[\left(\frac{2}{3}\Delta\gamma H^K q_1 q_2 f_{n+1}\right)^3\left(\sigma_y H^I\sinh\left(\frac{3q_2p_{n+1}}{2\sigma_y}\right)\right)^2\right]\right\}\frac{1}{(1-D)}$$

$$-\frac{2}{3}\sigma_y H\left[1+{q_3f_{n+1}}^2-2q_1f_{n+1}\cosh\left(\frac{3q_2p_{n+1}}{2\sigma_y}\right)\right] \qquad \text{(e.52)}$$

$$-q_1q_2f_{n+1}p_{n+1}H\sinh\left(\frac{3q_2p_{n+1}}{2\sigma_y}\right)$$

$$\frac{\partial r_{\Delta\gamma}}{\partial d} = \frac{1}{\left[1 + \frac{2G\Delta\gamma}{(1-D)} + \frac{2H^k\Delta\gamma}{3(1-D)}\right]^3}\left[\frac{2G\Delta\gamma}{(1-D)^2} + \frac{2H^k\Delta\gamma}{3(1-D)^2}\right]$$

$$\left\{\boldsymbol{\eta}_{n+1}^{trial} : \boldsymbol{\eta}_{n+1}^{trial} + \frac{1}{3}\left[\Delta\gamma\,\frac{2}{3}H^K\sigma_y q_1 q_2 f_{n+1}\sinh\left(\frac{3q_2 p_{n+1}}{2\sigma_y}\right)\right]^2\right\}\frac{1}{(1-D)} \qquad \text{(e.53)}$$

$$-J_{2\,n+1}\frac{1}{(1-D)^2}$$

LIST OF FIGURES

LIST OF TABLES

LIST OF BOXES

REFERENCES

Andrade Pires, F.M., César de Sá, J.M.A., Costa Sousa, L., Natal Jorge, R.M. (2003). Numerical Modelling of ductile plastic damage in bulk metal forming, *International Journal of Mechanical Sciences*, 45:273–294.

Bai, Y., Wierzbicki, T. (2007). A new model of metal plasticity and fracture with pressure and Lode dependence, *International Journal of Plasticity*, 24:1071-1096.

Bai, Y. (2008). Effect of Loading History on Necking and Fracture. Ph.D Thesis, *Massachusetts Institute of Technology*.

Bao, Y. (2003). Predition of Ductile Crack Formation in Uncrecked Bodies. Ph.D Thesis, *Massachusetts Institute of Technology*.

Bao, Y., Wierzbicki, T. (2004). On fracture locus in the equivalent strain and stress triaxiality space. *International Journal of Mechanical Sciences.* 46 (81):81-98.

Bardet, J. P. (1990). Lode Dependence for Isotropic Pressure-Sensitive Elastoplastic materials. *Jornal of Applied Mechanics*, 57:498-506.

Barsoum, I., Faleskog, J. (2007a). Rupture in combined tension and shear: experiments. *International Journal of Solids and Structures*, 44:1768–1786.

Barsoum, I., Faleskog, J. (2007b). Rupture in combined tension and shear: micromechanics. *International Journal of Solids and Structures*, 44:5481–5498.

Besson, J., Steglich, D. and Brocks, W. (2001). Modeling of crack growth in round bars and plane strain specimens. *International Journal of Solids and Structures*, 38(46–47):8259–8284.

Besson, J., (2010). Continuum Models of Ductile Fracture: A Review. *International Journal of Damage Mechanics*, 19:3-52.

Bridgman, P., 1952. Studies in Large Plastic and Fracture. McGraw-Hill Book Company, London.

Brünig, M., Chyra, O., Albrecht, D., Driemeier, L., Alves, M. (2008). A ductile damage criterion at various stress triaxialities, *International Journal of Plasticity*, 24: 1731–1755.

Brünig, M., Berger, S., Obrecht, H. (2000). Numerical simulation of the localization behavior of hydrostatic-stress-sensitive metals. *International Journal of Mechanical Sciences*, 42:2147-2166.

Brünig, M., (1999). Numerical simulation of the large elastic-plastic deformation behavior of hydrostatic stress-sensitive solids. International Journal of Plasticity 15, 1237-1264.

Butcher, C., Chen, Z., Bardelcik, A., Worswick M., (2009). Damage-based finite-element modeling of tube hydroforming. International Journal of Fracture, 155:55–65.

Cao, J., Yao, H., Karafillis, A. and Boyce, M. C., (2000). Prediction of localized thinning in sheet metal using a general anisotropic yield criterion. International Journal of Plasticity, 16(9):1105–1129.

Cescotto, S., & Zhu, Y. (1995). Modeling of ductile fracture initiation during bulk metal forming. In D. Owen, & E. Oñate, Computational Plasticity - Fundamentals and Applications (pp. 987-998). Swansea: Pineridge Press.

Chaboche, J.L. (1984). Anisotropic Creep Damage in the Framework of Continuum Damage Mechanics. *Nuclear Engineering and Design,*79: 309–319.

Chaboche, J.L. (1987). Continuum Damage Mechanics: Presents State and Future Trends. *Nuclear Engineering and Design,* 105:19-33.

Chaboche, J.L. (2003). Damage mechanics. *In: Milne, I., Ritchie, R.O. and B. Karihaloo (eds.) Comprehensive Structural Integrity*, vol. 2. Elsevier-Pergamon, pp. 213–284.

Chaboche, J.L., Boudifa, M., Saanouni, K., (2006). A CDM approach of ductile damage with plastic compressibility. *International Journal of Fracture*, 137:51–75.

Chow, C. L., Yu, L. G., Tai, W. H. and Demeri. M. Y., (2001). Prediction of forming limit diagrams for al6111-t4 under non-proportional loading. International Journal of Mechanical Sciences, 43(2):471–486.

Chu, C. C. and A. Needleman (1980). "Void Nucleation Effects In Biaxially Stretched Sheets." Journal Of Engineering Materials And Technology-Transactions of the ASME 102(3): 249-256.

Clift, S., Hartley, P., Sturgess, C., & Rowe, G. (1990). Fracture prediction in plastic deformation process. International Journal of Mechanics Science , pp. 1-17.

Cockcroft, M., & Latham, D. (1968). Ductility and workability of metals. J. Inst. Metals , pp. 33-39.

Coleman, B.D., & Gurtin, M.E. (1967). Thermodynamics with Internal State Variables. J. Chemical Physics, 47(2), 597–613.

Datsko, J. (1966). Material Properties and Manufacturing Process. New York: John Wiley & Sons.

De Souza Neto, E.A., Peri´c, D., Dutko, M., & Owen, D.R.J. (1996). Design of Simple Low Order Finite Elements for Large Strain Analysis of Nearly Incompressible Solids. *International Journal of Solids and Structures*, 33:3277–3296.

De Souza Neto E.A. (2002). A fast, one-equation integration algorithm for the Lemaitre ductile damage model. *Comm. Num. Meth. Engng.,*18:541–554.

De Souza Neto, E.A., Peri´c, Owen, D.R.J. (2008). Computational methods for plasticity: theory and applications. *John Wiley & Sons Ltd*.

Driemeier, L., Brünig, M., Micheli, G., Alves, M., (2010), Experiments on stress-triaxiality dependence of material behavior of aluminum alloys, *Mechanics of Materials*, vol.42, 2:207-217.

Engelen, Roy A.B. (2005). Plasticity-induced Damage in Metals / nonlocal modelling at finite strains. PhD Thesis – Eindhoven : Technische Universiteit Eindhoven.

Eterovic, A.L., & Bathe, K.-J. (1990). A Hyperelastic Based Large Strain Elasto-Plastic Constitutive Formulation with Combined Isotropic-Kinematic Hardening Using the Logarithmic Stress and Strain Measures. Int*. J. Num. Meth. Engng.*, 30, 1099–1114.

Freudenthal, A. (1950). The Inelastic Behavior of Engineering Materials and Strucutures. New York: John Wiley & Sons.

Gao, X., Wang, T., Kim, J., (2005). On ductile fracture initiation toughness: effects of void volume fraction, void shape and void distribution. *Int. J. Solids Struct.* 42, 5097–5117.

Gao, X., Kim, J., (2006). Modeling of ductile fracture: significance of void coalescence. *Int. J. Solids Struct.* 43, 6277–6293.

Gao, X., Zhang, G., Roe, C., (2009). A study on the effect of the stress state on ductile fracture. *Int. J. Damage Mech.*, 19, 75–94.

Gao, X., Zhang, T., Zhou, J., Graham, S.M., Hayden, M., Roe, C. (2011), On stress-state dependent plasticity modeling: Significance of the hydrostatic stress, the third invariant of stress deviator and the non-associated flow rule, International Journal of Plasticity, vol. 27, 2:217-231.

Gillemont, L. F., (1976), Criterion of crack initiation and spreading, Engng. Frac. Mech., 8, 239-253.

Gouveia, B., Rodrigues, J., & Martins, P. (1995). Fracture Predicting in Bulk Metal Forming. International Journal of Mechanical Sciences , pp. 361-372.

Graf, A. and Hosford, W., (1994). The influence of strain-path changes on forming limit diagrams of a1 6111 t4. International Journal of Mechanical Sciences, 36(10):897–910.

Gurson, A.L. (1977). Continuum Theory of ductile rupture by void nucleation and growth - Part I. Yield criteria and flow rules for porous ductile media. *J. Engrg. Mat. Tech.,* 99:2-15.

Gurtin, M.E. (1981). An Introduction to Continuum Mechanics. Academic Press.

Hancock, J. W., Mackenzie, A. C. (1976). On the mechanisms of ductile failure in high-strength steels subjected to multi-axial stress-states. Journal of the Mechanics and Physics of Solids, 24:147–160.

Holzapfel, G.A. (2000). Nonlinear Solid Mechanics. A Continuum Approach for Engineering. London: John Wiley & Sons.

Jiang, Y. and Sehitoglu, H., (1996), Comments on the Mroz Multiple Surface Type Plasticity Models. J. Solids Structures Vol. 33, No. 7, pp. 1053-1068.

Jiang, Y. and Kurach, P., (1996) Characteristic of THe Armstrong-Frederick Type Plasticity Models. International Journal of Plasticity 12, 387-415.

Johnson, G.R, Cook, W.H. (1985). Fracture characteristics of three metals subjected to various strains, strain rates, temperatures and pressures. *Engineering Fracture Mechanics*, 21(1):31–48.

Kachanov, L.M. (1958). Time of the Rupture Process under Creep Condition. Izv. Akad. Nauk. SSSR, Otd. Tekhn. Nauk., 8, 26–31.

Kachanov, L. M. (1986). Introduction to continuum damage mechanics, Martinus Nijhoff Publishers.

Kestin, J., & Bataille, J. (1977). Irreversible Thermodynamics of Continua and Internal Variables. Pages 39–67 of: Proceedings of the Int. Symp. on Continuum Models of Discrete Systems. Univ. of Waterloo Press.

Krajčinović, D., Fonseka, G.U. (1981). The Continuous Damage Theory of Brittle Materials – Part 1: General Theory. *J. Appl. Mech.*, 48, 809–815.

Kim, J., Gao, X., Srivatsan, T.S., (2003). Modeling of crack growth in ductile solids: a three-dimensional analysis. *Int. J. Solids Struct.* 40, 7357–7374.

Kim, J., Gao, X., Srivatsan, T.S., (2004). Modeling of void growth in ductile solids: effects of stress triaxiality and initial porosity. *Eng. Frac. Mech.* 71, 379–400.

Kim, J., Zhang, G., Gao, X., (2007). Modeling of ductile fracture: application of the mechanism-based concepts. *Int. J. Solids Struct.* 44, 1844–1862.

Krieg, R.D., & Krieg, .D.B. (1977). Accuracies of Numerical Solution Methods for the Elastic-Perfectly Plastic Model. J. Pressure Vessel Tech., ASME, 99, 510–515.

Lemaitre, J. (1984). How to Use Damage Mechanics. Nuclear Engng. Design, 80, 233–245.

Lemaitre, J. (1985). A continuous damage mechanics model for ductile fracture. *Journal of Engineering Materials and Technology - Trans. of the ASME*, 107:83–89.

Lemaitre, J., Chaboche, J.L. (1990). Mechanics of Solid Materials. Cambridge Univ. Press.

Lemaitre, J. (1996). A Course on Damage Mechanics. 2nd edn. Springer.

Lemaitre, J., Desmorat, R. (2005). Engineering Damage Mechanics, *Springer*.

Lemaitre, J., (2001), Handbook of Materials Behavior Models. Academic Press.

Li, H., Fu, M.W., Lu, J., Yang, H. (2011), Ductile fracture: Experiments and computations, International Journal of Plasticity, vol. 27, 2:147-180.

Malcher, L. ; Andrade Pires, F.M. ; César de Sá, J.M.A ; Andrade, F.X.C . (2009). Numerical integration algorithm of a new model for metal plasticity and fracture including pressure and Lode angle dependence. *International Journal of Material Forming - Springer*, 2:443-446.

Malcher, L. ; Andrade Pires, F.M. ; César de Sá, J.M.A., (2012), An Assessment of Isotropic Damage Constitutive Models under High and Low Stress Triaxialities. International Journal of Plasticity.

McClintock, F. A. (1968). A Criterion for Ductile Fracture by the Growth of Holes. J. Appl. Mech., 35, 363–371.

McClintock, F. A., (1971). Plasticity aspects of fracture. In: Leibowitz, H. (Ed.), Fracture, vol. 3. Academic Press, pp. 47–225.

Mirone, G., Corallo, D., (2010), A local viewpoint for evaluating the influence of stress triaxiality and Lode angle on ductile failure and hardening, International Journal of Plasticity, vol. 26, 3:348-371.

Mirza, M.S., Barton, D.C., Church, P. (1996). The effect of stress triaxiality and strain rate on the fracture characteristics of ductile metals. *J. Mater. Sci.* 31: 453–461.

Muschenborn, W. and Sonne, H., (1975). Influence of the strain path on the forming limits of sheet metal. Arch. Eisenhuttenwes, 46:597–602.

Mudry, F. (1985). Methodology and application of local criteria for prediction of ductile tearing. D.Reidel Publishing Co.

Murakami, S., & Ohno, N. (1981). A Continuum Theory of Creep and Creep Damage. Pages 422–443 of: Ponter, A.R.S. (ed), Proceedings of the IUTAM Symposium on Creep in Structures, Leicester, Berlin.

Nahshon, K., Hutchinson, J. (2008). Modification of the Gurson model for shear failure. *European Journal of Mechanics A/Solids,* 27:1–17.

Onat, E.T., & Leckie, F.A. (1988). Representation of Mechanical Behavior in the Presence of Changing Internal Structure. J. Appl. Mech., 55, 1–10.

Ortiz, M., & Popov, E.P. (1985). Accuracy and Stability of Integration Algorithms for Elastoplastic Constitutive Relations. Int. J. Num. Meth. Engng., 21, 1561–1576.

Oyane, M., Shima, S., & Tabata, T. (1978). Considerations of basic equations, and their application in the forming of metal powders and porous metals. J. Mech. Work. Tech., 1, 325–341.

Pardoen, T., Hutchinson, J.W., (2000), An extended model for void growth and coalescence. Journal of the Mechanics and Physics of Solids 48, 2467–2512.

Peric, D., Owen, D.R.J., & Honnor, M.E. (1992). A Model for Finite Strain Elasto-Plasticity Based on Logarithmic Strains: *Computational Issues. Comp. Meth. Appl. Mech Engng.*, 94:35–61.

Peri´c, D., & Owen, D.R.J. (2004). Encyclopedia of Computational Mechan-ics: Computational modelling of forming processes. Vol. 2. USA, Australia, Germany, Canada: John Wiley & Sons, Ltd.

Pineau, A. (1981). Review of fracture mechanisms and local approaches to predicting crack resistance in low strength steels. In: Franc¸ois, D. et al. (ed.) Advances in Fracture Researches. New-York, Pergamon Press, ICF5. Cannes.

Pineau, A., Pardoen, T. (2003). Damage mechanics. *In: Milne, I., Ritchie, R.O. and B. Karihaloo (eds.) Comprehensive Structural Integrity*, vol. 2. Elsevier-Pergamon, pp. 686–783.

Reis, F.J.P.; Malcher, L. ; Andrade Pires, F.M. ; César de Sá, J.M.A., (2010), A modified GTN model for the prediction of ductile fracture at low stress triaxialities. International Journal of Structural Integrity

Rice, J. R., Tracey, D., M. (1969). On the ductile enlargement of voids in triaxial stress fields. *Journal of the Mechanics and Physics of Solids*, 17:201–217.

Richmond, O. and Spitzig, W. A., (1980). Pressure dependence and dilatancy of plastic flow. In Theoretical and Applied Mechanics, Proceedings of the 15th International Congress of Theoretical and Applied Mechanics., pages 377–386, Toronto, Ont, Can, 1980. North-Holland Publ Co, Amsterdam, Neth.

Rousselier's, G. (1980). Finite deformation constitutive relations including ductile fracture damage. In: Nemat-Nasser (ed.) Three-Dimensional Constitutive Relations and Ductile Fracture. North-Holland Publ. Comp., 1981 pp. 331–355.

Rousselier's, G. (1987). Ductile fracture models and their potential in local approach of fracture. *Nuclear Engineering and Design* 105: 97–111.

Rousselier's, G. (2001). The Rousselier model for porous metal plasticity and ductile fracture. In: Lemaitre, J. (ed.) Handbook of Materials Behavior Models, vol. 2. Academic Press, New York, chapter 6.6, pp. 436–445.

Schittkowski, K., (2001). NLPQL: A New Fortran Implementation of a Seqüencial Quadratic Programming Algorithm for Parallel Computing. Report Department of Mathematics, University of Bayreuth, Alemanha.

Simo, J.C., & Hughes, T.J.R. (1998). Computational Inelasticity. New York: Springer-Verlag.

Simo, J.C., & Hughes, T.R.J. (1987). General Return Mapping Algorithms for Rate-Independent Plasticity. Pages 221–231 of: C.S. Desai et al. (ed), Constitutive Laws for Engineering Materials: Theory and Applications. Elsevier.

Simo, J.C., & Ju, J.W. (1987). Strain- and Stress-Based Continuum Damage Models – I. Formulation and II. Computational Aspects. Int. J. Solids Struct., 23, 821–869.

Simo, J.C. (1985). On the Computational Significance of the Intermediate Configuration and Hyperelastic Stress Relations in Finite Deformation Elastoplasticity. Mech. of Materials, 4, 439–451.

Simo, J.C., & Taylor, R.L. (1985). Consistent Tangent Operators for Rate-Independent Elastoplasticity. Comp. Meth. Appl. Mech. Engng., 48, 101–118.

Stoughton, T., B., Toon, J., W. (2011). A new approach for failure criterion for sheet metals. *International Journal of Plasticity*, vol 27, 440-459.

Stoughton, T., B., (2000). A general forming limit criterion for sheet metal forming. International Journal of Mechanical Sciences, 42(1):1–27.

Tai, W., & Yang, B. (1987). A new damage mechanics criterion for ductile fracture. *Engineering Fracture Mechanics* , pp. 371-378.

Tai, W., & Yang, B. (1986). A new microvoid-damage model for ductile fracture. *Engineering Fracture Mechanics* , pp. 377-384.

Teng, X., Wierzbicki, T. (2006). Evaluation of six fracture models in high velocity perforation. E*ngineering Fracture Mechanics*, 73(12):1653–1678.

Teng, X. (2008). Numerical prediction of slant fracture with continuum damage mechanics. *Engineering Fracture Mechanics*, 75:2020–2041.

Truesdell, C. (1969). Rational Thermodynamics. New York: McGraw-Hill.

Tvergaard, V. and Needleman, A. (1984). Analysis of the cup-cone fracture in a round tensile bar. *Acta Met.* 32:157–169.

Tvergaard, V. (2008). Shear deformation of voids with contact modeled by internal pressure. *International Journal of Mechanical Sciences*, 50:1459–1465.

Vaz Jr., M. (1998). Computational approaches to simulation of metal cutting process. Ph.D Thesis, University College of Swansea, Wales, U.K.

Wilson, C., D., (2002), A critical re-examination of classical metal plasticity. Journal of Applied Mechanics, Transactions ASME, 69(1):63–68, ISSN 0021-8936.

Xue, L. (2007). Ductile Fracture Modeling – Theory, Experimental Investigation and Numerical Verification, Ph.D Thesis, *Massachusetts Inst. of Technology*.

Xue, L. (2008). Constitutive modeling of void shearing effect in ductile fracture of porous materials. *Engineering Fracture Mechanics*, 75: 3343–3366.

Young-Woong, L. (2003). Fracture Prediction in Metal Sheets, Ph.D Thesis, *Massachusetts Inst. of Technology*.

Voyiadjis, G.Z., Kattan, P.I., (1999). Advances in Damage Mechanics: Metals and Metal Matrix Composites. Elsevier, Amsterdam.

Zadpoor, A.A., Sinke, J., Benedictus, R. (2009). Formability prediction of high strength aluminum sheets, *International Journal of Plasticity,* 25:2269–2297.

Zhang, K. S., Bai, J. B., and Francois, D., (2000). Numerical analysis of the influence of the lode parameteron void growth. International Journal of Solids and Structures, 38(32-33):5847–5856.